

Synthesis and Characterisation of Oxychalcogenides As Promising
Thermoelectric Materials For Waste Heat Recovery

by

Son Dac Ngoc Luu

A thesis submitted for the degree of Doctor of Philosophy

Heriot-Watt University

Institute of Chemical Sciences

Sep 2015

The copyright in this thesis is owned by the author. Any quotation from the thesis or use of any of the information contained in it must acknowledge this thesis as the source of the quotation or information.

ABSTRACT

This dissertation describes the preparation and investigation of crystal structure and thermoelectric properties of solid-solutions within three families of layered bismuth oxychalcogenides: BiOCuCh ($Ch = \text{S, Se, Te}$), $\text{Bi}_2\text{YO}_4\text{Cu}_2\text{Se}_2$, and $\text{Bi}_2\text{O}_2\text{Ch}$ ($Ch = \text{Se, Te}$). The crystal structures of all materials were investigated using powder X-ray and neutron diffraction (for BiOCuCh). BiOCuCh ($Ch = \text{S, Se, Te}$) compounds crystallise in the ZrCuSiAs structure type ($P4/nmm$ space group), and are composed of fluorite-type $[\text{Bi}_2\text{O}_2]^{2+}$ and anti-fluorite-type $[\text{Cu}_2\text{Ch}_2]^{2-}$ slabs, stacked alternatively along the c – axis. Results show that BiOCuCh ($Ch = \text{S, Se, Te}$) are p-type semiconductors. The electrical conductivity increases while thermal conductivity decreases systematically with changing from S to Te in these compounds. Analysis of neutron diffraction data shows that the rattling behaviour of copper in a rigid framework (BiOCh) is at the origin of their low thermal conductivity. The figure of merit increases with increasing atomic weight of the chalcogenide. BiOCuSe shows the larger potential for thermoelectric applications in terms of its combination of economic cost and properties. Therefore, the effect of doping with divalent cations (Pb^{2+} , Cd^{2+} , Zn^{2+}) on BiOCuSe was studied. Results show that substitution of trivalent Bi^{3+} with a 4-5 at.% of divalent Pb^{2+} leads to an enhancement of the power factor and a high figure of merit ($ZT \sim 0.62$ at 673 K), whilst the substitution of monovalent Cu^+ with divalent Cd^{2+} or Zn^{2+} leads to an increase in the magnitude of the electrical resistivity and the Seebeck coefficient. In addition, a reduction of the thermal conductivity ($\kappa \sim 0.77 \text{ W m}^{-1} \text{ K}^{-1}$) is achieved in ball-milled $\text{Bi}_{0.95}\text{Pb}_{0.05}\text{OCuSe}$.

$\text{Bi}_2\text{YO}_4\text{Cu}_2\text{Se}_2$ crystallises in the $\text{Sr}_2\text{Mn}_3\text{Sb}_2\text{O}_2$ structure type ($I4/mmm$ space group), and consists of fluorite-type $[\text{Bi}_2\text{MO}_4]^+$ and anti-fluorite-type $[\text{Cu}_2\text{Ch}_2]^-$ layers stacked alternatively along the c – axis. It possesses metallic behaviour, with hole charge carriers and a fairly low figure of merit ($ZT \sim 3 \times 10^{-2}$ at 673 K). This behaviour is related to the oxidation state of the copper (+1.5) in which more hole charge carriers have been produced.

$\text{Bi}_2\text{O}_2\text{Ch}$ ($Ch = \text{Se, Te}$) crystallises in the anti- ThCr_2Si_2 structure ($I4/mmm$ space group) and comprises fluorite-type $[\text{Bi}_2\text{O}_2]^{2+}$ and square net Ch^{2-} stacked alternatively along the c – axis. Results show that $\text{Bi}_2\text{O}_2\text{Te}_{1-x}\text{Se}_x$ ($0 \leq x \leq 0.25$) are n-type semiconductors, and that $\text{Bi}_2\text{O}_2\text{Te}$ shows the highest figure of merit ($ZT \sim 1.3 \times 10^{-1}$ at 573 K) while $\text{Bi}_2\text{O}_2\text{Te}_{1-x}\text{Se}_x$ ($0.5 \leq x \leq 1$) and $\text{Bi}_2\text{O}_2\text{Se}_{1 \pm \delta}$ ($0.05 \leq \delta \leq 0.15$) solid solutions show insulating behaviour.

ACKNOWLEDGEMENTS

This PhD. would have been impossibly finished without the support of many great people, groups and institutions. I would like to take this opportunity to express my sincere gratitude to them for all their help.

First and foremost, I would like to thank Dr. Paz Vaqueiro, a very conscientious supervisor that I could ever hope for. Thanks for her guidance, support and fruitful discussions during my PhD life. Her patience and enthusiasm on advising and correcting my dissertation are highly appreciated. Without her, I am definitely far away from this end of dissertation.

Special thanks would go to my second supervisor, Dr. Jan - Willem Bos and Prof. Anthony V. Powell. Without their supports, I would not have been able to start and complete the work in this dissertation favourably. It is a great honour for me to have been a part of Prof. Anthony V. Powell's group.

I would like to thank Prof. Andrew R. Knox (Glasgow University) and Mr. Kevin Simpson (European Thermodynamics Ltd) for initially helpful discussion and advices.

I also would like to acknowledge the financial supports of Heriot-Watt University, European Thermodynamics Ltd, Energy Technology Partnership in this project and University of Reading for offering me a position of visiting research student.

I am indebted to Dr. Sarah Ewing. She is not only a good colleague but also the best friend. She has always encouraged me to overcome all obstacles during my study life.

Thanks to Dr. Jack Corps, Dr. Steven Fuhrmann, Dr. Ruth Downie, Dr. Vijay Srirambhatla, Dr. Jesús Prado-Gonjal, Dr. Srinivas Popuri, Maryana Assad, Sarah Makin, Gabin Guélou and other members in our research group for their precious help as well as having good time together.

Thanks are also extended to:

Mr. Alan Barton, Paul Allan (Heriot – Watt university), Mark McClemon, Nick Spencer (University of Reading), for their technical supports.

Dr Ron Smith for his assistance during neutron diffraction experiments at ISIS.

Dr. Jim Buckman (Heriot-Watt University), Dr. Peter J F Harris and Ms. Amanpreet Kaur (University of Reading) for their assistance during SEM measurements.

Dr. Olga Khutoryanskaya (University of Reading) for her training on using TGA equipment.

And other administration staffs in Heriot-Watt University and University of Reading.

Finally, I would like to thanks my family for supporting me all times.

DECLARATION STATEMENT



ACADEMIC REGISTRY Research Thesis Submission

Name:	Son Dac Ngoc Luu		
School/PGI:	School of Engineering and Physical Sciences/ Institute of Chemical Sciences (ICS)		
Version: (<i>i.e.</i> <i>First,</i> <i>Resubmission,</i> <i>Final</i>)	Final	Degree Sought (Award and Subject area)	PhD Chemistry

Declaration

In accordance with the appropriate regulations I hereby submit my thesis and I declare that:

- 1) The thesis embodies the results of my own work and has been composed by myself
- 2) Where appropriate, I have made acknowledgement of the work of others and have made reference to work carried out in collaboration with other persons
- 3) The thesis is the correct version of the thesis for submission and is the same version as any electronic versions submitted*.
- 4) My thesis for the award referred to, deposited in the Heriot-Watt University Library, should be made available for loan or photocopying and be available via the Institutional Repository, subject to such conditions as the Librarian may require
- 5) I understand that as a student of the University I am required to abide by the Regulations of the University and to conform to its discipline.

**Please note that it is the responsibility of the candidate to ensure that the correct version of the thesis is submitted.*

Signature of Candidate:		Date:	
-------------------------	--	-------	--

Submission

Submitted By (<i>name in capitals</i>):	
Signature of Individual Submitting:	
Date Submitted:	

For Completion in the Student Service Centre (SSC)

Received in the SSC by (<i>name in capitals</i>):			
Method of Submission (<i>Handed in to SSC; posted through internal/external mail</i>):			
E-thesis Submitted (mandatory for final theses)			
Signature:		Date:	

TABLE OF CONTENTS

Synthesis and Characterisation of Oxychalcogenides As Promising Thermoelectric Materials For Waste Heat Recovery	i
LIST OF PUBLICATIONS BY THE CANDIDATE.....	vii
LIST OF ABBREVIATIONS.....	viii
Chapter 1 Introduction	1
1.1 Motivation	1
1.2 Thermoelectric Power Generation	2
1.2.1 Thermoelectric Devices	2
1.2.2 Figure of Merit and Approaches to Its Improvement	4
1.2.3 Natural Superlattice.....	10
1.3 Thermoelectric Materials	11
1.3.1 Metal Oxides	12
1.3.2 Metal Chalcogenides and Complex Solid Solutions.....	12
1.4 Layered Oxychalcogenides	13
1.4.1 Introduction	13
1.4.2 Some Common Structure Types and Their Interrelationship	14
1.1.1.1 Compounds With $(A_{2m}O_{2m})Ch_{2m-1}$ Structures	16
1.1.1.2 Compounds with $(A_2O_2)Ch_2$ Structures.....	19
1.1.1.3 Compounds with AOBCh Structures.....	20
1.1.1.4 Compounds with $(A_2O_2)(BCh_2)$ Structures	21
1.1.1.5 Compounds with $(A_2MO_2)(B_2Ch_2)$ Structures	21
1.1.1.6 Compounds with $(A_2M_2O)(B_2Ch_2)$ Structures	22
1.1.1.7 Compounds with $(A_2O_2)(B_2OCh_2)$ Structures	23
1.1.1.8 Compounds with Thicker Oxide Layers.....	23
1.1.1.9 Compounds with Thicker Chalcogenide Layers.....	25
1.4.3 Thermoelectric Properties	26
1.5 Aims	27

Chapter 2	Experimental Techniques.....	29
2.1	Introduction.....	29
2.2	Synthesis Methods.....	29
2.2.1	Solid State Reaction.....	29
2.2.2	Ball Milling Process.....	30
2.3	Characterisation Methods.....	31
2.3.1	Powder X-ray Diffraction.....	31
2.3.2	Powder Neutron Diffraction.....	33
2.3.2.1	The Polaris.....	35
2.3.3	Structural Refinement Using Powder Diffraction Data.....	37
2.3.3.1	Unit Cell Refinement.....	37
2.3.3.2	Rietveld Refinement.....	37
2.3.4	Thermogravimetric Analysis (TGA).....	39
2.3.5	Scanning Electron Microscope (SEM).....	40
2.4	Physical Properties Measurements.....	42
2.4.1	Hot Pressing.....	42
2.4.2	Ingot Fabrication.....	43
2.4.3	Electrical Resistivity.....	43
2.4.3.1	Low Temperature Measurements.....	44
2.4.3.2	Manual Measurements for Materials with Low Electrical Resistance	45
2.4.3.3	LabView Controlled Automatic Measurements.....	45
2.4.3.4	High Temperature Measurements.....	46
2.4.4	Hall Measurements.....	46
2.4.4.1	Hall Coefficient.....	47
2.4.4.2	Van De Pauw Method.....	48
2.4.4.3	Carrier Concentration and Hall Mobility.....	49
2.4.4.4	Sample Preparation.....	49
2.4.5	Seebeck Coefficient.....	50

2.4.5.1	Low Temperature Measurements	50
2.4.5.2	High Temperature Measurements.....	51
2.4.6	Thermal Conductivity	51
Chapter 3	Layered Oxychalcogenides BiOCuCh (<i>Ch</i> = S, Se, Te) and Bi ₂ YO ₄ Cu ₂ Se ₂	54
3.1	Introduction	54
3.2	Experimental Procedure	54
3.2.1	Sample Preparation	54
3.2.1.1	BiOCuS.....	55
3.2.1.2	BiOCuSe	55
3.2.1.3	BiOCuTe.....	55
3.2.1.4	Bi ₂ O ₂ Cu ₄ Se ₃	55
3.2.1.5	Bi ₂ YO ₄ Cu ₂ Se ₂	56
3.2.2	Characterisation and Physical Property Measurements	56
3.2.2.1	Structural Characterisation	56
3.2.2.1.1	X-Ray Diffraction.....	56
3.2.2.1.2	Neutron Diffraction	57
3.2.2.2	Microstructural Characterisation	57
3.2.2.3	Thermal Analysis.....	57
3.2.2.4	Electrical Transport Measurements	57
3.2.2.5	Thermal Transport Measurements	58
3.3	Results and Discussion.....	58
3.3.1	BiOCuCh (<i>Ch</i> = S, Se and Te) Compounds.....	58
3.3.1.1	Structural Characterisation	58
3.3.1.2	Microstructural Characterisation	67
3.3.1.3	Thermal Stability	68
3.3.1.4	Electrical Transport Properties	69
3.3.1.4.1	Low Temperature Electrical Transport Properties	69
3.3.1.4.2	High Temperature Electrical Transport Properties	71

3.3.1.5	Thermal Transport Properties and Figure of Merit ZT	73
3.3.1.5.1	Thermal Transport Properties	73
3.3.1.5.2	Figure of Merit ZT	74
3.3.2	$\text{Bi}_2\text{O}_2\text{Cu}_4\text{Se}_3$	75
3.3.3	$\text{Bi}_2\text{YO}_4\text{Cu}_2\text{Se}_2$	76
3.3.3.1	Structural Characterisation	76
3.3.3.2	Electrical Transport Properties	79
3.3.3.3	Thermal Conductivity and Figure of Merit.....	81
Chapter 4	Substitution of Divalent Cations on BiOCuSe and Synthesis by Mechanical Ball Milling	83
4.1	Introduction	83
4.2	Experimental Procedure	84
4.2.1	Sample Preparation	84
4.2.1.1	$\text{Bi}_{1-x}\text{Pb}_x\text{OCuSe}$ Compounds ($0 \leq x \leq 0.2$).....	84
4.2.1.2	Ball milled $\text{Bi}_{1.95}\text{Pb}_{0.05}\text{OCuSe}$ Powder	84
4.2.1.3	$\text{BiOCu}_{1-x}\text{M}_x\text{Se}$ ($\text{M} = \text{Cd}, \text{Zn}; 0 \leq x \leq 0.2$) Compounds	85
4.2.2	Characterization and Physical Property Measurements	85
4.2.2.1	Structural and Microstructure Characterisation	85
4.2.2.2	Physical Properties Measurements	86
4.3	Results and Discussion.....	86
4.3.1	$\text{Bi}_{1-x}\text{Pb}_x\text{OCuSe}$ Compounds ($0 \leq x \leq 0.2$).....	86
4.3.1.1	Structural and Microstructural Characterisation.....	86
4.3.1.2	Electrical and Thermal Transport Properties	93
4.3.2	Ball milled $\text{Bi}_{1.95}\text{Pb}_{0.05}\text{OCuSe}$	100
4.3.2.1	Structural and Microstructure Characterisation	100
4.3.2.2	Electrical transport properties	103
4.3.2.3	Thermal Conductivity and Figure of Merit.....	104
4.3.3	$\text{BiOCu}_{1-x}\text{M}_x\text{Se}$ ($\text{M} = \text{Cd}, \text{Zn}; 0 \leq x \leq 0.2$) Compounds.....	106
4.3.3.1	Structural Characterisation	106

4.3.3.2	Electrical Transport Properties	109
4.3.3.3	Thermal Transport Properties and Figure of Merit ZT.....	111
Chapter 5	Structures and Thermoelectric Properties of n-type Oxychalcogenide Bi ₂ O ₂ Ch (Ch = Te, Se) Materials.....	114
5.1	Introduction.....	114
5.2	Experimental Procedure.....	115
5.2.1	Sample Preparation	115
5.2.1.1	Bi ₂ O ₂ Te _{1-x} Se _x (0 ≤ x ≤ 1).....	115
5.2.1.2	Bi ₂ O ₂ Se _{1±δ} (0.05 ≤ δ ≤ 0.15).....	115
5.2.2	Characterization and Physical Property Measurements.....	115
5.2.2.1	Structural and Microstructural Characterisation.....	115
5.2.2.2	Thermal Analysis.....	116
5.2.2.3	Electrical transport measurements	116
5.2.2.4	Thermal transport measurements.....	116
5.3	Results and Discussion.....	117
5.3.1	Bi ₂ O ₂ Te _{1-x} Se _x (0 ≤ x ≤ 1) Compounds.....	117
5.3.1.1	Structural and Morphological Characterisation.....	117
5.3.1.2	Thermal Stability	124
5.3.1.3	Electrical Transport Properties	125
5.3.1.4	Thermal Transport Properties and Figure of Merit ZT.....	131
5.3.2	Bi ₂ O ₂ Se _{1±δ} (0.05 ≤ δ ≤ 0.15) Compounds.....	133
5.3.2.1	Structural and Morphological Characterisation.....	133
5.3.2.2	Electrical Transport Properties	138
5.3.2.3	Thermal Transport Properties	140
Chapter 6	Conclusions.....	143
6.1	BiOCuCh (Ch = S, Se, Te) and Effect of Divalent Cation Doping on BiOCuSe 143	
6.2	Bi ₂ O ₂ Cu ₄ Se ₃ Compound	144
6.3	Bi ₂ MO ₄ Cu ₂ Se ₂ (M = Y) Compound	144

6.4	$\text{Bi}_2\text{O}_2\text{Ch}$ ($\text{Ch} = \text{Te}, \text{Se}$) Compounds.....	144
6.5	Final Remarks	145
	References	146
	Appendix A	163
	Appendix B	186
	Appendix C	196

LIST OF PUBLICATIONS BY THE CANDIDATE

1. S. D. N. Luu and P. Vaqueiro, “*Synthesis, Structural Characterisation and Thermoelectric Properties of $Bi_{1-x}Pb_xOCuSe$* ”, J. Mater. Chem. A, **2013**, 1, 12270-12275.
2. S. D. N. Luu and P. Vaqueiro, “*Thermoelectric properties of $BiOCu_{1-x}M_xSe$ ($M = Cd$ and Zn)*”, Semicond. Sci. Tech., **2014**, 29, 064002.
3. S. D. N. Luu and P. Vaqueiro, “*Synthesis, Characterisation and Thermoelectric Properties of The Oxytelluride Bi_2O_2Te* ”, J. Solid State Chem., **2015**, 226, 219-223.
4. P. Vaqueiro, S. D. N. Luu, G. Guélou, A. V. Powell, R. I. Smith, R. A. R. A. Orabi, J-P. Song, D. Wee, and M. Fornari, “*The Role of Copper Rattling In Thermal Conductivity of Thermoelectric Oxychalcogenides: Do Lone Pairs Matter?*” (submitted).

LIST OF ABBREVIATIONS

TE	Thermoelectric
ZT	Thermoelectric figure of merit
PF	Thermoelectric power factor
PGEC	Phonon glass electron crystal
DOS	Density of states
CCP	Cubic close packed structure
CN	Coordination number
XRD	X-ray diffraction
GSAS	General structure analysis system
EDX	Energy dispersive X-ray analysis
SEM	Scanning electron microscopy
ADP	Atomic displacement parameter
BM	Ball milling
SSS	Solid state reaction
HP	Hot-press
HP_SSS	Hot-pressed sample synthesised by solid state reaction
HP_BM	Hot-pressed ball milled sample
SPS	Spark plasma sintering
FWHM	Full width at half maximum

Chapter 1 Introduction

1.1 Motivation

In recent years, population growth and depletion of fossil fuel reserves make our world hungry for energy. Indeed, the estimation of average global electrical power consumption was around 17.4 terawatts in 2011 [1]. It has been predicted that this consumption will continuously increase, to double or triple by 2050 and 2100, respectively [2]. Furthermore, the impact of global climate change, causing the warming of the earth due to CO₂ emissions (as around 80% of most energy comes from fossil fuels), is also a serious problem. This draws attention on efforts to ensure a green, sustainable environment for the future. Therefore, renewable energies including solar, wind, biomass, hydro and advanced energy recovery technologies have been taken into account in order to achieve an energy usage more effectively [3]. Nevertheless, heat, produced by automobiles, industrial facilities, power plants, and even through home heating, is discarded into the atmosphere or water as a waste. Indeed, more than 60% of the primary energy in fossil fuels is released as waste heat [4]. This raises the question of how to convert this waste heat into usable energy [5]. In the past, a costly boiler – turbine system was designed for factories to harvest waste heat but this is not efficient enough to make an economic sense [3, 6]. Fortunately, an alternative, thermoelectric (TE) energy conversion, in which electricity is produced directly from heat using thermoelectric materials, has been discovered and developed (Figure 1.1). This technique is based on the Seebeck effect: an electrical potential difference appears across a material when a gradient temperature is applied [7-11]. Thermoelectric power generators are solid-state, soundless, reliable, and scalable devices, making them ideal for small, remote located power generation, satellites or deep-space probes [11, 12]. This technology is also beneficial for portable applications. For example, mobile phones or other electronic devices could be charged by a simple wood burning stove via a thermoelectric generator. In addition, replacing an alternator in cars by a thermoelectric power generator has been demonstrated to reduce fuel consumption [13, 14]. Inversely, thermoelectric devices can also extract heat across materials when applying a voltage through the Peltier effect [15]. Thermoelectric coolers can replace compressor-based refrigeration, with absence of noise, a useful feature for some specific applications such as hotel/automobile mini-fridge, picnic cooler or for local cooling, removing heat from

microelectronic components or infrared sensing [7, 8, 14]. Although TE conversion technology shows many advantages, it has only been used in very specific fields. The low conversion efficiency of the system, and specifically, current thermoelectric materials, is the biggest obstacle, making them costly and preventing them from wider applications and mass production [5, 7, 8]. In this chapter, an overview of the basic background of thermoelectric devices and materials, strategies to improve the energy conversion efficiency and our aims are presented.

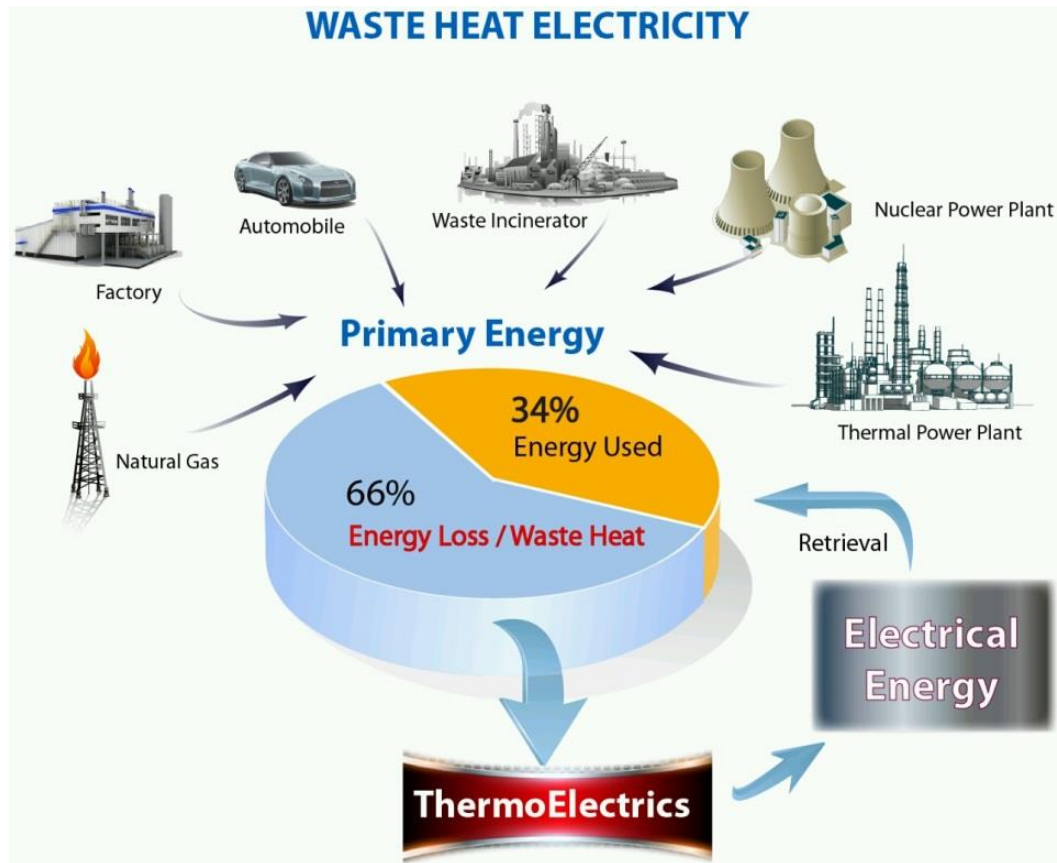


Figure 1.1. The conversion waste heat into electricity.

1.2 Thermoelectric Power Generation

1.2.1 Thermoelectric Devices

Thermoelectric devices comprise many thermoelectric couples. Each TE couple composes one n-type (electron charge carriers) and one p-type (hole charge carriers) semiconductor [7-11, 16]. These TE couples are connected electrically in series and thermally in parallel by metal contact pads and ceramic plates (Figure 1.2). When a temperature gradient is applied, electrons (n-type) and holes (p-type) in high temperature regions (hot sides) will diffuse to the low temperature regions (cold sides)

due to their increased kinetic energy. This creates different electrical potentials between n-type and p-type sides (Figure 1.3). The combination of these two semiconductors produces a current in an external circuit. The power output is determined by the voltage, provided by the applied temperature difference (ΔT) and Seebeck coefficient (S) [9, 14, 17]:

$$V = S \cdot \Delta T \text{ or } S = \frac{V}{\Delta T} \quad \text{Equation (1.1)}$$

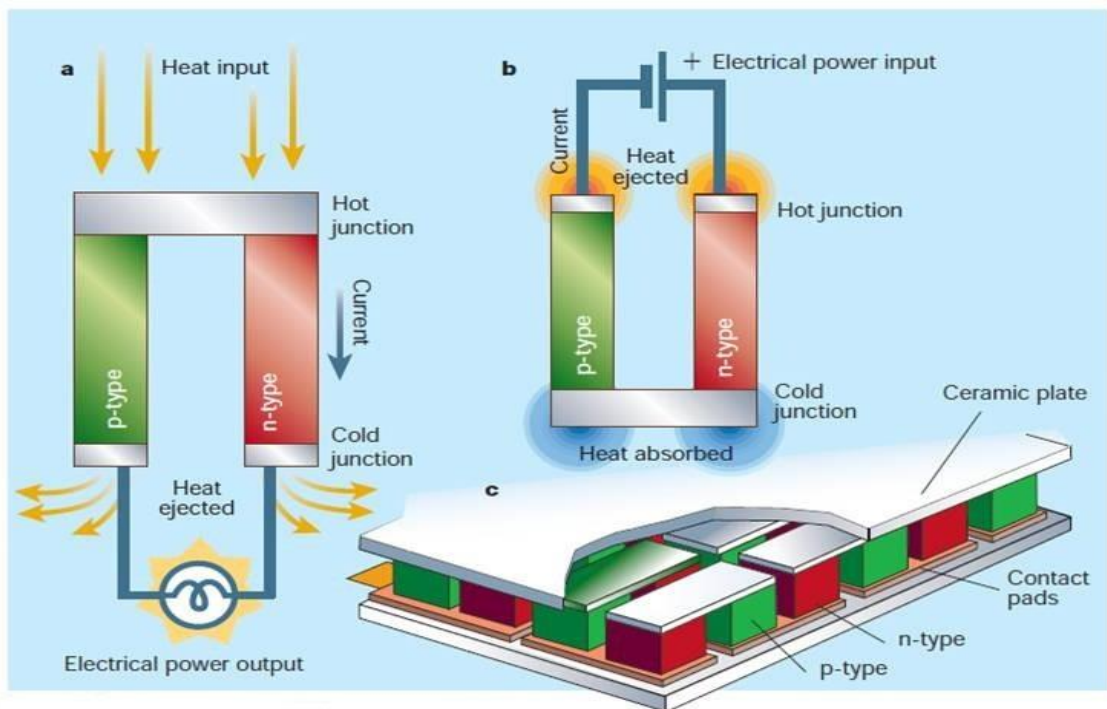


Figure 1.2. (a) Thermoelectric power couple, (b) Thermoelectric cooling couple, (c) Thermoelectric device [16].

The electrical current (I) is provided by the charge flow, and is related to the heat flow (Q) as heat is transported by charge carriers and phonon vibrations of the solid. Therefore, thermoelectric power generation might be used at a wide range of temperatures, depending on the heat source.

Inversely, in thermoelectric cooler (Peltier cooler), a d.c. power supply is the external circuit (Figure 1.2b) which drives the electric current and heat flow to cool the opposite side of the circuit, according to the relationship of Seebeck and Peltier effects [11, 16, 17]:

$$Q = S \cdot T \cdot I \quad \text{Equation (1.2)}$$

where S , T , I are Seebeck coefficient, absolute temperature and electrical current, respectively.

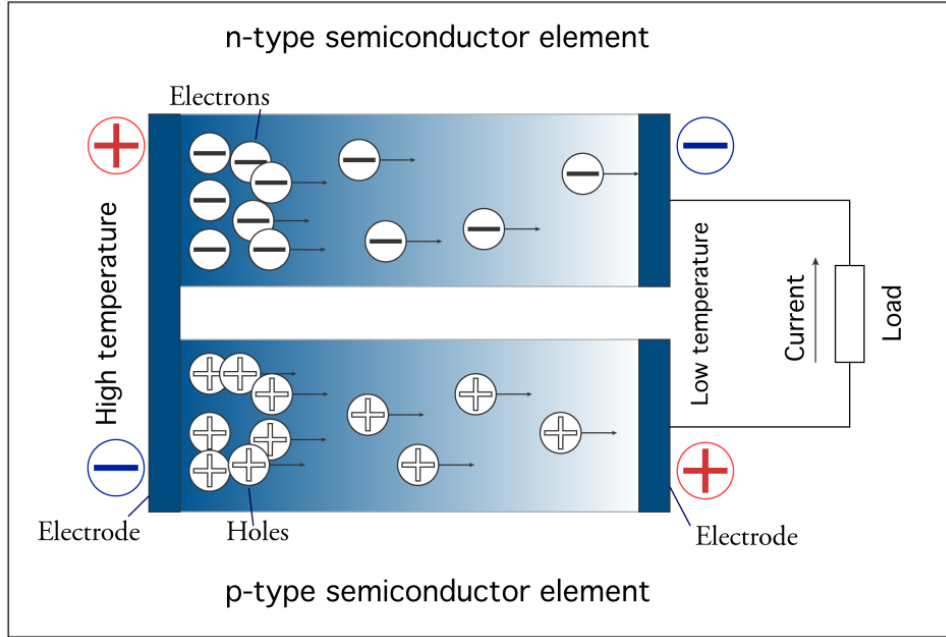


Figure 1.3. Mechanism of power generation in a thermoelectric couple [17].

1.2.2 Figure of Merit and Approaches to Its Improvement

The conversion efficiency of a TE device is determined by the Carnot efficiency and a dimensionless figure of merit (ZT) [18]. Ignoring contact resistance and optimising the load, the maximum conversion efficiency, η , is given by:

$$\eta = \left(\frac{T_{hot} - T_{cold}}{T_{hot}} \right) \left[\frac{\sqrt{1 + Z_m T_m} - 1}{\left(\frac{T_{cold}}{T_{hot}} \right) + \sqrt{1 + Z_m T_m}} \right] \quad \text{Equation (1.3)}$$

where the Carnot efficiency is given as the ratio of the temperature difference between the hot-end temperature (T_{hot}) and cold-end temperature (T_{cold}) to T_{hot} . T_m is the average temperature between T_{hot} and T_{cold} and $Z_m T_m$ is the figure of merit of the TE couple (including n- and p-type legs). Z_m is defined as [18]:

$$Z_m = \frac{(S_p - S_n)^2}{\left[(\rho_p \kappa_p)^{\frac{1}{2}} + (\rho_n \kappa_n)^{\frac{1}{2}} \right]^2} \quad \text{Equation (1.4)}$$

where S_p , S_n are Seebeck coefficient; ρ_p , ρ_n are electrical resistivities and κ_p , κ_n are thermal conductivities of p-type and n-type material legs respectively, while the figure of merit of material (n-type or p-type) ZT , is calculated by:

$$ZT = \frac{(S^2\sigma)T}{K} \quad \text{Equation (1.5)}$$

where S is the Seebeck coefficient, σ is the electrical conductivity, κ is the thermal conductivity and T is the absolute temperature. $S^2\sigma$ is normally referred to the thermoelectric power factor (PF).

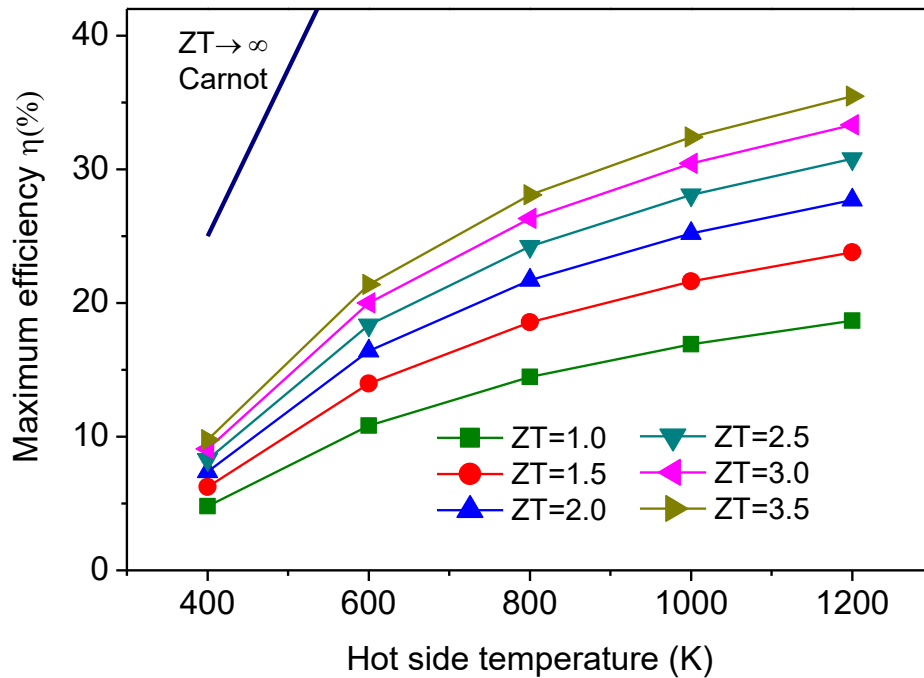


Figure 1.4. The theoretical calculation of maximum efficiency of TE generator with an assumption of the cold temperature at 300 K.

Figure 1.4 presents the theoretical calculation of maximum efficiency in a TE generator. Currently, the obtained efficiency of thermoelectric devices is below 10% with a ZT of around 1 [19, 20]. This means 90% of input energy is wasted. Therefore, improving the efficiency of TE generators is important. However, in order to approach 30% of the Carnot efficiency, ZT should be higher than 3.5 with the assumption that the temperature difference between hot and cold sides is 1.62 times (i.e if cold side temperature is ~ 300 K, the hot side temperature should be ~ 800 K). Therefore, from Equation (1.3), it is clear that the efficiency of TE devices is controlled by ZT and the temperature difference. Efforts to improve performance of TE devices have concentrated on the three following aspects [21, 22]:

- 1) Maximising the temperature difference between two sides of a TE device by applying an effective heat dissipation (heat sink) on the cold side or reusing the rejected heat at the cold side for secondary power generation cycles in hybrid systems.
- 2) Improving the ZT of TE materials. Approaches will be discussed later.
- 3) Optimising the design, structure and packaging technology of TE devices.

From Equation (1.5), ZT is optimised when S and σ are maximised while κ is minimised simultaneously. However, to get a high ZT over 3 is an extremely difficult task, up to date. The conflicting properties of TE bulk materials, illustrated in Figure 1.5, could explain the difficulty to optimise ZT [9]. An ideal TE material must theoretically possess metallic behaviour from the point of view of the electrical conductivity and insulating behaviour from the point of view of thermal conductivity. As shown in Figure 1.5, semiconductors are the materials that reach a compromise in TE performance when the power factor ($S^2\sigma$) is optimised. According to Figure 1.5, degenerate or heavily doped semiconductors with carrier concentrations from 10^{19} to 10^{21} cm^{-3} are good materials for TE applications [7-9, 18]. A theoretical calculation of C. Wood [23] shows that the optimum electron carrier concentration of a semiconductor at 300 K is around 3×10^{19} cm^{-3} , assuming that the effective mass is the electron mass and Fermi energy level is located on the conduction band edge. To achieve a large Seebeck coefficient, a single type of carrier should be selected, as mixing of n-type and p-type carriers will lead to the cancellation of the induced Seebeck voltages. The Seebeck coefficient is larger at a lower carrier concentration and vice versa according to Equation (1.6) for a simple model of electron transport in a semiconductor [11, 24]:

$$S = \frac{8\pi^2 k_B^2}{3eh^2} m^* T \left(\frac{\pi}{3n} \right)^{2/3} \quad \text{Equation (1.6)}$$

where k_B , h are the Boltzmann, Planck constants; e is the charge of an electron; n , m^* are the carrier concentration and the effective mass of the carrier, respectively.

The relationship between the electrical conductivity, electrical resistivity and carrier concentration is given by:

$$1/\rho = \sigma = ne\mu \quad \text{Equation (1.7)}$$

where μ is the carrier mobility, which is inversely proportional to the effective mass ($\mu \sim 1/m^*$).

The charge carrier concentration can be adjusted significantly by chemical doping or changing composition. Thus, tuning the electrical conductivity might be possible. However, dopants can also reduce the mobility of charge carriers via charge carrier scattering. A large effective mass of the charge carrier results in a high Seebeck coefficient but a low electrical conductivity because of its smaller mobility (Equation (1.6)) [7, 8, 15]. The electrical conductivity can also be enhanced by modifying band structure via degenerate multiple valley bands. Pei *et al.* [25] has shown that the entropy per charge passing through the material increases due to the increase of degenerate valley numbers. This results in a higher Seebeck coefficient and electrical conductivity.

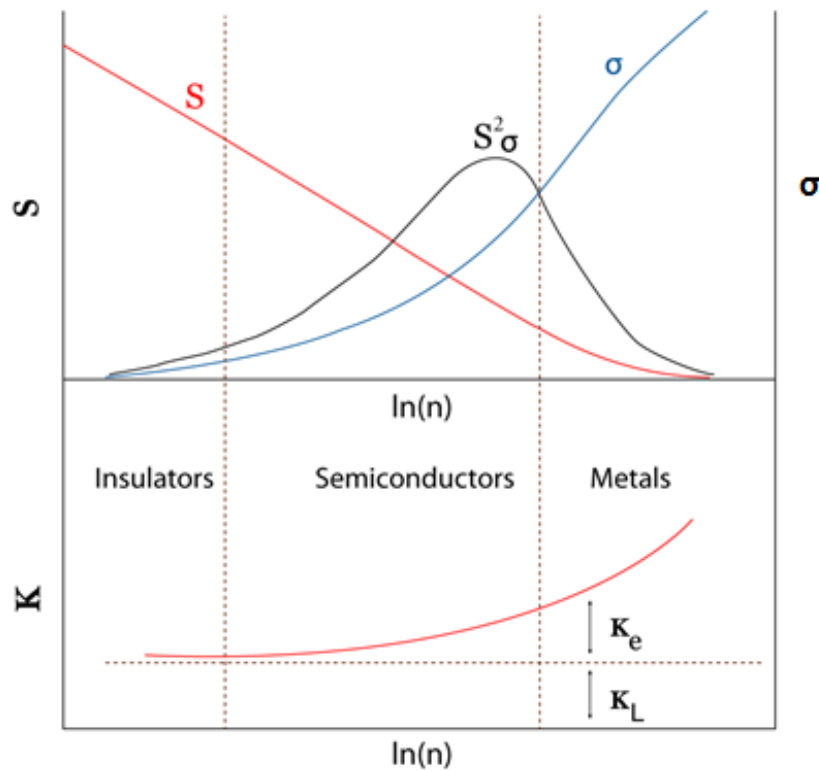


Figure 1.5. The conflict between the Seebeck coefficient (S), electrical conductivity (σ) and the electronic (κ_e), lattice (κ_l) contributions to thermal conductivity versus the charge carrier concentration for a bulk material [9].

In a solid, the thermal conductivity (κ) arises mainly from two sources: charge carriers (electrons or holes) moving through the material, the so-called electronic thermal conductivity (κ_e), and lattice vibrations (phonons) travelling through the lattice, or lattice thermal conductivity (κ_l):

$$\kappa = \kappa_e + \kappa_l \quad \text{Equation (1.8)}$$

Typically, an increase of electrical conductivity results in an increase of κ_e according to Wiedemann- Franz law:

$$\kappa_e = L_o \sigma T = ne\mu L_o T \quad \text{Equation (1.9)}$$

where L_o is the Lorentz factor. For metals, $L_o = L = \frac{\pi^2}{3} \left(\frac{k_B}{e}\right)^2 = 2.45 \times 10^{-8} \text{ W}\Omega/\text{K}^2$, is called as Lorentz number and generally used to estimate the κ_e in semiconductors [7]. Replacing Equation (1.8) and Equation (1.9) into Equation (1.5), the figure of merit is shown as:

$$ZT = \frac{(S^2 \sigma) T}{L \sigma T + \kappa_l} \quad \text{Equation (1.10)}$$

Equation (1.10) shows that the minimisation of κ_l will lead to the optimisation of ZT . The value of κ_l is controlled by the specific heat capacity of the material (C_v), which could be estimated using Dulong and Petit law [26], the velocity of sound (v_s) and mean free path of phonon (l), as given by Equation (1.11) [26]:

$$\kappa_l = \frac{1}{3} C_v l v_s \quad \text{Equation (1.11)}$$

C_v and v_s are basically temperature independent in typical materials at temperatures above the Debye temperature (θ_D). Therefore, κ_l is dependent on the mean free path of the phonons (l) or the phonon scattering in the lattice. In metals, the electronic contribution to thermal conductivity is dominant, while the phonon contribution to thermal conductivity is the principal contribution in semiconductors. Therefore, in order to reduce the thermal conductivity in semiconductors, efforts have focused on decreasing the lattice thermal conductivity. In addition, the reduction of the lattice thermal conductivity must avoid any adverse effects on the electrical conductivity. Consequently, the concept of phonon glass electron crystal (PGEC) materials was proposed by Slack in 1995 [27]. According to this concept, a good TE material possesses a high phonon scattering (low heat conduction) like a glass ($\kappa_{min} \sim 0.25 \text{ W m}^{-1} \text{ K}^{-1}$) and very little electron scattering (electrical conductivity is maintained) like a crystal [27, 28]. Skutterudites and clathrates are typical materials showing this type of behaviour [28]. However, M. Gao *et al.* [29] suggests that the sole reduction of lattice thermal conductivity only accomplishes a moderate improvement in ZT , reaching a value below 2 (at room temperature or below). For a ZT value significantly larger than

2, the improvement in electrical transport properties is important as well. Up to date, all approaches to reduce thermal conductivity concentrate on increasing phonon scattering between phonon – phonon, phonon – boundary or phonon – defect. This includes materials with a complex crystal structure [11]; rattling atoms in a rigid framework; point defects; mass fluctuation by creating vacancies in a solid solution of two different materials but same structures [30, 31]; natural superlattices [7, 9, 28].

Recently, nano-structured materials have also attracted a huge attention. Although the material itself does not change, the properties are altered by reducing the dimensionality [32-37]. Initially, Hicks, Harman and Dresselhaus used theoretical calculations to prove that the low-dimensionality in TE materials increases the Seebeck coefficient [35, 37], hence improves ZT . The basic idea is that mobile electrons are confined in a low-dimensional structure due to quantum confinement effects. This confinement results in an increase in the density of states of the charge carriers (Figure 1.6). In low-dimensional structures, the density of states is more discrete, sharper and larger at the edge of the band while in a three-dimensional structure, the density of states is a parabolic band and lowest at the edge of the band. A key consideration is that the Seebeck coefficient is proportional to the derivative of density of states via the Mott equation [38]:

$$S = \frac{\pi^2 k_B^2 T}{3e} \left(\frac{d \ln \sigma(E)}{dE} \Big|_{E = E_f} \right) \quad \text{Equation (1.12)}$$

where $\sigma(E)$ is the electrical conductivity and e is charge of carrier.

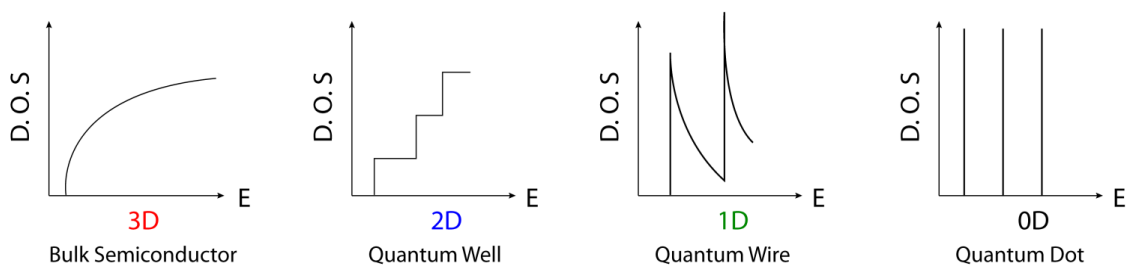


Figure 1.6. The schematic representation of electronic density of states (DOS) of bulk semiconductor, two dimensional quantum well, one dimensional quantum wire and zero dimensional quantum dot [39].

From Equation (1.12), it suggests that the larger Seebeck coefficient could be obtained at lower dimensional structures in which the density of states near the Fermi level, would change rapidly. Low-dimensional structures, which can be superlattices (2D), nanowires (1D) or quantum dots (0D), also increase grain boundary scattering and thus

decrease lattice thermal conductivity [36, 40, 43]. The smaller particle size of nano-structured materials increases phonon scattering at the interfaces, and results in a reduction of the mean free path of phonons [19, 44-48]. However, nano-structured materials are generally expensive while large scale production is very difficult.

1.2.3 Natural Superlattice

As discussed above, reducing the lattice thermal conductivity is a strategic approach to enhance ZT . According to the Einstein's model, the minimum thermal conductivity of a disordered crystal is never lower than that of the amorphous state (so-called glasslike lattice vibrations, $\kappa_{min} \sim 0.25 \text{ W m}^{-1} \text{ K}^{-1}$) [49]. This concept leads to an upper limit of ZT . However, in 2007, an ultralow thermal conductivity was first reported by C. Chiritescu *et al.* [50], who found that the thermal conductivity of disordered layered WSe_2 film reaches a value of $0.05 \text{ W m}^{-1} \text{ K}^{-1}$, five times lower than κ_{min} value and 30 times smaller than the c -axis thermal conductivity of single-crystal WSe_2 . Although this behaviour has not been understood in detail, this highlights a promising approach of using layered superlattices for TE applications.

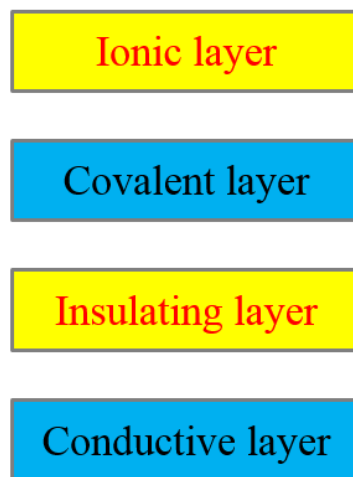


Figure 1.7. A natural superlattice structure.

Natural superlattices are defined as crystal structures containing low-dimensional structural building blocks, in which ionic and covalent bond layers are stacked alternately (Figure 1.7) [51, 57]. The ionic layers serve as phonon scatters while the covalent layers are electrically conducting layers. The insulating layers can be changed via intercalating host materials whilst the electronic transport properties could be varied

by engineering the electronic structure through doping, or changing the composition [52]. Evidence for the success of this concept can be found in layered cobalt oxides such as $\text{Ca}_3\text{Co}_4\text{O}_9$ ($ZT \sim 0.87$ at 973 K) [53] and NaCo_2O_4 ($\kappa \sim 1.77 \text{ W m}^{-1} \text{ K}^{-1}$, $ZT \sim 0.1$ at 300 K) [54, 55]. Recently, the misfit layered $(\text{AB})_{1+x}(\text{QB}_2)$ ($\text{A} = \text{Pb, Bi, Sn, Sb, rare-earth elements}$; $\text{B} = \text{S, Se}$; $\text{Q} = \text{Ti, V, Cr, Nb, Ta}$; $n = 1, 2, 3$) has been reported as promising thermoelectric materials, in which $(\text{SnS})_{1+x}(\text{TiS}_2)$ shows the highest ZT of 0.37 at 773 K while other materials possess lower ZT of ~ 0.2 [56, 57].

1.3 Thermoelectric Materials

The development of TE materials could be divided in three main periods. From 1821 to 1851, the discovery of the three TE effects (Seebeck, Peltier, and Thomson) built the foundations required for TE applications including temperature measurements, cooling and electricity production. Afterwards, significant progress occurred between 1930 and 1990. The theoretical and practical investigation for optimisation of current commercial TE materials (Bi-Sb , $\text{Bi}_2\text{Te}_3\text{-Sb}_2\text{Te}_3$, PbTe , Te-Ag-Ge-Sb) was carried out.

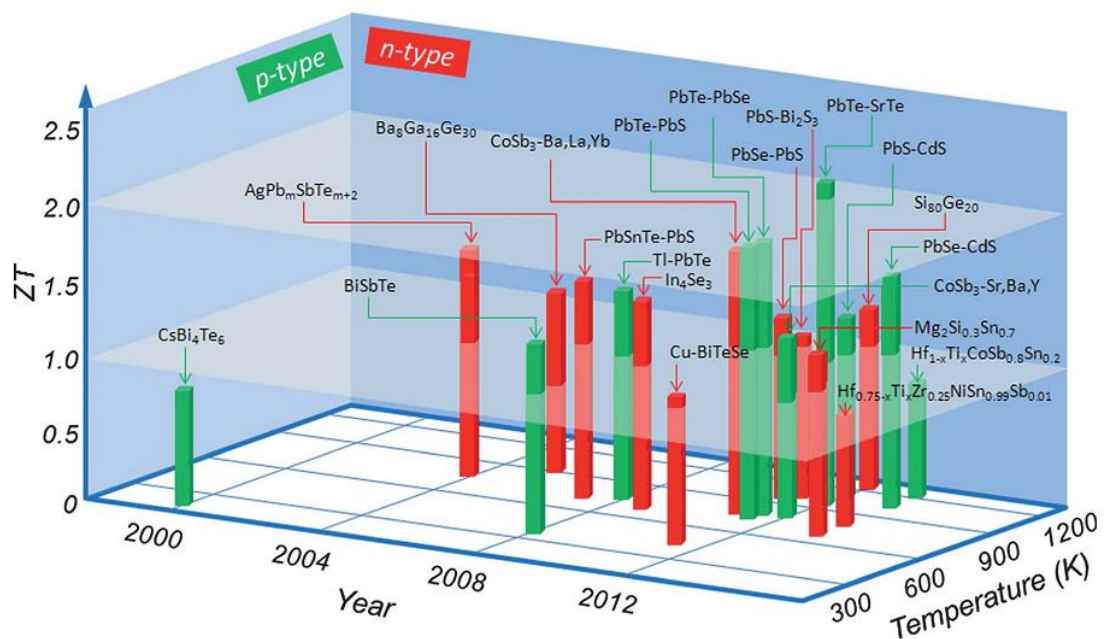


Figure 1.8. Some current TE bulk materials with high ZT [58].

Since 1960 TE materials based on Bi_2Te_3 with $ZT \approx 1$ in a temperature range of 400-700 K have been mainly used for cooling applications in a narrow market due to their low efficiency, when compared to compressor refrigerators. More recently, in the early 1990's, the greater concern of environmental impacts (greenhouse effects, refrigerant

gas, etc.) and increased energy demand have attracted greater interest in thermoelectric power generation and therefore resulted in extensive research of new thermoelectric materials over two decades [7, 8, 18]. A significant improvement in ZT has been reported at the laboratory scale, as shown in Figure 1.8. In general, the number of materials studied for TE application, is large [28]. However, the high ZT materials are almost all metal chalcogenides [58]. A brief summary on some selected TE materials is presented below.

1.3.1 Metal Oxides

Many metal oxides are attractive for high temperature TE applications due to their high chemical stability in air. This is beneficial for a high Carnot efficiency since a large temperature gradient can be applied to compensate for their lower TE performance. In addition, the low cost of raw materials makes them attractive for mass production. However, their naturally low electrical conductivity causes a low power factor. For example, ZnO, In₂O₃ and SrTiO₃ - based materials are representatives for n-type oxide TE materials. In 2011, Jood *et al.* reported a ZT of 0.44 at 1000 K for Al doped ZnO nanoparticles using microwave solvothermal technique [59], which is the best ZnO-based TE material. The nanostructured Zn and Ce co-doped In₂O₃ based TE materials fabricated by co-precipitation and consolidated by SPS approach a high ZT value of 0.4 at 1050 K [60]. Single crystal sodium cobalt oxides are promising p-type TE materials with $ZT > 1$ at 800 K [61]. Other representative of p-type oxide TE materials include Ca₃Co₄O₉ and CaMnO₃ - based materials. A nanofiber - sintered Ca₃Co₄O₉ approaches a ZT of around 0.4 at 975 K without any doping [62]. However, the high contact resistances at the junction of oxide/metal electrode and cracking/exfoliation during the operation cycles are a drawback for the construction of modules containing oxide materials [63].

1.3.2 Metal Chalcogenides and Complex Solid Solutions

Metal chalcogenides are air stable and often exhibit semiconducting behaviour. They are suitable for many energy conversion and storage applications, especially for TE devices due to their narrow band gap (0.1 - 0.8 eV). The current bulk PbTe compound has a maximum $ZT \approx 0.8$ at 770 K which is good for the intermediate temperature power generator [64]. The narrow indirect band gap (~ 0.15 eV) of alloys of Bi₂Te₃ with

Sb (p-type) or Se (n-type) results in a $ZT \approx 1$ near room temperature [65]. Recently, nano-structuring and engineering of the electronic structure of metal chalcogenides at laboratory scales has led to significant improvements of $ZT (> 2)$ [58, 66]. Single crystals of SnSe approach an unprecedented ZT value of 2.6; 2.3 and 0.8 at 923 K (along the b , c and a axis, respectively). This is the maximum ZT value reported to date for a metal chalcogenide at high temperature [66] while the melt-spinning of $\text{Bi}_{0.5}\text{Sb}_{1.5}\text{Te}_3$ alloy shows the highest ZT ($\sim 1.86 \pm 0.15$) at around room temperature (~ 320 K) [67]. However, their cost, primarily of tellurium, is an obstacle for mass production. For instance, the price of Bi_2Te_3 alloys is around \$140 -210/ kg [68] and keeps increasing due to increased demand and limited supply, given that Te is a scarce element, 1ppb in the earth's crust.

1.4 Layered Oxychalcogenides

1.4.1 Introduction

Layered oxychalcogenides are mixed-anion compounds, in which oxygen and chalcogenide ions (group 16 elements) indirectly bound via one or more cations, creating a stack of alternating oxide and chalcogenide layers. In this dissertation, oxide and chalcogenide anions are denoted as O and Ch , respectively while cations are denoted as A, B and M. The general formula of oxychalcogenides is given as $\text{A}_n\text{B}_m\text{M}_x\text{O}_y\text{Ch}_z$ ($n, y, z \geq 1$ and $x, m \geq 0$). Different to common anions such as sulphate $[\text{SO}_4]^{2-}$ or selenate $[\text{SeO}_4]^{2-}$, in which the chalcogen has a positive charge due to the high electronegativity of the coexisting oxygen, the oxidation state of all anions in oxychalcogenides is negative (O^{2-} , Ch^{2-}), whilst cations are monovalent, di-, tri- or tetravalent metals. Oxides are one of the most important classes of solid state materials, exhibiting a wide range of physical and chemical properties in many different areas such as electronics, superconductivity, catalysis or thermoelectrics. On the other hand, metal chalcogenides are also an interesting class of materials for thermoelectric applications (which was introduced section 1.3.2). The unique mixed anionic combination in oxychalcogenide materials facilitates the control of the properties of materials via both cationic and anionic layers. This can result in unexpected and fascinating properties, which are rarely observed in simple oxides. For instance, $\text{Ce}_2\text{O}_2\text{S}$ nanoparticles anchored on graphitised carbon has been recently found to be a promising anode material for Li-ion batteries, with a stable specific capacity up to 627 mA h g^{-1} after 180 charge-recharge cycles [69]. A new family of layered superconductors has

been reported in $\text{Bi}_4\text{O}_4\text{S}_3$ although the T_c is fairly low ~ 4.5 K [70-72]. An improvement of the superconducting properties of compounds containing $[\text{BiS}_2]^{2-}$ layers has been found in electron doped $\text{NdO}_{0.5}\text{F}_{0.5}\text{BiS}_2$ ($T_c \sim 5$ K) [73] or $\text{LaO}_{1-x}\text{F}_x\text{BiS}_2$ ($T_c \sim 10.6$ K) [74].

There are many different structures of oxychalcogenides. This includes layered structures and three dimensional structures, such as $\text{Gd}_4\text{O}_4\text{TiSe}_4$ [75] or $\text{La}_2\text{O}_2\text{MnSe}_2$ ($\text{M} = \text{Mn}, \text{Fe}$) [76] (Figure 1.9). However, the work in this dissertation has been focused on natural superlattice oxychalcogenides. Therefore, only natural superlattice structures of oxychalcogenides are presented in the next sections.

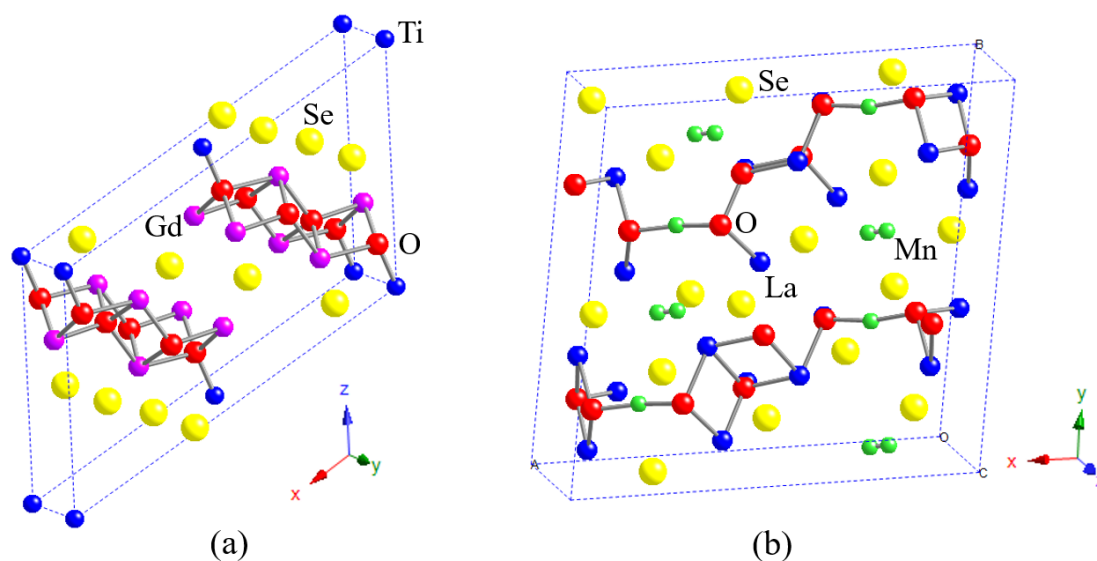


Figure 1.9. Three dimensional oxychalcogenides: (a) $\text{Gd}_4\text{O}_4\text{TiSe}_4$ [75] and (b) $\text{La}_2\text{O}_2\text{MnSe}_2$ [76].

1.4.2 Some Common Structure Types and Their Interrelationship

Structures of layered oxychalcogenides are normally described as a combination of some common building blocks of oxides and chalcogenides in a systematic arrangement. For example, the repetition of fluorite - type blocks of $[\text{La}_2\text{O}_2]^{2+}$ and rock salt-type blocks of $[\text{Bi}_2\text{S}_4]^{2-}$, stacked alternately along the c -axis, creates the layered structure of LaOBiS_2 (Figure 1.10) [74]. Similarly, Bi, Pb atoms are bound to chalcogenide atoms to form rock salt-like $[\text{M}_4\text{S}_6]^{2-}$ ($\text{M} = \text{Bi}, \text{Pb}$) slabs, stacked alternately with fluorite- like- type blocks of $[\text{La}_2\text{O}_2]^{2+}$ in $\text{LaPbBiS}_3\text{O}$ compound [77].

Table 1.1 presents four common building block types from structures of binary or ternary solids. The fluorite structure (for example, CaF_2) has a stoichiometry of QX_2 ($\text{Q} = \text{cations}, \text{X} = \text{anions}$). It is a cubic close packed (CCP) structure in which X^- anions are

located in all tetrahedral holes of the CCP Q^{2+} . Coordination numbers (CNs) of Q^{2+} and X^- are 8 and 4, respectively, forming polyhedra: edge-sharing QX_8 cubes and edge-sharing XQ_4 tetrahedra. In contrast, the anti-fluorite structure (such as Na_2O) possesses a stoichiometry of Q_2X , in which Q^+ cations are located in all tetrahedral holes of CCP X^{2-} . The CNs of the cation and anion are 4 and 8, respectively, forming polyhedra: edge-sharing QX_4 tetrahedra and edge-sharing XQ_8 cubes [78]. On the other hand, the stoichiometry of the rock-salt structure ($NaCl$) is QX . It crystallises in a face-centered unit cell. The Q^+ cations are located in octahedral holes of a CCP array of anions X^- , with a CN of 6:6 for both cations and anions, to form polyhedral-edge-sharing QX_6 and XQ_6 octahedra. Different to the above structure types, the general formula of the perovskite structure ($SrTiO_3$) is ABX_3 ($A, B =$ cations and $X =$ anions). It crystallises in a primitive cubic unit cell. The coordination numbers of A, B and X are 12, 6 and 2 respectively, forming polyhedra: face-sharing AX_{12} cuboctahedra, shown as hollow spaces, vertex-sharing BX_6 octahedra and face-sharing XA_4B_2 distorted octahedral [78]. Representative compounds containing these building blocks are presented in the next sections.

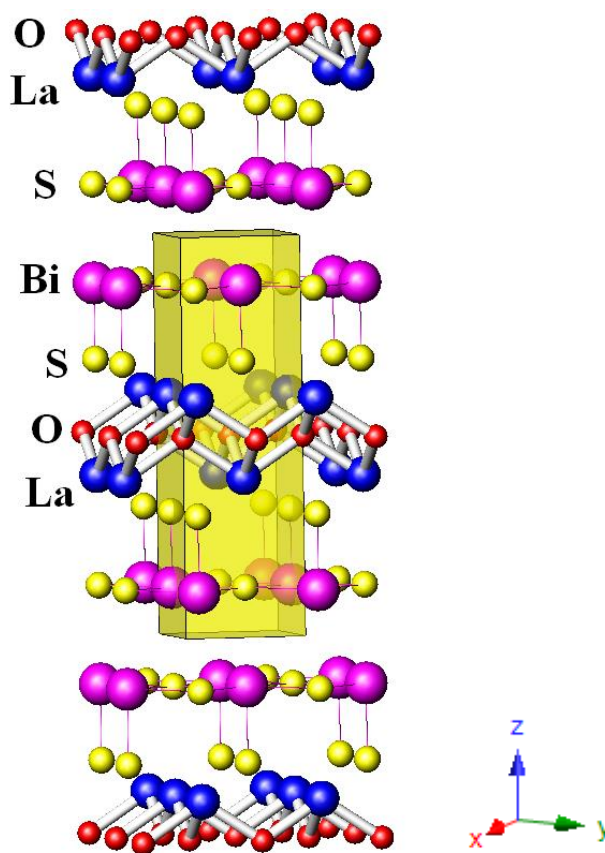
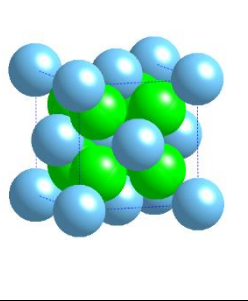
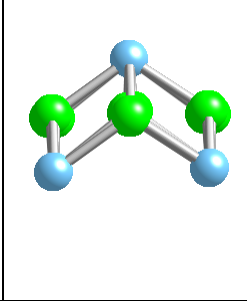
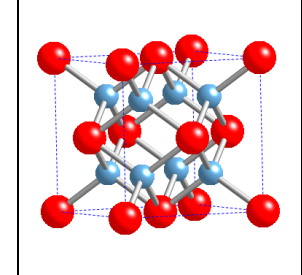
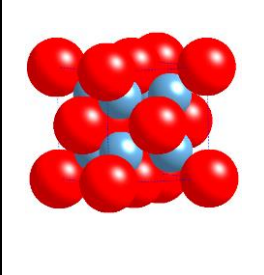
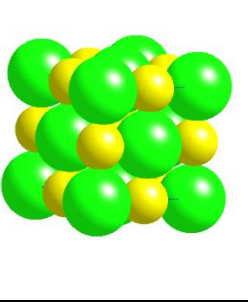
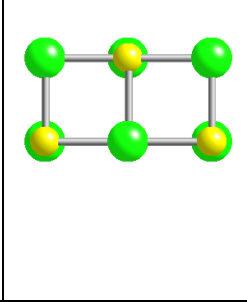
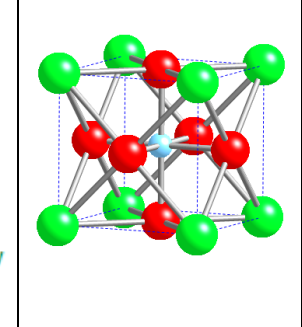
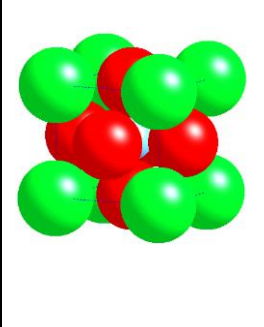


Figure 1.10. Crystal structure of $LaOBiS_2$: $[La_2O_2]^{2+}$ and $[Bi_2S_4]^{2-}$ stacked alternately.

Table 1.1. Building block type of oxychalcogenides.

Structure	Space filling	Building block type	Keys
Fluorite (CaF ₂)			Ca ²⁺ (blue) F ⁻ (green)
Anti-fluorite (Na ₂ O)			Na ⁺ (blue) O ²⁻ (red)
Rock-salt (NaCl)			Na ⁺ (yellow) Cl ⁻ (green)
Perovskite (SrTiO ₃)			Sr ²⁺ (green) Ti ⁴⁺ (blue) O ²⁻ (red)

1.1.1.1 Compounds With (A_{2m}O_{2m})Ch_{2m-1} Structures

When $m = 1$, they are A₂O₂Ch compounds, normally called as “122”- type structures due to their stoichiometry. A is rare earth element (La-Nd, Y, Sm-Ho) or pnictogen Bi and Ch is a chalcogen (S, Se, Te) [80]. The structure consists of fluorite-type [A₂O₂]²⁺ layers and Ch²⁻ layers alternately stacked along the *c*-axis. The oxygen anions are tetrahedrally coordinated by A³⁺ cations, forming A₄O tetrahedra, while the Ch²⁻ anions

form a chalcogenide array. Some typical “122”- type oxychalcogenides are presented in Table 1.2. Some of these compounds, for example A_2O_2Te ($A = La, Ce, Bi$) or A_2O_2Se ($A = Ce, Bi$), crystallise in *anti*- $ThCr_2Si_2$ tetragonal structure type with the $I4/mmm$ space group (Figure 1.11a) while other compounds crystallise in the orthorhombic or trigonal unit cells with $Pnmm$ space group (Bi_2O_2S) and $P\bar{3}m1$ space group (A_2O_2Ch , $A = La, Ce$; $Ch = S, Se$), respectively (Figure 1.11b).

Table 1.2. A_2O_2Ch ($A = La, Ce, Bi$) compounds.

Ch in La_2O_2Ch	$a, b/\text{\AA}$	$c/\text{\AA}$	Space group	Crystal system	Ref
S	4.049(1)	6.939(2)	$P\bar{3}m1$	Trigonal	[81]
Se	4.07(2)	12.4(2)	$P\bar{3}m1$	Trigonal	[82]
Te	4.1231(4)	13.096(1)	$I4/mmm$	Tetragonal	[83]
Ch in Ce_2O_2Ch					
S	4.01(1)	6.83(3)	$P\bar{3}m1$	Trigonal	[84]
Se	4.0365(2)	7.0821(8)	$P\bar{3}m1$	Trigonal	[85]
Te	4.0817(4)	12.947(1)	$I4/mmm$	Tetragonal	[83]
Ch in Bi_2O_2Ch					
S	3.874(1) 11.916(2)	3.840(1)	$Pnmm$	Orthorhombic	[89]
Se	3.88(4)	12.16(3)	$I4/mmm$	Tetragonal	[86]
Te	3.98025(4)	12.7039(2)	$I4/mmm$	Tetragonal	[87]

The difference between structures of tetragonal and trigonal compounds lies not only in their symmetry, but also in the oxide layers. In the case of the trigonal unit cell, the A_4O tetrahedra share three edges. Each Ch^{2-} ions exhibits octahedral coordination in which each A site is seven coordinate with four short bonds to O and three longer bonds to Ch ($4O+3Ch$). In contrast, in the tetragonal unit cell, the A_4O tetrahedra share four edges, forming a fluorite-like 2D slabs. The Ch^{2-} ion lies in a 8 fold square prismatic coordination and the A site is in a ($4O+4Ch$) distorted square anti-prism [88]. Different to tetragonal and trigonal compounds, in orthorhombic structures the O atom is bound to four A atoms to form A_4O tetrahedra, shared four edges stacked alternately with Ch^{2-}

layers along the b axis. This creates an apparent difference in the symmetry of the lattices. In addition, Koyama *et al.*, describes that the orthorhombic structure of $\text{Bi}_2\text{O}_2\text{S}$ is a slightly distorted form of the tetragonal structure of $\text{Bi}_2\text{O}_2\text{Se}$ [89].

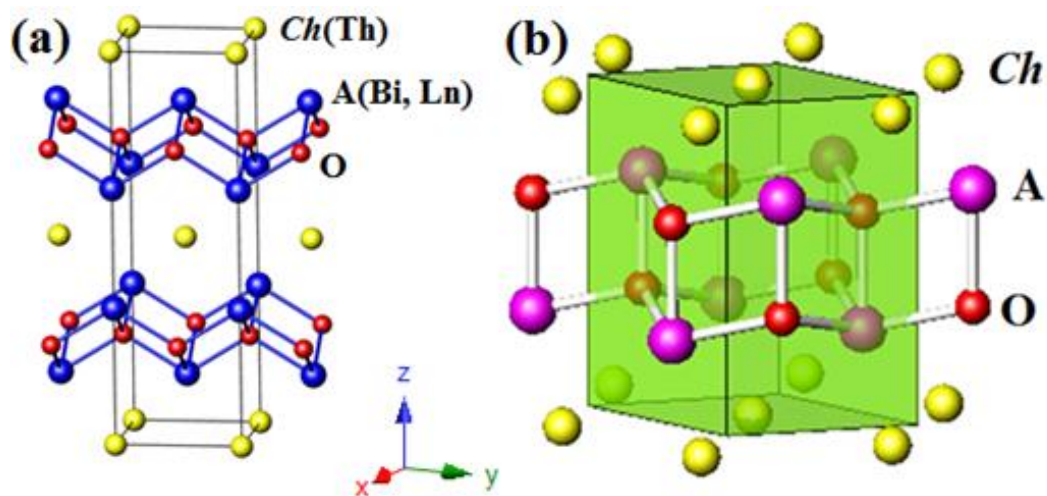


Figure 1.11. Crystal structure of $\text{A}_2\text{O}_2\text{Ch}$ with space group of (a) $I4/mmm$, (b) $P\bar{3}m1$.

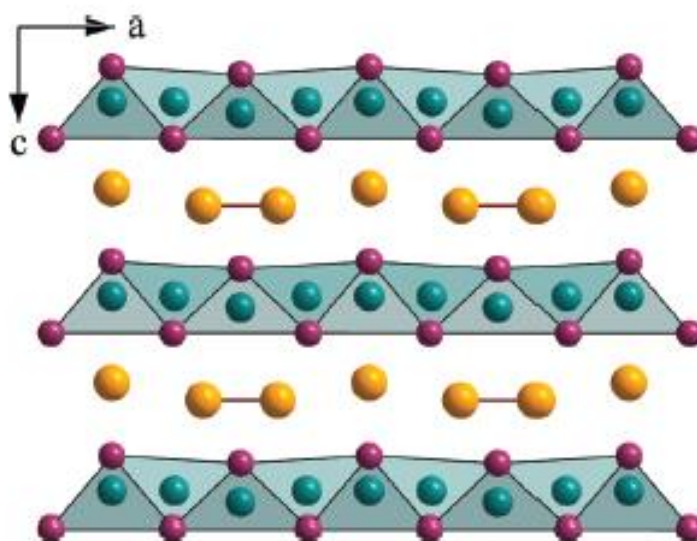


Figure 1.12. The view of $\text{A}_4\text{O}_4\text{Se}_3$ crystal structure along b -axis. A atoms (purple), O atoms (turquoise) and Se atoms (gold) [90].

When $m = 2$, they are $\text{A}_4\text{O}_4\text{Ch}_3$ compounds ($A = \text{La-Yb}$, Y and $\text{Ch} = \text{Se}$) [88, 90]. These compounds crystallise in the non-centrosymmetric orthorhombic structure with an $\text{Amm}2$ space group. In their structures, the $[\text{A}_4\text{O}_4]^{4+}$ layer is stacked alternately to Se^{2-} anions and $[\text{Se-Se}]^{2-}$ dumbbells along the c -axis. Each O^{2-} anion is bonded by four A^{3+} to form a distorted $[\text{A}_4\text{O}]^{10+}$ tetrahedron sharing four edges. The coordination numbers of Se^{2-} and $[\text{Se-Se}]^{2-}$ are six, two values lower than that of Se^{2-} anions in $\text{A}_2\text{O}_2\text{Se}$

structure, forming a triangular prism, in which $[\text{Se-Se}]^{2-}$ anions are in the middle [90]. Figure 1.12 shows $\text{A}_4\text{O}_4\text{Ch}_3$ ($\text{Ch} = \text{Se}$) structures in the view along b -axis. Depending on the radius of the A atom, a set of closely-related structure types, labelled as the α , β , γ and δ - $\text{A}_4\text{O}_4\text{Se}_3$ structures types, would exist. More details have been presented elsewhere [88, 90].

1.1.1.2 Compounds with $(\text{A}_2\text{O}_2)\text{Ch}_2$ Structures

The structure of these compounds is usually described as a “111”- type structure. It was first found by W. Wichelhaus, who reported compounds where A is La, Pr, Nd and Ch is S [91]. They were firstly described as tetragonal, with the $Pcam$ space group [91]. Later, J. Ostoréro *et al.* argued that $\text{La}_2\text{O}_2\text{S}_2$ crystallises in an orthorhombic crystal system with $Cmca$ space group [92]. The structure (reported by W. Wichelhaus) is similar to that of the “122”- type structure. It is composed of fluorite-type $[\text{A}_2\text{O}_2]^{2+}$ layers and Ch_2^{2-} planar sheets, stacked alternately along c -axis [91] while the one reported by J. Ostoréro *et al.* comprises $[\text{A}_2\text{O}_2]^{2+}$ layers and Ch_2^{2-} planar sheets, stacked alternately along a -axis [92].

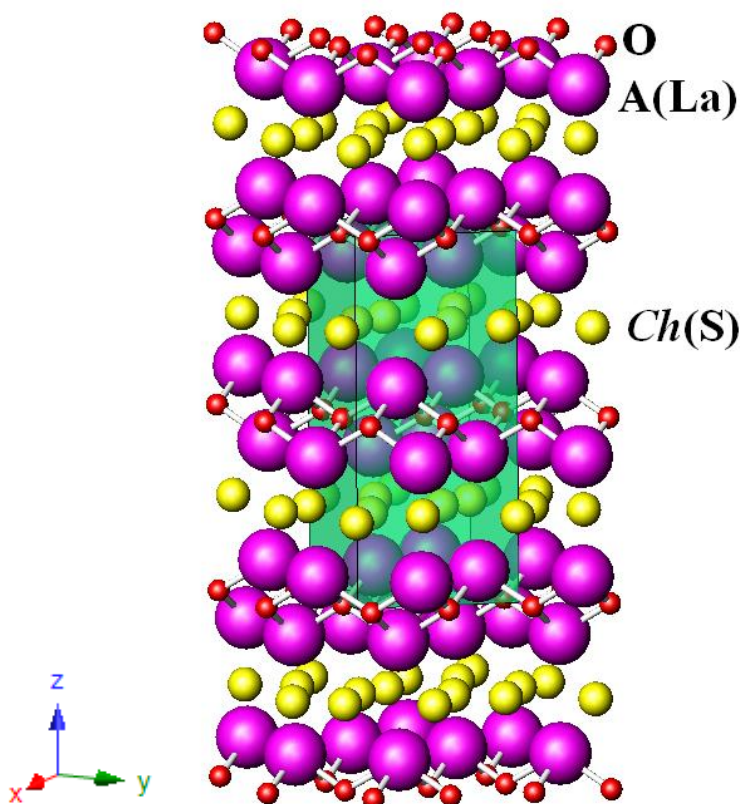


Figure 1.13. Crystal structure of $\text{La}_2\text{O}_2\text{S}_2$.

Table 1.3. Lattice parameters of $A_2O_2S_2$ crystal.

A in $A_2O_2S_2$	a/Å	b/Å	c/Å	Ref
La	5.935(2)	5.935(2)	13.216(4)	[91]
	13.215(2)	5.943(1)	5.938(1)	[92]
Pr	5.850(2)	5.850(2)	12.925(5)	[91]
Nd	5.827(2)	5.827(2)	12.878(5)	[91]

1.1.1.3 Compounds with AOBCh Structures

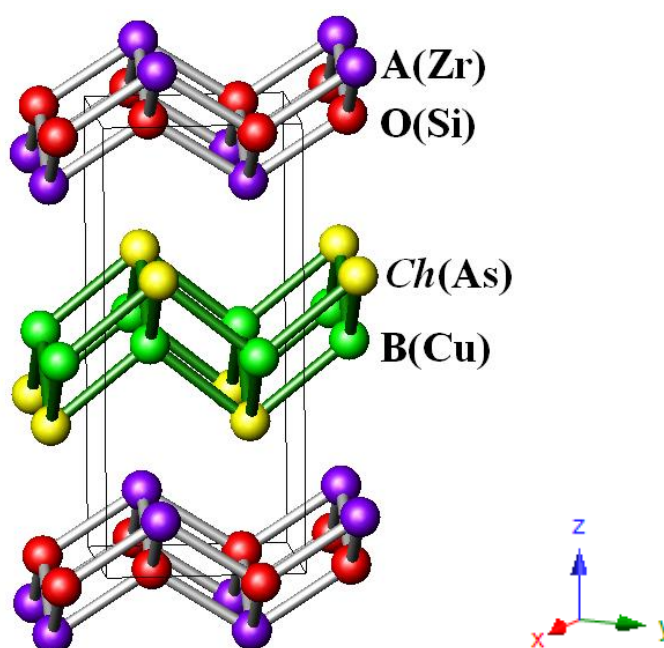


Figure 1.14. AOBCh crystal structure.

The AOBCh structure is denoted as a “1111” type structure, in which A is a trivalent cation such as Bi, La, Ce, Pr, Nd, Eu, Sm, Gd, Dy, Ho, Er, Yb, Y; B is a monovalent cation such as Cu, Ag and Ch is S, Se, Te [93-98]. It crystallises in a layered tetragonal ZrCuSiAs or HfCuSi₂ type (in the ICSD) structures with a $P4/nmm$ space group [99] in which fluorite-type $[A_2O_2]^{2+}$ and anti-fluorite-type $[B_2Ch_2]^{2-}$ slabs stacked alternately along the c -axis (Figure 1.14). In 1980, Palazzi *et al.* reported the first oxychalcogenide AOBCh (A = La, B = Ag, Ch = S) compound as an ionic conductor [97]. The A^{3+} ions in AOCuCh had been limited to Y^{3+} and lanthanide ions until 1993 when Kholodkovskaya *et al.* [98] reported the substitution of Bi^{3+} into the A site.

1.1.1.4 Compounds with $(A_2O_2)(BCh_2)$ Structures

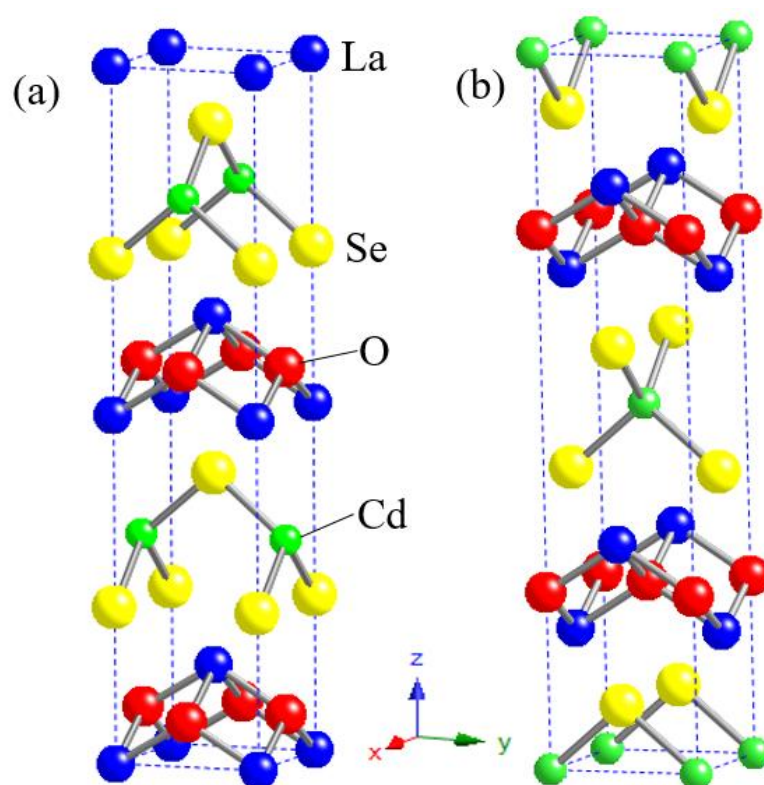


Figure 1.15. Crystal structure of $La_2O_2CdSe_2$ with two different model: (a) model with space group of $P4_2mc$, and (b) model with space group of $P4_2/nmc$ [100].

These structures are composed of $[BCh_2]^{2-}$ ($B = Fe, Cd$; $Ch = Se$) slabs separated by $[A_2O_2]^{2+}$ layers ($A = La, Ce$). Similarly to the $AOBCh$ structures, they consist of both fluorite-type $[A_2O_2]^{2+}$ and anti-fluorite-type $[BCh_2]^{2-}$ slabs. However, in the chalcogenide layer of $(A_2O_2)(BCh_2)$, B^{2+} cations occupy half of B sites of $AOBCh$ and form corner-shared BCh_4 tetrahedra, instead of the edge-shared BCh_4 tetrahedra found in $AOBCh$. Figure 1.15 represents this type of structure with $A = La$, $B = Cd$, $Ch = Se$, creating $La_2O_2CdSe_2$ compound [100]. Recently, details of different ordering patterns in $A_2O_2BSe_2$ phases have been discussed by C-H. Wang *et al.* [101].

1.1.1.5 Compounds with $(A_2MO_2)(B_2Ch_2)$ Structures

The representative compound of this type structure is $Sr_2MO_2Cu_2S_2$ ($M = Zn, Mn$) [102]. It crystallises in $Sr_2Mn_3Sb_2O_{10}$ (or $Sr_2MnO_2Mn_2Sb_2$) structure type [103]. The structure contains the anti-fluorite chalcogenide layers $[B_2Ch_2]^{2-}$ whilst the oxide $[MO_2]^{2-}$ planar sheets are separated from the $[B_2Ch_2]^{2-}$ blocks by A^{2+} ions (Figure 1.16).

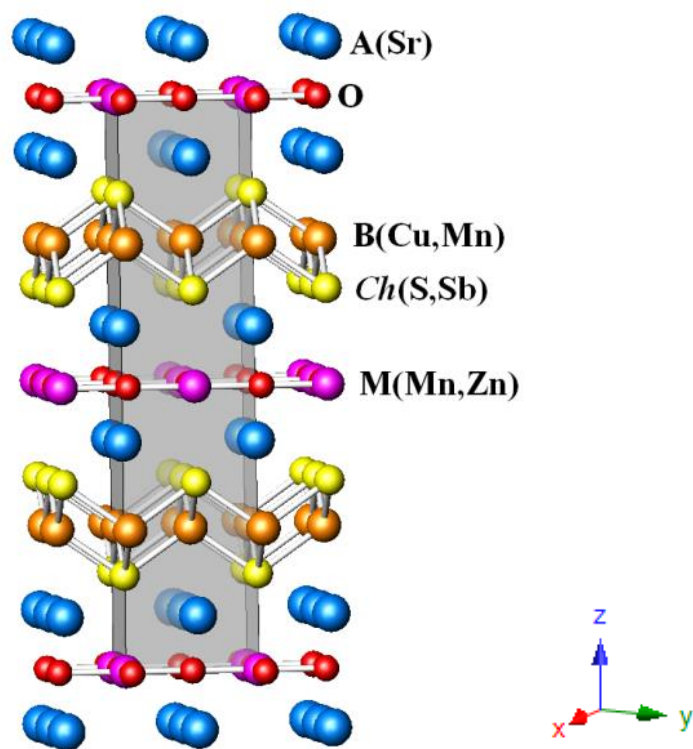


Figure 1.16. The $(A_2MO_2)(B_2Ch_2)$ structure-type.

1.1.1.6 Compounds with $(A_2M_2O)(B_2Ch_2)$ Structures

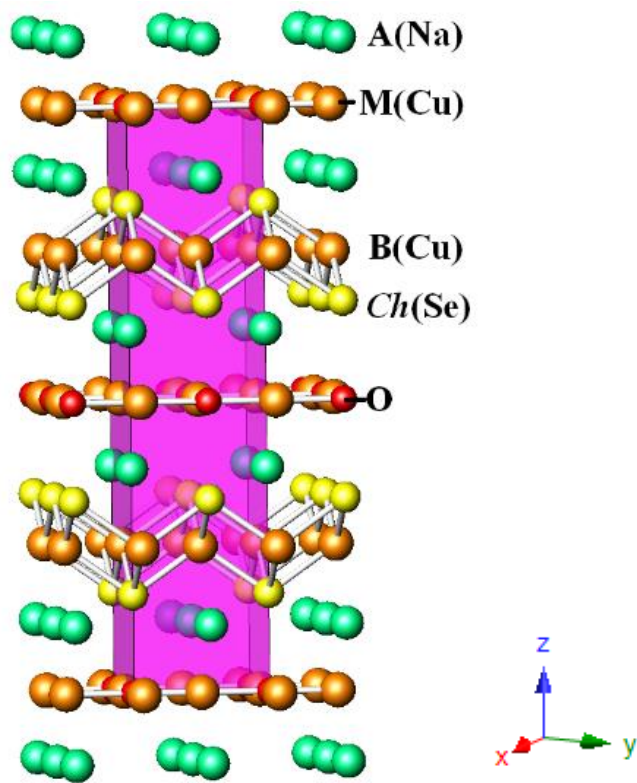


Figure 1.17. Crystal structure of $(A_2M_2O)(B_2Ch_2)$.

This structure type is a half anti-type of $(A_2MO_2)(B_2Ch_2)$, in which A, M are monovalent cations. It comprises the same anti-fluorite chalcogenide layers $[B_2Ch_2]^{2-}$ as that of “1111”- compounds whilst the oxide M_2O planar sheets are separated from $[B_2Ch_2]^{2-}$ by A^+ ions. A representative compound is $Na_2Cu_4OSe_2$ or $(Na_2OCu_2)(Cu_2Se_2)$ [104].

1.1.1.7 Compounds with $(A_2O_2)(B_2OCh_2)$ Structures

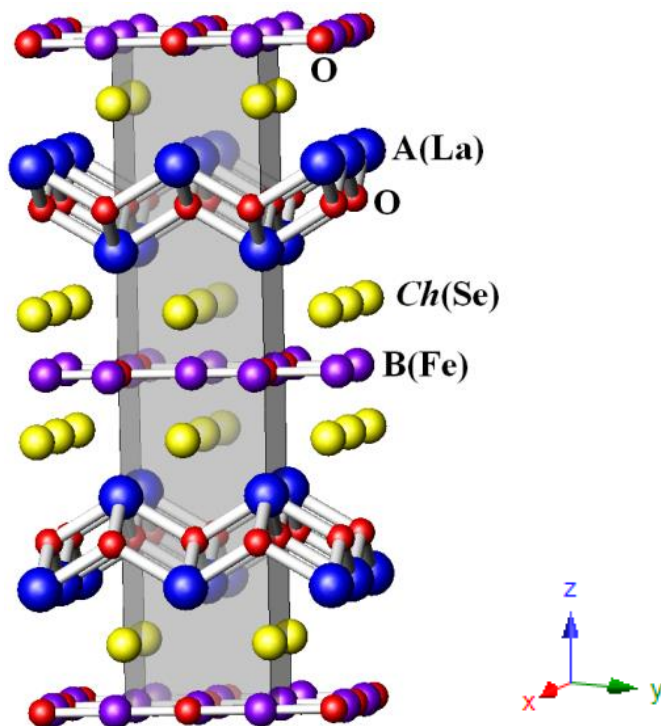


Figure 1.18. Crystal structure of $(A_2O_2)(B_2OCh_2)$.

This is an anti-structure of $(A_2MO_2)(B_2Ch_2)$ structure and half an anti-structure of $(A_2M_2O)(B_2Ch_2)$. The representative compound of this structure type is $La_2Fe_2O_3Se_2$ or $(La_2O_2)(Fe_2OSe_2)$ [105]. It consists of fluorite-type slabs $[A_2O_2]^{2+}$, while the oxide M_2O planar sheet is separated from $[A_2O_2]^{2+}$ by chalcogenide anions.

1.1.1.8 Compounds with Thicker Oxide Layers

The general formula of these compounds is $A_{n+1}M_nO_{3n-1}(B_2Ch_2)$ or $A_{n+1}M_nO_{3n+1}(B_2Ch_2)$ ($n \geq 1$), in which A is a divalent cation; M is di- or trivalent; B is Cu, Ag and Ch is S, Se, Te. $A_{n+1}M_nO_{3n-1}(B_2Ch_2)$ composes anti-fluorite $[B_2Ch_2]^{2-}$ layers stacked alternately with oxide slabs $[A_{n+1}M_nO_{3n-1}]^{2-}$.

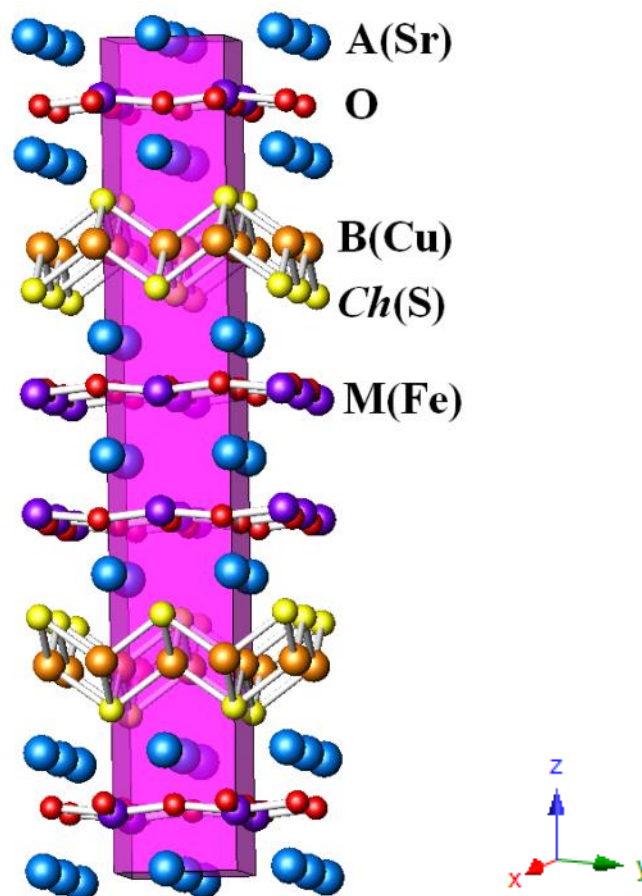


Figure 1.19. Crystal structure of $A_{n+1}M_nO_{3n-1}(B_2Ch_2)$.

When $n = 1$, it corresponds to the $(A_2MO_2)(B_2Ch_2)$ structure, presented in section 1.4.2.3. With $n = 2$; $A = Sr$, $M = Fe, Mn$; $B = Cu$; and $Ch = S$, the $Sr_3Fe_2O_5Cu_2S_2$ and $Sr_3Mn_2O_5Cu_2S_2$ compounds have been found [106]. These compounds are built up by anti-fluorite $[Cu_2S_2]^{2-}$ slabs stacked alternately with perovskite-like $[Sr_3(Fe/Mn)_2O_5]^{2+}$ slabs.

Different to $A_{n+1}M_nO_{3n-1}(B_2Ch_2)$ compounds, $A_{n+1}M_nO_{3n+1}(B_2Ch_2)$ compounds possess more oxygen, forming an anti-fluorite-type $[B_2Ch_2]^-$ layer ($B = Cu^{+1.5}$) stacked alternately with an oxide layer of fluorite-like $[A_{n+1}M_nO_{3n+1}]^+$ along the c -axis. In this structure, A and M are trivalent cations. M is bound to eight oxygens to form a double thickness of oxide layers while A atoms coordinate to four oxygen atoms and four chalcogenide atoms to form a square anti-prism. The typical compound of this kind structure is found with $n = 1$ for $Bi_2LnO_4Cu_2Se_2$ ($Ln = Y, Gd, Sm, Nd, La$) [107].

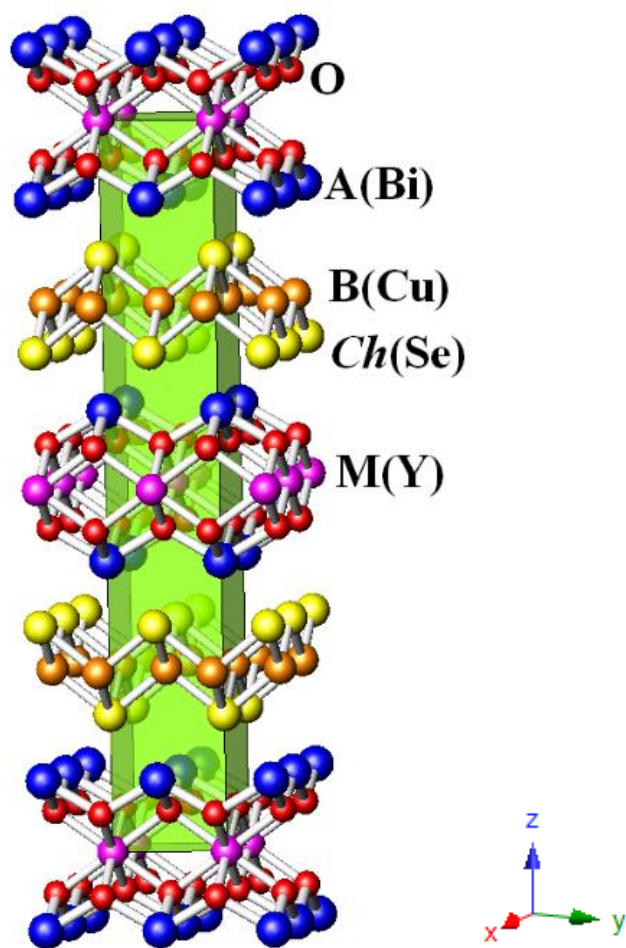


Figure 1.20. Crystal structure of $A_{n+1}M_nO_{3n+1}(B_2Ch_2)$.

1.1.1.9 Compounds with Thicker Chalcogenide Layers

The general formula of these compounds is $(A_2MO_2)(B_{2m-\delta}Ch_{m+1})$ with $m = 2, 3$ and $\delta = 0, 0.5$. A, M and B can have the following oxidation states: $2+$, $2.5+$ (mixed $2+$ and $3+$) and $1+$. For instance, if $A = Sr$, $M = Mn$, $B = Cu$ and $Ch = S$, a series of $Sr_2MnO_2Cu_{2m-\delta}S_{m+1}$ compounds have been formed with $m = 2, 3$ and $\delta = 0.5$ [108-111]. They compose thicker chalcogenide layers, separated by oxide layers, surrounded by A^{2+} ions periodically (Figure 1.21). Depending on the value of m , a larger thickness of chalcogenide layers is formed. The chalcogenide layers are anti-fluorite-type structures of cubic α - Cu_2S , containing copper disorder.

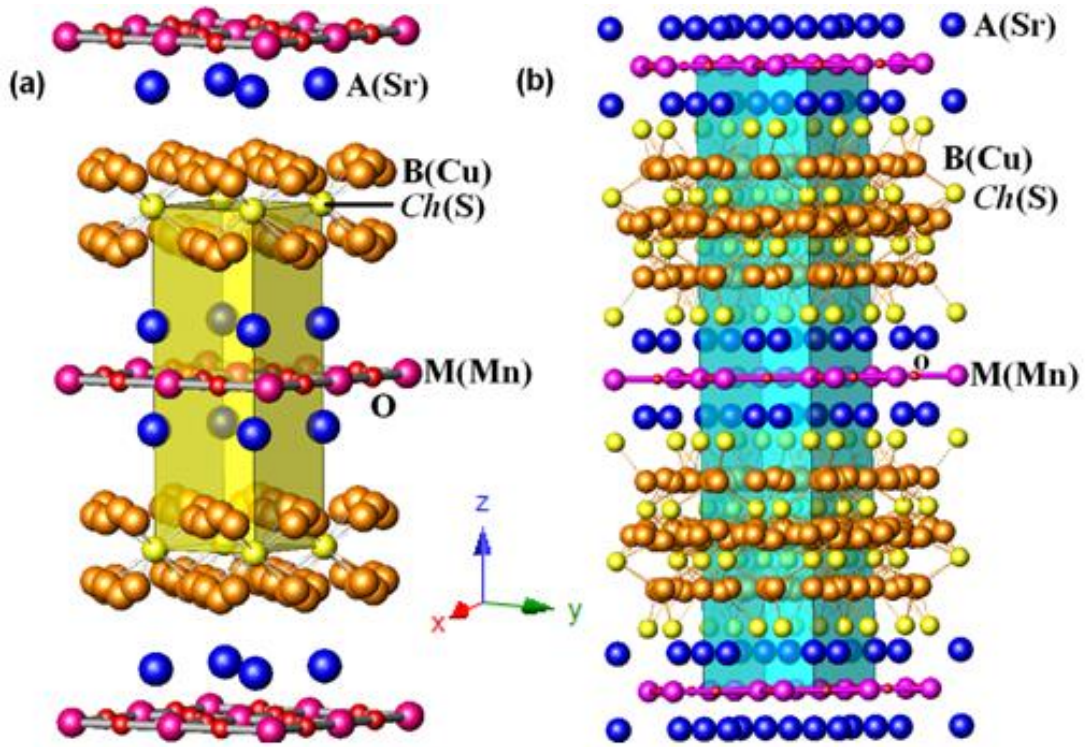


Figure 1.21. Crystal structure of $(A_2MO_2)(B_{2m-\delta}Ch_{m+1})$: (a) $Sr_2MnO_2Cu_{3.5}S_2$ ($m = 2$, $\delta = 0.5$) and (b) $Sr_2MnO_2Cu_{5.5}S_4$ ($m = 3$, $\delta = 0.5$).

1.4.3 Thermoelectric Properties

Despite the many classes of oxychalcogenides that have been discovered, most of the existing studies are concerned with optical and magnetic properties [76, 88, 100, 107, 112]. For reference, reviews of the structure and physical properties of layered oxychalcogenides have been presented in references [31, 112]. Little has been reported in thermoelectric properties, the exception being the “1111” structure-type of the copper-containing oxychalcogenide $AOBCh$ ($A = Bi$, $B = Cu$), which has been extensively investigated as a promising thermoelectric materials since 2010 [113, 114]. They are p-type semiconductors with bandgap $0.23 \text{ eV} \leq E_g \leq 1.2 \text{ eV}$ [96].

As described in section 1.1.1.3, the first oxychalcogenide $AOBCh$ ($A = La$, $B = Ag$, $Ch = S$) was reported as an ionic conductor in 1980 [97]. A few years later (1986), high temperature superconductivity was discovered in the cuprate family $Ba_xLa_{5-x}Cu_5O_{5(3-y)}$ [115]. This motivated the search for similar behaviour in copper – containing oxychalcogenides. However, all efforts were unsuccessful, making them fall into oblivion. In the early 2000s, H. Hiramatsu *et al.*, first reported the potential of these materials for optoelectronic applications as transparent conducting materials [96, 116, 117], and in 2008, this group reported the high- T_c superconductivity of

oxypnictides, $\text{LaFeAsO}_{1-x}\text{F}_x$ [118] which adopt the same layered ZrSiCuAs structure type. This strongly renewed the interest in investigating these materials. A few months later, the potential thermoelectric properties (possessing large Seebeck coefficient at around 100 K) of oxypnictides were reported by L. P. Gaudart *et al.* [119]. This again motivated a search for the same behaviour in structurally related oxychalcogenides. Two years later (2010), the first report of the thermoelectric properties of copper-containing oxychalcogenide, BiOCuSe , was presented [120] although the large electrical conductivity ($\sim 400 \text{ Sm}^{-1}$ at 333 K) was noted earlier in 2003 [121].

1.5 Aims

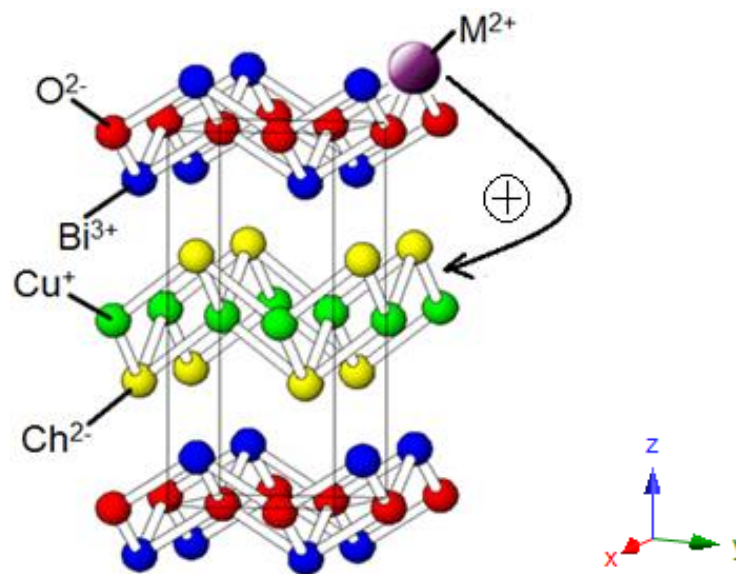


Figure 1.22. Schematic hole generation in crystal structure of BiOCuCh via doping M^{2+} into Bi^{3+} site.

In this dissertation, we have focused on investigating the nature of the thermoelectric behaviour of the parent compounds BiOCuCh ($\text{Ch} = \text{S}, \text{Se}, \text{Te}$), and then on improving the electronic and thermal transport properties of the most promising thermoelectric member of BiOCuCh . The combination of the heavy elements (Bi, Pb, Cd, Zn, Cu, Se, Te) and naturally-low dimensional crystalline structures is expected to result in materials with large values of ZT . The coexistence of covalent layers (chalcogenides – charge carrier channels) and ionic layers (oxides - charge reservoirs), stacked alternately along the c -axis, would allow us to adjust both electrical properties via doping (replacing partially Bi^{3+} by M^{2+} , Figure 1.22) and the thermal conductivity via phonon scattering at interlayers (modifying slab thickness, Figure 1.23). Therefore, the work in

this thesis aims to demonstrate that natural superlattice oxychalcogenides are promising TE oxides materials.

Currently, outstanding TE superlattice compounds are artificial thin films which are limited to laboratory scale [50, 122, 123]. The expensive manufacturing costs and complicated fabrication processes are main drawbacks, making them impractical for large scale production and application. Therefore, we have focused on fabricating layered superlattice materials using simple techniques, such as solid-state reactions in sealed tubes or ball milling. The consolidation technique used is hot press.

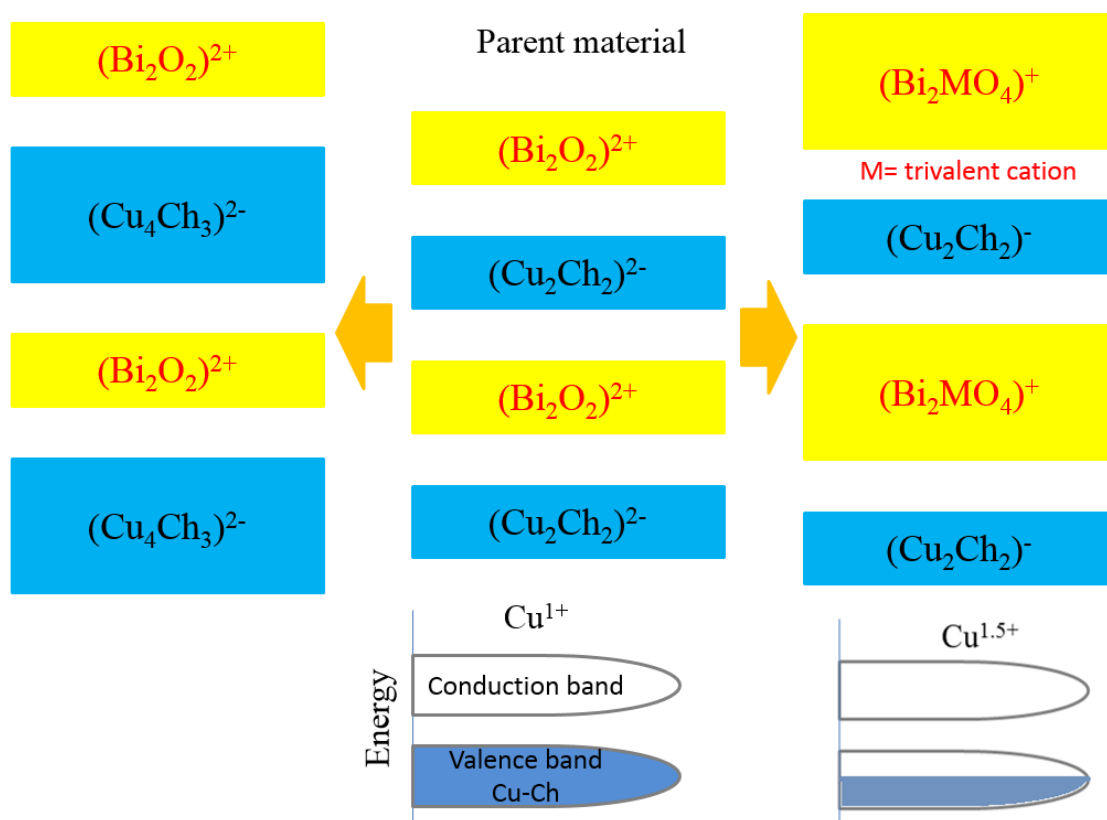


Figure 1.23. Schematic material design of oxychalcogenide BiOCuCh .

Chapter 2 Experimental Techniques

2.1 Introduction

This chapter describes the various synthetic procedures and selected reagents for preparing materials. General information on the techniques used to characterise the synthesised materials and to measure their physical properties is introduced. Meanwhile, the specific details of synthesis will be presented in Chapters 3-5.

2.2 Synthesis Methods

2.2.1 *Solid State Reaction*

This is a high temperature method based on the reaction of a mixture of solid reagents. At a sufficiently high temperature, atoms will diffuse between reagents to create a new stable phase. The limiting factor of this method is the low diffusion rate which requires long reaction time. Therefore, the elements must be initially mixed and ground thoroughly.

All syntheses were carried out using the same procedure of weighing out stoichiometric quantities of reagents. Elemental powders were all mixed and ground in an agate mortar before being put into a silica tube and sealed under a vacuum of $\sim 5 \times 10^{-3}$ torr using a methane and oxygen blow torch. Selenium and tellurium-containing compounds react with the silica tube at temperatures beyond 773 K. Therefore, the silica tube was coated with carbon by the pyrolysis of acetone for reactions below 973 K whilst a carbon crucible was employed for reactions above 973 K. To prepare the carbon-coated tube, the process of heating a silica tube soaked with acetone using a blow torch was repeated three times until a uniform and homogeneous layer was formed on the inner wall. The carbon coated-tube was cleaned with water and acetone. Then, it was dried using the oven at temperature of 373 K for a couple of hours.

The sealed tubes were placed into a furnace and heated up to a set temperature with duration of time according to the specific reaction conditions of each experiment. The specific details will be presented in Chapters 3-5. After the initial firing, the product was removed from the tube and re-ground. The same procedure of sealing an evacuated

tube was carried out again and the sample was subjected to a second annealing process. Then, the final powder was removed from the tube and reground before analysing it by powder X-ray diffraction to determine its phase purity. Further characterisation and measurements were carried out when a single phase was obtained. Figure 2.1 shows the as-prepared sealed tubes and furnace.



Figure 2.1. Silica sealed tubes and furnace.

2.2.2 Ball Milling Process

Ball milling or mechanical alloying involves the use of high-energy mechanical grinding, instead of temperature, to carry out solid-state reactions. This technique was initially developed by Benjamin and his colleagues in 1970 [124, 125]. The mixed precursors are placed in a stainless steel/ceramic jar which contains steel/ceramic balls. This jar is arranged eccentrically on the sun wheel of planetary ball mill. The reaction takes place as a consequence of the high energy collisions from the balls when they are spinning. This technique is considered as one of the methods that produces fine, uniform dispersions of particles. Benefits of this technique are a low-temperature synthesis, high reaction rate, and nanoscale formation. The induced kinetics of alloying or phase transformations depend on the energy transferred from the balls to the powder during ball milling. It is dependent on milling speed, time, size and distribution of balls, weight ratio of ball/powder, type of ball milling, i.e. dry or wet milling, temperature,

atmosphere and duration of milling [126].

In this work, samples were prepared by a planetary mill instrument, model PM100, manufactured by RETSCH [127]. A schematic view of balls with the powder mixture movement and PM100 ball mill machine are shown in Figure 2.2. The amount of mixed powder of each batch is put in a 25ml steel jar together with 40 steel balls with a diameter of 5 mm.

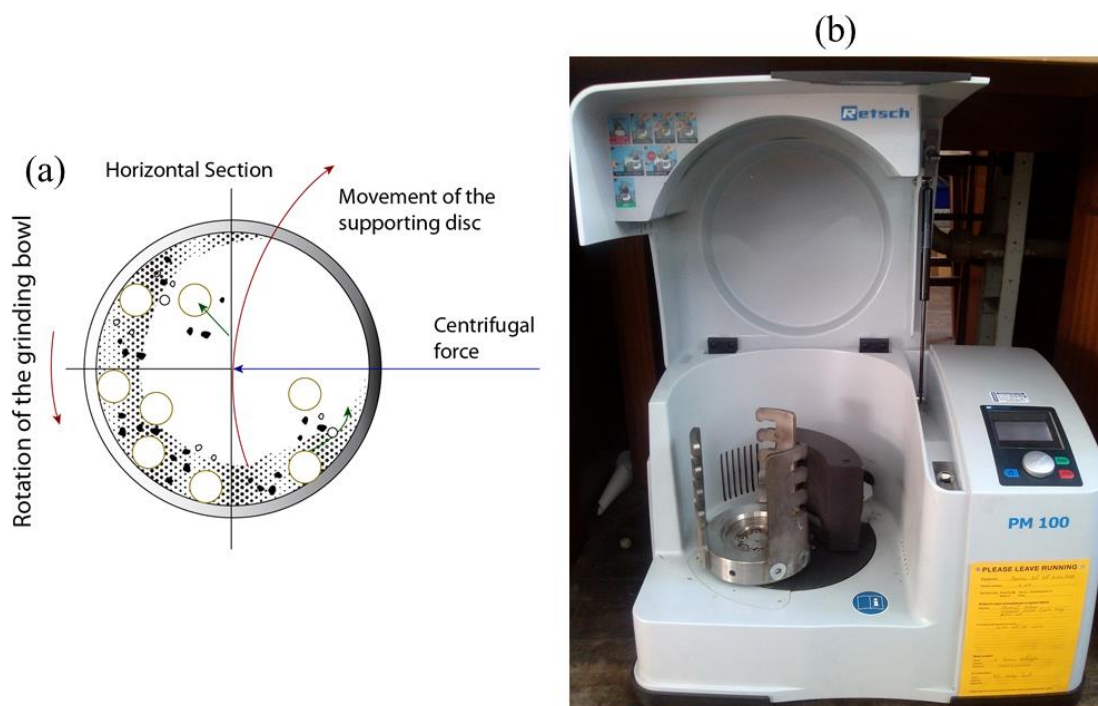


Figure 2.2. (a) Schematic view of balls and powder mixture movement in a planetary mill [126] and (b) PM100 ball milling machine.

2.3 Characterisation Methods

2.3.1 Powder X-ray Diffraction

X – rays are an electromagnetic radiation with a wavelength range of between 0.1 and 100 Å (1 – 120 keV) discovered by a Physics Nobel Prize holder, Wilhelm Röntgen in 1895 [128]. This radiation occurs when bombarding a metal target (generally Cu or Mo) with an electron beam emitted from a heated filament. The electrons decelerate throughout the metal and a few high intensity sharp peaks are produced at specific wavelengths over a continuous range of wavelengths. If the incident electrons have sufficient energy, they will knock an electron out of the inner shell of the metal to a

higher energy level. Then, electrons from other higher states drop down to fill the vacancy and emit the excess energy as an X-ray photon [129]. Due to the comparable wavelength of X-rays to the distance between atoms in solids, X-rays have been used for characterising the structure of a wide range of materials. However, diffraction only takes place if the incident and diffracted beams satisfy Bragg's law:

$$2d_{hkl}\sin\theta = n\lambda \quad \text{Equation (2.1)}$$

where d is the distance between crystallographic planes; θ is the angle between the incident beam and the plane; n is an integer representing the order of the diffraction peak and λ is the wavelength of the X-ray (Figure 2.3).

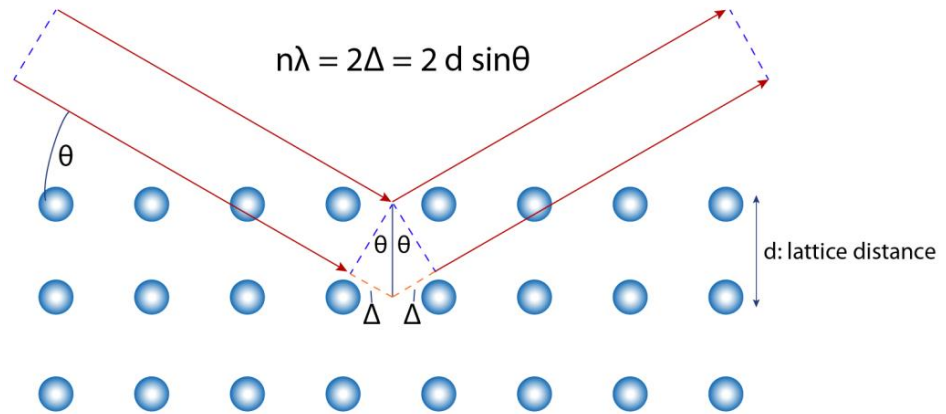


Figure 2.3. Diagram of diffraction at the adjacent planes of a crystal.

There are two diffraction geometries: Bragg-Brentano (reflection configuration) and Debye-Scherrer (transmission configuration). Depending on the diffraction geometry data are collected from the reflected or the transmitted beam through the sample (Figure 2.4).

Powder X-ray diffraction (XRD) is the most popular technique used for characterizing materials consisting of powders, fine grains of a single crystalline material, particles in liquid suspensions or polycrystalline solids. Structural characterization of our samples was carried out using a powder XRD Bruker AXS D8 Advance diffractometer, equipped with a Cu K_{α} X-ray source with $\lambda = 1.54056 \text{ \AA}$. Data were collected in short scans with step-scan mode over the angular range $5 \leq 2\theta^{\circ} \leq 85$ in 0.009° increments, counting for 261.6 s at each step for initial sample characterisation [130]. The phase

determination and purity of samples were initially examined using the EVA program according to ICSD databases [131]. Then, the long scan with step-scan mode over the angular range $5 \leq 2\theta/^\circ \leq 120$ in 0.022° increments, counting for 718.3 s at each step, was carried out for further structural analysis using Rietveld refinement.

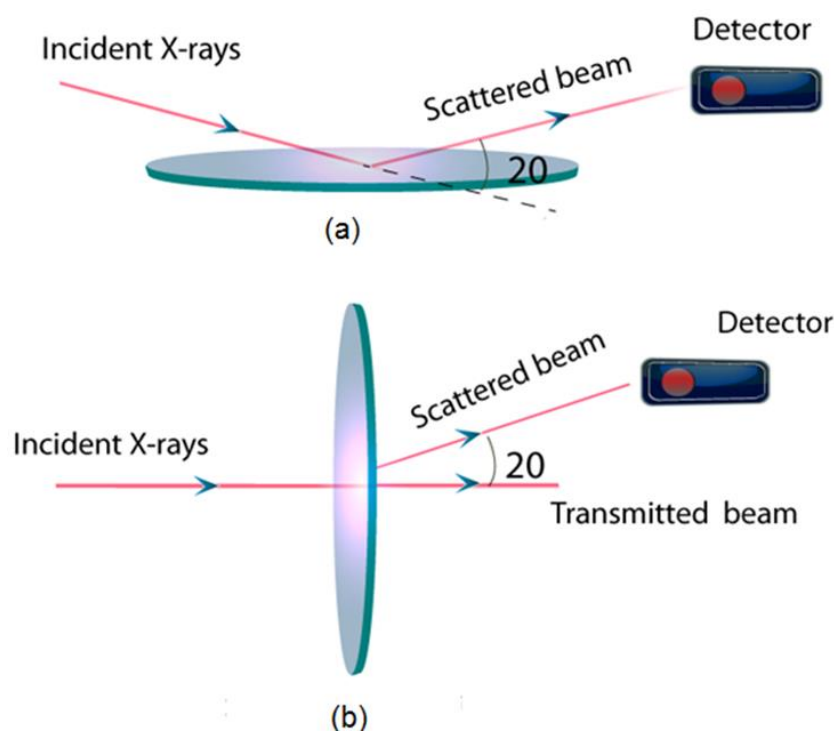


Figure 2.4. The reflection (a) and transmission (b) geometry of X – ray diffraction.

2.3.2 Powder Neutron Diffraction

Sir James Chadwick, an English physicist, who was awarded the 1935 Nobel Prize in physics, discovered neutron particles in 1932 [132]. According to the wave-particle duality of De Broglie hypothesis ($\lambda = h/mv$), free neutrons are elementary particles that have wave properties. The relationship between energy and wavelength of a neutron is presented by:

$$E [\text{meV}] \equiv 81.8204\lambda^{-2} [\text{\AA}^2] \quad \text{Equation (2.2)}$$

Similar to X-rays, neutrons possess a wavelength of atomic scale (\AA). Fundamentally, neutron diffraction has the same scattering theory as that of X-rays, i.e. diffraction

satisfies Bragg's law (Equation (2.1)). With a constant wavelength neutron source, λ is constant whilst the diffraction angle θ is changing. However, in pulsed neutron sources with a broad spectrum of neutron energies (i.e. with a range of λ), called "white" sources, a fixed angle is used. The different energies (velocities) of neutrons are separated by time-of-flight (TOF), by measuring the time neutrons use to travel a fixed distance through a medium.

There is a significant difference between X-rays and neutrons. X-rays interact with the electron cloud surrounding each atom whilst neutrons interact with nuclei. Therefore, in X-ray diffraction, the scattering is dependent on the atomic number, while this does not happen in neutron diffraction. This results in weak diffraction of X-rays by light atoms whilst those same atoms may be strong scatterers of neutrons. Furthermore, neutrons can penetrate deeply into the matter from μm to many cm and constitute a simple, non-destructive probe of matter. In general, neutron diffraction is a very useful technique for investigating structure of materials, especially for light ones.

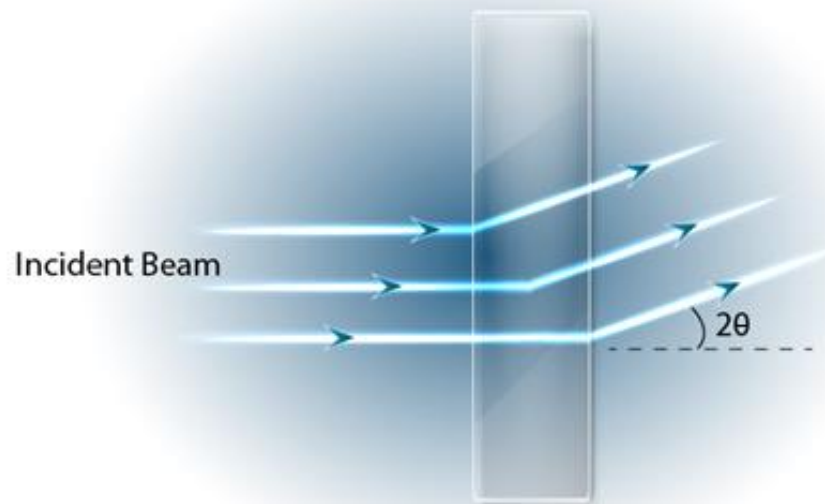


Figure 2.5. Diagram of transmission diffraction of powder neutron diffraction.

Free neutrons are very rare in the universe due to their bonding in nuclei or neutron stars. Hence, free neutrons must be released from the atomic nuclei in two possible ways: one is a fission reactor and the second one is a spallation source. ^{235}U nuclei break into lighter elements and liberate 2 to 3 neutrons for every fissioned atom, while proton

bombardment of tungsten nuclei releases spallation neutrons. Figure 2.5 shows the transmission diffraction of neutrons when they pass through a powder sample inside a holder. Vanadium is normally chosen as a sample holder for neutron diffraction because it is readily available and gives a featureless isotropic scattering pattern [133].

Figure 2.6 is a schematic drawing of the ISIS facility, Rutherford Appleton Laboratory, Didcot, Oxfordshire, UK [134], where neutron diffraction experiments of our samples were carried out. There are two target stations which produce beams of neutrons and muons. Depending on materials, resolutions, properties, the corresponding beams are chosen. These instruments are time-of-flight.

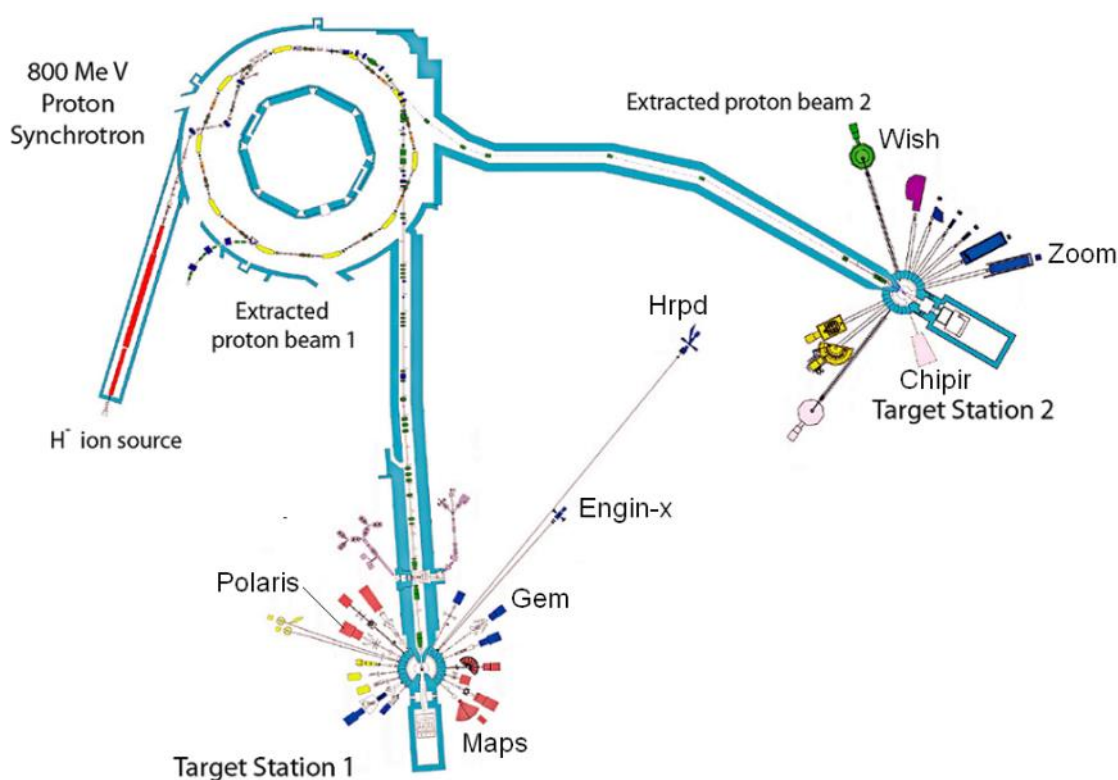


Figure 2.6. Schematic drawing of Diffractometer at ISIS [134].

2.3.2.1 The Polaris

Our powder neutron diffraction experiments were carried out using the POLARIS Diffractometer at the ISIS facility, Rutherford Appleton Laboratory, Didcot, Oxfordshire, UK.

POLARIS is the ideal for medium resolution, high intensity time-of-flight powder diffractometer due to its rapid characterisation of structures, small amount of materials

requirement ($\sim 1 \text{ mm}^3$), rapid time data collection (down to ~ 5 mins) and different temperature data collection. Wavelengths used on this instrument are in the range of $0.1 \leq \lambda/\text{\AA} \leq 6.0$. The technical summary of this instrument is presented on Table 2.1.

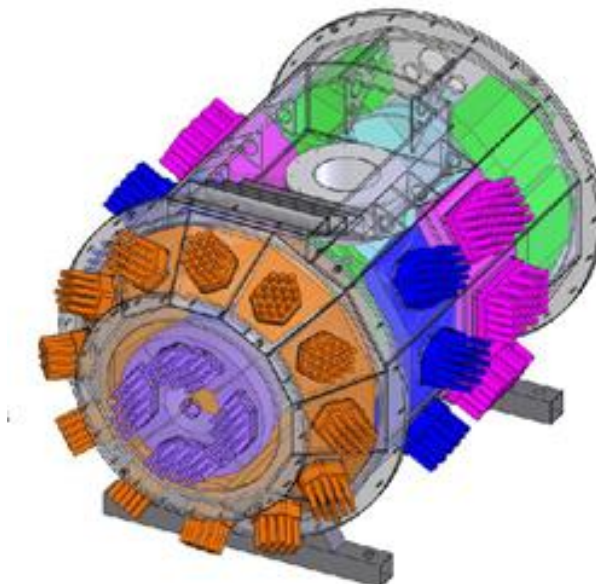


Figure 2.7. Design drawing POLARIS diffractometer [135].

Table 2.1. Details of POLARIS diffractometer detectors [135].

Detector Bank		2θ range ($^{\circ}$)	Secondary flight path(m)	Resolution $\Delta d/d$ (%)	$d_{\text{max}}(\text{\AA})$
Very low angle	1	6 – 14	2.3	> 2.7	19.6
Low angles	2	19 – 34	2.4 – 1.3	1.2 – 1.9	8.7
	3	40 – 67	1.6 – 1.0	0.85	7.0
90 degrees	4	75 – 113	1.1 – 0.7	0.51	3.2
Back scattering	5	135 – 143	1.5 – 1.4	0.30	2.7
	6	146 – 168	1.2 – 0.8	0.30	2.7

Data collection of powdered samples of BiOCuCh ($Ch = \text{S, Se, Te}$) and $\text{Bi}_{1-x}\text{Pb}_x\text{OCuSe}$ ($x = 0.05, 0.15$) from room temperature to 673 K was carried out inside a furnace placed in a sample chamber (Figure 2.7). These powdered samples were sealed into an evacuated low-boron content silica tube attached to a sample stick. The powdered sample of BiOCuTe for this experiment was prepared by my co-worker, Gabin Guélou [136].

2.3.3 Structural Refinement Using Powder Diffraction Data

2.3.3.1 Unit Cell Refinement

The Topas software package [137] was used to determine lattice parameters of samples from their powder X-ray diffraction patterns. The obtained lattice parameters were used as input data for Rietveld refinements.

2.3.3.2 Rietveld Refinement

Rietveld refinement is a method used for characterising crystalline materials. It was developed by Hugo Rietveld in 1969 [138]. It uses a least squares approach to refine a model to fit the observed powder neutron or X-ray diffraction data. The aim of this method is to get a goodness-of-fit which minimises the difference between the observed and calculated intensity of the individual Bragg reflection [139]. The shape of diffraction peaks (profile) and their intensity are included in the model used in the Rietveld refinement. The intensity is determined by structural parameters while the profile is determined by instrument and sample parameters, including instrument resolution, residual stress and crystallite (Scherrer) broadening. Most instrument and sample broadening contributions can be modelled by Lorentzian or Gaussian functions. The function we used for modelling peak shapes in both X-ray and neutron diffractions data is a pseudo-Voigt function [140] which combines Gaussian and Lorentzian functions.

A software named General Structure Analysis System (GSAS) has been used for our Rietveld refinements. After entering the powder X-ray or neutron diffraction profile, a structural model is created. In order to get a good agreement, several parameters

including lattice parameters, atomic coordinates, thermal parameters; background, scale factor, and peak shape are refined [141, 142].

The weighted pattern R factor, which is the weighted percentage difference between the model and the experimental data, is presented in Equation (2.3):

$$R_{wp} = \sqrt{\frac{M_p}{\sum w I_o^2}} \quad \text{Equation (2.3)}$$

where $w I_o$, M_p are the weights of the observed intensity and the minimization function for powder diffraction data, respectively.

$$M_p = \sum w (I_o - I_c)^2 \quad \text{Equation (2.4)}$$

where I_o , I_c are the observed and calculated intensity.

The goodness of fit, χ^2 represents how well the model fits the experimental data, and is described in Equation (2.5):

$$\chi^2 = \frac{M}{N_{obs} - N_{var}} \quad \text{Equation (2.5)}$$

where N_{obs} is the total number of observations in all histograms, N_{var} is the number of variables in the least squares refinement. M is comprised of the weighting factor, f_h , and the sum of each component, M_h .

$$M = f_h \sum M_h \quad \text{Equation (2.6)}$$

It should be noted that R_{wp} is the most meaningful factor because it reflects the progress of the refinement, due to the residual being minimised. Another useful factor is the “goodness of fit”, χ^2 , which shows the adequacy of model. A small χ^2 means that the counting statistical errors far outweigh the model errors [143].

The diffractometer constants and the profile parameters information are required in the time-of-flight neutron diffraction refinement. In order to calculate the relationship between the time-of-flight positions of the Bragg reflections and their d -spacing, diffractometer constants are used. To calculate the widths of each of these Bragg reflections, profile parameters are used. There are three diffractometer constants in GSAS: DIFC, DIFA and ZERO. DIFC relates to the theoretical time-of-flight of a measured Bragg reflection to its d -spacing. DIFA manages small corrections to the expected time-of-flight of a reflection. This allows the peak shifts due to absorption in

sample. ZERO relates to small differences between the various timing signals in the accelerator and the instrument data acquisition system as well as finite response times in the detector electronics [144]. At the beginning, DIFA might be fixed at 0.0 and could be refined in latter stages of refinement whilst ZERO must be fixed throughout refinement. DIFC is normally fixed during refinement in single detector bank. However, if multi detector banks are used, it is refined for the lower resolution histograms and fixed for the highest resolution histogram [144]. For the profile parameters refinement, Gaussian width, σ and Lorentzian width, γ are parameterised as:

$$\sigma^2 = \sigma_0^2 + \sigma_1^2 d^2 + \sigma_2^2 d^4 \quad \text{Equation (2.7)}$$

$$\gamma^2 = \gamma_0 + \gamma_1 d + \gamma_2 d^2 \quad \text{Equation (2.8)}$$

In GSAS, σ_1 and γ_1 may be refined.

2.3.4 Thermogravimetric Analysis (TGA)

TGA is an experimental technique used for measuring the mass change of sample as a function of temperature or time. The mass change is related to the possibility of the decomposition, absorption or desorption of the sample when heated, cooled or kept in isothermal conditions under a specific environment, for example, oxygen, nitrogen or argon. The percentage of mass change and the XRD pattern of the sample after the TGA measurement provide key chemical information about a sample.

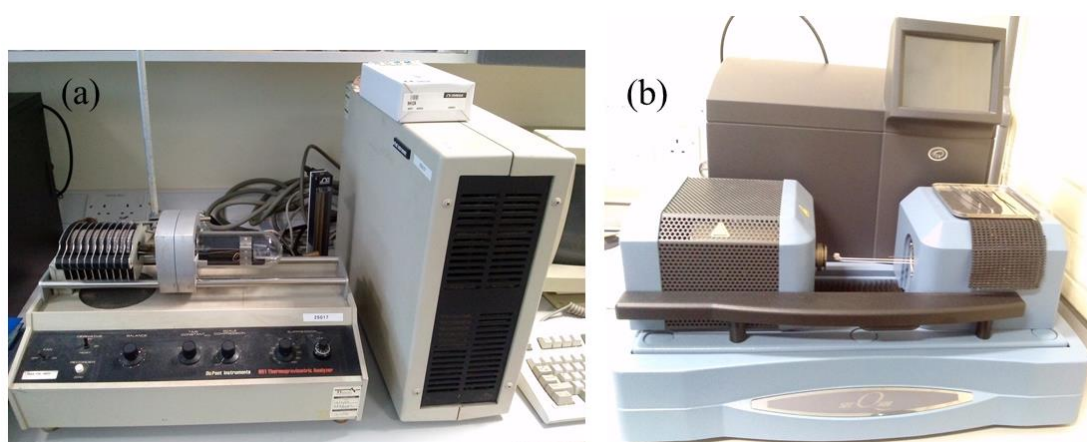


Figure 2.8. (a) DuPont 951 thermo gravimetric analyser and (b) TA-Q600SDT TGA instrument.

A DuPont 951 thermo gravimetric analyser [145] was employed to investigate the thermal stability of BiOCuSe under an O₂ or a N₂ flow whilst a TA-Q600SDT TGA instrument [146] was used to measure the mass change of BiOCuS, and Bi₂O₂Te samples at elevated temperatures under a N₂ flow. Samples were loaded into platinum/ceramic crucibles and heated from room temperature to the explored temperature under the chosen environment (Figure 2.8).

2.3.5 Scanning Electron Microscope (SEM)

SEM is a microscope instrument that uses a focused beam of high-energy electrons (0.1 – 40KeV) to examine surface features, morphology (shape and size of particles), and chemical composition of solid specimens (with a spacial resolution of 50 – 100 nm) based on the interaction of electrons with the surface of the specimen. The design and function of SEM are similar to that of an optical microscope, except that the light source is replaced by a focused electron beam.

Figure 2.9 shows the diagram of a typical SEM instrument. SEM is a method for high resolution imaging of surfaces. Normally, there are three main sources of electron [149, 150]:

- Field emission gun
- Tungsten filament
- A solid state crystal, for example, Lanthanum hexaboride (LaB₆)

The tungsten filament or LaB₆ are typical thermionic gun. In the field emission gun, a very high electric field (around 10⁹ V m⁻¹) is employed to release electrons from a metal filament in a high vacuum system. In contrast, in the thermionic gun, the filament is heated to extract electrons. Then, the divergent electron beam is accelerated towards an anode and arises at the anode hole.

The thermionic gun is cheaper and most commonly used without a requirement of ultra-high vacuum system. However, the field emission gun offers a much higher source brightness. In addition, the lower temperature is required for electron emission in the field emission gun than that of thermionic gun [149 - 151].

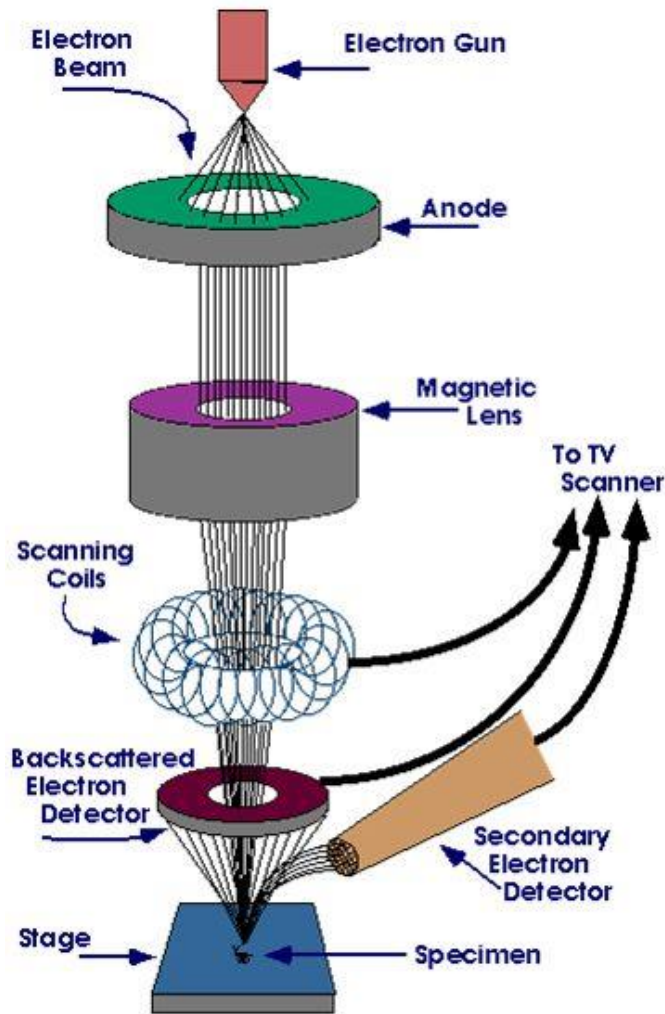


Figure 2.9. Diagram of a SEM instrument [147].

The fundamental components of an SEM are: (1) an electron beam is made using an electron gun in high vacuum. (2) This beam is accelerated towards the specimen by a positive electrical potential at the specimen. (3) Metal apertures and magnetic lenses (0.4-5nm diameter) are used to confine and focus this beam. (4) These accelerated electrons carry high kinetic energy and interact with atoms of the irradiated specimen. The signals of these interactions are collected and transformed into an image (Figure 2.9). These signals include secondary electrons, backscattered electrons (BSE), diffracted backscattered electrons, quantised photons (characteristic X-ray), visible light (cathodoluminescence) and heat. The secondary electrons produce SEM images, showing the morphology and topography of the sample whilst backscattered electrons are used to illustrate contrasts in the composition of multiphase samples. On the other hand, diffracted backscattered electrons are used to determine crystal structures or

orientations of minerals while quantised photons are used for elemental analysis. The X-ray emission occurs when the excited electrons produced by collisions of incident electrons to the electrons in discrete orbitals (shells) of atoms in a sample return to a lower energy states.

Though SEM commonly has been used for studying topography and morphology of solid materials, there are still some limitations. Firstly, it is impossible to detect very light elements (H, He and Li). Secondly, there is a limited crystallographic information and resolution. Finally, an electrically conductive coating must be prepared for insulating samples to produce the highest resolution images [148 - 151].

To study the morphology of BiOCuSe and Pb doped samples, a Quanta 3D FEG - FEI dual beam instrument, incorporating SEM and Ion Beam with SEM mode, was used whilst the remaining samples were measured using a FEI Quanta FEG 600 [152]. This instrument was run at an accelerating voltage of 5 - 20 kV. BiOCuS sample was coated with a thin film of carbon as a conducting layer due to its high electrical resistivity. The rest of samples were measured without any conductive coating. The aluminium sample holder with carbon tab was used to hold powdered samples.

2.4 Physical Properties Measurements

2.4.1 Hot Pressing

Hot pressing is the simultaneous combination of compressive stress and elevated temperature. This technique, shown in Figure 2.10, creates a high density compressed pellet. In addition, hot pressing reduces the porosity of materials. The density of pellet is important for accurate physical properties measurements.

For measuring electrical and thermal properties, the as-prepared powders were hot-pressed into high densified pellets ($\geq 90\%$ of theoretical density). The specific conditions for each type of sample will be presented in Chapters 3-5.

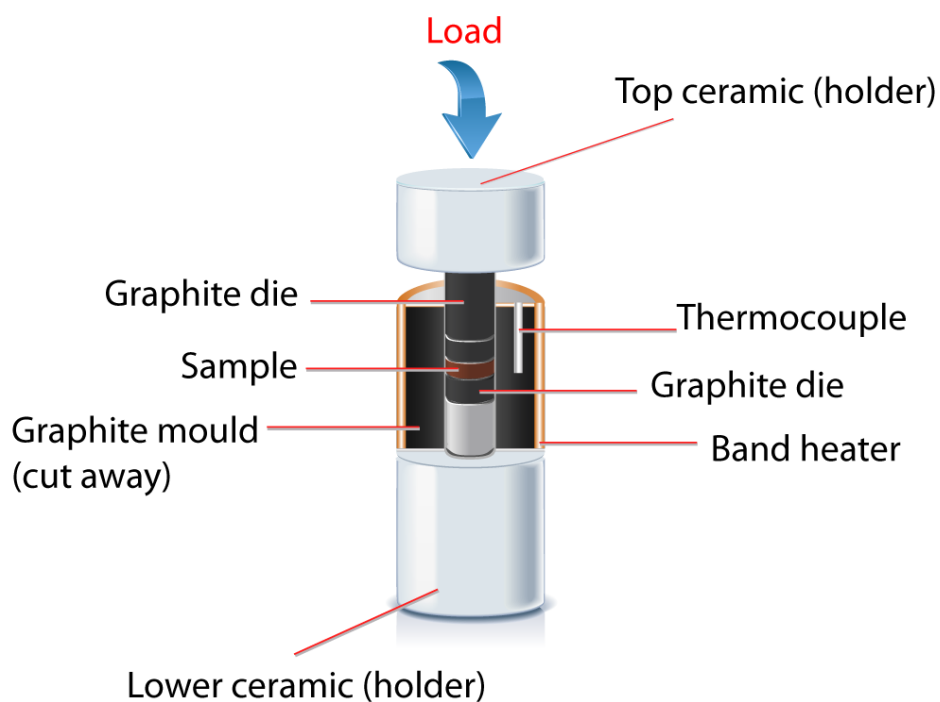


Figure 2.10. Schematic of hot press instrument.

2.4.2 *Ingot Fabrication*

Ingots used for electrical resistivity and Seebeck coefficient measurements were cut from hot-pressed pellets with a SYJ-150 Precision Low Speed Diamond Saw made by MTI Corporation, USA [153]. A rectangular ingot with an approximate size of 6 x 3 x 1 mm was prepared.

2.4.3 *Electrical Resistivity*

Electrical resistivity was normally measured using a four – probe DC method. A current was applied to the ends of the sample while the induced potential difference was measured across probes in the middle of the sample (Figure 2.11a). However, in thermoelectric materials, the thermoelectric voltages induced by Peltier and Seebeck effects may affect the accuracy of the electrical resistivity. Total voltage measured across the sample includes Seebeck voltage and the resistive (IR voltage). In order to minimise errors of measurement, the measurement should be made relatively fast ($\sim 2 - 3$ sec) or by switching the current direction in order to subtract out the Seebeck voltage. Therefore, AC or fast switching DC currents are usually used in resistivity measurement

of thermoelectric materials [154]. For our measuring, a rectangular bar ($\sim 6 \times 3 \times 1$ mm) was cut from a hot pressed pellet of sample.

2.4.3.1 Low Temperature Measurements

The ingot was silver painted and four 50 μm silver wires were attached. Then, the four wires were soldered to an eight-pin chip which was mounted on a probe and loaded into an Oxford Instruments CF1200 cryostat connected to an ITC502 temperature controller (Figure 2.12). The probe is connected to a multi-meter / nanovolt-meter, measuring the voltage across the bar when it is heated over the range of 100 – 300 K under helium (Figure 2.11b). The resistivity is calculated according to Ohm's law:

$$R = \frac{V}{I} \text{ and } \rho = \frac{R.A}{l} \quad \text{Equation (2.9)}$$

where R , V , I , ρ , A , l are resistance (Ω), voltage (V), applied current (A), resistivity (Ωm), cross sectional area (m^2) and the length of the bar (m), respectively.

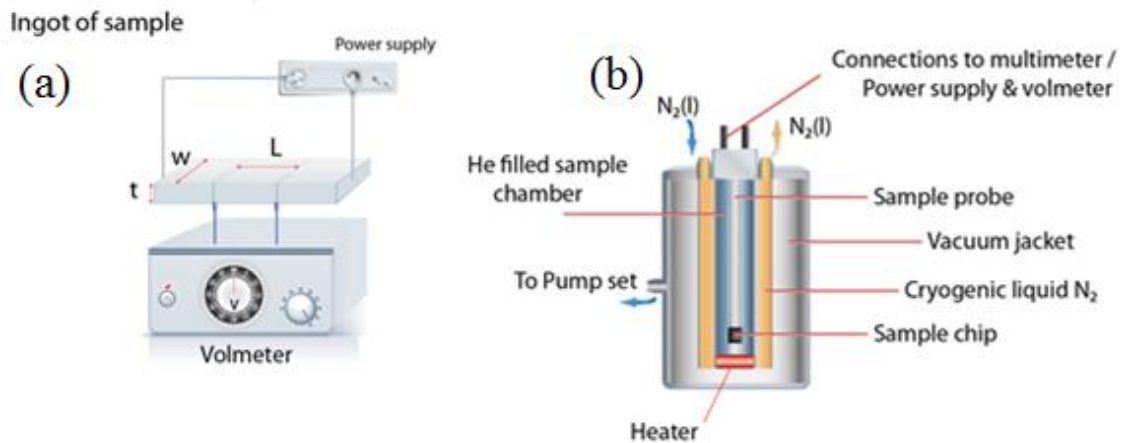


Figure 2.11. (a) Ingot of sample; (b) Schematic set up of the resistivity instrument

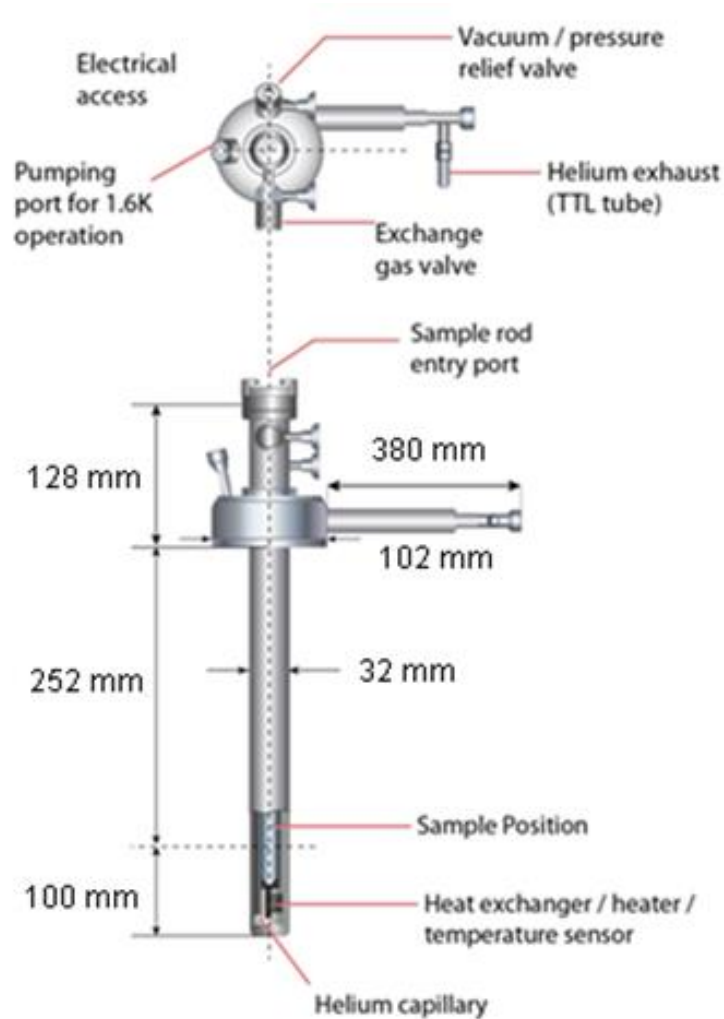


Figure 2.12. Schematic diagram of CF1200 cryostat [155].

2.4.3.2 *Manual Measurements for Materials with Low Electrical Resistance*

This mode is chosen for samples with low electrical resistivity values ($\rho \leq 10 \text{ meV}$) such as metals and small band gap semiconductors. A TTi QL564P power supply and a Keithley 2182 nanovoltmeter was connected to the probe shown above (Figure 2.12). The resistivity was measured manually by increasing temperature in 25 K steps. The voltages at 0 mA and 10 mA currents were recorded. Then, the resistivity values versus temperature were manually calculated using Equation (2.9).

2.4.3.3 *LabView Controlled Automatic Measurements*

More resistive samples were measured using an automatic LabView program written by Dr. Paz Vaqueiro. The probe shown above was connected to a multi-meter which

automatically recorded the voltage across the ingot and calculated the resistivity as a function of temperature using Equation (2.9).

2.4.3.4 High Temperature Measurements

Higher temperature (300 – 700 K) resistivity measurements were carried out using Linseis LSR-3 instrument [156]. The ingot sample was heated up from 300 K to 700 K in 10 K steps; and a current of 100 mA for samples with low electrical resistivity or a current of 20 – 50 mA for samples with higher electrical resistivity ($> 0.1 \Omega \text{ cm}$) (Figure 2.13).

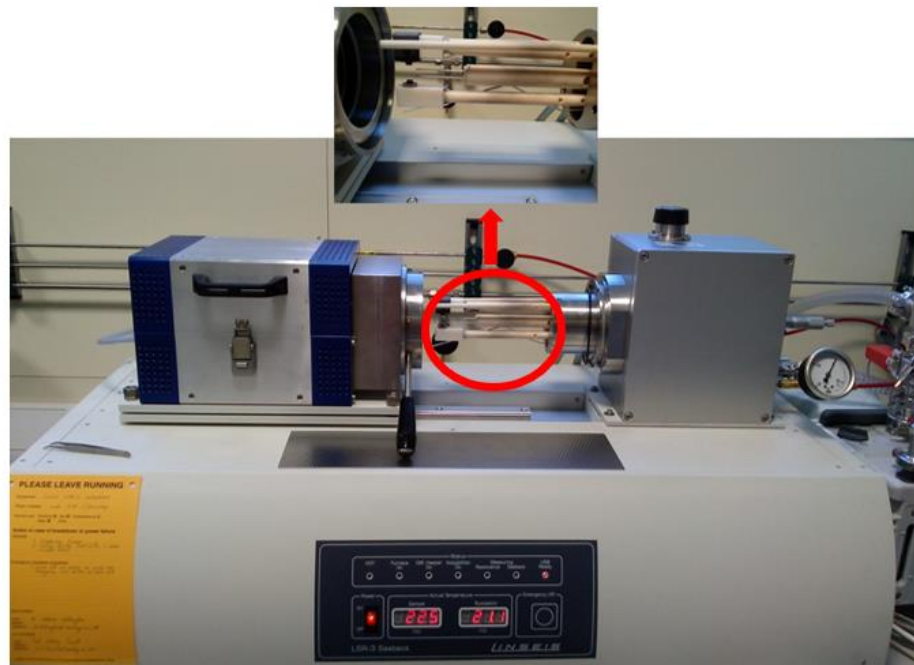


Figure 2.13. Linseis LSR-3 instrument.

2.4.4 Hall Measurements

The Hall Effect was discovered by Edwin H. Hall in 1879 when he first observed a voltage difference appearing across a current-carrying thin metal strip under a magnetic field. The induced voltage is transverse to the electric current when the magnetic field is applied perpendicularly to the current [157]. The Hall effect plays an important role in determining the carrier concentration, electrical resistivity and mobility of carriers in semiconductors.

2.4.4.1 Hall Coefficient

The Hall Effect arises as a consequence of the effect of Lorentz force on charge carriers (electron, hole) under electric and magnetic fields.

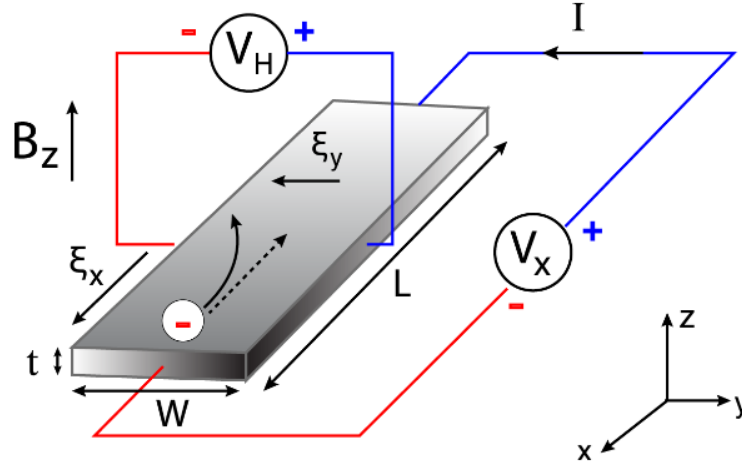


Figure 2.14. Schematic of Hall Effect of electron carriers under a magnetic field $|B|$. The E_x induced by applied current while E_y created by Hall Effect.

When a magnetic field is applied perpendicularly to the direction of the moving charge carriers (i.e. same direction of applied current for holes and in opposite side for electrons), these carriers experience a Lorentz force. This force drives carriers away from the straight line of current direction and accumulates carriers at the edge of direction path (Figure 2.14). This results in an asymmetric distribution of carrier density, then creating an electric field perpendicular to the direction of applied current across the material. This second electric field suppresses the migration of further carriers. Therefore, an electrical potential, called Hall voltage (V_H), is established during the flowing of charge carriers [158]:

$$V_H = \frac{IB}{qnt} \quad \text{Equation (2.10)}$$

where I , B , t , n are the current across the plate length, magnetic field, thickness of the plate and charge carrier density respectively; q is elementary charge (1.602×10^{-19} C), positive for holes and negative for electrons.

The Hall voltage is negative and positive for n-type and p-type semiconductors, respectively.

The Hall coefficient (R_H) is defined as a ratio of the induced electric field and product of electric current and magnetic field:

$$R_H = \frac{\varepsilon_y}{j_x B} = \frac{V_H t}{IB} = \frac{1}{nq} \quad \text{Equation (2.11)}$$

where ε_y and j_x are induced electric field and current density, respectively.

From Equation (2.11), the charge carrier density could be determined when the Hall coefficient is measured.

2.4.4.2 Van De Pauw Method

Van De Pauw (VDP) method is a method which four probes located at four edges of a square or disk shaped material to measure the electrical resistivity accurately. The voltage induced by the current applied to the edges of two adjacent probes is measured by two additional probes on the other edges of the sample [159].

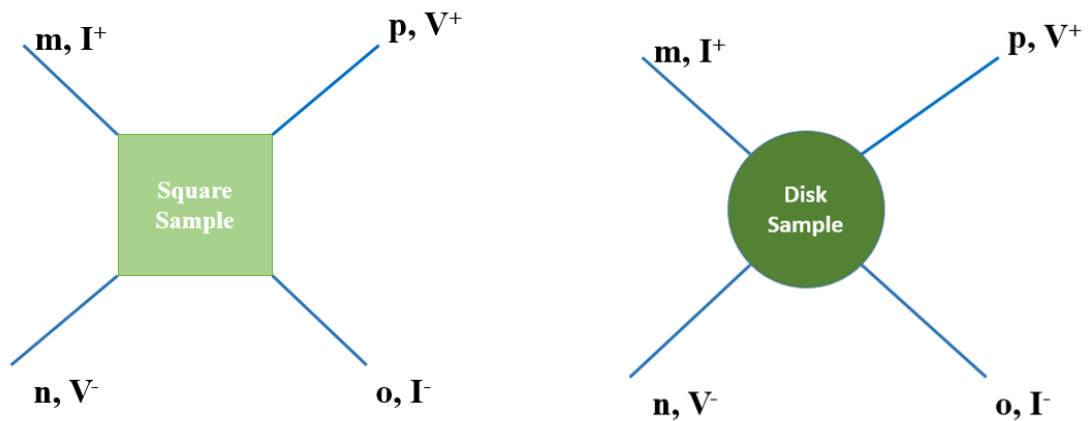


Figure 2.15. A typical geometry of sample set up for Hall Effect measurement with the VDP method.

In this method, the measurement of the thickness of the sample is needed. The Hall coefficient can be determined using the Equation (2.12) [154, 158]:

$$R_H = \frac{t \cdot R_{mO,nP}}{B} \quad \text{Equation (2.12)}$$

where t , $R_{mO,nP}$ are the thickness and resistance of sample, respectively. B is the magnetic field.

This measurement is repeated in both positive and negative fields to subtract the Ohmic voltage signal.

2.4.4.3 Carrier Concentration and Hall Mobility

The VDP method enables the measurement of the resistance of sample, which involves the charge carrier density and mobility (μ). Once the Hall voltage V_H is measured, the Hall mobility is determined from the Equation (2.13) [154, 158]:

$$\mu = \frac{V_H}{I \cdot B \cdot R_{mO,nP}} \quad \text{Equation (2.13)}$$

And charge carrier concentration (n) is determined by Equation (2.14):

$$n = \frac{1}{q \mu R_{mO,nP}} \quad \text{Equation (2.14)}$$

where q is elementary charge (1.602×10^{-19} C), positive for holes and negative for electrons.

2.4.4.4 Sample Preparation

A square shaped sample with length of ~ 4 mm and thickness of ~ 1 mm was prepared. Indium solder was used to achieve good electrical contacts. A magnetic field of -1 to 1 Tesla and the van der Pauw method were applied to measure Hall coefficient and resistivity of sample, respectively. The charge carrier concentration (n) and mobility (μ) of samples were calculated from the Hall coefficient and resistivity values measured using an Ecopia HMS-3000 Hall measurement system (Korea).

2.4.5 Seebeck Coefficient

In order to measure the Seebeck coefficient, the simple method used is to measure the magnitude of the induced voltage (ΔV) versus the temperature difference across that material (ΔT), given that:

$$S = \frac{\Delta V}{\Delta T} \quad \text{Equation (2.15)}$$

2.4.5.1 Low Temperature Measurements

In order to measure this parameter, two $50 \mu\Omega$ copper wires were attached to the ends of sample bar ($\sim 6 \times 3 \times 1 \text{ mm}$) using silver paint. The sample then was mounted onto a copper bar sample holder which is attached to two Au: 0.07 % Fe vs. chromel thermocouples connected to a Lakeshore LS-331 temperature controller.

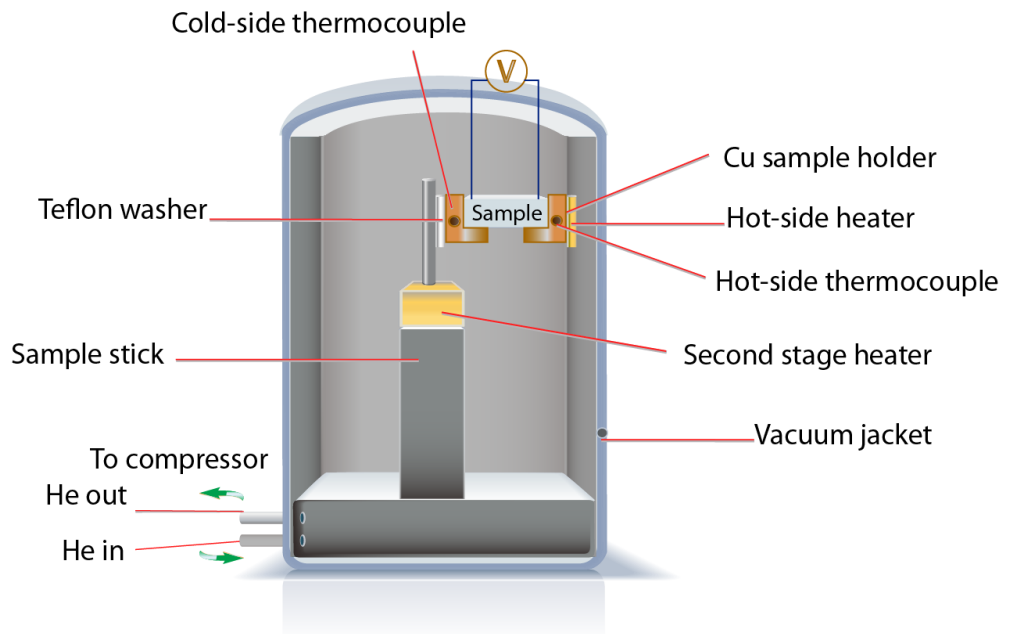


Figure 2.16. Schematic set up of Seebeck instrument.

The sample was heated from 100 K to 320 K in 5 K steps. A small heater (120Ω strain gauge), located close to an end of the sample was used to create a temperature gradient at each temperature. The system was evacuated and measurements run using an Advanced Research System Inc. ASR-2HW compressor and a closed cycle refrigerator (DE-202, Advanced Research Systems). The copper holder attached to the hot stage of

the closed cycle refrigerator was connected to a Lakeshore LS-331 temperature controller. The other ends of the sample copper wires were connected to a Keithley 2182A nanovoltmeter to record the induced voltage (Figure 2.16). P-type and n type semiconductors will show positive and negative Seebeck coefficients, respectively.

2.4.5.2 High Temperature Measurements

Higher temperature (300 – 700 K) Seebeck coefficients were measured simultaneously with high temperature resistivity measurements using Linseis LSR-3 instrument, mentioned above, with an applied temperature gradient of 30 K [153].

2.4.6 Thermal Conductivity

In order to measure the thermal conductivity of the material, its thermal diffusivity is measured, and the relationship among the thermal conductivity, thermal diffusivity, specific heat and density of material, shown in the equation below, is taken into account:

$$\alpha = \frac{\kappa}{\rho \cdot C_p} \quad \text{Equation (2.16)}$$

where α , κ , ρ , C_p is thermal diffusivity, thermal conductivity, density, and heat capacity, respectively.

The flash method is used for measuring thermal diffusivity. The advantage of this method is a fast, and reproducible measurement with excellent accuracy [160, 161]. A small, thin graphite coated pellet is subjected to a short duration radiant energy pulse of high intensity. The energy of the pulse is absorbed on the front surface of the sample and propagates through the whole sample thickness. The temperature of the rear surface is recorded by an IR sensor as a function of time. Then, the thermal diffusivity of all samples is obtained using Parker's expression:

$$\alpha = 0.13879 \cdot \frac{Th^2}{t_{1/2}} \quad \text{Equation (2.17)}$$

where T_h , $t_{1/2}$ are the sample thickness and the time required to reach half of the limiting temperature whilst the specific heat and density are already known [160, 161]. A Pyroceram™ 9606 reference material (known heat capacity) was used to determine the heat capacity of samples [160-162]. Figure 2.17 shows the schematic diagram of a thermal conductivity instrument.

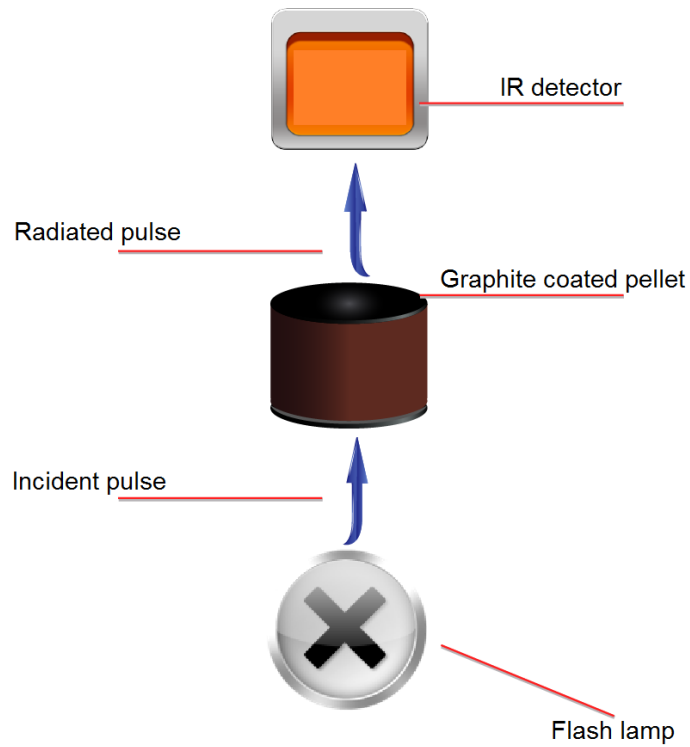


Figure 2.17. Schematic of a thermal conductivity instrument.

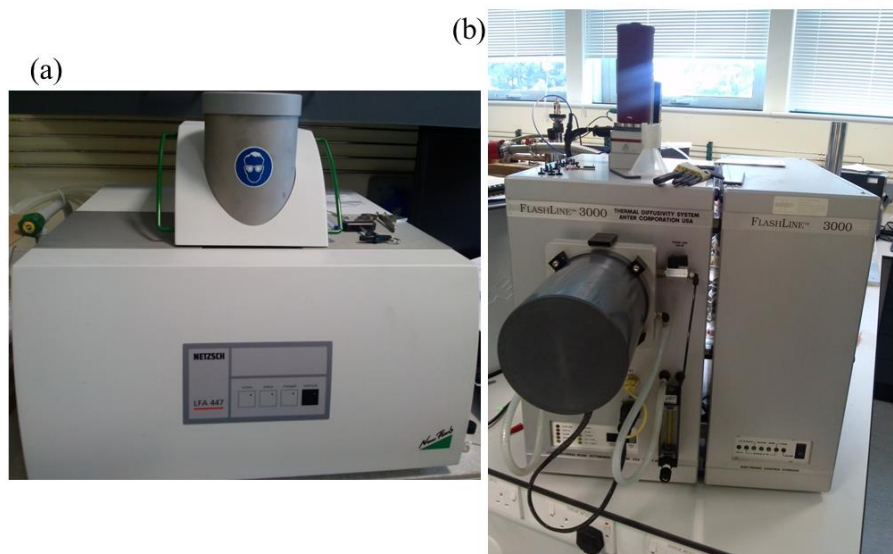


Figure 2.18. Thermal conductivity measurement instrument at temperature of (a) $300 \leq T/K \leq 573$ and (b) $373 \leq T/K \leq 1273$ K.

LFA 447 NanoFlash[®] was employed to measure the thermal conductivity of samples at room temperature and up to 573 K (Figure 2.18a). Figure 2.19 shows the operating mechanism of this instrument [162]. A hot-pressed cylindrical or square sample with approximate 12.7 mm diameter and 1 – 2 mm thickness was prepared with a carbon coating on its surfaces.

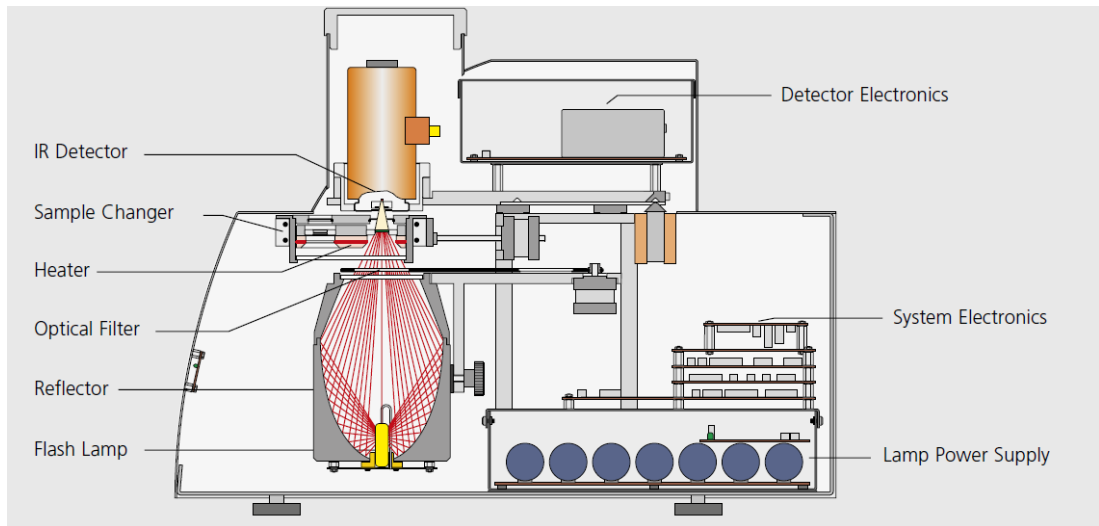


Figure 2.19. Schematic drawing of LFA 447 NanoFlash^{®35} [163].

In order to collect data at temperatures beyond 373 K, an Anter FL3000 instrument was used [164] (Figure 2.18b). A hot-pressed cylindrical pellet with approximate 13mm diameter and 1 – 2 mm thickness was prepared. Then, a graphite coating on its surfaces was applied in order to maximise heat absorption. The sample was then loaded into the sample chamber which was purged with flowing nitrogen during the measurement.

Chapter 3 Layered Oxychalcogenides BiOCuCh ($Ch = S, Se, Te$) and Bi₂YO₄Cu₂Se₂

3.1 Introduction

As discussed in Chapter 1, the bismuth copper oxychalcogenides BiOCuCh (also known as BiCuChO or BiCuOCh; $Ch = S, Se, Te$) have received considerable attention recently, especially for optoelectronic and thermoelectric applications [96, 116, 120, 136, 165-182]. Since the first report in 2010 of the promising thermoelectric properties of hole doped BiOCuSe, with a ZT value of 0.76 at 873 K [120], the number of publications on these oxyselenides has been increased significantly [113]. The most common approach to achieve a high ZT in these compounds is to modify the electrical conductivity via doping, given its naturally low thermal conductivity (approaching the low value of PGEC materials introduced in Chapter 1). However, the root cause of this low thermal conductivity is unclear although the effect of its natural superlattice layered structure has been mentioned. Therefore, the work in this chapter focuses on analysing the structures of these materials via powder X-ray and neutron diffraction, as well as on the relationship between structure and electrical and thermal transport properties. In addition, results on attempts to modify the thickness of the layers, will be presented. Yttrium was chosen as M element in the proposed Bi₂MO₄Cu₂Se₂ compound (containing thicker oxide slabs) while Bi₂O₂Cu₄Se₃ was chosen as the target for thicker chalcogenide slabs.

3.2 Experimental Procedure

3.2.1 Sample Preparation

Samples of polycrystalline BiOCuCh ($Ch = S, Se$) were prepared by solid-state reaction from mixtures of bismuth (III) oxide, Bi₂O₃ (99.99%, Sigma Aldrich); elementary bismuth, Bi (99.5%, Sigma Aldrich); copper, Cu (99.5%, Matthey Materials); elementary selenium, Se (99.99%, Sigma Aldrich) and sulphur, S (flakes, 99.99%, Sigma Aldrich) using evacuated and sealed silica tubes ($\sim 5 \times 10^{-4}$ Torr). Bi₂O₃ and S were dried before using. Samples were prepared in air and ground in an agate pestle. Details of reaction time and temperature of samples are presented in the next sections.

3.2.1.1 *BiOCuS*

A stoichiometric mixture of BiOCuS was first heated up to 673 K for 48 hours with a 1 K / min ramp rate for heating and cooling process. A second annealing process at 873 K for a further 48 hours was carried out after regrinding. Final products were reground and phase purity was initially determined by powder X-ray diffraction. Then, the BiOCuS powder was hot-pressed at 833 K and a uniaxial pressure of 120 bars for 15 minutes under N₂ flow to produce the highly densified ~ 13 mm diameter pellet (~ 90 % of theoretical density). A tungsten die and graphite mould were used to consolidate the powder as the graphite die would break when the pressure is higher than 80 bars.

3.2.1.2 *BiOCuSe*

A stoichiometric mixture of BiOCuSe was first heated up to 623 K for 20 hours and then up to 773 K for 10 hours with a 2 K / min ramp rate. A second annealing process at 873 K for a further 7 hours was carried out after regrinding the obtained powder. Final products were reground and phase purity was initially determined by powder X-ray diffraction. Then, the BiOCuSe powder was hot-pressed into a highly densified pellet (~ 94% of theoretical density) with a diameter of around 13 mm at 853 K and a uniaxial pressure of 50 bars for 30 minutes under N₂ flow. A graphite mould and dies were used.

3.2.1.3 *BiOCuTe*

The preparation and physical properties of BiOCuTe were reported by our coworkers and published in [136].

3.2.1.4 *Bi₂O₂Cu₄Se₃*

A mixture of bismuth (III) oxide, Bi₂O₃ (99.99%, Sigma Aldrich); elementary bismuth, Bi (99.5%, Sigma Aldrich); copper, Cu (99.5%, Matthey Materials); elementary selenium, Se (99.99%, Sigma Aldrich) with a molar weight ratio of Bi:O:Cu:Se equalling to 1:1:2:1.5 was prepared in an evacuated and sealed silica tube (~ 5x10⁻⁴ Torr). The stoichiometric mixture was first heated up to 623 K for 20 hours and then up to 773 K for 10 hours with a 2 K / min ramp rate. The second annealing process at 873 K for a further 7 hours was carried out after regrinding the obtained powder. The

product was characterised by powder X-ray diffraction. The X-ray pattern of collected powder shows that BiOCuSe (> 90% intensity) and CuSe phases exist. Then, a third and fourth firing processes at 1073 K for 5 hours and 24 hours with a 1 K / min ramp rate were carried out. The final product was reground and phase purity was determined by powder X-ray diffraction. The X-ray pattern is consistent with a mixture of BiOCuSe, Bi₂O₃ and Cu₄Se₃.

3.2.1.5 Bi₂YO₄Cu₂Se₂

Bi₂YO₄Cu₂Se₂ was synthesised by solid state reaction in an evacuated silica tube ($\sim 5 \times 10^{-4}$ Torr) from a mixture of bismuth (III) oxide, Bi₂O₃ (99.99%, Sigma Aldrich); elementary bismuth, Bi (99.5%, Sigma Aldrich); copper, Cu (99.5%, Johnson Matthey Materials), elementary selenium, Se (99.99%, Sigma Aldrich) and yttrium oxide, Y₂O₃ (99.99%, Aldrich, with an excess of 5% atomic weight) at a temperature of 673 K for 19 hours. Before mixing the precursors, the Y₂O₃ powder was heated up to 1273 K for 1 hour and quickly removed from the furnace to reduce its moisture content. The second firing of reground powder was at 1073 K for 4 hours with a ramp rate of 1 K / min. The final product was reground and phase purity was initially determined by powder X-ray diffraction. To prepare a pellet ($\sim 81\%$ of theoretical density) with diameter of ~ 13 mm, the powder was hot-pressed at 943 K and a uniaxial pressure of 80 bars for 45 minutes under N₂ flow. It should be noted that this temperature is the maximum temperature of our heater. We have tried to increase the pressing time to one hour but the density of pellet was not improved.

3.2.2 Characterisation and Physical Property Measurements

3.2.2.1 Structural Characterisation

3.2.2.1.1 X-Ray Diffraction

Powder X-ray diffraction data of all samples was collected over the range of $5 \leq 2\theta^\circ \leq 120$ in 0.022° increments, counting for 718.3 s at each step on. Data were analysed using the GSAS package [141]. The input lattice parameters for Rietveld refinement were determined using Topas [137].

3.2.2.1.2 Neutron Diffraction

Neutron diffraction data on powdered samples of BiOCu Ch ($Ch = S, Se, Te$) were collected on the POLARIS diffractometer at the ISIS facility, Rutherford Appleton Laboratory. Time of flight data were collected on heating from ambient temperature to 673 K, at the following temperatures: 293, 373, 473, 573, 623 and 673 K. Neutron diffraction data from the backscattering (146.7°), 92.6° and low angle (52.2°) detector banks were summed, normalised and used simultaneously in Rietveld refinements, carried out using the GSAS package [141].

3.2.2.2 Microstructural Characterisation

To study the morphology of BiOCuSe, a Quanta 3D FEG - FEI dual beam instrument, incorporating SEM and Ion Beam with SEM mode, was used whilst BiOCuS was measured using a FEI Quanta FEG 600 [152]. These instruments were run at 5 kV and 20 kV accelerating voltages, respectively without a carbon coating on the surface of the samples.

3.2.2.3 Thermal Analysis

The thermal stability of BiOCu Ch ($Ch = S, Se$) was investigated using by thermogravimetric analysis (described in Chapter 2). The BiOCuSe sample was loaded into a platinum crucible and heated from room temperature to 973 K with a rate of 2 K / min under an O₂ or a N₂ flow, whilst BiOCuS was loaded into a ceramic crucible and heated from room temperature to 973 K with a rate of 5 K / min under a N₂ flow.

3.2.2.4 Electrical Transport Measurements

The electrical transport properties were measured over the temperature range $100 \leq T/K \leq 673$. It should be noted that, over the temperature range of $100 \leq T/K \leq 300$, the manual electrical resistivity mode (described in Chapter 2) was chosen for BiOCuSe and the Bi₂YO₄Cu₂Se₂ samples due to their low electrical resistivity. On the other hand, the automatic measuring mode (which is also described in Chapter 2) was used for the BiOCuS sample. The charge carrier concentration (n) and mobility (μ) of BiOCu Ch ($Ch = Se, Te$) were calculated from the Hall coefficient and resistivity values measured

using an Ecopia HMS-3000 Hall measurement system (Korea). It should be noted that due to high electrical resistivity of BiOCuS sample, which is over the measurable limit of Ecopia HMS-300, its charge carrier concentration and mobility could not be determined. A square sample of BiOCuCh ($Ch = \text{Se, Te}$) with a length of ~ 4 mm and thickness of ~ 1 mm was prepared. Indium solder was used to achieve good electrical contacts. A magnetic field of -1 to 1 Tesla and the van der Pauw method [159] were applied to measure Hall coefficient and electrical resistivity of the sample, respectively.

3.2.2.5 Thermal Transport Measurements

Thermal transport measurements of these samples were carried out using different instruments. An Anter FL3000 system was employed for measuring thermal diffusivity (α) and the heat capacity (C_p) of BiOCuSe and Bi₂YO₄Cu₂Se₂, over a temperature range of $373 \leq T/\text{K} \leq 673$ in 50 K steps, whilst an LFA 447 NanoFlash[®] was employed to measure the thermal conductivity of BiOCuS sample at room temperature and up to 523 K in 50 K steps.

3.3 Results and Discussion

3.3.1 BiOCuCh ($Ch = \text{S, Se and Te}$) Compounds

3.3.1.1 Structural Characterisation

Powder X-ray (Appendix A) and neutron diffraction data collected on as-synthesised samples of BiOCuCh ($Ch = \text{S, Se}$) (Figure 3.3 – Figure 3.5) indicate that these materials are single phases and crystallise in the ZrSiCuAs structure (space group $P4/nmm$) which consists of alternating $[\text{Bi}_2\text{O}_2]^{2+}$ and $[\text{Cu}_2\text{Ch}_2]^{2-}$ layers stacked along the c -axis (Figure 3.2). Bi and Ch atoms occupy the $2c$ positions ($1/4, 1/4, z$) while Cu and O atoms occupy the $2b$ ($3/4, 1/4, 1/2$) and the $2a$ ($3/4, 1/4, 0$), respectively. The edge-sharing CuCh₄ tetrahedra form the sublattice of the $[\text{Cu}_2\text{Ch}_2]^{2-}$ layers whilst the $[\text{Bi}_2\text{O}_2]^{2+}$ layers are constituted by Bi₄O tetrahedra, where Bi³⁺ is located at the centre of a BiO₄Ch₄ square antiprism (Figure 3.2c).

Representative Rietveld refinements using the neutron diffraction collected for BiOCuCh ($Ch = \text{S, Se, Te}$) at room temperature are shown from Figure 3.3 to Figure 3.5. The remaining refinements as a function of temperature and tabulated results from

these refinements are presented in Appendix A. In all cases, a good agreement between experimental and calculated patterns is obtained with reasonable values of R_{wp} .

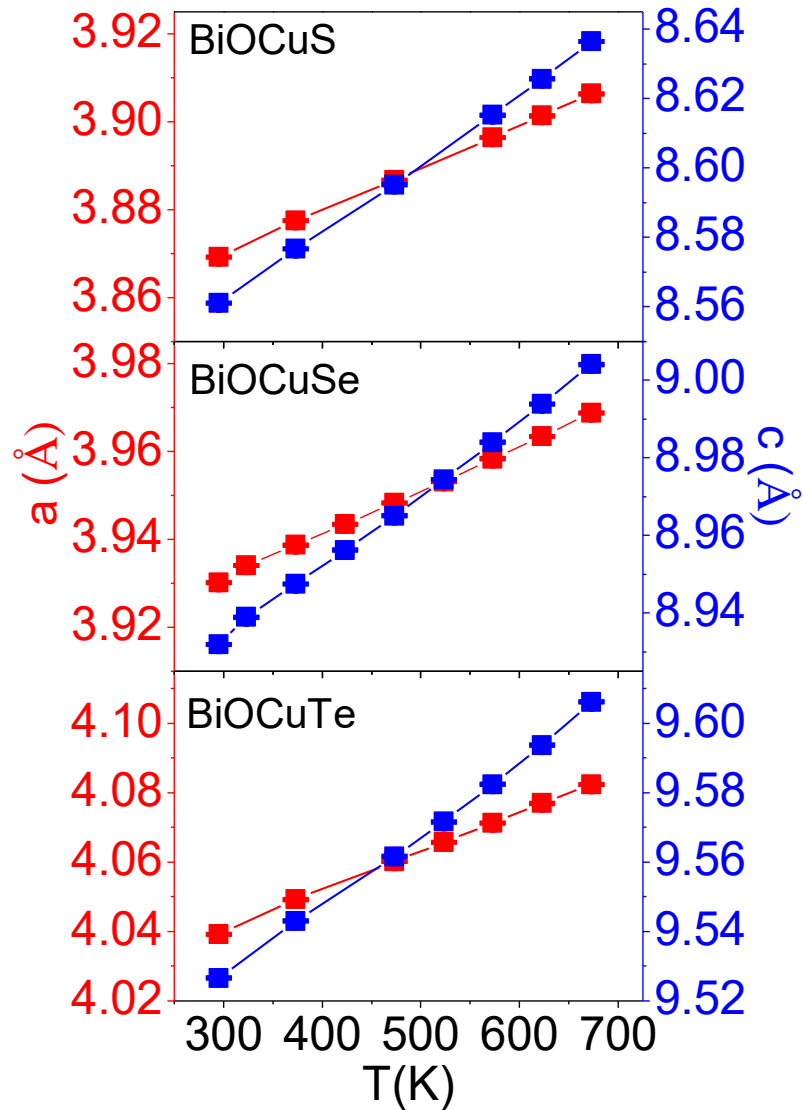


Figure 3.1. Lattice parameters of BiOCuCh ($Ch = \text{S, Se, Te}$) as a function of temperature at $300 \leq T/\text{K} < 700$.

The lengths of both a and c lattice parameters at room temperature agree well with reported values in the literature [96, 183] and increase from S to Te, as the ionic radii of Ch^{2-} ions increase. Similarly, lattice parameters increase with increasing temperature (Figure 3.1). The Bi-O, Bi- Ch and Cu- Ch bond lengths increase slightly with increasing temperature while the Bi- Ch lengths increase from S to Te (Figure 3.6a). The edge-sharing CuCh_4 tetrahedra become more distorted with increasing atomic size of Ch . The variation of the Ch -Cu- Ch bond angles in the CuCh_4 tetrahedra with temperature is

presented in Figure 3.6b. The slight changes in bond angles of these atoms is related to the change of atomic size of Ch^{2-} ions

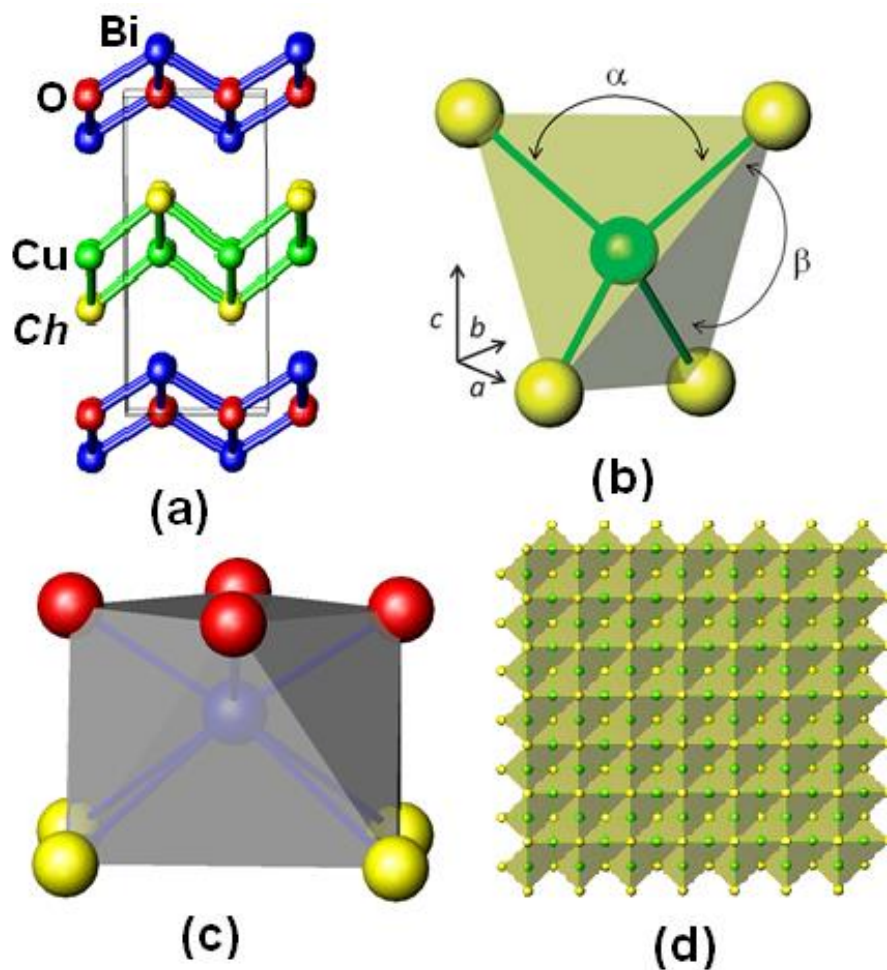


Figure 3.2. (a) Crystal structure of BiOCuCh ($Ch = S, Se, Te$), (b) CuCh₄ tetrahedra, (c) BiO₄Ch₄ square antiprims, (d) (Cu₂Ch₂)²⁻ layer.

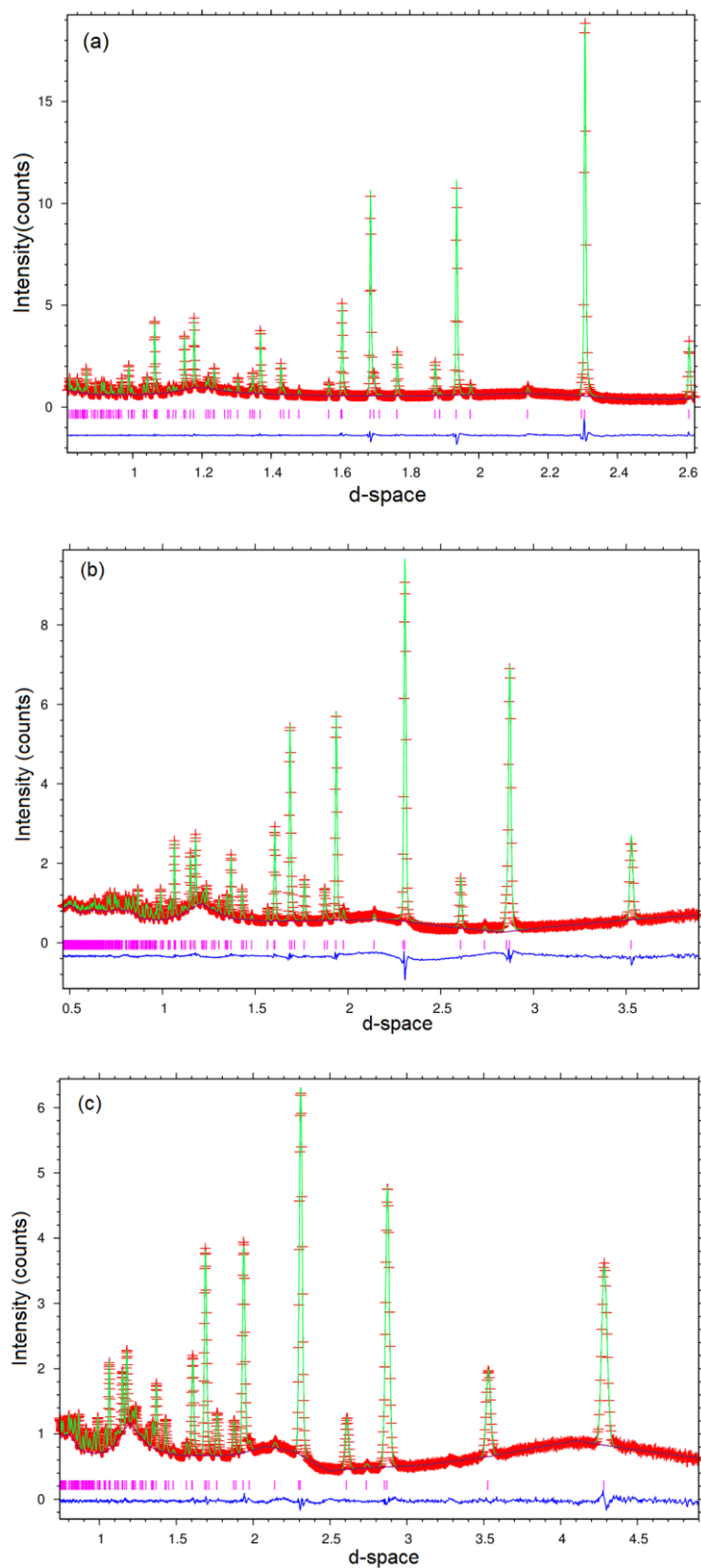


Figure 3.3. Rietveld refinement using powder neutron diffraction data collected on POLARIS for BiOCuS at room temperature from (a) backscattering bank ($2\theta = 146.72^\circ$), (b) 92.59° bank and (c) low angle bank ($2\theta = 52.21^\circ$). Key: observed data (red cross); difference curve (blue line); calculated pattern (green line) and reflection positions (pink markers).

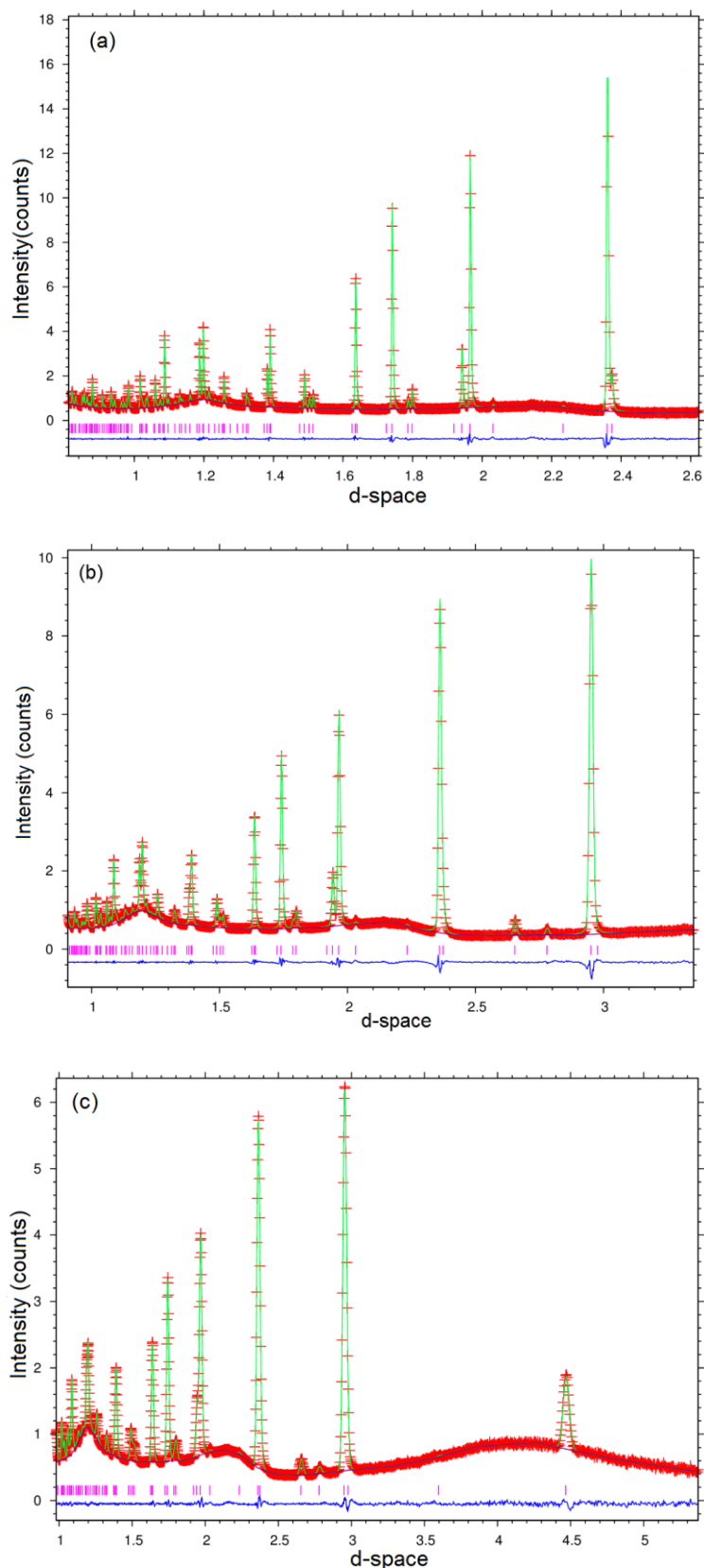


Figure 3.4. Rietveld refinement using powder neutron diffraction data collected on POLARIS for BiOCuSe at room temperature from (a) backscattering bank ($2\theta = 146.72^\circ$), (b) 92.59° bank and (c) low angle bank ($2\theta = 52.21^\circ$). Key: observed data (red cross); difference curve (blue line); calculated pattern (green line) and reflection positions (pink markers).

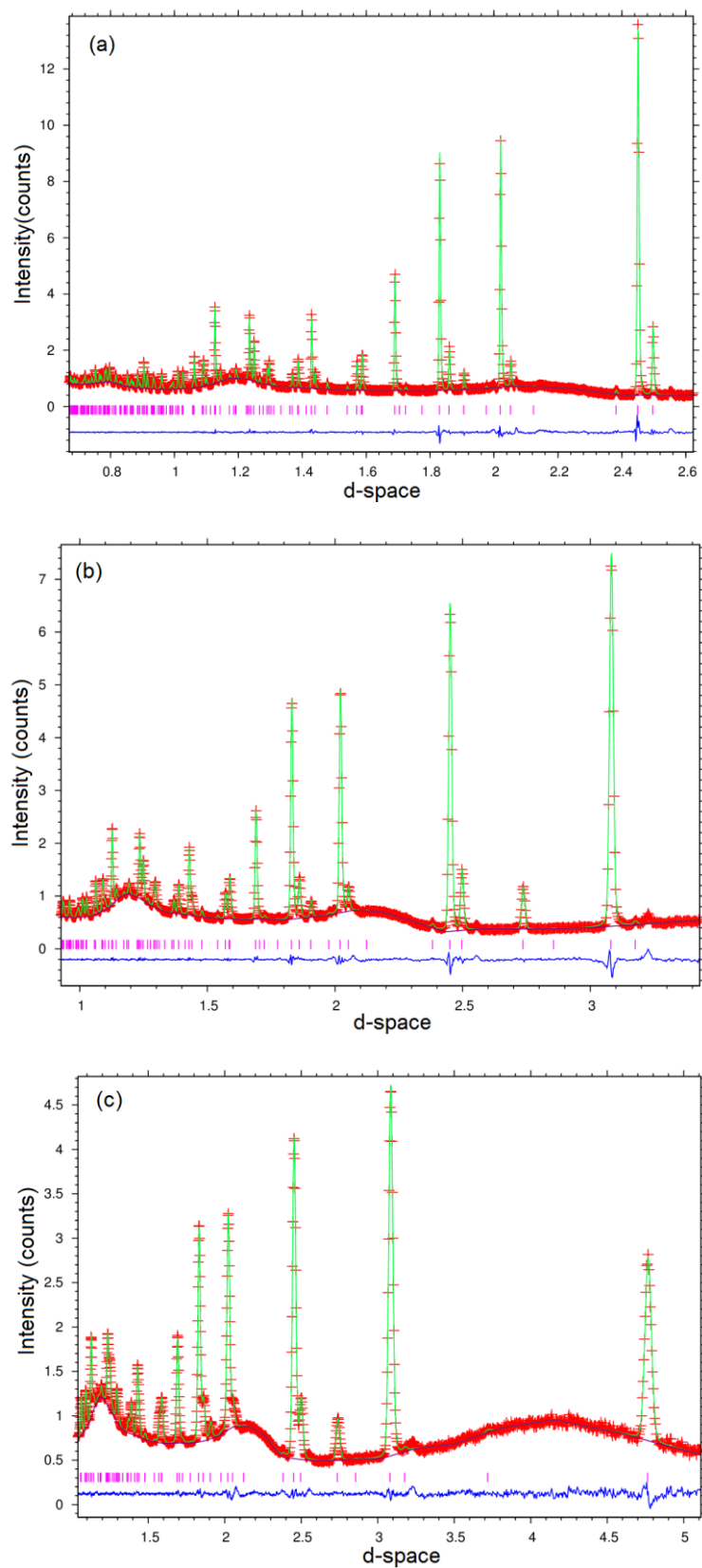


Figure 3.5. Rietveld refinement using powder neutron diffraction data collected on POLARIS for BiOCuTe at room temperature from (a) backscattering bank ($2\theta = 146.72^\circ$), (b) 92.59° bank and (c) low angle bank ($2\theta = 52.21^\circ$). Key: observed data (red cross); difference curve (blue line); calculated pattern (green line) and reflection positions (pink markers).

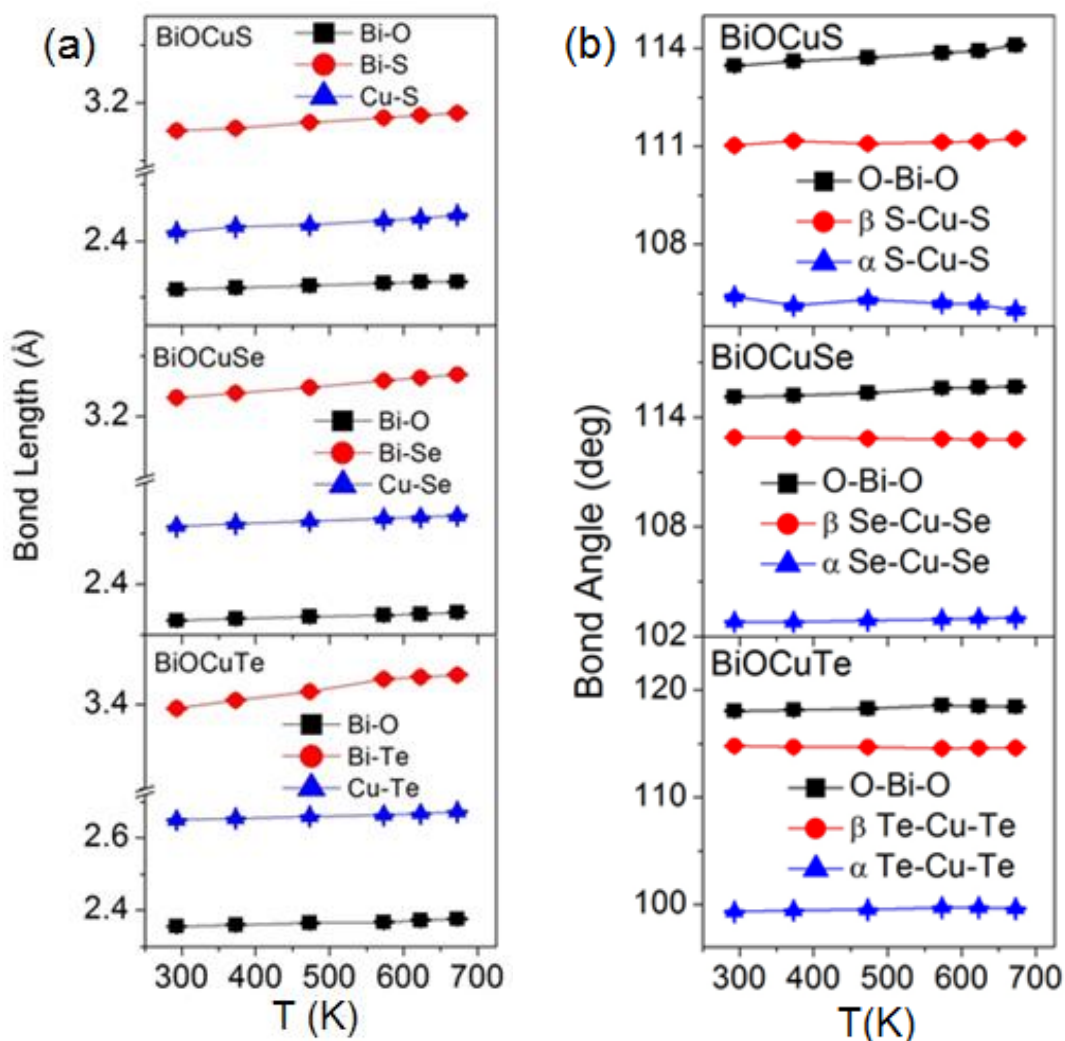


Figure 3.6. (a) Selected bond distances and (b) selected bond angles in BiOCuCh ($Ch = S, Se, Te$) as a function of temperature.

Figure 3.7 shows the atomic displacement parameter (ADP) for BiOCuCh as a function of temperature. All ADPs increase linearly with increasing temperature. However, the ADP for copper is significantly larger at room temperature and increases more rapidly than those for other elements. This behaviour has been previously found in skutterudites [184]. For example, in the $Tl_{0.22}Co_4Sb_{12}$ skutterudite [185], the ADP value for Tl ($\sim 0.023 \text{ \AA}^2$) is much larger than that for Sb and Co ($\sim 0.002 \text{ \AA}^2$) [185]. Clathrates are also materials possessing this behaviour [186], which has been attributed to a “rattling” behaviour due to the presence of a weakly bonded filler atom. This suggests the same behaviour may occur here. A representative example of the large thermal ellipsoids of copper, corresponding to the motion of copper atoms in BiOCuS structure at room temperature and 673 K, is presented in Figure 3.8. Similar trends of ADP for BiOCuCh ($Ch = Se, Te$) can be found in Appendix A.

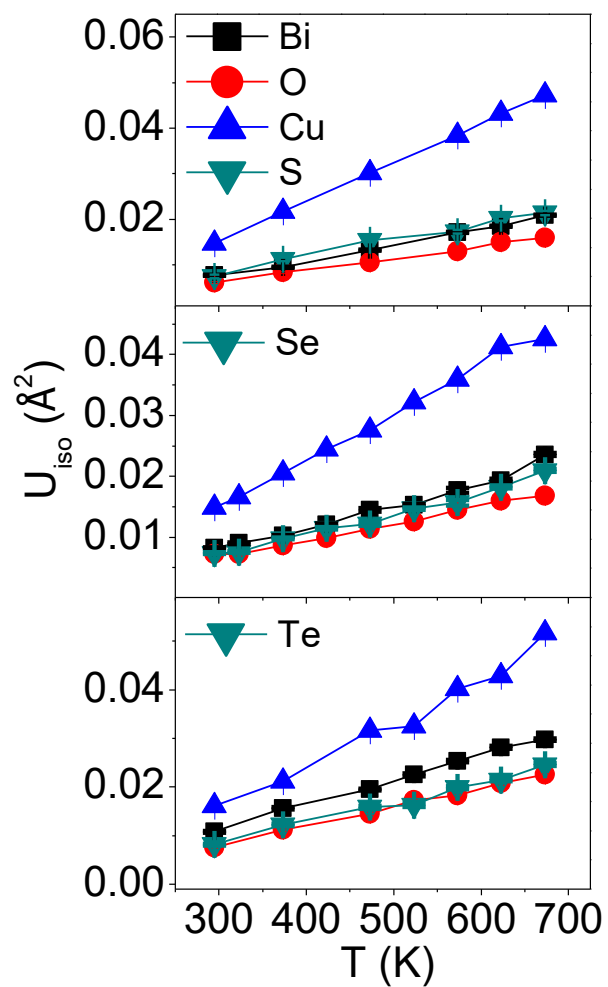


Figure 3.7. Thermal parameters (U_{iso}) of BiOCuCh ($Ch = \text{S, Se, and Te}$) as a function of temperature at $300 \leq T/\text{K} < 700$.

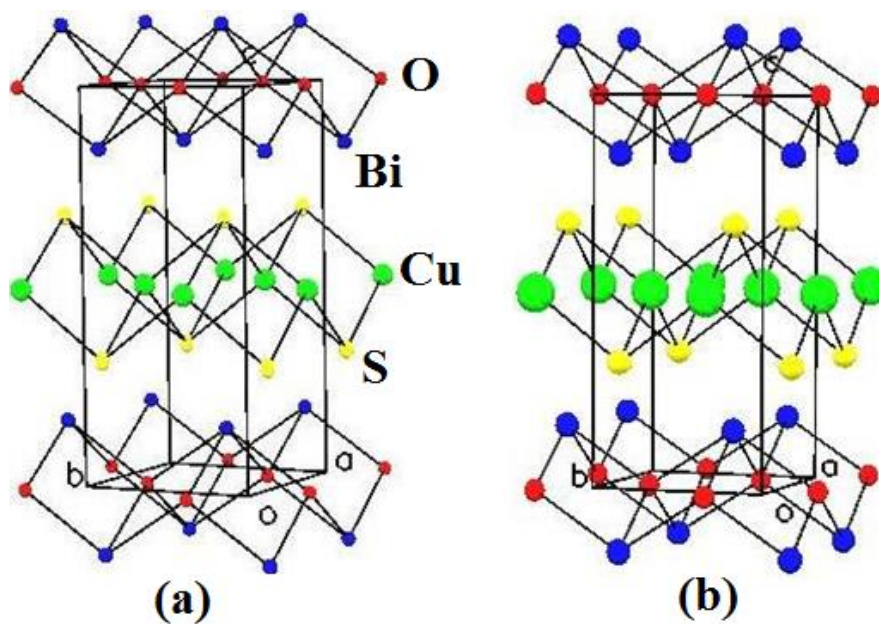


Figure 3.8. Thermal ellipsoids of atoms in BiOCuS at (a) 293 K and (b) 673 K.

To analyse the ADP data, a model is needed. Assuming that the rattling Cu atoms are treated as localised harmonic oscillators (Einstein oscillators), the slope of plot of U_{iso} as a function of temperature can be used to estimate the Einstein temperature, following Equation (3.1) [184]:

$$U_{iso} = \frac{k_B T}{K} = h^2 T / (m k_B \theta_E^2 4\pi^2) \quad \text{Equation (3.1)}$$

where K , θ_E are the spring constant of the oscillator and the Einstein temperature of the oscillator; k_B , h , m are the Planck, Boltzmann constants and atomic mass of rattler, respectively. The vibration frequency is calculated using the following equation:

$$\nu = k_B \theta_E / h \quad \text{Equation (3.2)}$$

In addition, by assuming that a rigid framework formed by Bi, O and Ch , the average mass and U_{iso} for those atoms could be used to calculate the Debye temperature, following the Equation (3.3):

$$U_{iso} = [3h^2 / m k_B \theta_D^2 4\pi^2] T \quad \text{Equation (3.3)}$$

where m , θ_D are average atomic mass and Debye temperature, respectively. The average velocity of sound in the Debye solid model is determined by Equation (3.4):

$$v_s = \frac{(2\pi k_B \theta_D) / h}{[6\pi^2 n]^{1/3}} \quad \text{Equation (3.4)}$$

where n is the number of atoms per unit volume.

Our estimates are presented in Table 3.1. In order to evaluate these experimental results, computation with phonon vibration for BiOCu Ch using first principles calculations was carried out by our collaborators, Prof. Marco Fornani's group. There is an excellent agreement between our estimates and computed results [187]. This also agrees well in Debye temperature (~ 243 K) and the average sound velocity (~ 2107 ms⁻¹) values, obtained from heat capacity data for BiOCuSe, which were reported by other groups

[170, 188]. These results suggests a new mechanism, relating to weak copper bonding, leads to the low thermal conductivity of these natural superlattice materials.

Table 3.1. Einstein (θ_E), Debye (θ_D) temperatures; the frequency of the localised Cu mode (ν_{Cu}) and the average velocity of sound (ν_s) for BiOCuCh ($Ch = S, Se, Te$).

Material	BiOCuS	BiOCuSe	BiOCuTe
θ_E (K)	93	95	89
ν_{Cu} (cm^{-1})	65	66	62
θ_D (K)	230	210	170
ν_s (ms^{-1})	2100	2000	1700

3.3.1.2 Microstructural Characterisation

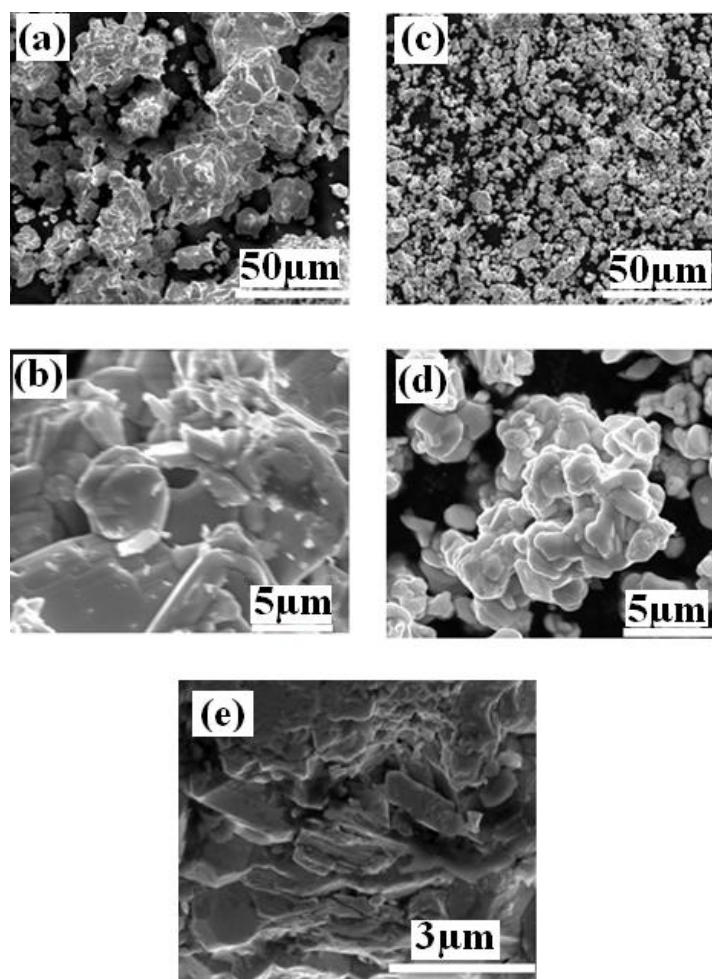


Figure 3.9. SEM micrographs for powders of (a, b): BiOCuS & (c, d): BiOCuSe and (e) hot pressed pellet of BiOCuSe.

Figure 3.9 shows the SEM images of BiOCuCh ($Ch = S, Se$). Three random regions of materials were examined and the average size of these particles was calculated. The examination of these materials indicates they contain plate-like grains with a different length and thickness for each material. BiOCuS powder shows larger thickness and longer length (*c.a.* $\sim 5 \mu\text{m}$) than that of BiOCuSe (*c.a.* $\sim 2 \mu\text{m}$). The grains observed on fractured surfaces of hot-pressed BiOCuSe ingot have similar plate-like shapes, although grain growth has clearly occurred (Figure 3.9e).

3.3.1.3 Thermal Stability

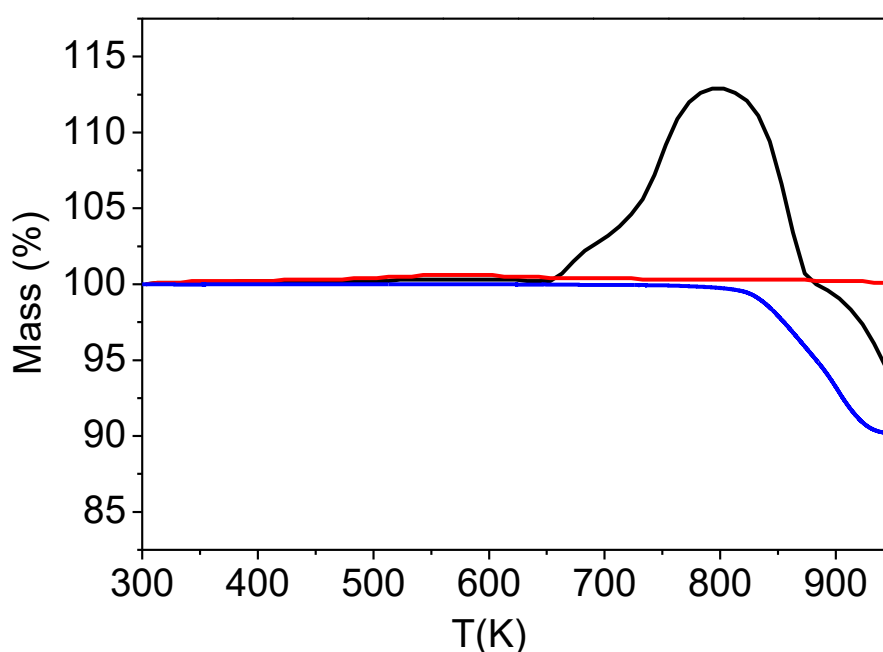


Figure 3.10. Thermogravimetric data for BiOCuS collected under N₂ (blue line); BiOCuSe collected under a N₂ (red line) and an O₂ (black line).

Thermogravimetric analysis of BiOCuS and BiOCuSe powders under a N₂ atmosphere indicates that these materials are stable up to a temperature of 800 K and the maximum investigated temperature, 973 K, respectively. These values are consistent with those of other later reports. For instance, under Ar atmosphere, the stability of BiOCuS and BiOCuSe are up to $\sim 833 \text{ K}$ [189] and $\sim 923 - 973 \text{ K}$ [189,190]. However, the thermogravimetric analysis of BiOCuSe under O₂ atmosphere shows an increase of weight at *ca.* 653 K, indicating that oxidation is occurring (Figure 3.10). This result is supported by that of C. Barreteau *et al.* who have determined the oxidation temperature of BiOCuSe in air as $\sim 573 \text{ K}$ [190]. Taking this into account, in our study, the measurement of the thermoelectric properties of these materials was limited to the

temperature range $100 \leq T/K \leq 673$. However, it should be noted that the use of these materials in thermoelectric devices for higher temperature operations would be feasible under a protective atmosphere, with PbTe-containing thermoelectric devices as examples [191].

3.3.1.4 Electrical Transport Properties

3.3.1.4.1 Low Temperature Electrical Transport Properties

Figure 3.11 shows the electrical conductivity and Seebeck coefficient of BiOCuCh ($Ch = S, Se$) samples over the temperature range of $100 \leq T/K \leq 300$. BiOCuS possesses an insulating behaviour with a very low electrical conductivity at room temperature and follows an increasing trend with increasing temperature. This result is consistent with those of previous reports [1,189,192]. Attempts to measure the hole concentration and mobility of this sample have been unsuccessful due to its high resistance, which is over the limit of Hall measurement instrument.

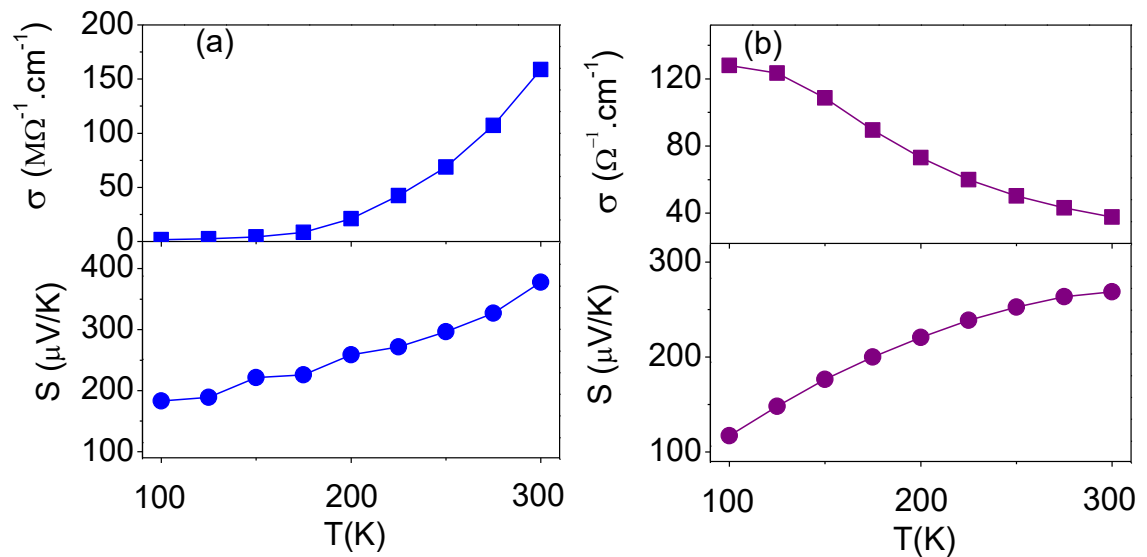


Figure 3.11. Temperature dependence of conductivity (σ) and Seebeck coefficient (S) of (a): BiOCuS and (b): BiOCuSe at a temperature range of $100 \leq T/K \leq 300$.

According to D. Berardan *et al.* [189], the volatility of sulphur at relatively low temperatures could cause a large decrease in the hole concentrations in BiOCuS sample, due to the reduction of copper vacancies' concentration. In addition, our activation energy calculation from the Arrhenius plot (Figure 3.12) shows a value similar to that of

H. Hiramatsu *et al.* [96] (~ 0.1 eV) over the temperature region of 300 – 175 K, demonstrating that a thermal activation process controls hole conduction, while the optical bandgap of BiOCuS has been reported as ~ 1.1 eV [96, 166, 189, 192]. This reveals that the low electrical conductivity of BiOCuS could be caused by low hole carrier concentration, due to acceptor defect formation, in which copper vacancies deduced by fraction of volatized sulphur [189]. The Seebeck coefficient of BiOCuS is positive and increases with increasing temperature (Figure 3.11a). The Seebeck coefficient at room temperature agrees well with that of H. Hiramatsu *et al.* [96] (~ 400 $\mu\text{V/K}$), indicating that the electrical behaviour of this sample is similar to that of H. Hiramatsu *et al.* [96]. Although the Seebeck coefficient of BiOCuS is fairly high, the insulating behaviour of the electrical resistivity results in a very low thermoelectric power factor.

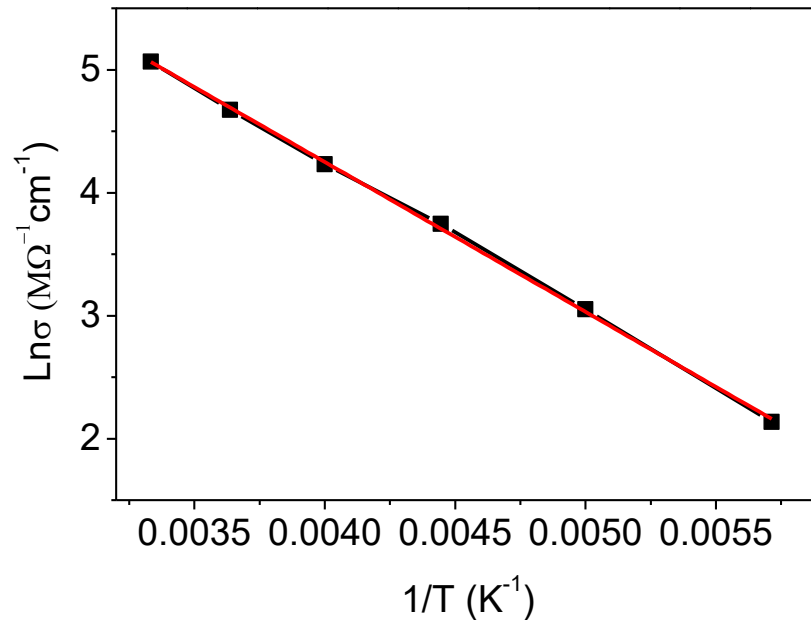


Figure 3.12. Temperature dependence of electrical conductivity in BiOCuS. The red linear line is a fit to $\ln(\sigma) \sim (-\frac{E_a}{K_B T})$; E_a : activation energy; K_B : Boltzmann constant.

In sharp contrast to BiOCuS, the electrical conductivity of BiOCuSe is significantly larger. The plot of electrical conductivity as a function of temperature shows that it decreases with increasing temperature, indicating that this material behaves as a degenerate semiconductor, with a conductivity of ~ 40 $\text{S}\cdot\text{cm}^{-1}$ at 300 K (Figure 3.11b). This decreasing trend of the electrical conductivity is consistent with that reported by D. Berardan *et al.* [189]. However, the behaviour of BiOCuSe found here differs from that of BiOCuSe prepared by cold pressing and sintering, which shows a semiconducting

behaviour [193]. It should be noted that the difference in density between cold-pressed and hot-pressed materials may lead to a significant contribution of grain boundaries to the overall sample resistance of cold pressed materials. A metal-like behaviour is also observed at low temperature ($T < 400$ K) for other samples of BiOCuSe prepared by spark plasma sintering (SPS), while semiconducting behaviour is observed at above this temperature [120]. Changes in stoichiometry (e.g. oxygen deficiency) or reduction in hot pressing or SPS samples should be taken into account as the graphite dies could be a reducing agent at high temperatures [194]. Even though the powder X-ray diffraction data collected on our hot-pressed samples shows no preferred orientation or impurities when compared to the starting powder, small changes in stoichiometry caused by the pressing process could cause the different properties between hot-pressed and SPS samples.

The Seebeck coefficient of BiOCuSe sample is positive, indicating that the electrical transport properties are still dominated by holes, and behaves as a p-type degenerate semiconductor. For this family of oxychalcogenides, p-type conduction is normally observed [96, 193, 195-197]. This could be attributed to the formation of a covalent hybridised band between Cu and Se orbitals at the top of the valence band [198]. However, the origin of this p-type behaviour may also be related to copper deficiency, which can generate mobile holes [178].

3.3.1.4.2 High Temperature Electrical Transport Properties

Due to the limitation of the Linseis instrument on measurements of samples with high electrical resistance, only the electrical transport properties of BiOCuSe were measured. There is an excellent agreement between the low- and high-temperature values of the Seebeck coefficient of BiOCuSe sample. However, the low-temperature electrical conductivity data are affected by the uncertainties in sample dimensions, as well as the Peltier effect arising from the use of a constant dc current source, which could cause greater uncertainties in the final value [199]. For this reason, low-temperature conductivity data have not been used in a quantitative way for the calculation of the power factor, $S^2\sigma$. The electrical conductivity of BiOCuSe decreases with increasing temperature while the Seebeck coefficient ($\sim 264 \mu\text{V}/\text{K}$ at 300 K) increases steadily with increasing temperature (Figure 3.13). This results in a moderate power factor for BiOCuSe ($\sim 4.5 \times 10^{-4} \text{ W m}^{-1} \text{ K}^{-2}$ at 300 K). A similar trend could be found in BiOCuTe

[136] in which the electrical conductivity decreases and the Seebeck coefficient increases with temperature. However, BiOCuTe possesses a much higher electrical conductivity ($\sim 289 \text{ S cm}^{-1}$ at 300 K) while the Seebeck coefficient of this material is lower, with a value of $\sim 170 \text{ } \mu\text{V/K}$ at 300 K. This results in a high power factor of BiOCuTe sample ($\sim 8.7 \times 10^{-4} \text{ W m}^{-1} \text{ K}^{-2}$ at 300 K).

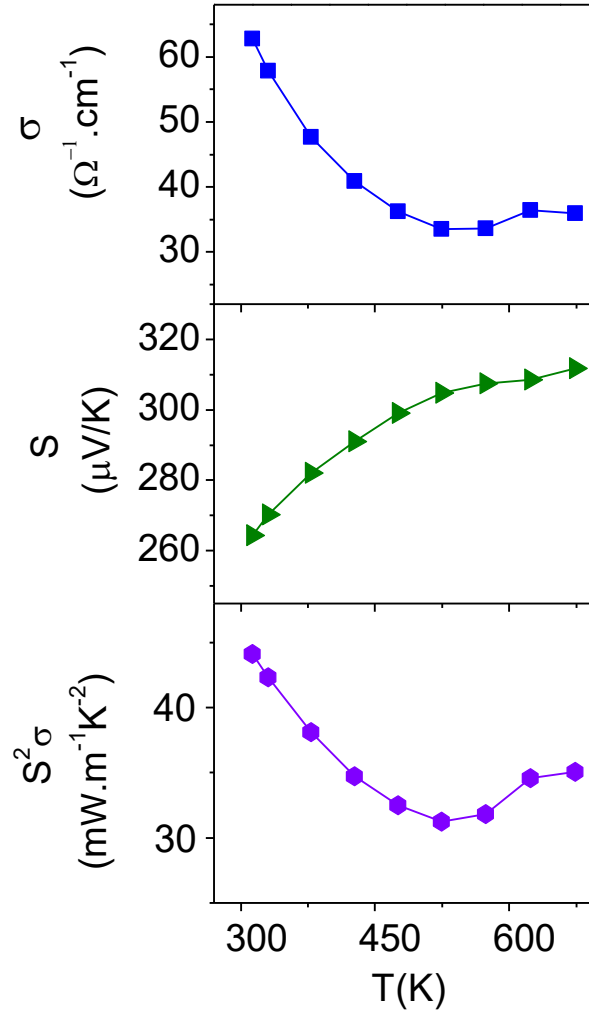


Figure 3.13. Temperature dependence of electrical conductivity (σ), Seebeck coefficient (S), and power factor ($S^2\sigma$) of BiOCuSe at the temperature range of $300 < T/\text{K} < 673$.

Table 3.2. Charge carrier concentration (n) and mobility (μ) at room temperature of BiOCuCh ($Ch = \text{Se, Te}$).

BiOCuCh samples	n (cm^{-3})	μ ($\text{cm}^2 \text{ V}^{-1} \text{ s}^{-1}$)
Se	2×10^{18}	15
Te	9×10^{19}	9

The charge carrier concentration and hole mobility of BiOCuCh ($Ch = \text{Se}, \text{Te}$) are presented in Table 3.2. These values are in reasonable agreement with those in other reports [200,201]. For instance, the charge carrier concentration and mobility of BiOCuSe are reported as $\sim 10^{18} \text{ cm}^{-3}$ and $\sim 20 \text{ cm}^2 \text{ V}^{-1}\text{s}^{-1}$, respectively [200] while the charge carrier concentration and mobility of BiOCuTe have been reported as $\sim 13 \text{ cm}^2 \text{ V}^{-1}\text{s}^{-1}$ and $\sim 7 \times 10^{19} \text{ cm}^{-3}$, respectively [201]. The increase in electrical conductivity when switching from Se to Te is related to the band gap tuning [96, 136, 183, 200] and the contribution of the hole concentration via copper deficiency or point defects [136, 183, 201].

3.3.1.5 Thermal Transport Properties and Figure of Merit ZT

3.3.1.5.1 Thermal Transport Properties

The thermal conductivity as a function of temperature for the BiOCuCh ($Ch = \text{S}, \text{Se}$) is shown in Figure 3.14. The total thermal conductivity BiOCuS ($1.17 \text{ W m}^{-1}\text{K}^{-1}$ at 373 K) and BiOCuSe ($0.97 \text{ W m}^{-1}\text{K}^{-1}$ at 373 K) are comparable to previously reported values [189], but slightly higher than that of BiOCuTe ($\sim 0.7 \text{ W m}^{-1}\text{K}^{-1}$ at 373 K) [136]. However, BiOCuCh compounds are significantly lower than that of Bi_2Te_3 ($\sim 2 \text{ W m}^{-1} \text{K}^{-1}$) [202]. The electronic and lattice contributions were estimated using the electrical conductivity data in conjunction with the Wiedemann–Franz law, with a Lorenz constant of $2.45 \times 10^{-8} \text{ W } \Omega \text{ K}^{-2}$.

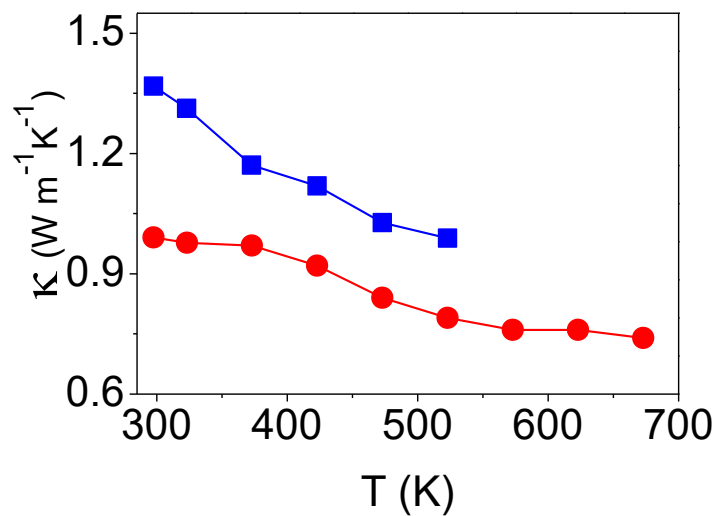


Figure 3.14. Thermal conductivity of BiOCuS (blue square) and BiOCuSe (red circle) at a range temperature of $297 < T/\text{K} < 700$.

For BiOCuS, the electronic contribution is negligible whilst for BiOCuSe and BiOCuTe [136], the electronic contribution is *ca.* 4% and $\sim 33\%$ of the total thermal conductivity, respectively. It has been suggested that the remarkably low thermal conductivity of BiOCu Ch ($Ch = S, Se, Te$) arises from the two-dimensional nature of the structure of this material, which leads to scattering of phonons at the interfaces between the $[Cu_2Se_2]^{2-}$ and $[Bi_2O_2]^{2+}$ layers [120, 175-179]. However, our neutron diffraction data suggests that the Cu atom is found acting as a “rattler” in a BiO Ch rigid framework. This indicates that BiOCu Ch could be a PGEC material, with weak bonding of copper atoms.

3.3.1.5.2 Figure of Merit ZT

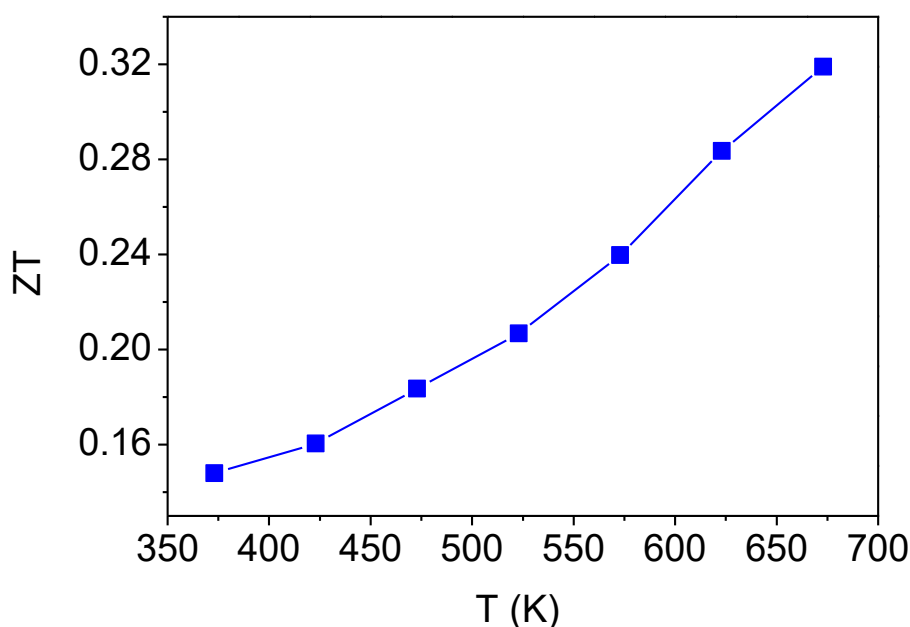


Figure 3.15. The temperature dependence of figure of merit (ZT) of BiOCuSe at a temperature range of $300 < T/K < 700$.

The insulating behaviour of electrical conductivity of BiOCuS indicates that this material is not a thermoelectric material ($ZT \sim 0$ at 300 K). The thermoelectric figure of merit as a function of temperature for BiOCuSe is shown in Figure 3.15. The value found for BiOCuSe is comparable to those previously reported by Zhao *et al.* [120]. ZT value approaches approximately 0.32 at a temperature of 673 K, but it is lower than that of the BiOCuTe ($ZT \sim 0.66$ at 673 K) [136]. Although the figure of merit of BiOCuSe is half of that of BiOCuTe, the effect of cost reduction is most considered. For example,

the average price for Se in 2014 was around \$59/kg while that of Te was \$117/kg [203]. If the figure of merit of BiOCuSe is improved (via doping or nanostructuring) to equal or higher than that of BiOCuTe, the cost reduction is very significant (around twice).

3.3.2 $\text{Bi}_2\text{O}_2\text{Cu}_4\text{Se}_3$

Unfortunately, all attempts to synthesise a material containing a thicker chalcogenide layer were not successful. It is likely that the $\text{Bi}_2\text{O}_2\text{Cu}_4\text{Se}_3$ phase does not exist or that the phase is unstable with our reaction environment and conditions.

Table 3.3. Summary of reaction conditions for synthesis attempt of $\text{Bi}_2\text{O}_2\text{Cu}_4\text{Se}_3$.

Sample	Reaction temperature (K)	Reaction time (hrs)	Final phases
S1	623	20	BiOCuSe (>92%), Cu_2Se (<6%), SeO_2 (<4%), Bi_2SeO_5
	673	10	
	873	7	
S2 (post annealing S1)	1073	5	BiOCuSe (>80%), Cu_2Se (<4%), $(\text{SeO}_3)_4$, Bi_4Se_3 (>5%)
S3 (post annealing S2)	1073	24	BiOCuSe (<60%), Bi_4Se_3 (>40%), Cu_2Se (<4%), Se, Bi_2O_3
S4 (new batch)	1073	8	BiOCuSe (>94%), Cu_2Se (<2%), Bi_4Se_3 (<4%), Bi (<2%)
S5 (post annealing S4)	1073	24	BiOCuSe (>85%), Cu_2Se (<2%), Bi_4Se_3 (>5%), Bi (>4%)
S6 (post annealing S5)	1173	24	Bi_4Se_3 (>60%), Cu_2Se (<20%), BiO_2 (<20%)
S7 (new batch)	623	20	Bi_2O_3 (>55%), BiOCuSe (<45%), Bi_3Se_4 (<5%), $\text{Cu}_{1.6}\text{Bi}_{4.8}\text{Se}_8$ (<2%)
	673	24	
S8 (post annealing S7)	923	24	BiOCuSe (>98%), Cu_2Se (<2%)

Table 3.3 summarise our reactions and results. The X-ray patterns of these samples are presented in Appendix A. Powder X-ray patterns indicate that a mixture of BiOCuSe and Cu₂Se exists mainly at temperatures below 873 K, while at temperatures higher than 873 K, the samples consist of a mixture of BiOCuSe, Bi₄Se₃, Cu₂Se and BiO₂.

3.3.3 Bi₂YO₄Cu₂Se₂

3.3.3.1 Structural Characterisation

Powder X-ray diffraction data collected for Bi₂YO₄Cu₂Se₂ indicates that this material contains a small amount of Bi₄Se₃ and BiOCuSe impurity phases. It should be noted that efforts to obtain a single phase of this material have been carried out with different heating times and temperature ranges (Appendix A). The reaction conditions presented in this dissertation are our best conditions to minimise the impurity content. Recent work on this material also confirms that it is difficult to avoid impurities in the solid-state reaction synthesis [205]. Although we have not been able to determine precisely the reason, the moisture-sensitive nature of yttrium oxide might be the cause.

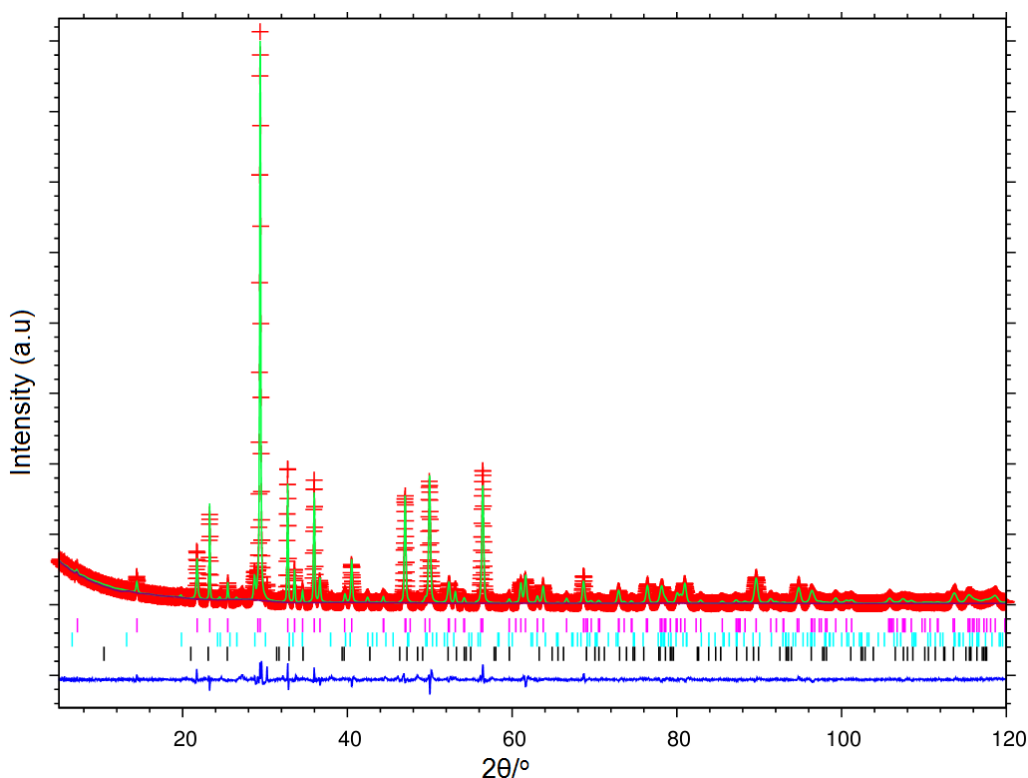


Figure 3.16. Rietveld refinement using powder X-ray diffraction data of Bi₂YO₄Cu₂Se₂. Key: observed data (red cross); difference curve (blue line); calculated pattern (green line) and reflection positions of Bi₂Y_{1.05}O₄Cu₂Se₂ (pink markers), BiOCuSe (black markers) and Bi₄Se₃ (aqua markers).

A Rietveld refinement was carried out using the previously reported crystal structure of this material [107] and those of the impurities: BiOCuSe [96], Bi₄Se₃ [204]. This results in a good agreement between observed and calculated intensities. Figure 3.16 shows the final observed, calculated and difference profiles for this refinement. The main reflections could be indexed in the tetragonal lattice of Bi₂YO₄Cu₂Se₂ with an *I4/mmm* space group. The crystal structure of Bi₂YO₄Cu₂Se₂ consists of layers of [Bi₂YO₄]⁺ and [Cu₂Se₂]⁺, stacked alternatively along the *c* axis (Figure 3.17). The [Cu₂Se₂]⁺ layer is similar to that of BiOCuSe, and is formed by distorted CuSe₄ tetrahedra, whilst the (Bi₂YO₄)⁺ layer is composed of yttrium atoms in a centre of cube coordinating to 8 surrounding oxygen atoms while bismuth is in a square anti-prism BiO₄Se₄. The oxygen is tetrahedrally coordinated by two Bi and Y atoms. The same structure can be found with other rare earth elements such as Gd, Sm, Nd and La, as reported by J. S. O. Evans *et al.* [107].

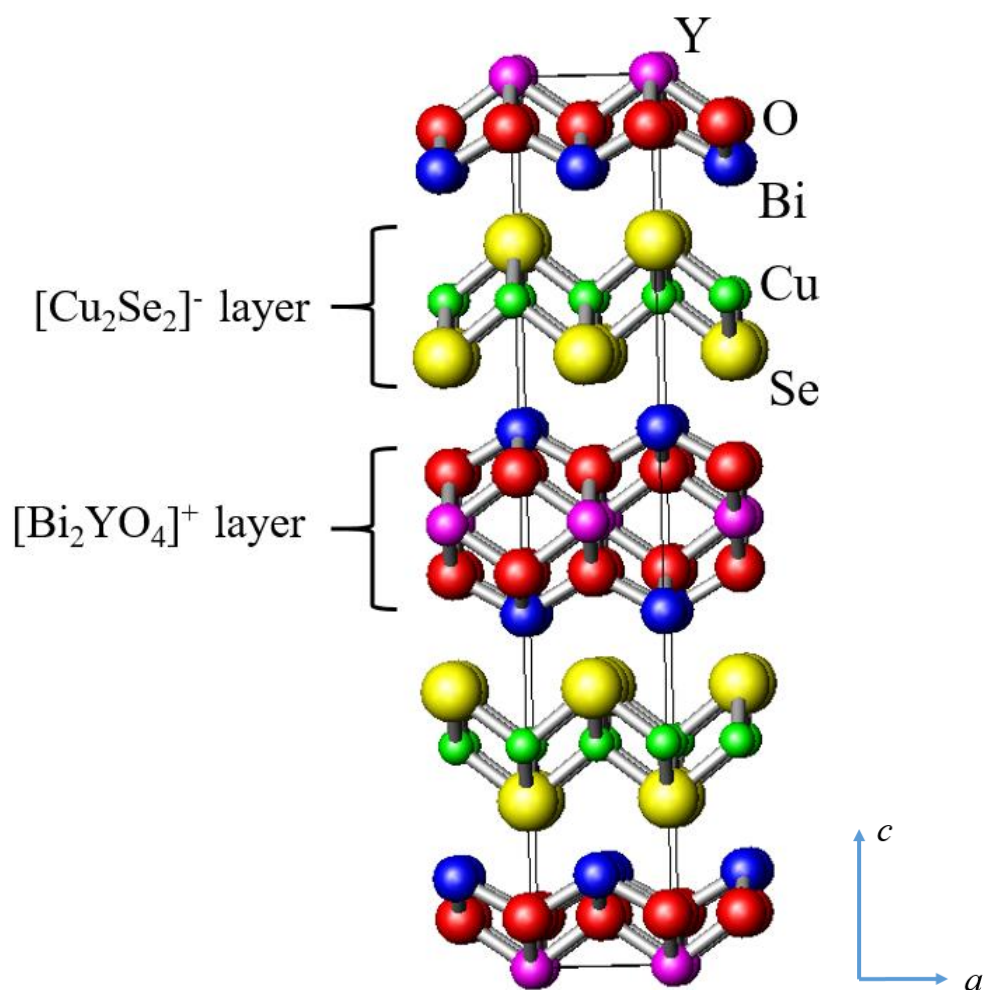


Figure 3.17. The atomic bond view of crystal structure of Bi₂YO₄Cu₂Se₂.

Table 3.4. Fractional atomic coordinates of Bi₂YO₄Cu₂Se₂.

Atom	SOF	x	y	z	U _{iso} (Å ²)
Bi	1.0	0.5	0.5	0.89783(7)	0.0050(4)
O	1.0	0	1/2	0.94507(6)	0.0091(5)
Cu	1.0	0	1/2	1/4	0.0091(2)
Se	1.0	1/2	1/2	0.31220(2)	0.0067(1)
Y	1.0	1/2	1/2	1/2	0.0031(9)

Table 3.5. Rietveld refinement of structural parameters at room temperature.

Bi ₂ YO ₄ Cu ₂ Se ₂	
Space group	I4/mmm
<i>a</i> (Å)	3.86204(5)
<i>c</i> (Å)	24.47985(6)
V(Å ³)	365.126(0)
R _{wp} (%)	13.58
χ ²	4.899
Bond length (Å)	
<i>d</i> _{Bi-O}	2.3251(8)
<i>d</i> _{Bi-Se}	3.2581(1)
<i>d</i> _{Cu-Se}	2.4969(1)
<i>d</i> _{Y-Bi}	3.7031(1)
<i>d</i> _{Y-O}	2.3530(8)
Bond angle (deg.)	
O-Bi-O	115.61(5)
O-Y-O	109.10(3)
Se-Cu-Se	112.27(3)

The structural parameters arising from our Rietveld refinement, listed in Table 3.4 and Table 3.5, agree well with previously reported results for $\text{Bi}_2\text{YO}_4\text{Cu}_2\text{Se}_2$ [205]. The weight percentage of $\text{Bi}_2\text{YO}_4\text{Cu}_2\text{Se}_2$ is more than 94%, whilst the contents of Bi_4Se_3 and BiOCuSe are less than 3.6% and 2.4%, respectively. The refined lattice parameters are $a = b = 3.86204(5) \text{ \AA}$, and $c = 24.47985(6) \text{ \AA}$, respectively. In comparison with those of BiOCuSe ($a = b = 3.93026(2) \text{ \AA}$, $c = 8.93193(5) \text{ \AA}$), the unit cell of $\text{Bi}_2\text{YO}_4\text{Cu}_2\text{Se}_2$ is slightly contracted along the a and b axes, while it is expanded along the c axis. This causes a reduction in Cu-Se and Bi-O distances of $\text{Bi}_2\text{YO}_4\text{Cu}_2\text{Se}_2$, in which are $\sim 2.4969(1) \text{ \AA}$ and $\sim 2.3251(8) \text{ \AA}$ for Cu-Se and Bi-O while those of BiOCuSe are $\sim 2.5140(8) \text{ \AA}$, $2.3302(3) \text{ \AA}$, respectively. By contrast, the Bi-Se distance is $\sim 3.2581(1) \text{ \AA}$, which is larger than that of BiOCuSe ($\sim 3.2298(7) \text{ \AA}$). The existence of yttrium atoms in the $\text{Bi}_2\text{YO}_4\text{Cu}_2\text{Se}_2$ structure leads to more distortion of the edge-sharing CuCh_4 tetrahedra in the Cu_2Se_2 layers and to less distortion of the edge-sharing Bi_4O tetrahedra in the $[\text{Bi}_2\text{O}_2]^{2-}$ layers, in comparison with those of BiOCuSe .

3.3.3.2 Electrical Transport Properties

As shown in Figure 3.18 and Figure 3.19, the electrical conductivity of polycrystalline $\text{Bi}_2\text{YO}_4\text{Cu}_2\text{Se}_2$ is consistent with a metallic behaviour over the temperature range of $100 \leq T/\text{K} \leq 673$.

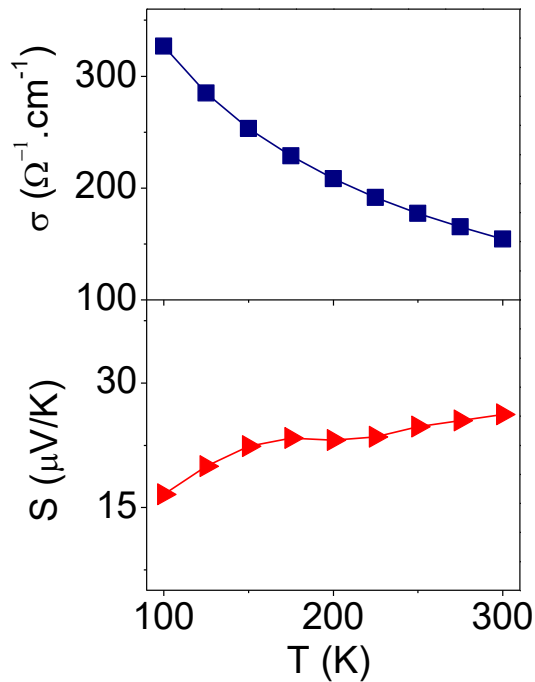


Figure 3.18. Temperature dependence of electrical conductivity (σ), Seebeck coefficient (S) of $\text{Bi}_2\text{YO}_4\text{Cu}_2\text{Se}_2$ at a temperature range of $100 \leq T/\text{K} \leq 300$.

The values of electrical conductivity and Seebeck coefficient are very consistent with results of S. G. Tan *et al.* [205]. However, our electrical conductivity is very different to that of J. S. O. Evan *et al.* [107]. For example, at room temperature, the value of resistivity ($\sim 5 \times 10^{-3} \Omega \text{ cm}$) is approximately one order of magnitude lower than that reported by J. S. O. Evan *et al.* ($\sim 2 \times 10^{-2} \Omega \text{ cm}$) [107]. This results in a very low power factor. It should be noted that the impurities might have minor effect on the absolute value of resistivity of $\text{Bi}_2\text{YO}_4\text{Cu}_2\text{Se}_2$. However, its metallic behaviour is intrinsic to this material, as explained by S.G.Tan *et al.* [205], who indicated that the replacement of $[\text{Bi}_2\text{O}_2]^{2+}$ layer by $[\text{Bi}_2\text{YO}_4]^+$ introduces more holes than in BiOCuSe .

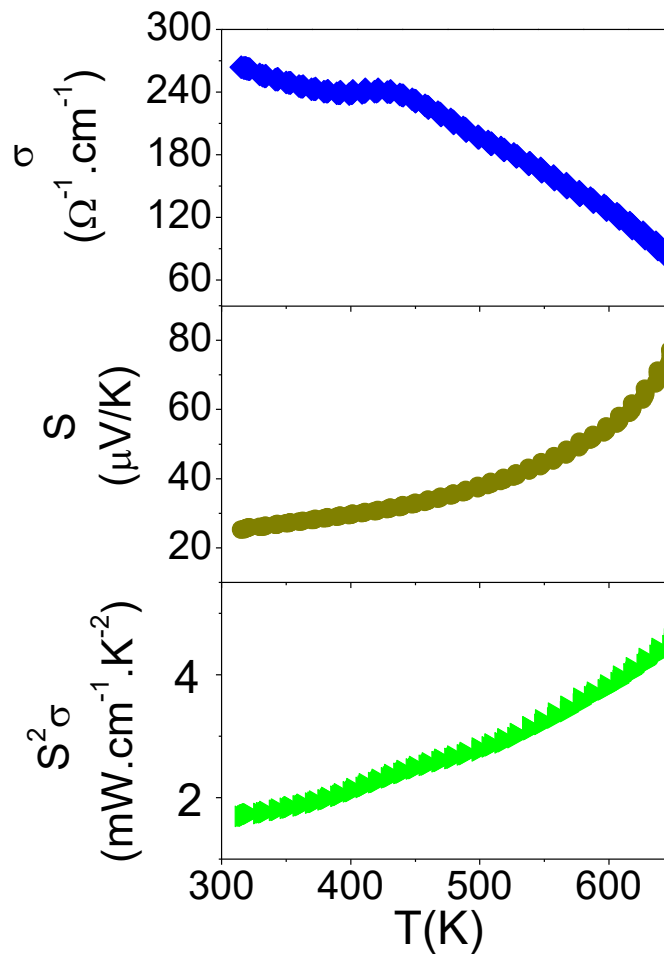


Figure 3.19. Temperature dependence of electrical properties: electrical conductivity (σ), Seebeck coefficient (S), Power factor ($S^2\sigma$) of $\text{Bi}_2\text{YO}_4\text{Cu}_2\text{Se}_2$ at a temperature range of $300 < T/\text{K} < 673$.

In fact, in BiOCuSe , the insulating $[\text{Bi}_2\text{O}_2]^{2+}$ layer contributes two electrons to the conductive $[\text{Cu}_2\text{Se}_2]^{2-}$ layer, whilst the $[\text{Bi}_2\text{YO}_4]^+$ layer contributes only one electron to the conductive $[\text{Cu}_2\text{Se}_2]^{2-}$ layer in $\text{Bi}_2\text{YO}_4\text{Cu}_2\text{Se}_2$. The oxidation state of copper is

determined as +1.5, and the presence of a significant number of additional holes, explains why this compounds behaves as a metal. The positive Seebeck values indicate that the major charge carriers are holes. Its value is very low at room temperature ($\sim 25 \mu\text{V}/\text{K}$) and increases to $\sim 93 \mu\text{V}/\text{K}$ at 676 K. The power factor (PF) increases with increasing temperature, indicating that this material may be a potential candidate for high temperature thermoelectric conversion. At $\sim 676 \text{ K}$, the value of the power factor is $\sim 48 \mu\text{W m}^{-1} \text{ K}^{-2}$.

3.3.3.3 Thermal Conductivity and Figure of Merit

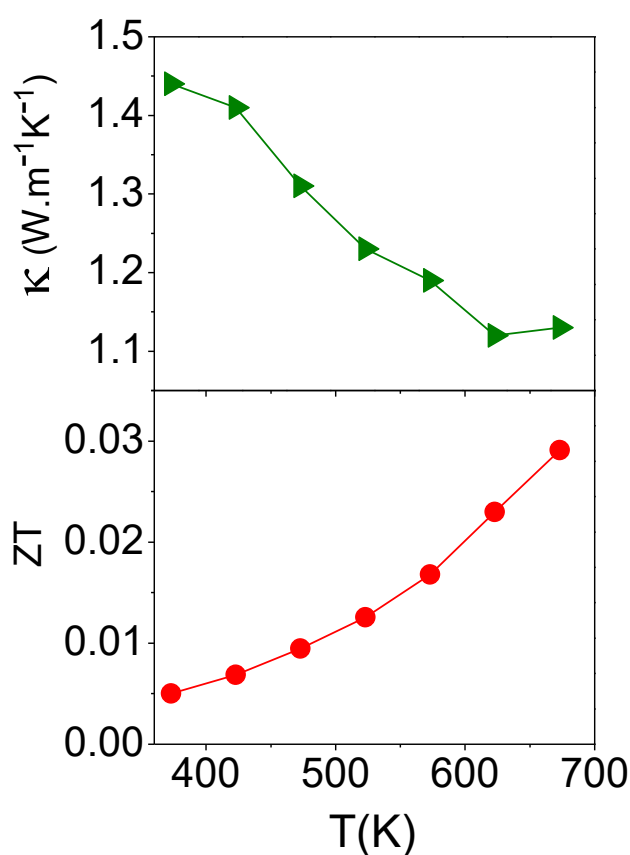


Figure 3.20. Temperature dependence of thermal conductivity (κ) and ZT of



Figure 3.20 shows the temperature dependence of the total thermal conductivity and the figure of merit. At 373 K, the value of total thermal conductivity (κ_{tot}) is around $1.4 \text{ W m}^{-1} \text{ K}^{-1}$ and drops down to $\sim 1.1 \text{ W m}^{-1} \text{ K}^{-1}$ at 673 K, following the normal decreasing trend with increasing temperature in crystalline materials. The lattice thermal conductivity (κ_{lat}) value at 373 K is $\sim 1.2 \text{ W m}^{-1} \text{ K}^{-1}$ ($\sim 85\% \kappa_{\text{tot}}$) and decreases to ~ 1.1

$\text{W m}^{-1} \text{K}^{-1}$ ($\sim 95.5\% \kappa_{\text{tot}}$) at 673 K. This indicates that the thermal conductivity of this sample is dominated by phonon transport. The value of the figure of merit ZT is ~ 0.03 at 673 K and would be expected to be higher at higher temperatures, given the fact that the power factor keeps increasing while the thermal conductivity decreases. Extrapolation of the thermal conductivity and power factor to 1073 K (synthesis temperature) leads to an estimated value of $ZT \sim 0.05$.

Chapter 4 Substitution of Divalent Cations on BiOCuSe and Synthesis by Mechanical Ball Milling

4.1 Introduction

In Chapter 3, BiOCuSe was identified as the material with most potential for thermoelectric (TE) applications in the BiOCuCh ($Ch = S, Se, Te$) family, in terms of a good combination of both raw material cost and thermoelectric properties. Indeed, the outstanding thermoelectric performance of aliovalent substitution at the Bi^{3+} site in p-type BiOCuSe has been proven recently [120, 171, 174, 175, 206]. For instance, doping with Sr^{2+} , Ca^{2+} , and Mg^{2+} leads to high values of ZT of 0.76 (at 873 K) [120], 0.8 (at 773 K) [175], and 0.74 (at 923 K) [174], respectively. In addition, the thermal conductivity of Ba^{2+} doped $Bi_{1-x}Ba_xOCuSe$ could be decreased down to approximately by 40% when reducing the grain sizes down to 200 - 400 nm. It results in even higher ZT values of 1.1 at 923 K [171]. As mentioned in Chapter 1, since 2010, many world leading thermoelectric research groups have been exploring how to improve the thermoelectric properties of BiOCuSe. This is evidenced by the number of publications, which has increased from a few in 2010 to tens in 2015. However, to the best of our knowledge, the substitution of Pb^{2+} at Bi^{3+} site had not been reported at the time we did the initial literature review in 2011. Therefore, in this chapter we present the effect of the partial substitution of Bi^{3+} by Pb^{2+} on the structure and transport properties of BiOCuSe. The effect of isotropic structure on thermoelectric properties of selected sample is also studied.

Reductions in thermal conductivity have been found for ball milled BiOCuSe [180] and $Bi_{1-x}Ba_xOCuSe$ [171], strongly supporting the idea that nano-structuring may be an effective approach to enhance the thermoelectric response of these materials. Moreover, a simple mechanical alloying process, instead of high temperature solid state synthesis, also produces single phase nano-crystalline BiOCuCh ($Ch = Se, Te$) [207]. Texturing of $Bi_{0.875}Ba_{0.125}OCuSe$ by hot-forging also increases ZT up to 1.4 at 923 K [206]. This motivated us to study the effect of mechanical ball milling synthesis on the microstructure and transport properties of the optimised Pb doped $Bi_{1-x}Pb_xOCuSe$.

As mentioned above, up to date, most of improvements in the thermoelectric performance of pristine BiOCuSe have been primarily focused on doping at the bismuth site to modify its electrical transport properties [120, 171-177, 207, 208]. Manipulating

carrier concentration by defect chemistry plays an important role on switching thermoelectric materials from p- to n-type and vice versa. For instance, the transition of electrical conductivity from n- to p-type has been studied on CoSb_3 [209], $\text{Co}_3\text{Sn}_{2-x}\text{In}_x\text{S}_2$ [210] compounds. Besides, band gap tuning by isoelectronic substitution of Te at the Se site, $\text{BiOCuSe}_{1-x}\text{Te}_x$, leads to improved electrical transport properties [179]. Again, to the best of our knowledge at the time of carrying out this study, the effect of aliovalent substitution at the copper site on the thermoelectric properties had not been investigated. However, the introduction of holes into copper deficient BiOCu_xSe leads to a remarkable enhancement of the thermoelectric performance ($ZT \sim 0.81$ at 923 K) [178]. Here, the effect of the partial substitution of Cu^+ by divalent cations (Cd^{2+} and Zn^{2+}) on the structure and transport properties of BiOCuSe by conventional solid state reaction in which hot-press was used as densification technique are presented.

4.2 Experimental Procedure

4.2.1 Sample Preparation

4.2.1.1 $\text{Bi}_{1-x}\text{Pb}_x\text{OCuSe}$ Compounds ($0 \leq x \leq 0.2$)

A series of $\text{Bi}_{1-x}\text{Pb}_x\text{OCuSe}$ ($0 \leq x \leq 0.2$) were prepared by solid-state reaction from a mixture of bismuth (III) oxide, Bi_2O_3 (99.99%, Sigma Aldrich); elementary bismuth, Bi (99.5%, Sigma Aldrich); lead dioxide, PbO_2 (99.5%, BHD Chemicals); copper, Cu (99.5%, Matthey Materials), and elementary selenium pellet, Se (99.99%, Sigma Aldrich) using evacuated and sealed silica tubes ($\sim 5 \times 10^{-4}$ Torr). The stoichiometric mixture was first heated up to 623 K for 20 hours and then up to 773 K for 10 hours with a 2 K min^{-1} ramp rate. The second annealing process at 873 K for a further 7 hours was carried out after regrinding the obtained powders. Final products were reground and phase purity was determined by powder XRD diffraction.

4.2.1.2 Ball milled $\text{Bi}_{1.95}\text{Pb}_{0.05}\text{OCuSe}$ Powder

To prepare mechanically ball milled (BM) $\text{Bi}_{1.95}\text{Pb}_{0.05}\text{OCuSe}$, a stoichiometric mixture of bismuth (III) oxide, Bi_2O_3 (99.99%, Sigma Aldrich); elementary bismuth, Bi (99.5%, Sigma Aldrich), lead dioxide, PbO_2 (99.5%, BHD Chemicals); copper, Cu (99.5%, Matthey Materials), and elementary selenium, Se (99.99%, Aldrich) was placed in a 25

ml stainless steel jar in air environment. This mixture was first milled at a speed of 400 rpm for 15 hours with a 5-minute interval time and a 2-minute break. Then, it was reground and a second milling was carried out at a speed of 600 rpm for 24 hours with a 5-minute interval time and 0-minute break. Final products were reground and phase purity was determined by powder XRD diffraction.

4.2.1.3 *BiOCu_{1-x}M_xSe (M = Cd, Zn; 0 ≤ x ≤ 0.2) Compounds*

A series of polycrystalline BiOCu_{1-x}M_xSe (M = Cd, 0.05 ≤ x ≤ 0.20 and M = Zn, 0.05 ≤ x ≤ 0.10) compounds were synthesized by solid-state reaction in evacuated and sealed silica tubes (~5x10⁻⁴ Torr) from a mixture of bismuth (III) oxide, Bi₂O₃ (99.99%, Sigma Aldrich); elementary bismuth, Bi (99.5%, Aldrich); copper, Cu (99.5%, Matthey Materials); cadmium oxide, CdO (≥ 99.99%, Aldrich); zinc, Zn (99%, Aldrich) powders and selenium pellet, Se (99.99%, Aldrich). Each stoichiometric mixture was first heated up to 623 K for 20 hours and then up to 773 K for 10 hours with a 2 K/min ramp rate. Final products were reground and phase purity was determined by XRD diffraction.

4.2.2 *Characterization and Physical Property Measurements*

4.2.2.1 *Structural and Microstructure Characterisation*

Powder X-ray diffraction data of samples were collected over the range of $5 \leq 2\theta^\circ \leq 120$ in 0.022° increments, counting for 718.3s at each step. Data were analysed using the GSAS package [141]. The input lattice parameters for Rietveld refinements were determined using Topas [137].

Neutron diffraction data on powdered samples of Bi_{1-x}Pb_xOCuSe (x = 0.05, 0.15) were collected on the POLARIS diffractometer at the ISIS facility, Rutherford Appleton Laboratory. Time of flight data were collected at ambient temperature. Neutron diffraction data from the backscattering (146.7°), 92.6° and low angle (52.2°) detector banks were summed, normalised and used simultaneously in Rietveld refinements, carried out using the GSAS package [141]. It should be noted that some broad peaks were observed in these neutron diffraction data. Therefore, the strain broadening factor for anisotropic broadening peaks (Lorentz factor) was taken into account when refining the model to get a better agreement between observed and calculated patterns.

The powder X-ray diffraction pattern of the ball milled (BM) sample shows very broad peaks, and attempts to carry out Rietveld refinements were unsuccessful. However, Pawley refinements, implemented using the TOPAS package, were used to determine the lattice parameters of this sample.

To study the morphology of the samples, the electron microscope FEI Quanta FEG 600 [152] was used, with a 5 kV accelerating voltage. Samples are highly electrically conductive, and hence could be measured without any conductive coating. The aluminium sample holder with a carbon tab was used to hold powdered samples. Measurements were carried out in different areas of the samples and an average value is given for sizes.

4.2.2.2 *Physical Properties Measurements*

The electrical properties of samples were measured over the temperature range of $100 \leq T/K \leq 673$. The electrical transport properties of a rectangular $\text{Bi}_{0.95}\text{Pb}_{0.05}\text{OCuSe}$ ingot, cut perpendicular and parallel to the direction of pressing were measured as well. Thermal transport measurements of samples were carried out using different instruments. An Anter FL3000 system was employed for measuring thermal diffusivity (α) and the heat capacity (C_p) of doped samples over a temperature range of $373 \leq T/K \leq 673$ in 50 K steps, whilst LFA 447 NanoFlash[®] was employed to measure the thermal conductivity of a ball milled sample at $373 \leq T/K \leq 573$ in 50 K steps.

4.3 Results and Discussion

4.3.1 *Bi_{1-x}Pb_xOCuSe Compounds (0 ≤ x ≤ 0.2)*

4.3.1.1 *Structural and Microstructural Characterisation*

Powder X-ray diffraction data collected on as-prepared samples of $\text{Bi}_{1-x}\text{Pb}_x\text{OCuSe}$ with compositions over the range $0 \leq x \leq 0.20$ at room temperature indicate that the ZrSiCuAs structure is retained. Representative X-ray diffraction patterns are presented in Figure 4.1, while Rietveld refinements using all of these data are included in Appendix B. Most samples are single phases, with the exception of $x = 0.15$ for which a trace amount of Bi_2O_3 can be detected. In sharp contrast with other reports which suggested that the maximum doping level of $x = 0.07$ [188]; 0.08 [211] and 0.1 [212], we have found that lead can be incorporated up to a doping level of $x \approx 0.20$. This is comparable to the solubility limit found for other divalent cations, such as Mg^{2+} , Ba^{2+} ,

Sr^{2+} , for which doping contents of $x = 0.20$, 0.15 and 0.35 , respectively have been reported [169, 171, 174]. Values of x greater than 0.2 result in samples containing significant amounts of impurities. It should be noted that there is probably a small amount of lead oxide as an impurity in as-purchased elemental lead. Therefore, the lower doping level reported in ref [188] and [212] might be related to the use of elemental lead for the synthesis of these phases. In addition, there are discrepancies in the solubility limit of the same dopants reported by different research groups. For instance, using the same Sr^{2+} ions as dopants, the solubility limit of L.D Zhao *et al.* is ca. 15 %, [120] while that of C. Barreteau *et al.* is ca. 35% [169]. The maximum doping content of Mg^{2+} in J. Li *et al.* [172] is 0.125 while that of J-L Lan *et al.* is 0.20 [174].

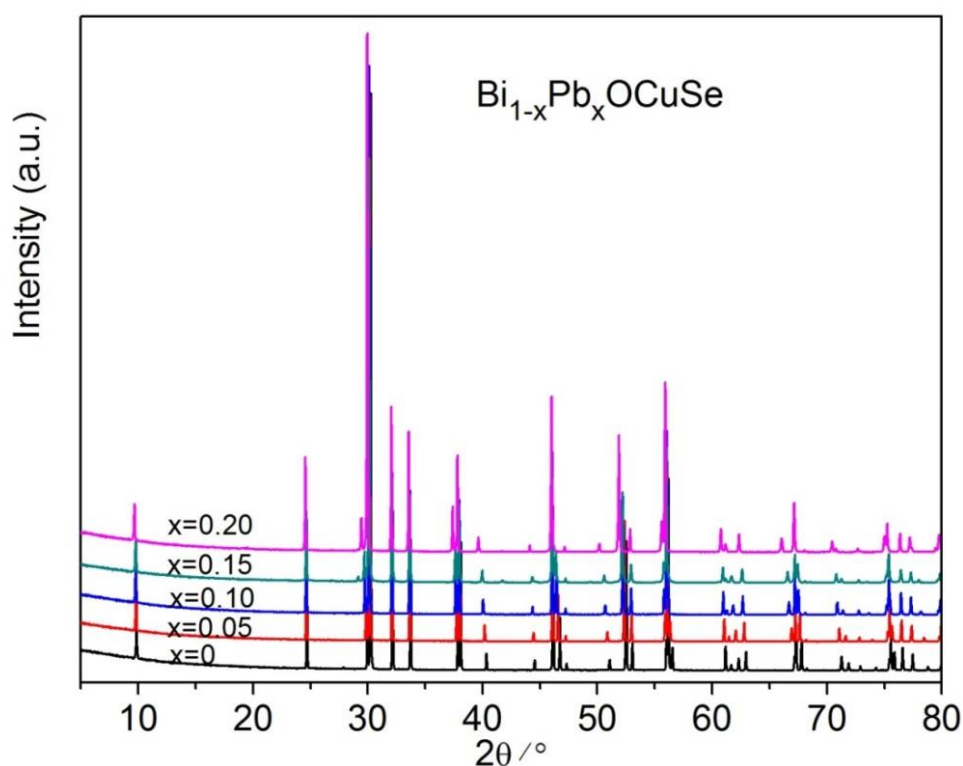


Figure 4.1. Selected powder X-ray diffraction patterns of $\text{Bi}_{1-x}\text{Pb}_x\text{OCuSe}$ ($0.01 \leq x \leq 0.20$).

A representative example of final observed, calculated and difference profiles for the neutron diffraction data of $\text{Bi}_{0.95}\text{Pb}_{0.05}\text{OCuSe}$ is shown in Figure 4.2, while the remaining refinements are included in Appendix B. Tables of refined parameters, selected distances and angles for refinements carried out using neutron diffraction data are presented in Table 4.1 and Table 4.2, while those determined using X-ray diffraction data are presented in Appendix B. In all cases, a good agreement between experimental and calculated patterns is obtained, with reasonable values of R_{wp} and χ^2 .

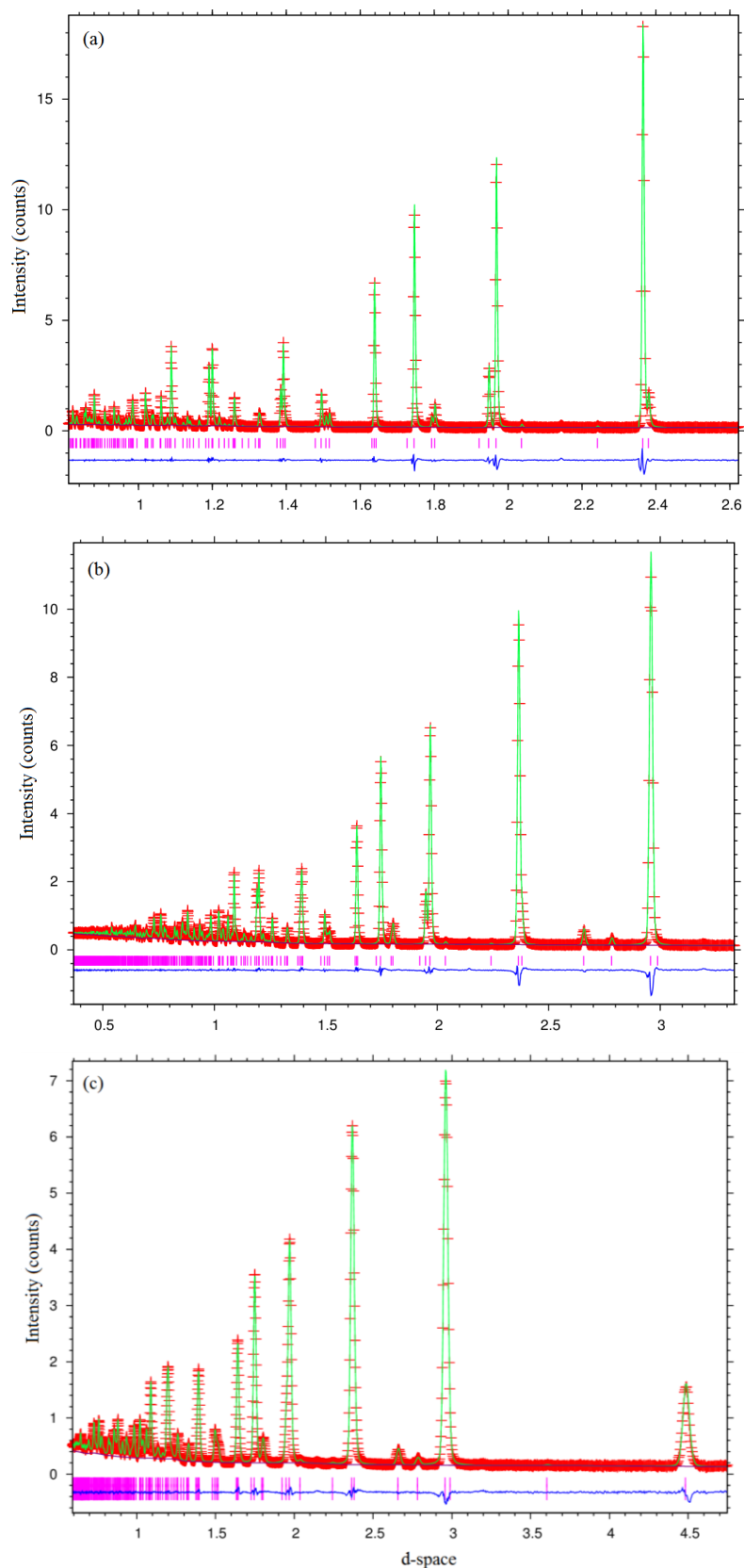


Figure 4.2. Rietveld refinement using powder neutron diffraction data collected on POLARIS for Bi_{1.95}Pb_{0.05}OCuSe at room temperature from (a) backscattering bank ($2\theta = 146.72^\circ$), (b) 92.59° bank and (c) low angle bank ($2\theta = 52.21^\circ$). Key: observed data (red cross); difference curve (blue line); calculated pattern (green line) and reflection positions (pink markers).

The values of the parameters determined using powder X-ray diffraction are in good agreement with those determined by neutron diffraction, although defects through doping produce an anisotropic broadening of the Bragg reflections, observed clearly in the refinement of neutron diffraction data (mentioned in section 3.3.2.1). The coordination of each atom in the structure of the doped samples is similar to that of BiOCuSe, in which Cu is tetrahedrally coordinated by Se while O is tetrahedrally coordinated by Bi/Pb atoms (Figure 4.3). To evaluate the effect of doping on the structure, the lattice parameters, bond lengths and angles obtained from refinements using X-ray diffraction data are presented in Figure 4.4. The lattice parameters of Bi_{1-x}Pb_xOCuSe increase with increasing x (Figure 4.4a). The increase is larger along the c -axis. For example, the difference in lattice parameter between undoped sample and Bi_{0.8}Pb_{0.2}OCuSe is $\sim 0.2\%$ and 1.6% along the a and c -axis, respectively. This may be related to the larger ionic radius of Pb²⁺ (129 pm) when compared to that of Bi³⁺ (117 pm) [213].

Table 4.1. Final refined parameters for neutron diffraction data of Bi_{1-x}Pb_xOCuSe ($x = 0; 0.05; 0.15$). Site occupancy factors for Bi and Pb were fixed at the stoichiometric composition.

		x in Bi _{1-x} Pb _x OCuSe		
		0	0.05	0.15
	$a/\text{\AA}$	3.93011(1)	3.93454(1)	3.93857(1)
	$c/\text{\AA}$	8.93188(5)	8.96523(5)	9.03237(8)
Bi/Pb ^a	z	0.13983(5)	0.13913(4)	0.13773(5)
	$U_{iso}/\text{\AA}^2$	0.00712(1)	0.00844(8)	0.00959(1)
O ^b	$U_{iso}/\text{\AA}^2$	0.00648(2)	0.00763(1)	0.00924(2)
Cu ^c	$U_{iso}/\text{\AA}^2$	0.01474(2)	0.01480(1)	0.01407(2)
Se ^a	z	0.67542(6)	0.67376(4)	0.66992(5)
	$U_{iso}/\text{\AA}^2$	0.00688(2)	0.00767(1)	0.00706(1)
$R_{wp}/\%$		1.6	2.41	2.83
χ^2		2.92	4.59	6.03

^aBi/Pb and Se on 2(c) (1/4, 1/4, z); ^bO on 2(a) (3/4, 1/4, 0); ^cCu on 2(b) (3/4, 1/4, 1/2).

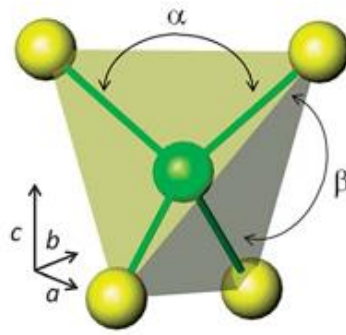


Figure 4.3. The CuSe_4 polyhedron found in the BiOCuSe structure: Se (yellow), Cu (green) atoms.

Table 4.2. Selected bond lengths and angles for neutron diffraction data of $\text{Bi}_{1-x}\text{Pb}_x\text{OCuSe}$ samples ($x = 0; 0.05; 0.15$).

Bond length (Å)			
x in $\text{Bi}_{1-x}\text{Pb}_x\text{OCuSe}$	Bi-O (Å)	Bi-Se (Å)	Cu-Se (Å)
$x = 0$	2.3283(2)	3.2312(3)	2.5143(3)
$x = 0.05$	2.3294(2)	3.2487(3)	2.5094(2)
$x = 0.15$	2.3293(3)	3.2825(4)	2.4968(3)
Bond angles (deg.)			
x in $\text{Bi}_{1-x}\text{Pb}_x\text{OCuSe}$	O-Bi-O	Se-Cu-Se	Se-Cu-Se
$x = 0$	115.12(2)	102.81(2)	112.90(9)
$x = 0.05$	115.25(2)	103.25(1)	112.67(7)
$x = 0.15$	115.44(2)	104.14(2)	112.20(9)

As mentioned above, the structure of the host material is retained and no trace of impurity is observed in the X-ray pattern of $\text{Bi}_{0.8}\text{Pb}_{0.2}\text{OCuSe}$ sample. This suggests that the insertion of divalent Pb^{2+} ions into BiOCuSe structure creates significant hole concentrations. Compensation between positive and negative charge of each elements in this structure is balanced by the valence state of coppers. As discussed in Chapter 3, the oxidation state of copper could be varied between +1 to +1.5 (i.e a mixed valence state of $\text{Cu}^{2+}/\text{Cu}^{1+}$), as found in $\text{Bi}_2\text{YO}_4\text{Cu}_2\text{Se}_2$. The expansion of the unit cell along the c axis leads to an increase of the Bi–Se distances (Figure 4.4b), suggesting that increasing lead content weakens the bonding between the oxide and chalcogenide

layers. The increase in lead content also changes the α and β Se–Cu–Se angles (Figure 4.3), resulting in a reduction of the distortion of the CuSe_4 tetrahedra.

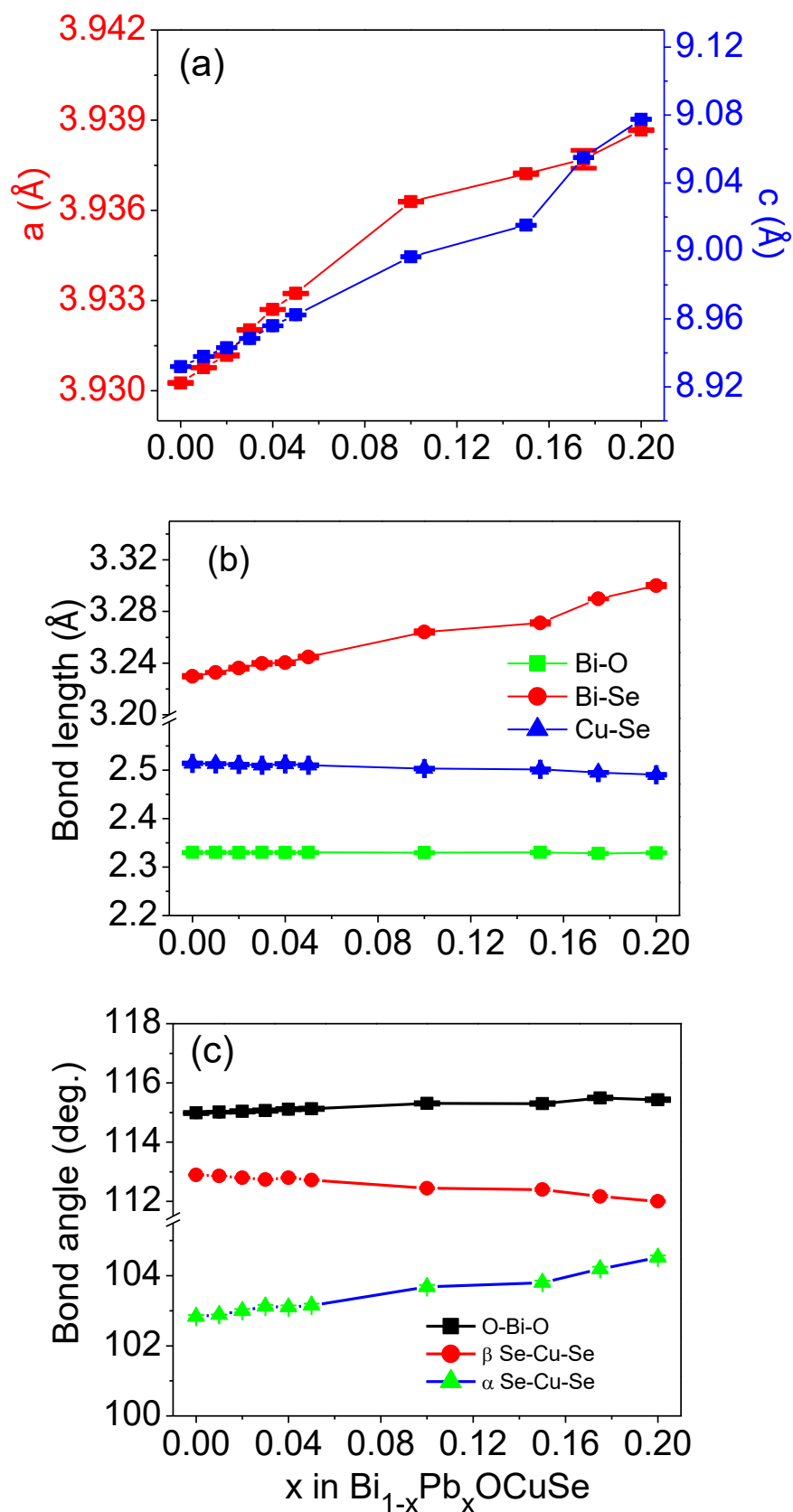


Figure 4.4 (a) Lattice parameters, (b) selected bond distances, and (c) selected bond angles in $\text{Bi}_{1-x}\text{Pb}_x\text{OCuSe}$ obtained from powder X-ray refinement.

A significantly larger atomic displacement parameter of the copper site than those of the other three crystallographic sites is found for Pb doped samples at room temperature (Appendix B). This behaviour has been discussed in Chapter 3 for BiOCuSe. This suggests the same behaviour may occur here as well.

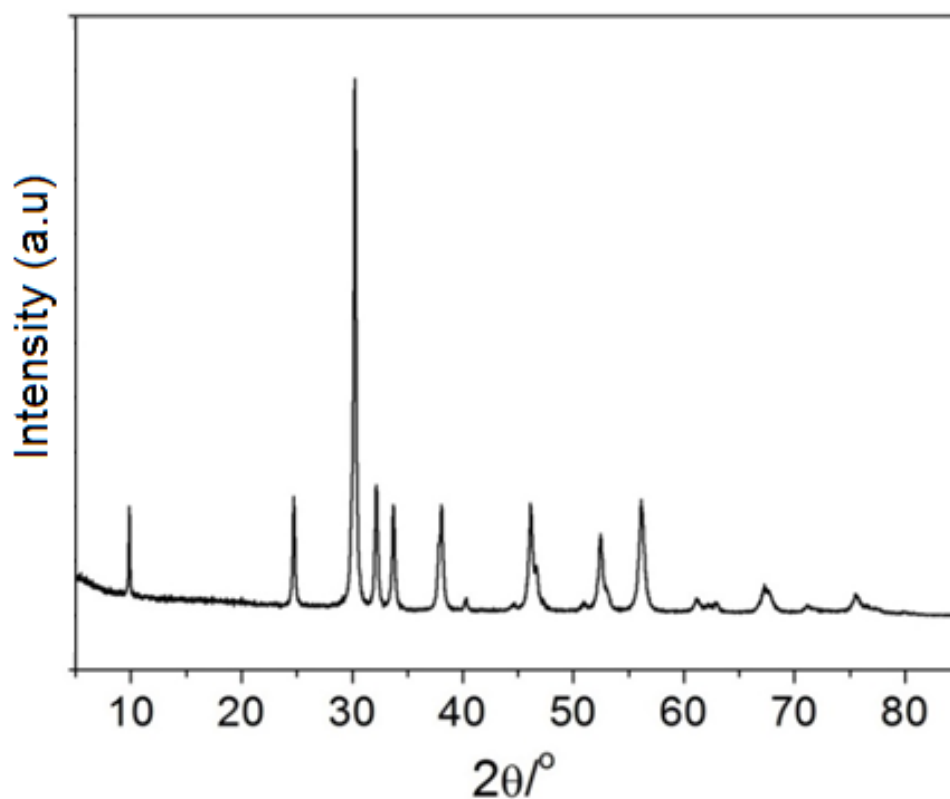


Figure 4.5. Powder XRD of hot-pressed Bi_{0.95}Pb_{0.05}OCuSe sample.

The ZrSiCuAs structure of these materials is retained on hot-pressed samples, for which no decomposition is observed when X-ray diffraction data are analysed. A representative sample is shown in Figure 4.5. In addition, no evidence of preferred orientation is found in diffraction measurements of hot-pressed ingots. This is confirmed by measurements of the electrical transport properties of a rectangular Bi_{0.95}Pb_{0.05}OCuSe ingot, cut perpendicular and parallel to the direction of pressing, which are presented in section 4.3.1.2. However, marked broadening diffraction peaks are observed in these hot pressed samples, which may be related to microstrain grown during hot-pressing.

Examination of selected as-prepared and hot-pressed samples by electron microscopy is shown in Figure 4.6. The as-prepared samples contain plate-like grains, with an average thickness of *ca.* 0.2 μm and lengths of $\sim 2.5 \mu\text{m}$. Although the grains observed on

fractured surfaces of hot-pressed ingots have similar plate-like shapes, there is clear grain growth.

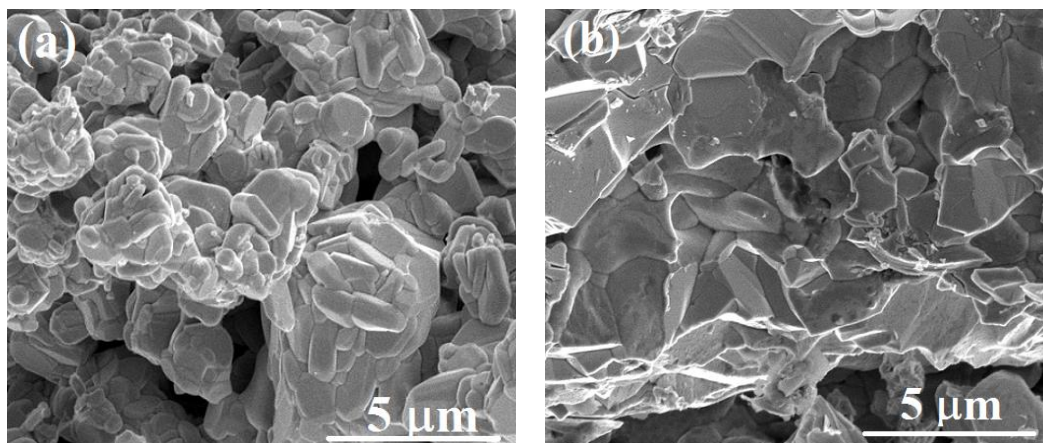


Figure 4.6. SEM micrographs for (a) as-synthesised powder and (b) hot-pressed $\text{Bi}_{1.80}\text{Pb}_{0.20}\text{OCuSe}$.

4.3.1.2 Electrical and Thermal Transport Properties

The increase in charge carrier concentration through doping leads to a decrease of the electrical resistivity in a systematic way with increasing level of doping (Figure 4.7 and Figure 4.8). This indicates that Pb^{2+} is a very effective dopant, given the large improvement of the electrical conductivity at relatively low levels of doping. For instance, at room temperature the electrical conductivity increases from 63 S cm^{-1} for BiOCuSe to $\sim 500 \text{ S cm}^{-1}$ for $\text{Bi}_{0.95}\text{Pb}_{0.05}\text{OCuSe}$ while doping with 5% of Ba^{2+} , Sr^{2+} in BiOCuSe results in a conductivity of 250 S cm^{-1} [171] and only 100 S cm^{-1} , respectively [120]. The increase of charge carrier concentration through doping causes a reduction in the Seebeck coefficient with increasing doping levels, but all samples remain p-type materials with positive values. This decrease in Seebeck coefficient is more than 50% between the pristine material ($\sim 264 \mu\text{V/ K}$) and 5% Pb doped sample ($\sim 127 \mu\text{V/ K}$) at room temperature. With 20% dopant content, the Seebeck coefficient decreases up to $\sim 53 \mu\text{V/ K}$ at the same temperature ($\sim 80\%$ reduction of the original value), indicating that $\text{Bi}_{0.8}\text{Pb}_{0.2}\text{OCuSe}$ has more metallic behaviour, with a very high electrical conductivity ($\sim 1450 \text{ S cm}^{-1}$) at room temperature. A similar trend could be observed in heavily doped $\text{Bi}_{0.85}\text{Sr}_{0.15}\text{CuSeO}$ ($\sim 82 \mu\text{V/ K}$ at 300 K) [120] or $\text{Bi}_{0.875}\text{Ba}_{0.125}\text{CuSeO}$ ($\sim 69 \mu\text{V/ K}$ at 300 K).

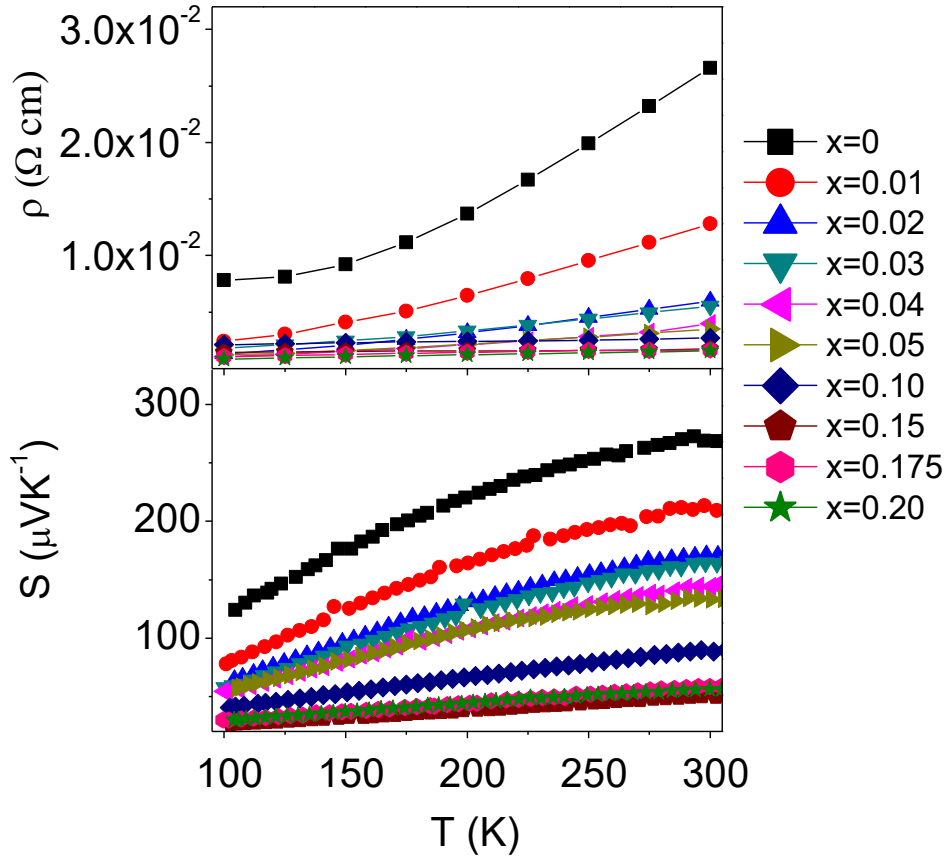


Figure 4.7. Temperature dependence of electrical resistivity (ρ) and Seebeck coefficient (S) for $\text{Bi}_{1-x}\text{Pb}_x\text{OCuSe}$ at a temperature range of $100 \leq T/\text{K} \leq 300$.

It should be noted that there is an excellent agreement between the low- and high-temperature values of the Seebeck coefficient for each sample. However, for the low-temperature resistivity data, the large uncertainties in sample dimensions, as well as the Peltier effect, arising from the use of a constant dc current source (mentioned in Chapter 3), could cause greater uncertainties in the final value [18]. Therefore, the power factor (PF) has been calculated only for the temperature range $300 < T/\text{K} < 673$ (Figure 4.9). The PF decreases slightly with increasing temperature for samples with $x \leq 0.05$. In contrast, it shows a significant increase with increasing temperature for higher doping levels. Samples with a Pb^{2+} content between 4 and 10 % show the highest values of PF at the maximum temperature investigated. This agrees well with other reports, in which optimal properties have also been found for a similar level of doping [188, 211]. However, our hot-pressed materials exhibit higher power factors than those prepared by other techniques: solid state and SPS [188], ball milling and SPS [212] or ball milling and annealing at high temperature, then using SPS for consolidation [211]. For instance, at room temperature with $\sim 5\%$ Pb dopant, our PF reaches a value $\sim 7 \mu\text{W cm}^{-1} \text{ K}^{-2}$ while those of Pan *et al.* [188], Y-Ch Liu *et al.* [212] and J-L. Lan *et al.* [211] are

~ 4 ; 5 and $\sim 6 \mu\text{W cm}^{-1} \text{K}^{-2}$, respectively. Therefore, the optimisation of the consolidation process might also play an important role in the improvement of thermoelectric performance, given that processing parameters may have a significant effect on their final performance. Indeed, the effect of processing parameters on the thermoelectric properties has been shown in the oxide $\text{Ca}_3\text{Co}_4\text{O}_9$, in which not only the thermoelectric properties show a marked improvement, but the mechanical properties are also improved significantly [214].

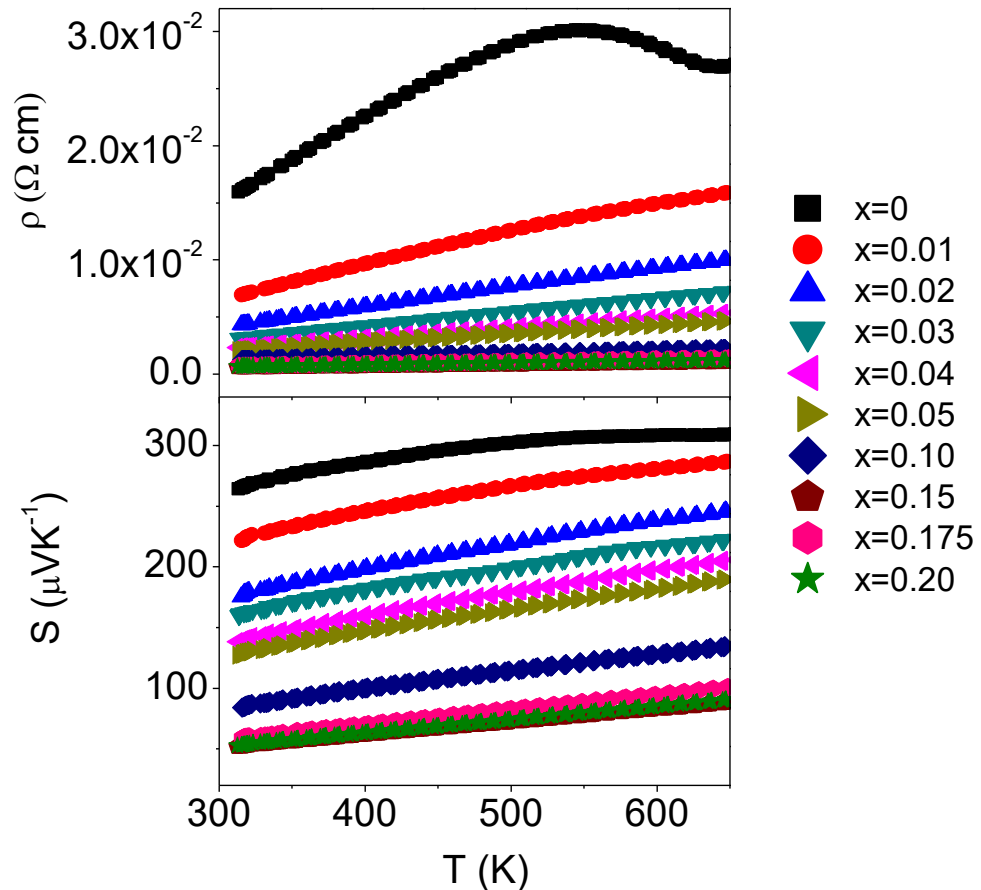


Figure 4.8. Temperature dependence of electrical resistivity (ρ) and Seebeck coefficient (S) for $\text{Bi}_{1-x}\text{Pb}_x\text{OCuSe}$ at a temperature range of $300 < T/\text{K} < 700$.

The power factors of our materials are moderate in comparison to that of Bi_2Te_3 ($\sim 40 \mu\text{W cm}^{-1} \text{K}^{-2}$) [202]. However, it is similar to those of other thermoelectric materials such as Zn_4Sb_3 ($\sim 13 \mu\text{W cm}^{-1} \text{K}^{-2}$ at 673 K) [215]. Calculations of the band structure of BiOCuQ ($Q = \text{S, Se, Te}$) shows that the top of the valence band consists of a mixture of light- and heavy-mass bands [183]. Taking into account that a light-mass band promotes good electrical conduction and a heavy-mass band promotes high Seebeck coefficients, this combination leads to good thermoelectric performance of this material [216].

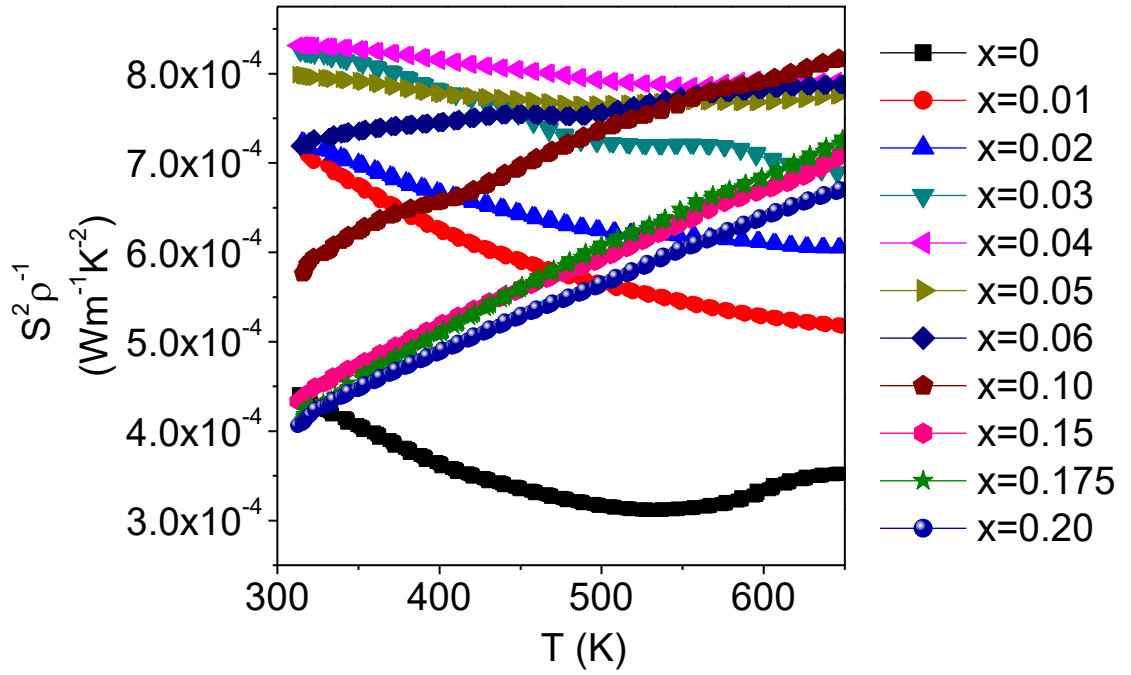


Figure 4.9. Power factor for $\text{Bi}_{1-x}\text{Pb}_x\text{OCuSe}$ as a function of temperature.

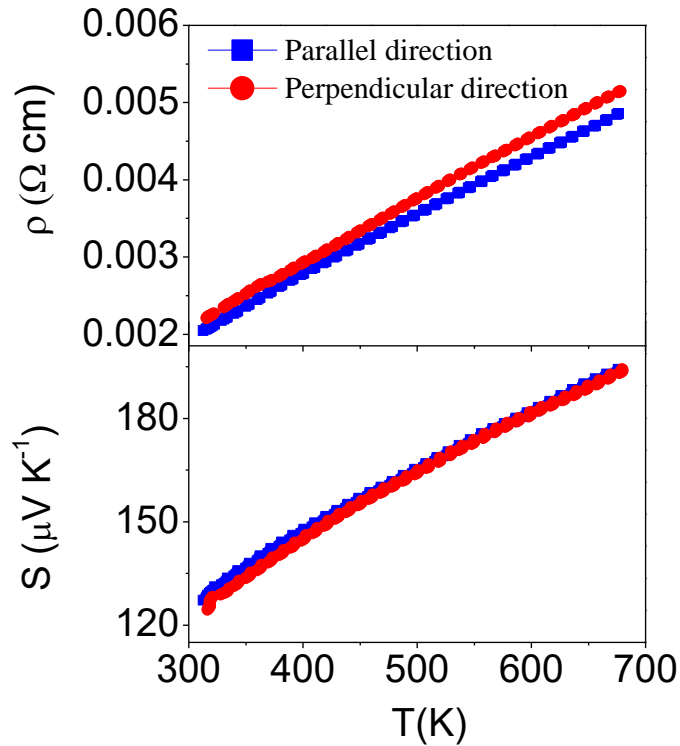


Figure 4.10. Electrical resistivity and Seebeck coefficient for $\text{Bi}_{0.95}\text{Pb}_{0.05}\text{OCuSe}$ vs temperature measured parallel and perpendicularly to the direction of pressing.

However, the low hole mobility in BiOCuSe , which varies in different measurements from ~ 11 [188] to $20 \text{ cm}^2 \text{ V}^{-1} \text{ K}^{-1}$ [168], is quite small, and decreases noticeably with doping due to point-defect scattering [168]. As the thermoelectric figure of merit is proportional to the mobility, according to the expression $Z \propto (m^*)^{3/2} \mu$ (where m^* is the

effective mass and μ the mobility) [23], the moderate power factors observed for these materials are reasonable.

Figure 4.10 shows a comparison of the electrical transport properties of a rectangular $\text{Bi}_{0.95}\text{Pb}_{0.05}\text{OCuSe}$ ingot, cut perpendicular and parallel to the direction of pressing. Values of the Seebeck coefficient are in good agreement between these two measurements, revealing that electrical properties can be assumed to be isotropic, which is consistent with the lack of preferred orientation observed in X-ray diffraction pattern of hot-pressed samples. There is a small difference in the electrical resistivity values of these two measurements which is around $\sim 5\%$. This might be related to the measurement error of sample dimensions which was mentioned earlier.

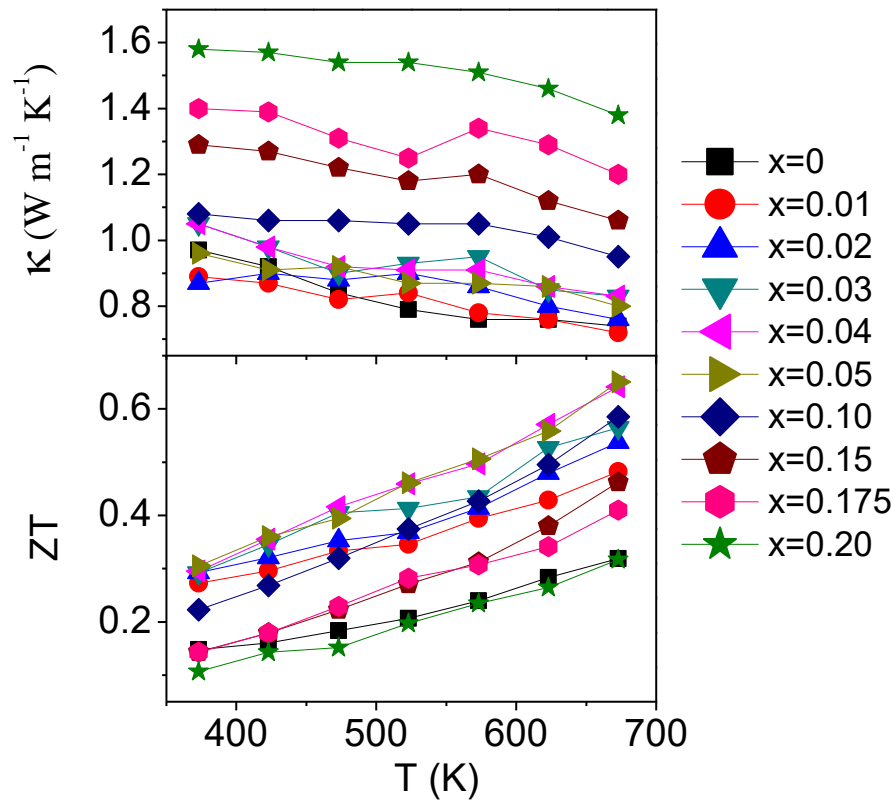


Figure 4.11. Thermal conductivity (κ) and figure of merit (ZT) for $\text{Bi}_{1-x}\text{Pb}_x\text{OCuSe}$ series as a function of temperature.

The thermal conductivity as a function of temperature for the $\text{Bi}_{1-x}\text{Pb}_x\text{OCuSe}$ samples is shown in Figure 4.11 and Figure 4.12. The total thermal conductivity of $\text{Bi}_{0.99}\text{Pb}_{0.01}\text{OCuSe}$ at 373 K is $\sim 0.89 \text{ W m}^{-1} \text{ K}^{-1}$, significantly lower than that of Bi_2Te_3 ($\sim 2 \text{ W m}^{-1} \text{ K}^{-1}$) [202]. The electronic and lattice contributions were calculated using the electrical conductivity data in conjunction with the Wiedemann–Franz law, with a Lorenz constant of $2.45 \times 10^{-8} \text{ W } \Omega \text{ K}^{-2}$. The electronic contribution is

only *ca.* 4% of the total thermal conductivity in BiOCuSe. The trend with increasing lead dopant content is that the total thermal conductivity rises up to $1.58 \text{ W m}^{-1} \text{ K}^{-1}$ at 373 K for $\text{Bi}_{0.8}\text{Pb}_{0.2}\text{OCuSe}$ (Figure 4.11), due to an increased electronic contribution, of up to *ca.* 74% of the total. Our thermal conductivity is slightly higher than in other reports [211, 212], because the lattice contribution to the total thermal conductivity (κ_{lat}) in our sample is higher. For example, our κ_{lat} of 5% Pb dopant is $\sim 0.61 \text{ W m}^{-1} \text{ K}^{-1}$ at 373 K whilst those of J-L. Lan *et al.* [211] and Y-Ch Liu *et al.* [212] are $0.38 \text{ W m}^{-1} \text{ K}^{-1}$ and $0.53 \text{ W m}^{-1} \text{ K}^{-1}$, respectively. This could be related to the different grain size between our sample and the other`s ones, given that those authors use a ball milling process, which should lead to higher phonon scattering at boundaries [217].

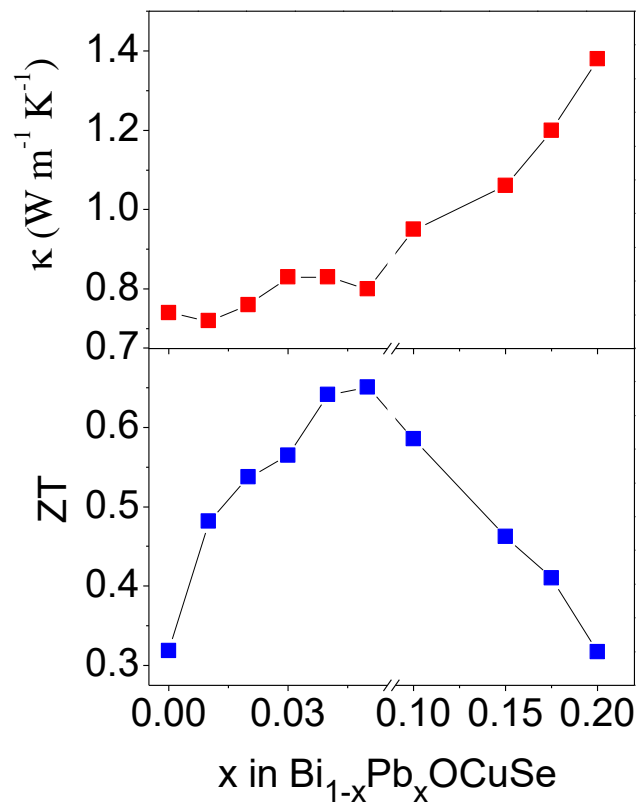


Figure 4.12. Thermal conductivity (κ) and figure of merit (ZT) of $\text{Bi}_{1-x}\text{Pb}_x\text{OCuSe}$ series at 673 K.

As discussed above, the electronic contribution to the total thermal conductivity for the doped samples increases markedly with increasing x (from *ca.* 4% of κ_{total} in BiOCuSe to 74% of κ_{total} in $\text{Bi}_{0.8}\text{Pb}_{0.2}\text{OCuSe}$). This suggests that the increase in the total thermal conductivity through doping arises from the rise in electronic thermal conductivity caused by larger charge carrier concentrations. The surprising low thermal conductivity of BiOCuSe has been presumed to arise from the two-dimensional nature of the

structure of this material, in which scattering of phonons at the interfaces between the $[\text{Cu}_2\text{Se}_2]^{2-}$ and $[\text{Bi}_2\text{O}_2]^{2+}$ layers occurs [120,180]. However, as presented in Chapter 3, our neutron diffraction data shows that the atomic displacement parameter of copper is significantly larger than those of other atoms. This suggests that the bonding of copper atoms within the structure is rather weak and that copper may act as a rattling atom in a rigid framework. The same behaviour may occur here when the atomic displacement parameter of copper is also remarkably larger than those of other atoms.

The thermoelectric figure of merit (ZT) for $\text{Bi}_{1-x}\text{Pb}_x\text{OCuSe}$ series as a function of temperature is shown in Figure 4.11. ZT of all our samples increases with increasing temperature up to the maximum temperature investigated. According to the trend shown in Figure 4.11, higher values of ZT would be achieved at higher temperatures. However, our thermogravimetric data (shown in Chapter 3) suggests that a protective atmosphere for these materials must be used to prevent oxidation when using these materials at higher temperatures. Samples with doping levels of 4–5% lead shows a maximum value of ZT , which is 0.65 at 673 K (Figure 4.12). An improvement (ZT) of *ca.* 50% is achieved in our sample when compared with ZT values found for other dopants at the same temperature. For instance, at 673 K, $\text{Bi}_{1-x}\text{Sr}_x\text{OCuSe}$ possesses a $ZT \sim 0.35$ for $x = 0.15$ [120], $\text{BiOCu}_{1-x}\text{Se}$ obtains a $ZT \sim 0.3$ for $x = 0.985$ [178], and a $ZT \sim 0.3$ has been reported for $x = 0.125$ in $\text{Bi}_{1-x}\text{Mg}_x\text{OCuSe}$ [172]. The performance of our samples is also equivalent to that of ball-milled $\text{Bi}_{1-x}\text{Ba}_x\text{OCuSe}$. In this material, the thermal conductivity is reduced by *ca.* 40% due to the reduction of grain sizes to 200 – 400 nm. This results in an improved $ZT \sim 0.6$ at 673 K for $x = 0.10$ [171]. It is also comparable with results reported by Y-Ch. Liu *et al.* [212] in which $ZT \sim 0.68$ at 673 K is obtained for $\text{Bi}_{0.92}\text{Pb}_{0.08}\text{OCuSe}$. However, it is noted that the introducing nano-dots (5 - 10 nm) into $\text{Bi}_{0.94}\text{Pb}_{0.06}\text{OCuSe}$ nano-particle (~ 30 nm) leads to a $ZT \sim 0.95$ at 673 K [211]. The combination of the increase of hole carrier concentration through Pb doping and the significantly reduced thermal conductivity due to point defects (phonon scattering is enhanced drastically) results in a very high ZT in this sample [211]. The slightly higher hole mobility in Pb-doped samples may play a critical role in the enhancement of their performance when compared to those doped with Ba^{2+} or Sr^{2+} [188, 212]. This is confirmed by the significantly higher electrical conductivities found for the same levels of doping. This may be related to the similarity in atomic masses of Pb^{2+} and Bi^{3+} , which may minimise point-defect scattering.

4.3.2 Ball milled $\text{Bi}_{1.95}\text{Pb}_{0.05}\text{OCuSe}$

4.3.2.1 Structural and Microstructure Characterisation

Figure 4.13 shows a TOPAS refinement using powder X-ray diffraction data of a ball-milled (BM) sample. The sample is single phase, with Bragg peaks that can be indexed in the ZrCuSiAs structure type. In comparison with solid state synthesis (SSS), ball milling is a simpler technique which could be used for large scale production.

The a lattice parameter of the BM sample is $3.942(5)$ Å, comparable with that of SSS sample while c lattice parameter is $9.015(2)$ Å, slightly larger than that of the SSS one. A comparison of the powder X-ray diffraction patterns of both samples is presented in Appendix B. The change in unit cell (c axis) might be related to defects induced during the powder's deformation [218].

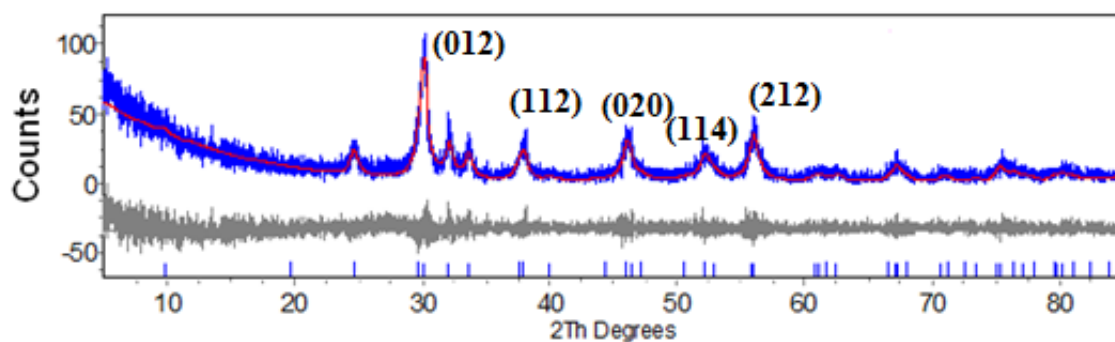


Figure 4.13. A TOPAS refinement using powder X-ray diffraction data collected for ball milled $\text{Bi}_{1.95}\text{Pb}_{0.05}\text{OCuSe}$ at room temperature. Key: observed data (blue line); difference curve (grey line); calculated pattern (red line) and reflection positions (blue markers).

Powder X-ray diffraction data collected on hot-pressed samples indicates that the ZrSiCuAs structure is retained, and no decomposition of the samples is observed (Figure 4.14). For comparison, the average crystalline sizes of SSS and BM samples and their hot-pressed pellets were calculated from the average value of full width at half maximum (FWHM) of three reflection peaks of (012), (020) and (212) using the Scherrer formula (Equation (4.1)) [219].

$$D_v = \frac{k\lambda}{\beta_{hkl}\cos\theta} \quad \text{Equation (4.1)}$$

where D_v is the volume weighted crystalline size, k is the shape factor (0.93), λ is the wavelength of Cu $K_{\alpha 1}$ radiation (1.542 Å), β_{hkl} is the full width at half maximum intensity of reflection (in radians) located at 2θ , after correcting it for an instrumental broadening of 0.001° , determined using Si powder (Sigma Aldrich, mesh 325) as a reference, and θ is the angle of reflection (in degrees).

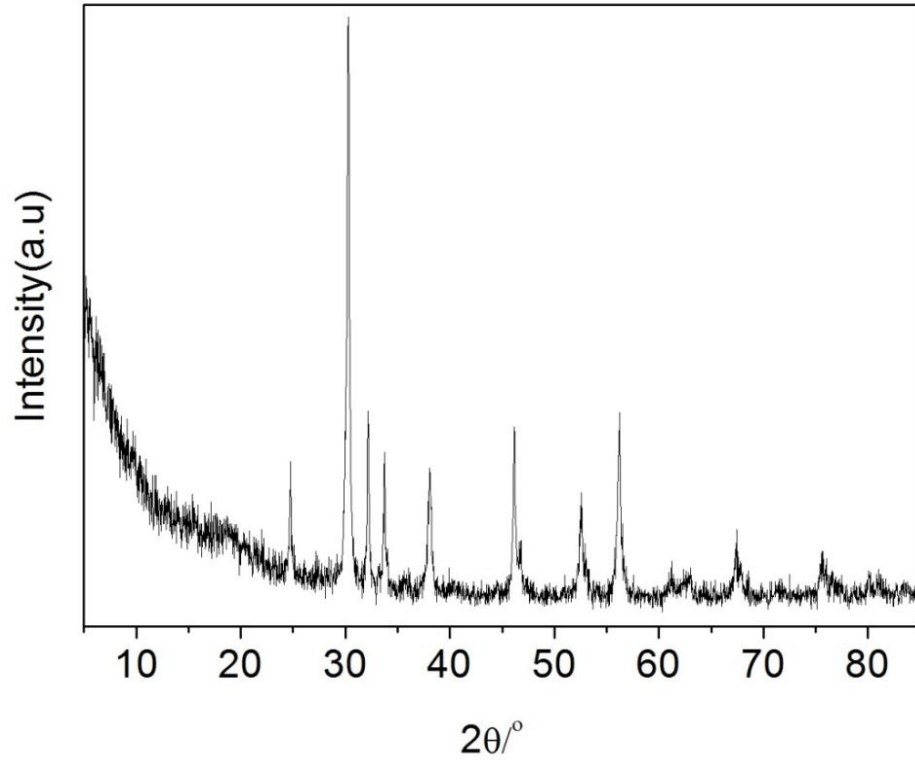


Figure 4.14. X-ray diffraction pattern of hot-pressed BM $\text{Bi}_{1.95}\text{Pb}_{0.05}\text{OCuSe}$.

Table 4.3. Crystallite size of samples.

Sample	SSS	BM	HP_SSS	HP_BM
Crystalline size (nm)	~ 248(4)	~ 22(4)	~ 67(4)	~ 62(4)

Table 4.3 presents a comparison of the crystallite size of BM and SSS samples. In sharp contrast, the crystallite size of the SSS sample is reduced during the hot-pressing process whilst that of the BM sample grows. The broadening of the peak width of the hot-pressed SSS sample (HP_SSS) might be related to an increase in microstrain, while the crystallite growth of hot-pressed BM sample (HP_BM) is likely to be related to the annealing process. The crystalline size of both hot-pressed samples are similar,

suggesting that the small crystallite size of the BM sample may be retained by using fast heating (e.g. spark plasma sintering) instead of hot-pressing.

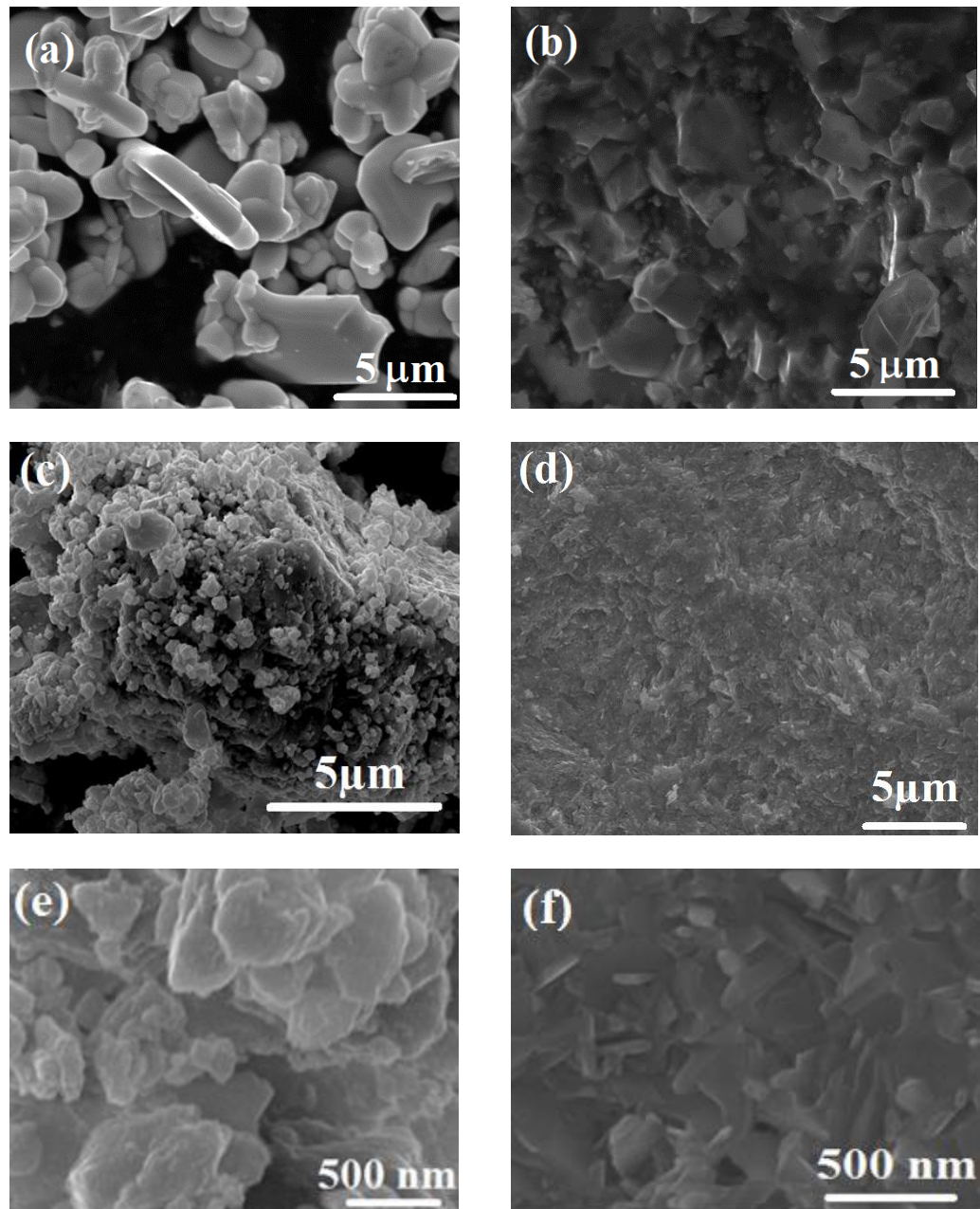


Figure 4.15. SEM micrographs for (a) as-SSS powder; (b) hot-pressed SSS $\text{Bi}_{1.95}\text{Pb}_{0.05}\text{OCuSe}$; (c-e) as-BM powder and (d-f) hot-pressed BM $\text{Bi}_{1.95}\text{Pb}_{0.05}\text{OCuSe}$.

The microstructure was investigated using an SEM. Figure 4.15 shows the SEM images of powders and hot-pressed samples. For comparison purposes, the SEM images of SSS samples are included as well. The BM powder possesses a disk – like grain with an average diameter of $\sim 100 - 500$ nm while the grains observed on fractured surfaces of hot pressed BM sample have plate-like shapes with larger grains (Figure 4.15 (c) & (d)).

The BM powder has smaller disk-like grains with an average diameter of *ca.* 0.1 μm whilst the SSS powder has a plate-like grains, with an average thickness of *ca.* 0.2 μm and lengths of $\sim 4.5 \mu\text{m}$. The fractured surfaces of the hot-pressed SSS sample have similar plate-like shapes with a clear grain growth.

4.3.2.2 Electrical transport properties

The temperature dependence of the electrical transport properties over the range $300 \leq T/\text{K} \leq 573$ is presented in Figure 4.16.

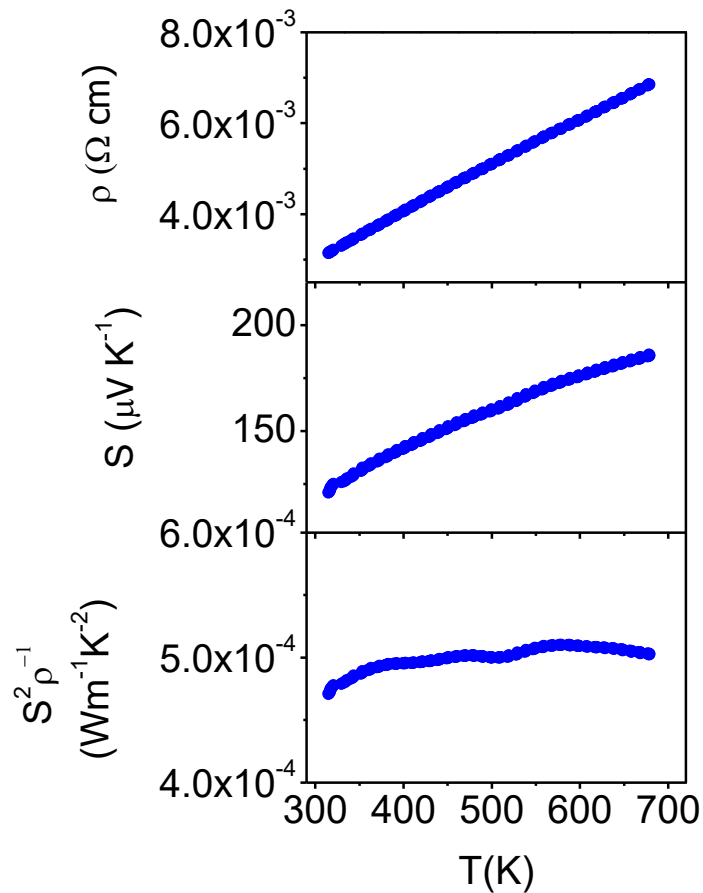


Figure 4.16. Temperature dependence of the electrical resistivity (ρ); Seebeck coefficient (S) and power factor ($S^2\rho^{-1}$) of BM $\text{Bi}_{1.95}\text{Pb}_{0.05}\text{OCuSe}$ over the temperature range $300 < T/\text{K} < 673$.

The electrical resistivity, Seebeck coefficient and power factor of the sample increase as a function of temperature, showing a metallic-like behaviour. The value of the electrical resistivity at $\sim 300 \text{ K}$ is $\sim 3.14 \text{ m}\Omega \text{ cm}$ and increases to $\sim 6.83 \text{ m}\Omega \text{ cm}$ at 673 K , while the Seebeck coefficient is $\sim 120 \mu\text{V}/\text{K}$ at $\sim 300 \text{ K}$ and reaches to $\sim 185 \mu\text{V}/\text{K}$ at 673 K .

This leads to an increase of PF from $4.71 \times 10^{-4} \text{ W m}^{-1} \text{ K}^{-2}$ at $\sim 300 \text{ K}$ to $\sim 5.03 \times 10^{-4} \text{ W m}^{-1} \text{ K}^{-2}$ at 673 K . These values are comparable with those of Y-Ch. Liu *et al.* ($\sim 5 \times 10^{-4} \text{ W m}^{-1} \text{ K}^{-2}$ with $x = 0.04 - 0.06$ at 673 K) [212] and higher than those of undoped ball milled BiOCuSe ($\sim 0.43 \text{ W m}^{-1} \text{ K}^{-1}$ at 773 K) [180]. However, in comparison to the sample synthesised by SS reaction, the electrical resistivity of the BM sample is slightly higher, while the Seebeck coefficient is slightly lower. This results in a lower power factor for the BM sample. It should be noted that the ball mill process could produce more homogeneous samples, but the reduction in grain size may increase the charge carrier scattering at the grain boundaries. This leads to a decrease in the charge carrier mobility, hence reducing the electrical conductivity [113, 220].

Although the power factor of this BM material is moderate in comparison to that of the SSS sample ($\sim 8.5 \mu\text{W cm}^{-1} \text{ K}^{-2}$ at 673 K), its magnitude is similar to that of other thermoelectric materials such as $\text{Ca}_3\text{Co}_4\text{O}_9$ ($\sim 4.8 \mu\text{W cm}^{-1} \text{ K}^{-2}$ at 973 K) [221], $\text{Ca}(\text{Mn}_{0.9}\text{In}_{0.1})\text{O}_3$ ($\sim 4.8 \mu\text{W cm}^{-1} \text{ K}^{-2}$ at 1173 K) [222]. A similar reduction in electrical and thermal transport properties has been also found in ball milled bulk ZnSb with adding Ag particles [223]. The thermal conductivity of this ball milled material was reduced up to 40 % but the electrical conductivity and Seebeck coefficient were negatively affected as well. Consequently, the reduction of thermal conductivity is not enough to compensate for the significant reduction of the power factor. However, taking the simplicity of the synthesis into account, these electrical transport property values are acceptable for large scale thermoelectric material production and applications. In addition, heavy doping to supply more charge carrier concentrations into pristine material might compensate for the increase of grain boundary scattering in the electrical conductivity. This has been observed in the heavy doped ball milled $\text{Bi}_{0.9}\text{Pb}_{0.1}\text{OCuSe}$ [212], in which a higher figure of merit was obtained than that of SSS sample.

4.3.2.3 Thermal Conductivity and Figure of Merit

The thermal conductivity as a function of temperature is shown in Figure 4.17. The total thermal conductivity is $\sim 0.8 \text{ W m}^{-1} \text{ K}^{-1}$ at 373 K , which is significantly lower than those of other TE oxides such as ZnO-based ($\geq 2 \text{ W m}^{-1} \text{ K}^{-1}$) [59, 224], and that of SSS sample ($\sim 0.96 \text{ W m}^{-1} \text{ K}^{-1}$). At 573 K , the total thermal conductivity of the BM sample reduces to $\sim 0.77 \text{ W m}^{-1} \text{ K}^{-1}$ while the SSS one reaches $\sim 0.87 \text{ W m}^{-1} \text{ K}^{-1}$. These values are comparable with results of Y-Ch. Liu *et al.* ($\sim 0.78 \text{ W m}^{-1} \text{ K}^{-1}$ at 373

K and $0.66 \text{ W m}^{-1} \text{ K}^{-1}$ at 573 K for $x = 0.04$ & 0.1) [212] and that of up-doped BM BiOCuSe ($\sim 0.8 \text{ W m}^{-1} \text{ K}^{-1}$ at 373 K and $0.65 \text{ W m}^{-1} \text{ K}^{-1}$ at 573 K) [180]. The electronic and lattice contributions were estimated using the same method mentioned previously (section 4.3.1.2). Results show that the electronic contribution is *ca.* 30 % of the total thermal conductivity at 373 K while that of SSS sample is *ca.* 63.5 % of the total thermal conductivity. This may be indicative of the lower charge carrier mobility for the BM sample. The lattice thermal conductivity of the BM sample is $\sim 0.57 \text{ W m}^{-1} \text{ K}^{-1}$ at 373 K and reduces to $\sim 0.54 \text{ W m}^{-1} \text{ K}^{-1}$ at 573 K, which is much lower than those of PbTe-based TE materials [225] and those of other oxide TE materials, such as $\text{Sr}_{1-x}\text{Dy}_x\text{TiO}_3$ ($\sim 3.5 - 4.5 \text{ W m}^{-1} \text{ K}^{-1}$ at 573 K) [226]. Although the naturally extremely low thermal conductivity of pristine and Pb-doped BiOCuSe has been discussed earlier, here it is found that further reduction is still possible. This indicates that the grain size of the ball milled sample might be the cause of the low thermal conductivity due to the decrease in the electronic contribution and the increase of phonon scattering at boundaries [227].

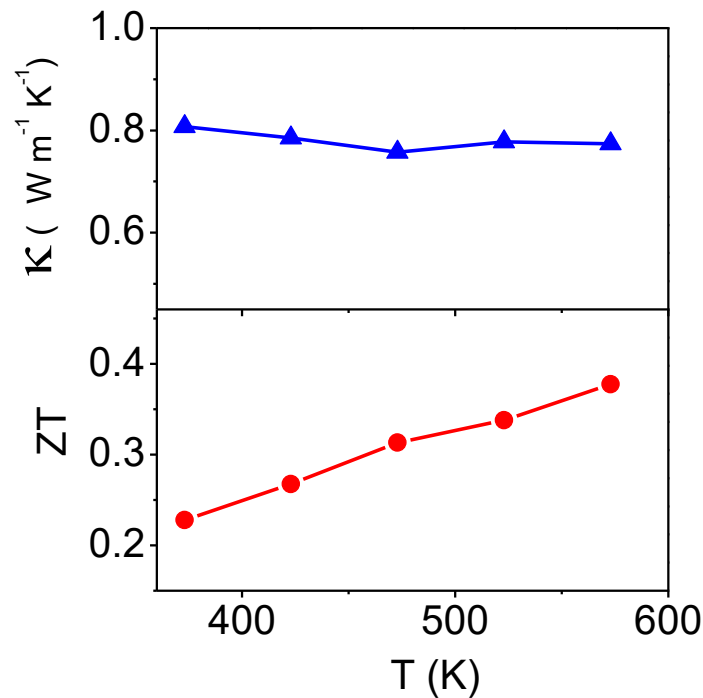


Figure 4.17. Temperature dependence of (a) thermal conductivity (κ) and (b) figure of merit (ZT) of BM $\text{Bi}_{1.95}\text{Pb}_{0.05}\text{OCuSe}$.

The thermoelectric figure of merit as a function of temperature is shown in Figure 4.17. ZT increases with increasing temperature up to the maximum temperature investigated.

At 373 K, ZT value is 0.23 and rises to 0.38 at 573 K which is lower than that of SSS sample ($ZT \sim 0.51$ at 573 K). However, it is comparable with those of Y-Ch. Liu *et al.* (~ 0.38 at 573 K for $x = 0.04 - 0.06$) [212] and higher than those of undoped BM BiOCuSe (~ 0.2 at 573 K) [180] as well as those of other dopants such as Sr^{2+} [120] and Ag^+ [208]. It is also comparable with that of $\text{Bi}_{1.875}\text{Ba}_{0.125}\text{CuSeO}$ ($ZT \sim 0.4$ at 573 K) [171]. It should be noted this is not the maximum temperature for the stability of material. However, due to the limitation of the available instrument, this is the maximum temperature we could measure. Higher values of ZT would be achieved at higher temperatures according to its increasing trend. Although thermal conductivity is reduced significantly in our ball milled sample, it does not compensate for the reduction in power factor. Therefore, retaining small grain size by spark plasma sintering might help to improve the electrical conductivity of sample.

4.3.3 $\text{BiOCu}_{1-x}\text{M}_x\text{Se}$ ($M = \text{Cd}, \text{Zn}; 0 \leq x \leq 0.2$) Compounds

4.3.3.1 Structural Characterisation

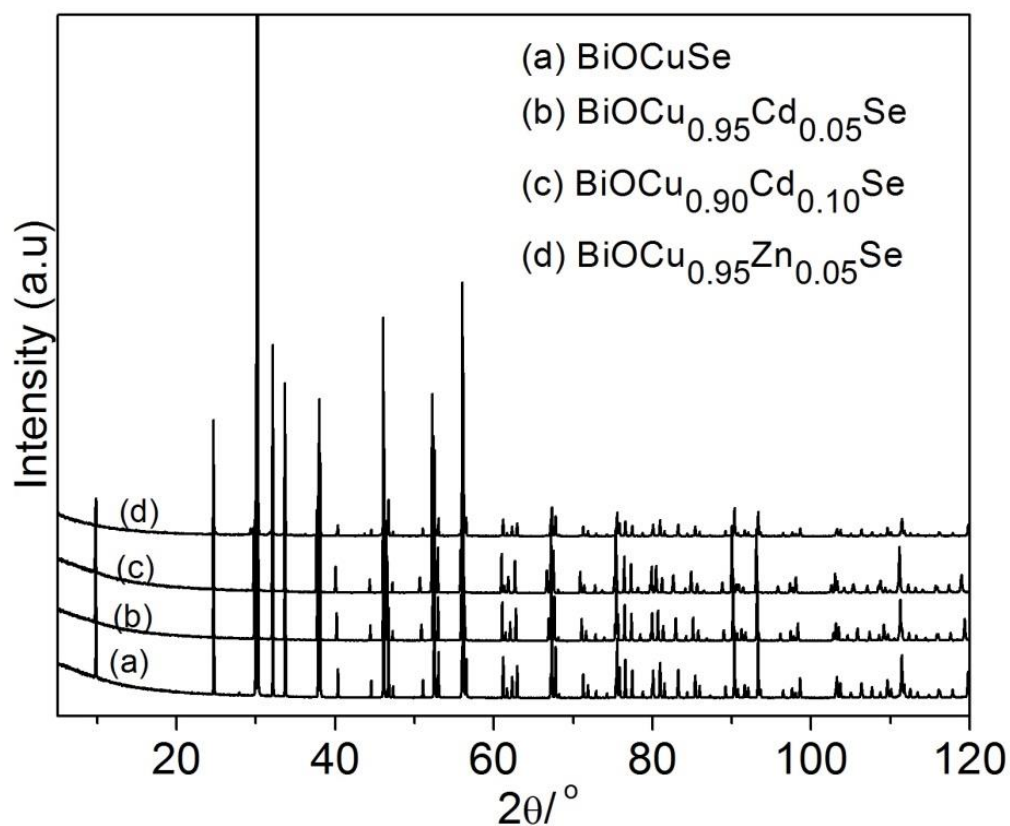


Figure 4.18. Powder X-ray diffraction patterns of $\text{BiOCu}_{1-x}\text{M}_x\text{Se}$ ($M = \text{Cd}, \text{Zn}$ and $x = 0.05; 0.10$).

Figure 4.18 shows selected powder X-ray diffraction patterns of the $\text{BiOCu}_{1-x}\text{M}_x\text{Se}$ ($\text{M} = \text{Cd}, \text{Zn}$ and $x = 0.05; 0.10$) samples. Analysis of these data indicates that the ZrCuSiAs structure type is retained. Cd-containing samples with low dopant contents are single phases, while for the Zn-doped samples trace amounts of $\text{Bi}_2\text{O}_2\text{Se}$ were detected. The maximum doping level was found at about $x = 0.10$ and 0.05 for Cd^{2+} and Zn^{2+} , respectively. Samples with larger values of x (Appendix B) contain significant amounts of impurities, which were identified by powder X-ray diffraction as CdSe and $\text{Bi}_{10}\text{Cd}_3\text{O}_{20}$ for Cd-containing samples and as $\text{Bi}_2\text{O}_2\text{Se}$ for Zn-containing samples. In sharp contrast with our Zn-doped samples, G. Ren *et al.* reported the impurities in their samples are Bi_2O_3 and ZnSe nano-particles [228, 229]. This discrepancy could be related to the difference in synthesis techniques, given that G. Ren *et al.* used a ball milling technique. This technique is believed to create more defects and more homogeneity than the conventional solid state reaction [113, 220].

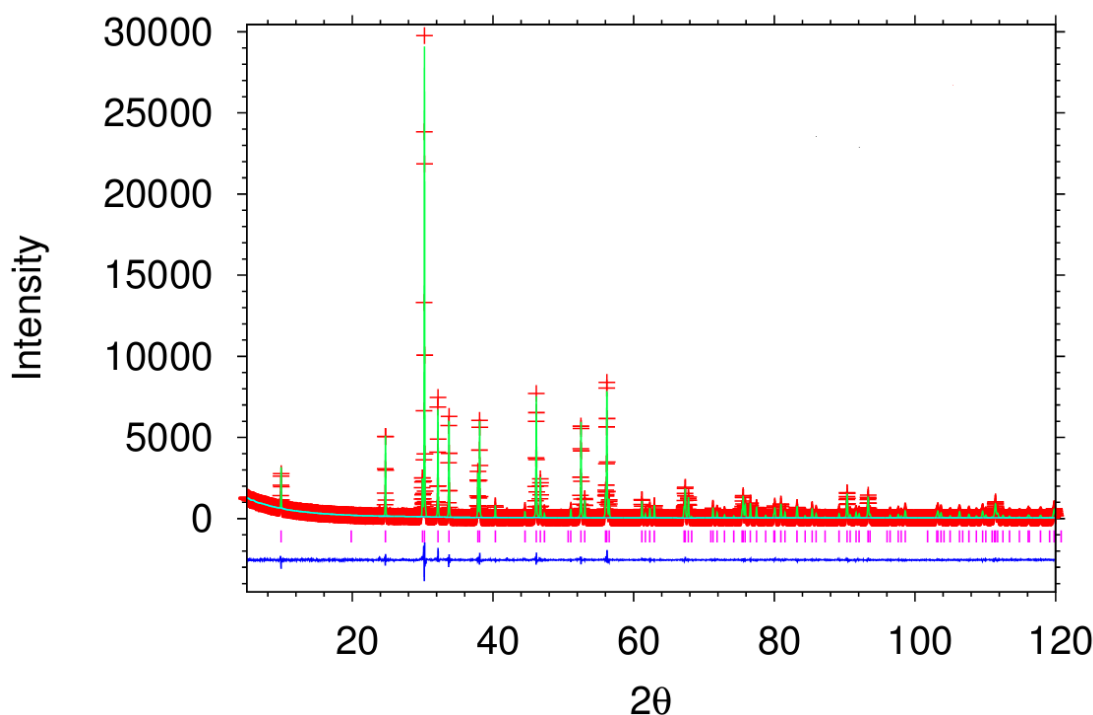


Figure 4.19. Rietveld refinement using powder X-ray diffraction data for $\text{BiOCu}_{0.95}\text{Cd}_{0.05}\text{Se}$ ($R_{\text{wp}} = 10.71\%$). Key: observed data (red crosses); difference curve (blue line); calculated pattern (green line) and reflection positions (pink markers).

A representative Rietveld refinement is shown in Figure 4.19. The remaining refinements, together with tables of refined parameters are given in Appendix B, while the selected distances and angles are given in Table 4.4. As shown in Figure 4.20, the c lattice parameter of $\text{BiOCu}_{1-x}\text{Cd}_x\text{Se}$ increases with increasing x . This expansion of the

unit cell along the c axis might be related to the larger ionic radius of Cd^{2+} (109 pm) when compared to that of Cu^+ (91pm) [213]. By contrast, the substitution with Zn^{2+} results in a reduction in the lattice parameters (Appendix B), which may be related to the smaller ionic radius of Zn^{2+} (74 pm). In all cases, there are only very small changes ($\sim \pm 0.05 - 0.1\%$) in bond distances and angles with doping (Table 4.4).

Table 4.4. Selected bond lengths and angles for $\text{BiOCu}_{1-x}\text{M}_x\text{Se}$ ($\text{M} = \text{Cd}$, and Zn & $x = 0; 0.05$; and 0.10).

Sample	Bond length		
	Bi-O / Å	Bi-Se / Å	Cu-Se / Å
BiOCuSe	2.3302(3)	3.2298(7)	2.5140(8)
BiOCu _{0.95} Cd _{0.05} Se	2.3294(4)	3.2297(9)	2.5148(1)
BiOCu _{0.90} Cd _{0.10} Se	2.3288(4)	3.2311(9)	2.5175(1)
BiOCu _{0.95} Zn _{0.05} Se	2.3284(5)	3.2295(1)	2.5136(2)
Sample	Bond angle		
	O-Bi-O (deg.)	Se-Cu-Se (deg.)	Se-Cu-Se (deg.)
BiOCuSe	114.98(2)	102.83(5)	112.89(3)
BiOCu _{0.95} Cd _{0.05} Se	115.03(3)	102.76(6)	112.93(3)
BiOCu _{0.90} Cd _{0.10} Se	115.12(3)	102.64(6)	112.99(3)
BiOCu _{0.95} Zn _{0.05} Se	115.06(4)	102.80(8)	112.91(4)

The decrease of the Bi-O bond length through the Cd and Zn substitutions may be indicative of a stronger bonding of “insulating layer” $[\text{Bi}_2\text{O}_2]^{2+}$. The increase of the Bi-Se bond length which occurs at *ca* 10% Cd doping level may be indicative of a weaker bonding between the “insulating layer” $[\text{Bi}_2\text{O}_2]^{2+}$ and the “conducting layer” $[\text{Cu}_2\text{Se}_2]^{2-}$. The slight increase of O-Bi-O and Se-Cu-Se bond angles indicates Bi_4O and CuSe_4 tetrahedra are slightly more distorted.

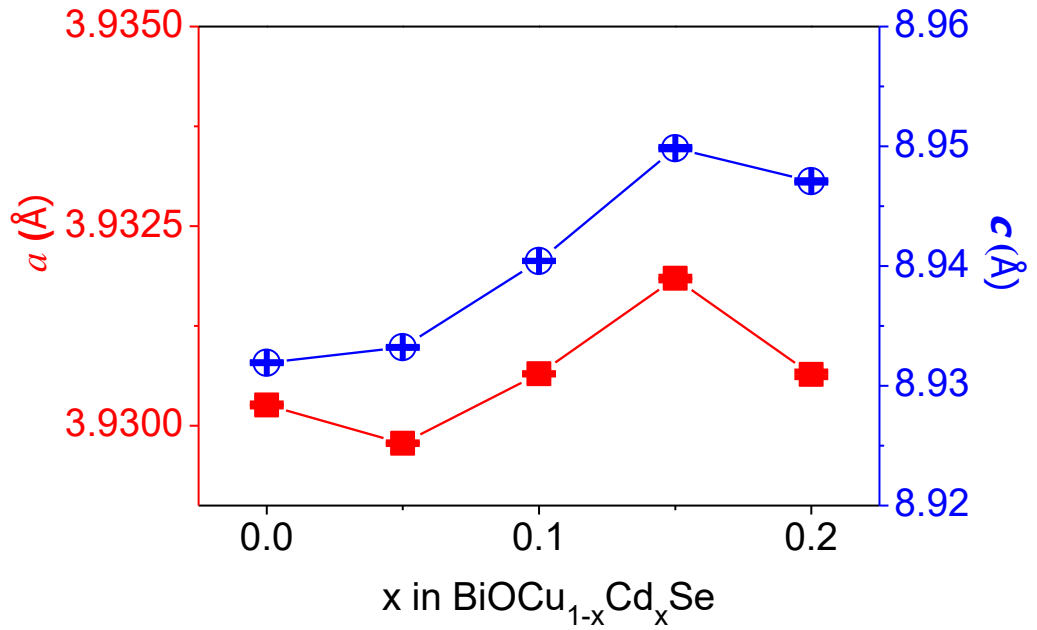


Figure 4.20. Lattice parameters as a function of composition in BiOCu_{1-x}Cd_xSe.

4.3.3.2 Electrical Transport Properties

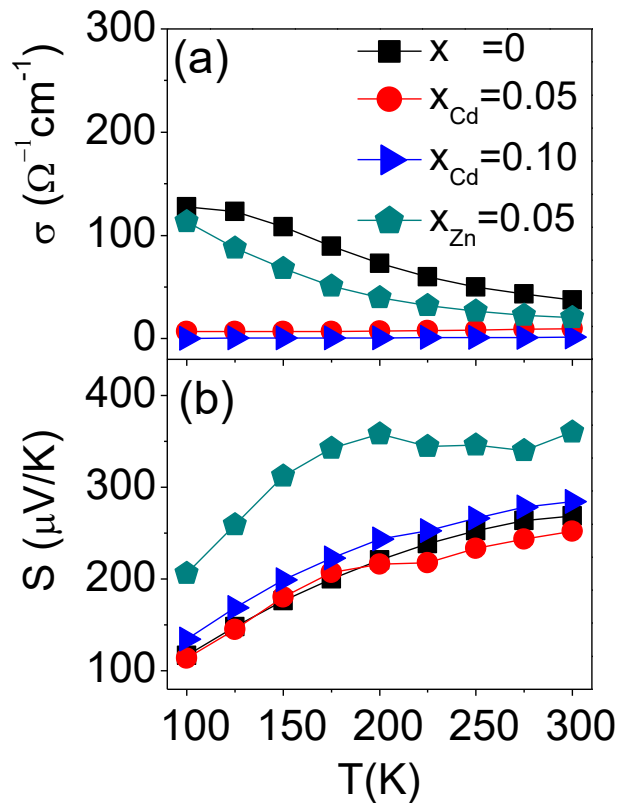


Figure 4.21. Temperature dependence of the electrical properties of BiOCu_{1-x}M_xSe over the temperature range $100 \leq T/K \leq 300$: (a) electrical conductivity (σ); and (b) Seebeck coefficient (S).

In sharp contrast with doping at the Bi^{3+} site with divalent cations, which results in a significant reduction of the electrical resistivity of BiOCuSe due to an increase in the concentration of holes [120, 171, 174, 175, 188, 207, 208], the substitution at the Cu^+ site with divalent ions leads to a major increase in the electrical resistivity (Figure 4.21 and Figure 4.22). With increasing levels of dopants, the electrical resistivity increases in a systematic fashion, and the temperature dependence changes from that characteristic of a degenerate semiconductor to that expected for intrinsic behaviour. This may be indicative of a reduction in the charge carrier concentration from the value of $2 \times 10^{18} \text{ cm}^{-3}$ found for undoped BiOCuSe (presented in Table 3.2, Chapter 3). Whilst Cd^{2+} and Zn^{2+} would be expected to act as n-type dopants, Cu^+ vacancies, which would act as acceptors, are known to form easily in this family of oxychalcogenides [230, 231], and this would lead to charge carrier compensation.

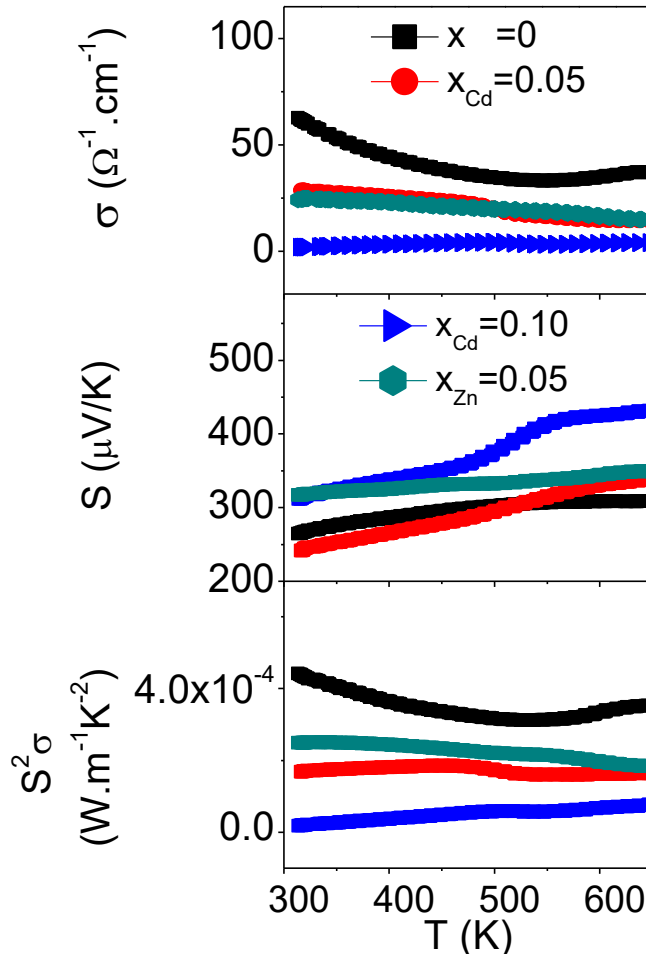


Figure 4.22. Temperature dependence of the electrical conductivity (σ), Seebeck coefficient (S) and power factor ($S^2\rho^{-1}$) of $\text{BiOCu}_{1-x}\text{M}_x\text{Se}$ over the temperature range $300 < T/\text{K} < 673$.

Attempts to donor doping in the related materials such as $\text{Sr}_2\text{ZnO}_2\text{CuS}$ and $\text{Sr}_2\text{MO}_3\text{CuS}$ ($\text{M} = \text{Ga}, \text{In}$), which also contain $[\text{Cu}_2\text{Ch}_2]^{2-}$ anti-fluorite-type layers, show that p-type behaviour was retained [232]. This was attributed to charge carrier compensation due to the formation of Cu^+ vacancies in the $[\text{Cu}_2\text{S}_2]^{2-}$ layers [232]. In sharp contrast to solid state synthesis, G. Ren *et al.* [229] reports that a Zn-doped $\text{BiOCu}_{1-x}\text{Zn}_x\text{Se}$ sample produced by ball milling shows a higher hole concentration, and hence has a reduction in electrical resistivity. It has been suggested that the formation of second phase, nanostructured ZnSe, through the ball milling process causes an increase in copper vacancies, suppressing the electron providing tendency of Zn^{2+} doping. This contradictory result indicates that the electrical resistivity of the material is strongly affected by synthesis conditions and densification method. The error in measurements could be larger than one order of magnitude [230].

For $\text{BiOCu}_{1-x}\text{M}_x\text{Se}$, the Seebeck coefficient of all doped samples remains positive, indicating that the electrical transport properties are still dominated by holes. This is consistent with the p-type semiconducting behaviour normally found for this family of oxychalcogenides. With the exception of $\text{BiOCu}_{0.95}\text{Cd}_{0.05}\text{Se}$, doped samples exhibit higher Seebeck coefficients than those of undoped BiOCuSe . This would be consistent with a reduction in the charge carrier concentration on donor doping. For $\text{BiOCu}_{0.9}\text{Cd}_{0.10}\text{Se}$, a step change in the Seebeck coefficient occurs between 480 and 550 K (Figure 4.22). This behaviour may be indicative of a phase transition. Variable-temperature powder X-ray diffraction measurements may be required to elucidate this.

There is an excellent agreement between the low- and high- temperature values of the Seebeck coefficient. At temperatures above 300 K, the power factor of the doped samples (Figure 4.22) decreases with increasing temperature. However, its magnitude is significantly reduced when compared to that of BiOCuSe . This reduction arises from the very low electrical conductivities found for doped samples.

4.3.3.3 Thermal Transport Properties and Figure of Merit ZT

The thermal conductivity of the $\text{BiOCu}_{1-x}\text{M}_x\text{Se}$ samples as a function of temperature is shown in Figure 4.23. The total thermal conductivity of $\text{BiOCu}_{0.95}\text{Zn}_{0.05}\text{Se}$ is slightly higher than that of pristine BiOCuSe at the same temperature, whilst the Cd-doped samples ($\sim 0.88 - 0.81 \text{ W m}^{-1} \text{ K}^{-1}$) exhibit lower thermal conductivities than that of pristine BiOCuSe ($\sim 0.96 \text{ W m}^{-1} \text{ K}^{-1}$). The total thermal conductivity of the doped samples is significantly lower than that of Bi_2Te_3 ($\sim 2 \text{ W m}^{-1} \text{ K}^{-1}$) [202], which is the

result of rattling behaviour of copper in a rigid framework (BiO*Ch*), leading to high scattering of phonons, discussed in Chapter 3. The electronic and lattice contributions of the thermal conductivity were estimated using the same method mentioned previously. For doped samples, the electronic contribution is below *ca.* 0.1% of total thermal conductivity which is much lower than that of pristine BiOCuSe (*ca.* 4%). This indicates that the charge carrier concentration of these doped samples is very low or their mobility is low.

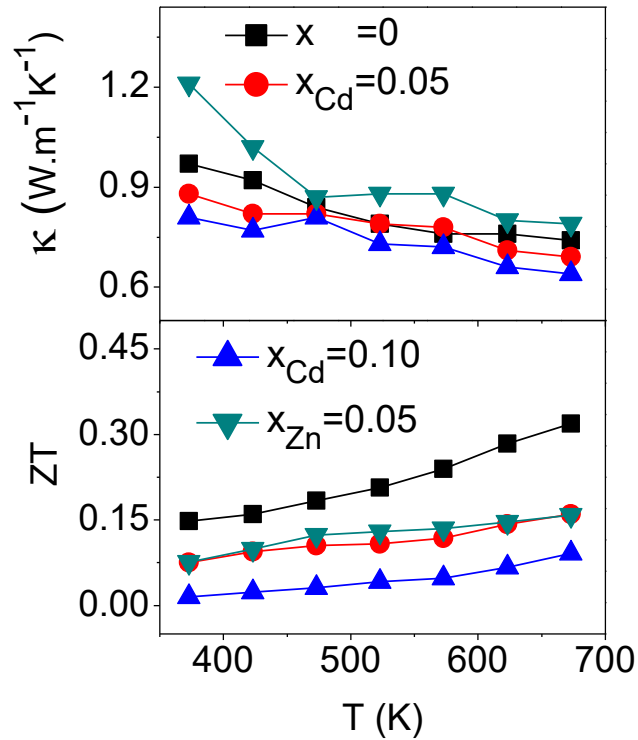


Figure 4.23. Temperature dependence of thermal conductivity (κ) and figure of merit (ZT) of $\text{BiOCu}_{1-x}\text{M}_x\text{Se}$.

The thermoelectric figure of merit of the donor-doped samples was reduced in comparison to that of BiOCuSe (Figure 4.23). The low electrical conductivity of these materials has a deleterious effect on the thermoelectric performance, despite the low thermal conductivity found for these phases. The results presented here suggest that BiOCu*Ch* may be difficult to dope n-type using conventional solid state reactions in sealed silica tubes, due to charge carrier compensation arising from the presence of Cu^+ vacancies. The ease of formation of copper vacancies has been previously related to difficulties in n-type doping in other copper chalcogenides, in particular CuGaSe_2 [233]. Manipulating the carrier concentration in thermoelectric materials for switching from n-type to p-type or vice versa has been found in some TE materials such as

$\text{Co}_3\text{Sn}_{2-x}\text{In}_x\text{S}_2$ ($0 \leq x \leq 2$) [210], $\text{CoSb}_{3(1+x)}$ ($0 \leq x \leq 0.08$) [209], $\text{Pb}_{1-x}\text{Na}_x\text{S}$ ($0 \leq x \leq 0.04$) [234]. The lack of n-type BiOCuSe has significant implications for the construction of thermoelectric devices based on this family of oxychalcogenides, given that compatible n- and p-type materials are required.

Chapter 5 Structures and Thermoelectric Properties of n-type Oxychalcogenide $\text{Bi}_2\text{O}_2\text{Ch}$ ($\text{Ch} = \text{Te}, \text{Se}$) Materials

5.1 Introduction

Although BiOCuCh ($\text{Ch} = \text{Se}, \text{Te}$) compounds possess a high ZT value by doping, and nanostructuring [171, 211], these materials are p-type semiconductors. Efforts to prepare n-type phases, discussed in Chapter 4 have been unsuccessful (section 4.3.2). However, for the construction of thermoelectric devices, the identification of n-type oxychalcogenides is important. Moreover, the thermoelectric properties of n-type bismuth chalcogenides have been widely investigated [198] while little is known about bismuth oxychalcogenides. Recently, the experimental [235 - 237] and theoretical studies [238, 239] of $\text{Bi}_2\text{O}_2\text{Se}$ as n-type thermoelectric materials have been reported. $\text{Bi}_2\text{O}_2\text{Se}$ crystallises in the *anti*- ThCr_2Si_2 structure type, was first investigated by Boller [240]. Later, a German group studied the thermal stability and phase diagram of this material [86, 241]. However, to the best of our knowledge up to the time we carried out this literature survey, efforts to improve the thermoelectric properties by doping or modifying the stoichiometry, as well as by tuning the electronic band gap of $\text{Bi}_2\text{O}_2\text{Se}$ have not been reported. In addition, the substitution of Se by Te in the related BiOCuSe oxychalcogenide leads to an increase in electrical conductivity [179, 183], together with a reduction in the thermal conductivity ($\sim 0.97 \text{ W m}^{-1} \text{ K}^{-1}$ for BiOCuSe [248] and $0.68 \text{ W m}^{-1} \text{ K}^{-1}$ for BiOCuTe [136] at 373 K). Thus, the figure of merit of the oxytelluride is improved significantly with a $ZT = 0.42$ at 373 K while that of the oxyselenide is 0.15 at the same temperature [136, 248]. In sharp contrast, the effect of substituting Se by Te in $\text{Bi}_2\text{O}_2\text{Se}$ as well as a systematic investigation of the thermoelectric properties of a solid solution $\text{Bi}_2\text{O}_2\text{Te}_{1-x}\text{Se}_x$ ($x = 0, 0.25, 0.5, 1$), has never been reported, although the phase study and thermal stability of stoichiometry $\text{Bi}_2\text{O}_2\text{Te}$ have been reported by Schmidt *et al.* [86, 244]. In this chapter, the details of the synthesis, structure, electrical and thermal transport properties of $\text{Bi}_2\text{O}_2\text{Te}_{1-x}\text{Se}_x$ are presented. In addition, efforts to improve the electrical properties of $\text{Bi}_2\text{O}_2\text{Se}$ by modifying its stoichiometry, $\text{Bi}_2\text{O}_2\text{Se}_{1\pm\delta}$ ($0.05 \leq \delta \leq 0.15$), are reported as well.

5.2 Experimental Procedure

5.2.1 Sample Preparation

5.2.1.1 $\text{Bi}_2\text{O}_2\text{Te}_{1-x}\text{Se}_x$ ($0 \leq x \leq 1$)

A solid solution $\text{Bi}_2\text{O}_2\text{Te}_{1-x}\text{Se}_x$ ($x = 0, 0.25, 0.5, 1$) was synthesised by solid state reaction in evacuated and sealed silica tubes ($< 10^{-4}$ Torr), from a mixture of Bi_2O_3 (99.99%, Sigma Aldrich); Bi (99.5%, Sigma Aldrich); Se (99.99%, Sigma Aldrich) and Te shot (99.9999%, Alfa Aesar). Each stoichiometric mixture was first heated up to 623 K for 15 hours and then up to 873 K for 5 hours with a 1 K min^{-1} ramp rate. A second annealing process at 873 K for a further 10 hours with a 2 K min^{-1} ramp rate was carried out after regrinding the obtained powders. For electrical and thermal transport measurements, the as-prepared powder was hot-pressed into highly densified pellets ($\geq 95\%$ of theoretical density) at 823 K and with a uniaxial pressure of 50 bars for 30 minutes under a N_2 flow.

5.2.1.2 $\text{Bi}_2\text{O}_2\text{Se}_{1\pm\delta}$ ($0.05 \leq \delta \leq 0.15$)

$\text{Bi}_2\text{O}_2\text{Se}_{1\pm\delta}$ ($0.05 \leq \delta \leq 0.15$) were synthesised by solid state reaction in an evacuated and sealed silica tube ($< 10^{-4}$ Torr) from a mixture of Bi_2O_3 (99.99%, Sigma Aldrich); Bi (99.5%, Sigma Aldrich); Se (99.99%, Sigma Aldrich). Mixtures were first heated up to 623 K for 15 hours and then up to 873 K for 5 hours with a 1 K min^{-1} ramp rate. A second annealing process at 873 K for a further 10 hours with a 2 K min^{-1} ramp rate was carried out after regrinding the obtained powders. For electrical and thermal transport measurements, the as-prepared powder was hot-pressed into highly densified pellets ($\geq 95\%$ of theoretical density) at 823 K and with a uniaxial pressure of 50 bars for 30 minutes under a N_2 flow.

5.2.2 Characterization and Physical Property Measurements

5.2.2.1 Structural and Microstructural Characterisation

Samples were characterised by powder X-ray diffraction (XRD) using a Bruker D8 Advance Powder X-ray diffractometer, operating with germanium monochromated $\text{CuK}_{\alpha 1}$ radiation ($\lambda = 1.54056 \text{ \AA}$) and fitted with a LynxEye detector. Data were collected over a range of $5 \leq 2\theta/^\circ \leq 120$, with a 0.022° step, for a period of 7 hours.

Rietveld refinements were carried out using the GSAS software [141]. A FEI Quanta FEG 600 scanning electron microscope, with a voltage of 20 kV was used to study the morphology and composition of selected samples.

5.2.2.2 Thermal Analysis

A TA-Q600SDT TGA instrument was used to investigate the thermal stability of $\text{Bi}_2\text{O}_2\text{Ch}$ ($\text{Ch} = \text{Se}, \text{Te}$) as a function of temperature under a N_2 flow. The samples were loaded into a ceramic crucible and heated from room temperature to 1000 K, with a 5 K min^{-1} ramp rate.

5.2.2.3 Electrical transport measurements

To measure the electrical transport properties of samples, a rectangular ingot ($\sim 6 \times 3 \times 1.2 \text{ mm}^3$) was cut from a hot pressed pellet. The electrical resistivity and Seebeck coefficient were measured simultaneously, parallel to ingot press direction using a Linseis LSR-3 instrument (Germany) over the temperature range $300 \leq T/\text{K} \leq 673$, under a temperature gradient of 30 K and an applied current of 15 mA for samples possessing electrical resistivity less than $5 \Omega \text{ cm}$ at room temperature whilst those of samples possessing electrical resistivity higher than $5 \Omega \text{ cm}$ were measured using the cryostat system described in Chapter 2, over the temperature range $100 \leq T/\text{K} \leq 300$. The charge carrier concentration (n) and mobility (μ) of $\text{Bi}_2\text{O}_2\text{Te}_{1-x}\text{Se}_x$ ($x = 0, 0.25$) were calculated from the Hall coefficient and resistivity values measured using an Ecopia HMS-3000 Hall measurement system (Korea). It should be note that due to high electrical resistivity of remaining samples, which is over the measurable limit of Ecopia HMS-300, its charge carrier concentration and mobility, could not be measured. A square sample of $\text{Bi}_2\text{O}_2\text{Te}_{1-x}\text{Se}_x$ ($x = 0, 0.25$) with a length of $\sim 4 \text{ mm}$ and thickness of $\sim 1 \text{ mm}$ was prepared. Indium solder was used to achieve good electrical contacts. A magnetic field of -1 to 1 Tesla and the van der Pauw method [159] were applied to measure Hall coefficient and resistivity of sample, respectively.

5.2.2.4 Thermal transport measurements

A LFA 447 NanoFlash[®] instrument was employed to measure the thermal diffusivity (α) and the heat capacity (C_p) of the $\text{Bi}_2\text{O}_2\text{Te}_{1-x}\text{Se}_x$ ($x = 0; 0.25; 0.5$) samples over a

temperature range of $373 \leq T/K \leq 573$ in 50 K steps while an Anter FL3000 system was used for $\text{Bi}_2\text{O}_2\text{Se}_{1\pm\delta}$ ($0.05 \leq \delta \leq 0.15$) over a temperature range of $373 \leq T/K \leq 673$. Samples were a highly densified pellet with a diameter of approximate 12.7 mm and a thickness of ~ 1.2 mm. A graphite coating on the surface of the pellet was applied to maximise heat absorption. A PyroceramTM 9606 was used as a reference material for heat capacity determination of samples. Measurements were carried out perpendicular to the direction of pressing. Smaller square ingots (5 x 5 x 2 mm) cut parallel and perpendicular to the direction of pressing, were also measured.

5.3 Results and Discussion

5.3.1 $\text{Bi}_2\text{O}_2\text{Te}_{1-x}\text{Se}_x$ ($0 \leq x \leq 1$) Compounds

5.3.1.1 Structural and Morphological Characterisation

Figure 5.1 shows the powder X-ray diffraction data collected for $\text{Bi}_2\text{O}_2\text{Te}_{1-x}\text{Se}_x$ ($0 \leq x \leq 1$). A trace of very small amount of Bi_2TeO_5 impurity is found for $x = 0$ while a small amount of BiTe is detected in samples with $x = 0.25$ and 0.5 .

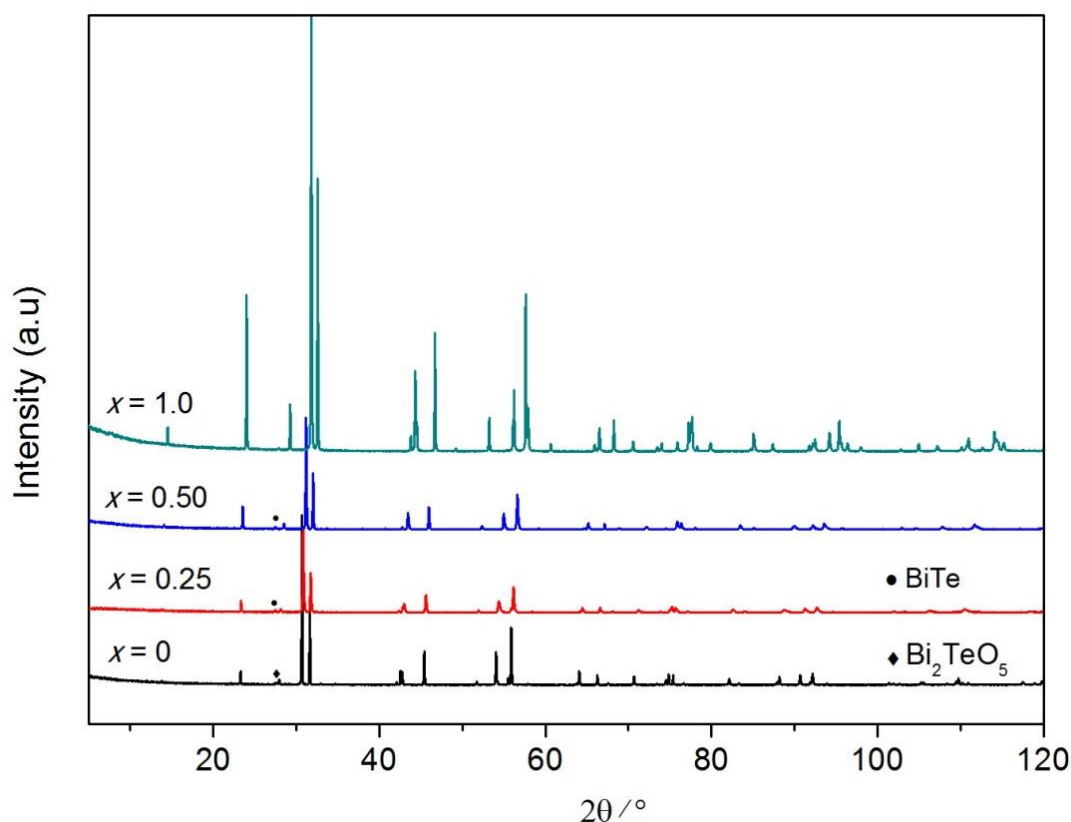


Figure 5.1. Powder XRD patterns of $\text{Bi}_2\text{O}_2\text{Te}_{1-x}\text{Se}_x$ ($0 \leq x \leq 1$).

All diffraction patterns could be indexed on the basis of a body-centered tetragonal unit cell, with similar lattice parameters to those of previous reports ([240] for $\text{Bi}_2\text{O}_2\text{Se}$, [86, 245] for $\text{Bi}_2\text{O}_2\text{Te}$ and $\text{Bi}_2\text{O}_2\text{Te}_{0.5}\text{Se}_{0.5}$), suggesting that the structures of $\text{Bi}_2\text{O}_2\text{Te}_{1-x}\text{Se}_x$ are closely related to that of $\text{Bi}_2\text{O}_2\text{Se}$. It should be noted that we mention this closely structural relationship because there is no database entry for $\text{Bi}_2\text{O}_2\text{Te}$ crystal structure is reported on Inorganic Crystal Structure database (ICSD) run by the leading international FIZ Karlsruhe provider [249]. Therefore, a Rietveld refinement of $\text{Bi}_2\text{O}_2\text{Te}$ was carried out using the previously reported crystal structure of $\text{Bi}_2\text{O}_2\text{Se}$ [240] as the initial structural model (space group $I4/mmm$), with the Se atom at the $2(a)$ site replaced by Te. This results in the good agreement between observed and calculated intensities, and shows a low R_{wp} value. Then, a fixed fraction of Te was replaced by Se for refinements of samples with $x = 0.25$ and 0.50 . A representative refinement of the final observed, calculated and difference profiles of $\text{Bi}_2\text{O}_2\text{Te}$ are shown in Figure 5.2. The remaining refinements are presented in Appendix C. The final refined parameters of samples are presented in Table 5.1 while selected bond distances and angles are summarised in Table 5.2.

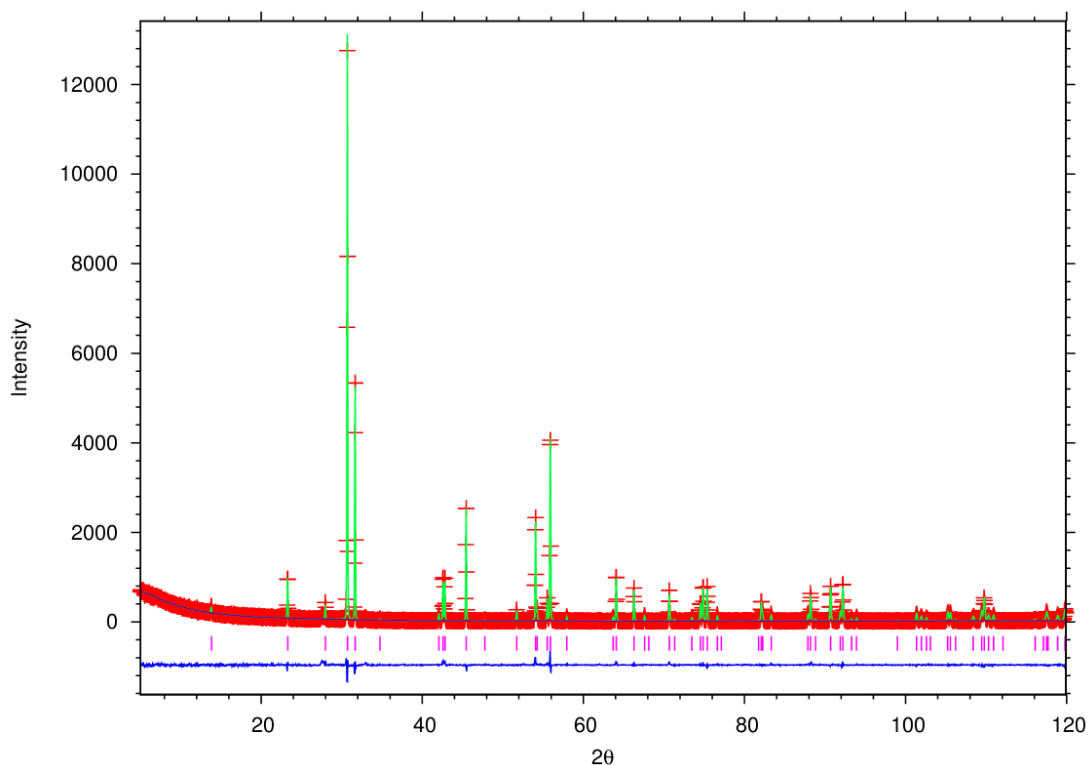


Figure 5.2. Rietveld refinement using powder X-ray diffraction data for $\text{Bi}_2\text{O}_2\text{Te}$. Key: observed data (red cross); difference curve (blue line); calculated pattern (green line) and reflection positions of $\text{Bi}_2\text{O}_2\text{Te}$ (pink markers).

Our refinements indicate that $\text{Bi}_2\text{O}_2\text{Te}_{1-x}\text{Se}_x$ ($0 \leq x \leq 1$) crystallise in the *anti*- ThCr_2Si_2 structure type. The crystal structure of $\text{Bi}_2\text{O}_2\text{Ch}$ ($\text{Ch} = \text{Se}, \text{Te}$) consists of $[\text{Bi}_2\text{O}_2]^{2+}$ layers and Ch^{2-} square net layers alternately stacked along the *c*-axis (Figure 5.3). In the $\text{Bi}_2\text{O}_2\text{Te}_{1-x}\text{Se}_x$ structure, the oxygen anions are tetrahedrally coordinated by four bismuth cations, forming fluorite-type slabs at a distance of 2.3424(6) Å for $x = 0$ and decreasing with increasing x . The substitution of Te by Se leads to a decrease of lattice parameters (Figure 5.4) due to the smaller ionic radii of Se atoms. Each bismuth cation is at the centre of a square antiprism, surrounded by four oxygen and four tellurium anions, while the tellurium anions form a square array, with Te - Te distances of 3.98025(4) Å for $x = 0$ and decreasing with increasing x (Table 5.2).

Table 5.1. Final refined parameters for $\text{Bi}_2\text{O}_2\text{Te}_{1-x}\text{Se}_x$ ($0 \leq x \leq 1$) compounds at room temperature.

		x in $\text{Bi}_2\text{O}_2\text{Te}_{1-x}\text{Se}_x$			
		0	0.25	0.5	1.0
$a/\text{Å}$		3.98025(4)	3.96058(4)	3.93574(5)	3.88528(5)
$c/\text{Å}$		12.7039(2)	12.6058(2)	12.4665(2)	12.2034(2)
Bi ^a	z	0.34724(9)	0.34861(9)	0.35051(7)	0.35357(5)
	$U_{\text{iso}}/\text{Å}^2$	0.0033(3)	0.0069(3)	0.0056(2)	0.0039(2)
O ^b	$U_{\text{iso}}/\text{Å}^2$	0.0030(5)	0.0087(5)	0.0070(4)	0.0050(3)
Te/Se ^c	$U_{\text{iso}}/\text{Å}^2$	0.0026(6)	0.0071(7)	0.0095(8)	0.0069(6)
$R_{\text{wp}}/\%$		11.78	13.49	8.33	11.16

In $\text{Bi}_2\text{O}_2\text{Te}$, the Bi-O bond length of 2.3424(6) Å is shorter than the Bi-Te bond length of 3.4187(6) Å. This is consistent with the larger ionic radius of Te when compared with O, and with Bi-O and Bi-Te distances found in other bismuth oxytellurides [96]. The bond lengths of Bi-Bi, Bi-O and Bi-*Ch* have the same decreasing trend of lattice parameters, whilst the Bi-O-Bi bond angle is stretched along the *a* axis and O-Bi-O bond angle is reduced along the *c* axis when more Te is substituted by Se. A similar situation is also found in BiOCuTe oxytelluride when substituted by Se [200]. For

$\text{Bi}_2\text{O}_2\text{Se}$, although the lattice parameters are significantly reduced due to smaller ionic radius of Se when compared with that of Te, they are in good agreement with those of previous reports [235, 236]. The structure of $\text{Bi}_2\text{O}_2\text{Ch}$ can also be found for $\text{Th}_2\text{N}_2\text{X}$ and $\text{U}_2\text{N}_2\text{X}$ ($\text{X} = \text{Te}, \text{Sb}, \text{Bi}$) [250] as well as $\text{RE}_2\text{O}_2\text{X}$ ($\text{RE} = \text{rare-earth element}, \text{X} = \text{Te}, \text{Sb}, \text{Bi}$) [83,251-252]. The fluorite-type $[\text{Bi}_2\text{O}_2]^{2+}$ layers are also found in the related BiOCuCh oxychalcogenide, in which they are separated by anti-fluorite $[\text{Cu}_2\text{Ch}_2]^{2-}$ layers periodically [96, 136]. A characteristic structural motif in poly-telluride compounds is presented in the two-dimensional square nets of Te atoms found here in this $\text{Bi}_2\text{O}_2\text{Te}_{1-x}\text{Se}_x$ structure. In many cases it has been shown that the square nets are in fact average structures, with the real structures being strongly modulated [253]. The Te-Te distances in the $\text{Bi}_2\text{O}_2\text{Te}$ square net are significantly larger ($\sim 3.98 \text{ \AA}$) than those in other poly-telluride compounds containing square nets (typically $2.8 - 3.4 \text{ \AA}$), although still within the van der Waals contact distance of 4.2 \AA . This suggests that the Te-Te interactions in $\text{Bi}_2\text{O}_2\text{Te}$ will be rather weak. A commensurately modulated structure has been recently found for the related $\text{Pr}_2\text{O}_2\text{Sb}$ [254], but our powder diffraction data for $\text{Bi}_2\text{O}_2\text{Te}$ provides no evidence for a modulated structure. In contrast, the Bi-Se bond length ($\sim 3.2773(4) \text{ \AA}$) is shorter than that of Bi-Te ($\sim 3.4187(6) \text{ \AA}$), indicating bonding of the interlayers of $\text{Bi}_2\text{O}_2\text{Se}$ is stronger than that of $\text{Bi}_2\text{O}_2\text{Te}$.

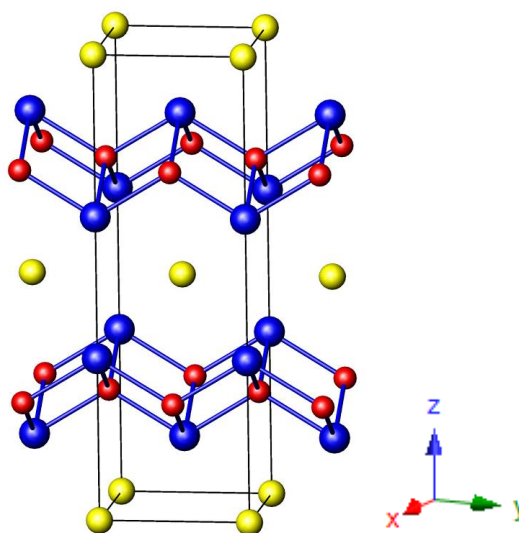


Figure 5.3. Ball-and-stick representation of the crystal structure of $\text{Bi}_2\text{O}_2\text{Ch}$ ($\text{Ch} = \text{Se}, \text{Te}$). Key: Bi (blue circle); O (red circle); Ch (yellow circle).

To investigate the possibility of non-stoichiometry in $\text{Bi}_2\text{O}_2\text{Te}$, a series of $\text{Bi}_2\text{O}_2\text{Te}_{1\pm\varepsilon}$ ($\varepsilon = 0.05$) was synthesised using the same procedure and reaction conditions. However, the powder XRD of $\text{Bi}_2\text{O}_2\text{Te}_{0.95}$ shows large amounts of impurity phases of Bi_2O_3 ,

Bi₂TeO₅, while that of Bi₂O₂Te_{1.05} shows a more intense peak of Bi₂TeO₅ than that in Bi₂O₂Te (Figure 5.7). This suggests that Bi₂O₂Te is stable only within a very restricted range of chemical compositions around the stoichiometric composition.

Powder X-ray diffraction data collected on hot-pressed samples indicate that the *anti*-ThCr₂Si₂ structure of Bi₂O₂Te_{1-x}Se_x ($0 \leq x \leq 1$) is retained during the consolidation process. No additional impurities are introduced (Appendix C).

Table 5.2. Selected bond lengths and angles from powder X-ray diffraction data for Bi₂O₂Te_{1-x}Se_x ($0 \leq x \leq 1$) compounds.

Sample	Bond length			
	Bi-Bi (Å)	Bi-O (Å)	Bi-Te/Se(Å)	Te-Te/Se(Å)
$x = 0$	3.7451(1)	2.34240(6)	3.41870(6)	3.98025(4)
$x = 0.25$	3.7451(3)	2.33821(2)	3.38885(3)	3.96058(4)
$x = 0.50$	3.7450(1)	2.33290(5)	3.34930(5)	3.93574(5)
$x = 1.0$	3.7333(9)	2.31760(4)	3.27730(4)	3.88528(5)
Sample	Bond angle			
	O-Bi-O (deg.)		Bi-O-Bi (deg.)	
$x = 0$	116.34(5)		106.15(2)	
$x = 0.25$	115.76(1)		106.42(1)	
$x = 0.50$	115.03(4)		106.77(2)	
$x = 1.0$	113.90(3)		107.30(1)	

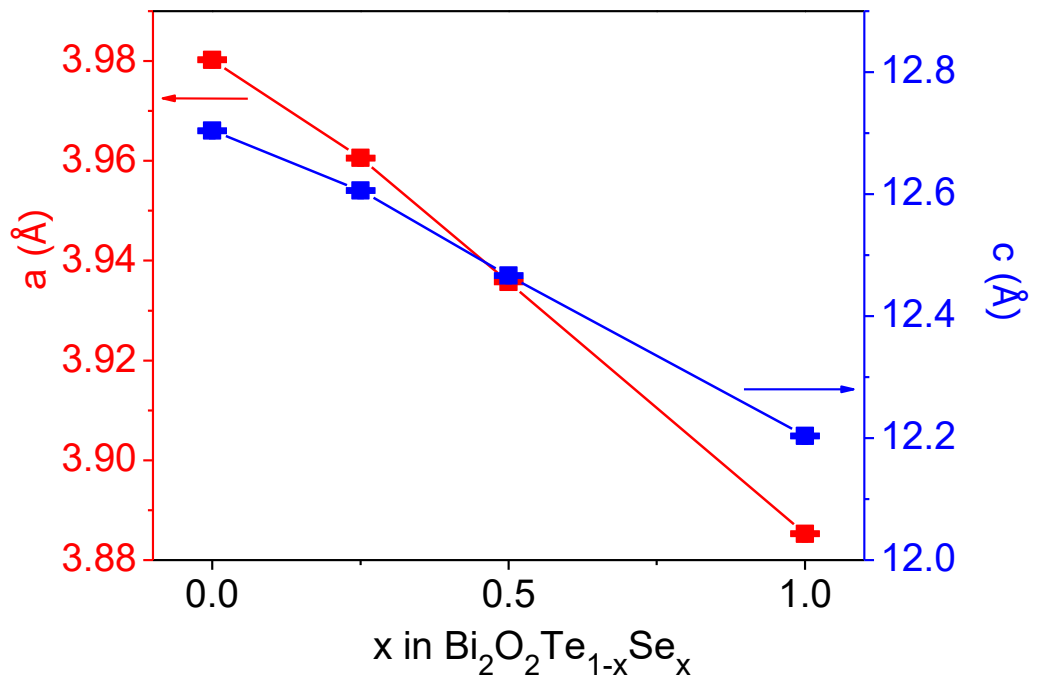


Figure 5.4. Lattice parameters of Bi₂O₂Te_{1-x}Se_x ($0 \leq x \leq 1$).

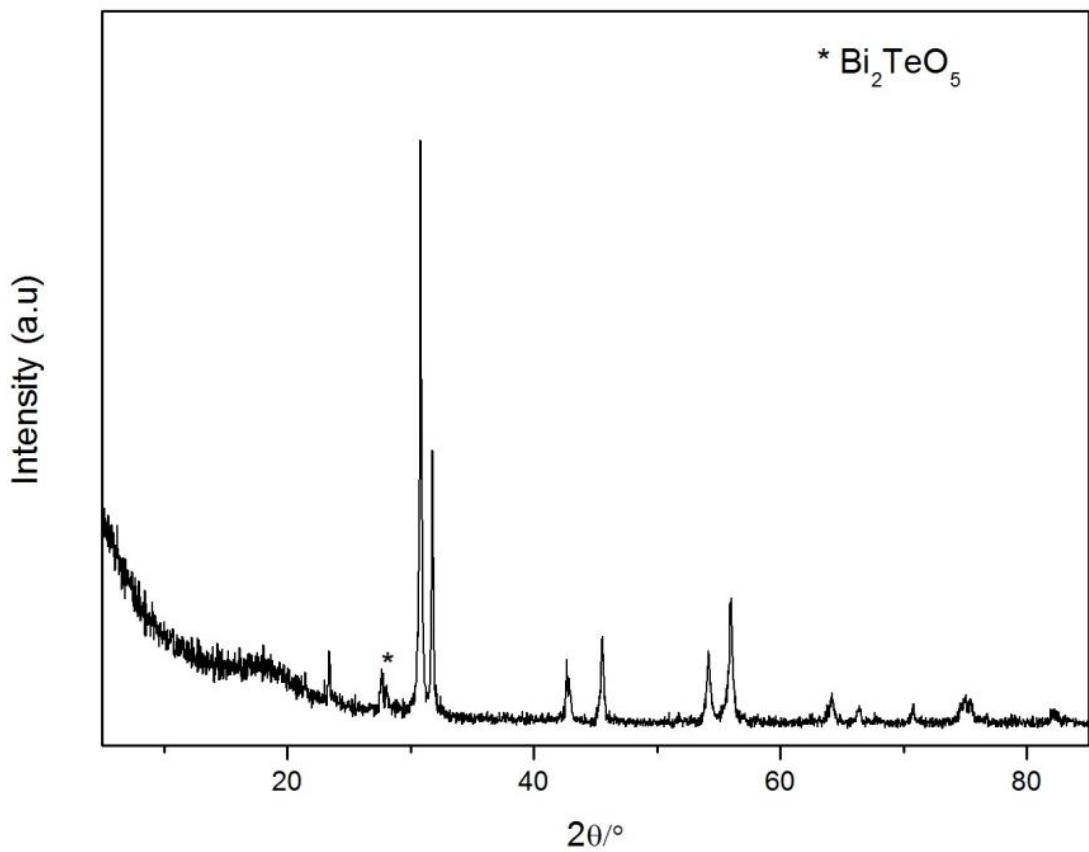


Figure 5.5. XRD pattern of hot pressed Bi₂O₂Te pellet.

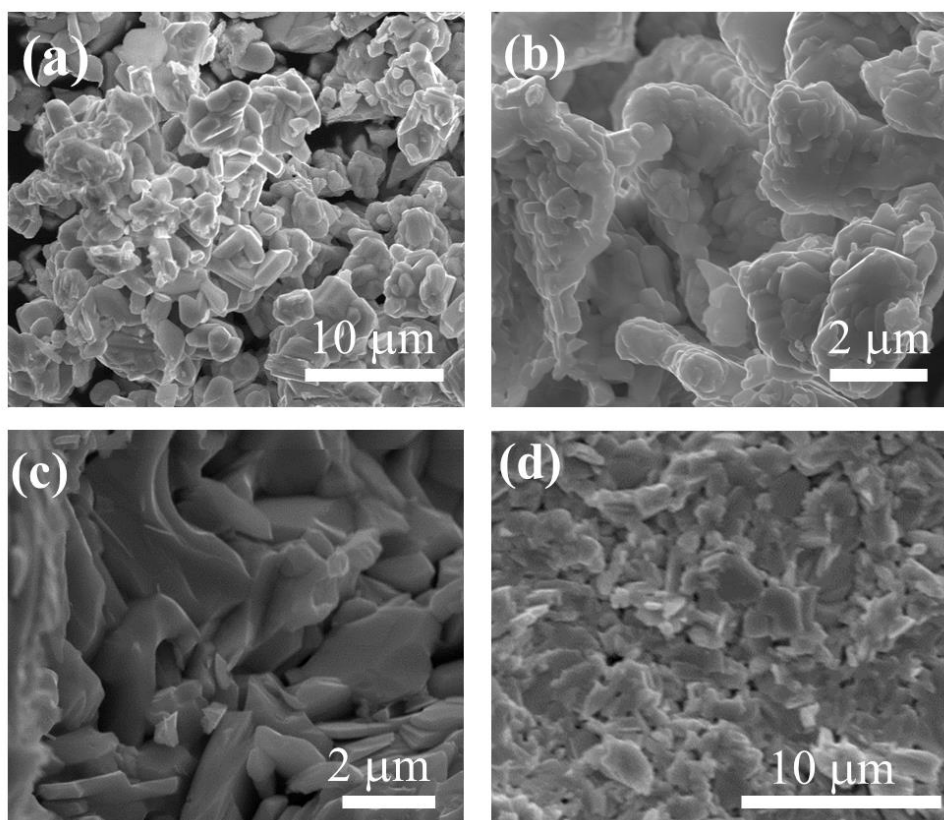


Figure 5.6. SEM micrographs of as-synthesised powders of (a) Bi₂O₂Te; (b) Bi₂O₂Se and hot-pressed sample of (c) Bi₂O₂Te; (d) Bi₂O₂Se.

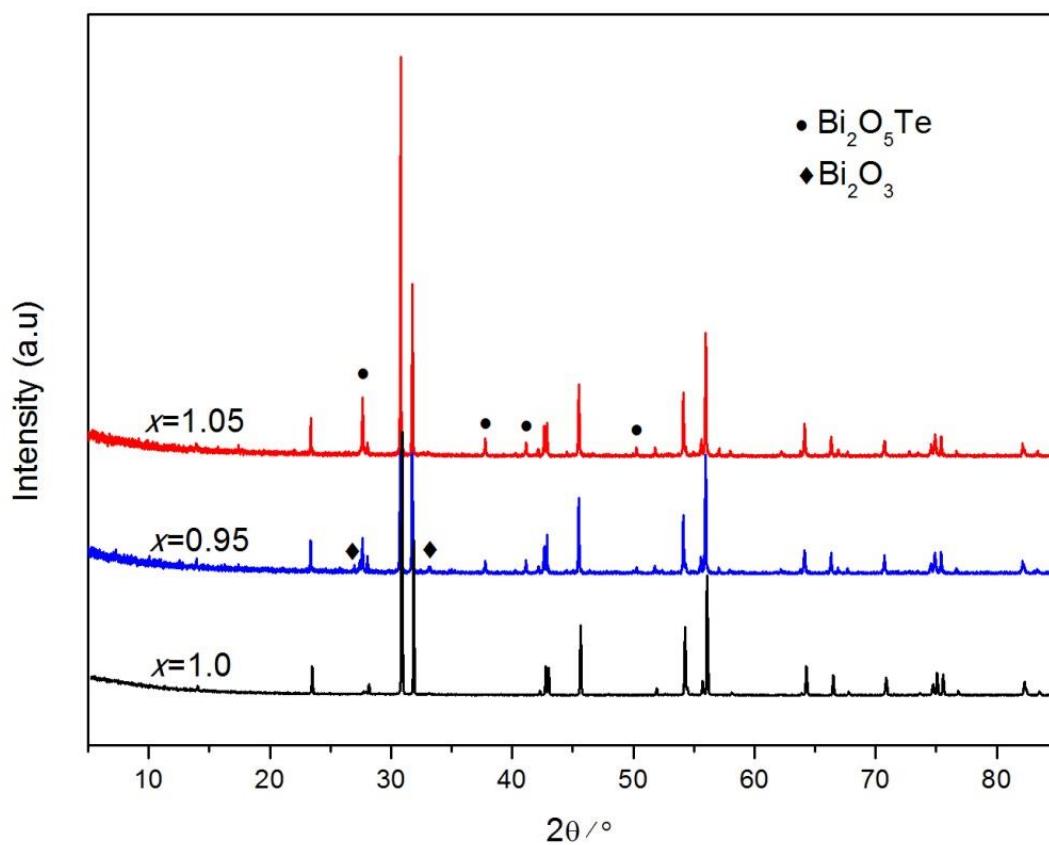


Figure 5.7. XRD patterns of Bi₂O₂Te_{1±ε} (ε = 0.05); x denotes Te content.

A representative X-ray pattern of hot pressed $\text{Bi}_2\text{O}_2\text{Te}$ sample is shown in Figure 5.5. No preferred orientation is observed. This observation is consistent with the observation that the measurement of the thermal conductivity along different directions results in identical values (Appendix C). Examination of selected as-synthesised powders and a fracture surface of a hot-pressed pellet by electron microscopy (Figure 5.6) indicates that the initial $\text{Bi}_2\text{O}_2\text{Te}$ powder contains plate-like grains with a length of *ca.* 2 μm and a thickness of *ca.* 0.2 μm , whilst the $\text{Bi}_2\text{O}_2\text{Se}$ powder contains agglomerates with different shapes and a grain size of *ca.* 0.2 - 2 μm . The hot-pressed samples show larger grain sizes.

5.3.1.2 Thermal Stability

TGA data collected on $\text{Bi}_2\text{O}_2\text{Ch}$ ($\text{Ch} = \text{Te}, \text{Se}$) under an inert atmosphere indicate that these materials are stable up to 900 K and 1000 K, respectively (Figure 5.8), which is consistent with the decomposition temperature of 893 K and 1213 K, respectively previously reported by Schmidt *et al.*[244].

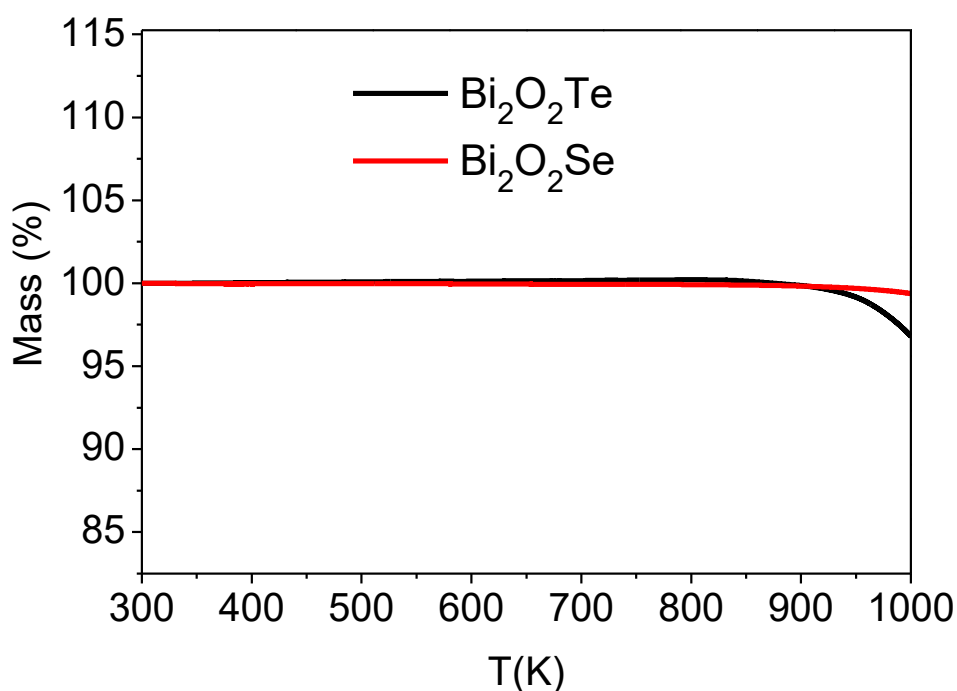


Figure 5.8. Thermogravimetric data for $\text{Bi}_2\text{O}_2\text{Ch}$ ($\text{Ch} = \text{Te}, \text{Se}$) collected under a N_2 atmosphere.

5.3.1.3 Electrical Transport Properties

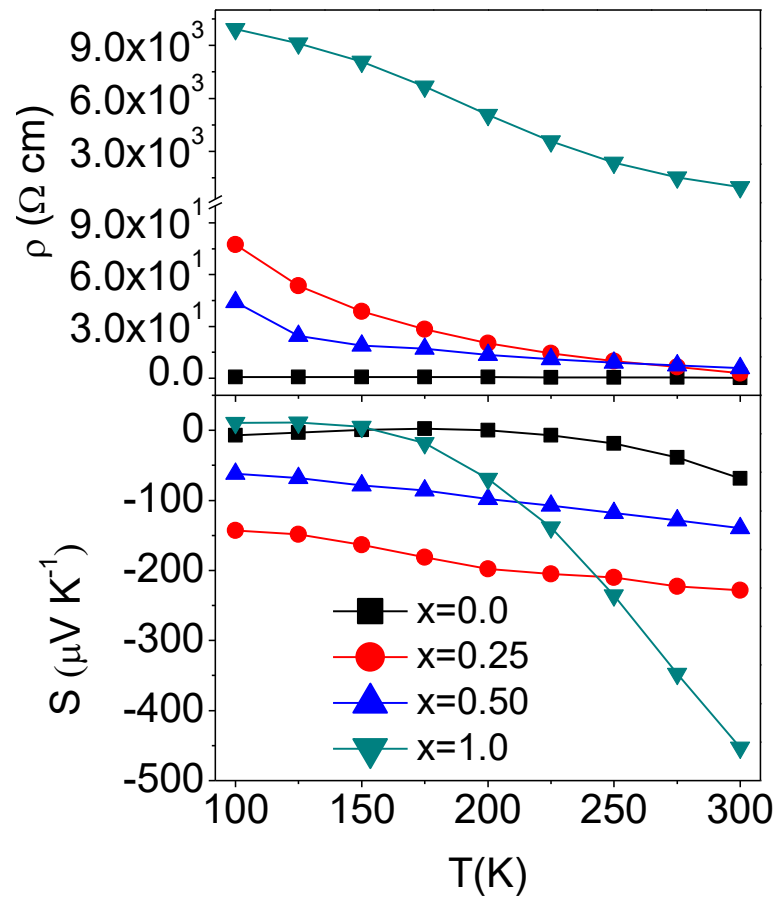


Figure 5.9. Temperature dependence of electrical resistivity (ρ); and Seebeck coefficient (S) of $\text{Bi}_2\text{O}_2\text{Te}_{1-x}\text{Se}_x$ ($0 \leq x \leq 1$) over the temperature range $100 \leq T/\text{K} \leq 300$.

Figure 5.9 presents the temperature dependence of electrical transport properties of $\text{Bi}_2\text{O}_2\text{Te}_{1-x}\text{Se}_x$ ($0 \leq x \leq 1$) over the temperature range $100 \leq T/\text{K} \leq 300$. The Seebeck coefficient of samples with $x = 0; 0.25$ and 0.5 is negative and ranges between $-229 \leq S$ ($\mu\text{V}/\text{K}$) ≤ -3 over the temperature range of $100 \leq T/\text{K} \leq 300$, indicating that these materials behave as *n*-type semiconductors. By contrast, a positive Seebeck coefficient is observed for $\text{Bi}_2\text{O}_2\text{Se}$, with a value of $\sim 10 \mu\text{V}/\text{K}$ at 100 K , decreasing to $\sim 0.7 \mu\text{V}/\text{K}$ at 157 K and turning to a negative value of $\sim -453 \mu\text{V}/\text{K}$ at 300 K . This positive value indicates that the hole charge carriers concentration is predominant in $\text{Bi}_2\text{O}_2\text{Se}$ at temperature below 160 K and decreases when temperature increases. These values differ from the results of Ruleova *et al.* [235] while a similar positive value could be observed at temperature around 70 K in C. Drasar *et al.* [236]. The discrepancy might be related to the different stoichiometry of each compound due to the fact that Se

element is volatile at temperature above 600 K. In general, the Seebeck coefficient of these Se doped samples is quite high, and around - 300 to - 430 $\mu\text{V}/\text{K}$ at room temperature. This might be related to the flat valence band edge of $\text{Bi}_2\text{O}_2\text{Se}$, where heavy hole with low mobility is found [238].

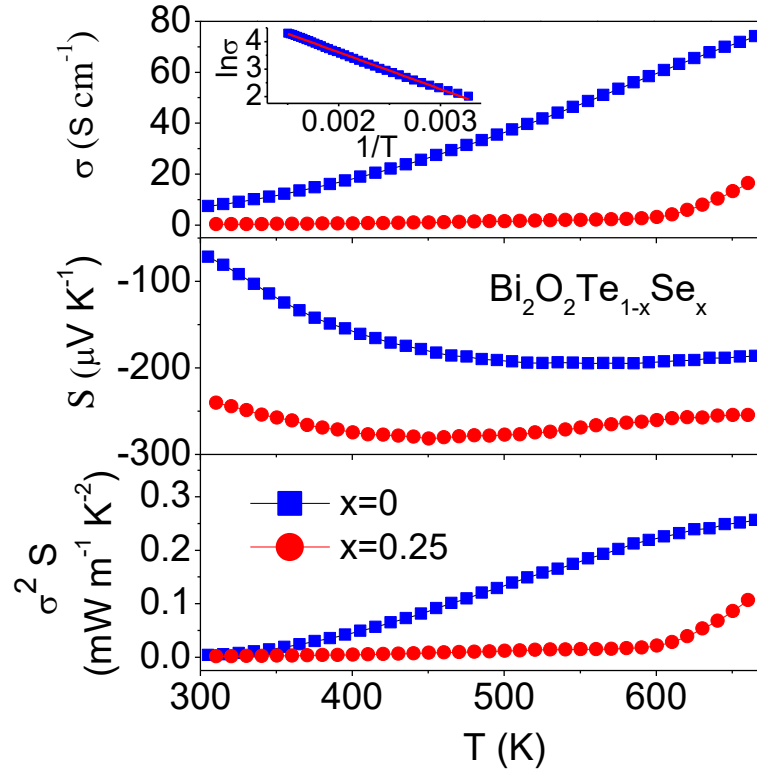


Figure 5.10. Temperature dependence of electrical properties: electrical conductivity (σ), Seebeck coefficient (S), Power factor ($\sigma^2.S$) at $300 \leq T/\text{K} \leq 665$ of $\text{Bi}_2\text{O}_2\text{Te}_{1-x}\text{Se}_x$ ($x = 0; 0.25$). The inset (top left) shows the linear line of $\ln\sigma$ vs $1/T$.

The Seebeck coefficient and electrical resistivity of $\text{Bi}_2\text{O}_2\text{Te}_{1-x}\text{Se}_x$ ($0 \leq x \leq 1$) samples as a function of temperature do not follow any trend with increasing x . In addition, the decrease in electrical resistivity in each sample is not linear with increasing temperature (Figure 5.9). A similar situation has been reported in the substitution of selenium by sulphur in $\text{BiOCuSe}_{1-x}\text{S}_x$ [189] or in the solid solution of $\text{BiOCuTe}_{1-x}\text{Se}_x$ [179]. It has not been possible to determine the activation energy of $\text{Bi}_2\text{O}_2\text{Te}_{1-x}\text{Se}_x$ sample with $x = 0.5$ and 1, as the electrical conductivity does not follow an Arrhenius law at a temperature range of $100 \leq T/\text{K} \leq 300$. The electrical conductivity of samples with $x = 0.25$ ($\text{Bi}_2\text{O}_2\text{Te}_{0.75}\text{Se}_{0.25}$) and $x = 1$ ($\text{Bi}_2\text{O}_2\text{Te}$) follows an Arrhenius law at temperatures beyond 600 K and 300 K, respectively which will be discussed later. The electrical resistivity at room temperature of $x = 0$ ($\text{Bi}_2\text{O}_2\text{Te}$) is $\sim 0.23 \Omega \text{ cm}$ while those of $x = 0.25, 0.50$ and 1.0 are $\sim 2.81; 5.71$ and $975.67 \Omega \text{ cm}$, respectively. This might be

indicative that the partial Se substitution enlarges the band gap and reduces the charge carrier concentration, similarly to findings for Se-substituted $\text{BiOCuTe}_{1-x}\text{Se}_x$ samples [179, 200]. In addition, the substitution of Te by Se has been found that it makes the thermal band gap change from 1.2 eV to 3 eV between pure Te and $\text{Te}_{0.3}\text{Se}_{0.7}$ alloy [255]. It is likely a similar situation happens here, given that the activation energy changes from 0.12 eV ($\text{Bi}_2\text{O}_2\text{Te}$) to 0.96 eV ($\text{Bi}_2\text{O}_2\text{Te}_{0.75}\text{Se}_{0.25}$) (Table 5.3).

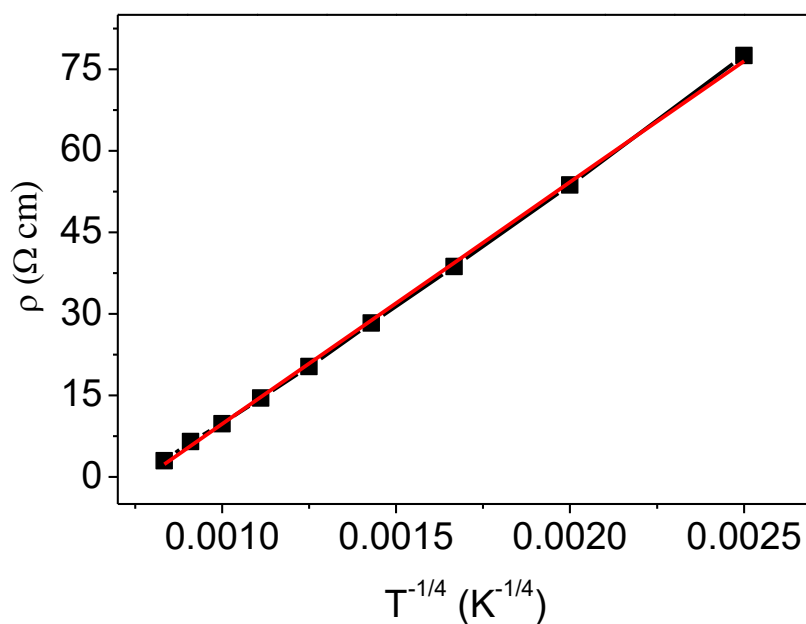


Figure 5.11. Temperature dependence of electrical resistivity (ρ) of $\text{Bi}_2\text{O}_2\text{Te}_{0.75}\text{Se}_{0.25}$.

Red line is a fit to ρ vs $T^{-1/4}$.

The electrical resistivity of $\text{Bi}_2\text{O}_2\text{Se}$ ($x = 1$) is quite high in comparison with that of other reports [235, 236]. This might be related to the different stoichiometry due to the easy volatilisation of Se at high temperature. According to the positive Seebeck coefficient observed in our sample at low temperatures, there might be mixed conduction. This might be related to narrow defects, given that the hole concentration is dominated by vacancies at low temperature. At higher temperature, more electrons become thermally activated and, then the Seebeck coefficient switches from positive to negative. A similar phenomenon could be observed in CoSb_3 , where the Sb lost during the hot-pressing process causes a change from p-type to n-type [256]. A recent report of $\text{Bi}_2\text{O}_2\text{Se}$ showing a very large Seebeck coefficient ($\sim 500\mu\text{V/K}$ at 423 K) is comparable to that of our sample although its electrical resistivity is much lower than that of our sample [257]. However, the high electrical resistivity of $\text{Bi}_2\text{O}_2\text{Se}$ is consistent with the high Seebeck coefficient value at room temperature. In addition, the carrier

compensation by lattice defects could cause this high electrical resistivity. For example, electrically insulating behaviours of n-type $\text{La}_2\text{CdO}_2\text{Se}_2$ and $\text{La}_2\text{SnO}_2\text{S}_3$ oxychalcogenides ($\rho > 10^{10} \Omega \text{ cm}$) were reported in [198] and [100].

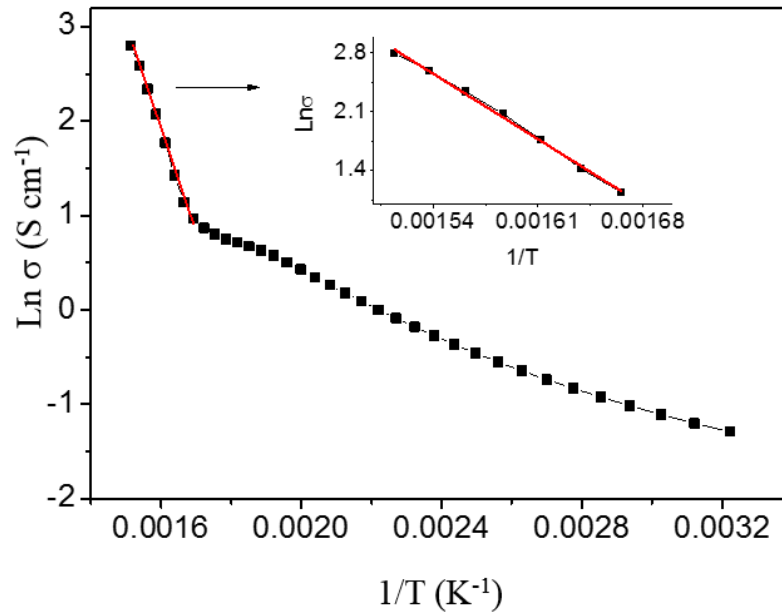


Figure 5.12. Temperature dependence of electrical conductivity (σ) of $\text{Bi}_2\text{O}_2\text{Te}_{0.75}\text{Se}_{0.25}$.

Red line is a fit to $\ln \sigma$ vs $1/T$.

It is not possible to measure the electrical resistivity or Seebeck coefficient of $\text{Bi}_2\text{O}_2\text{Te}_{1-x}\text{Se}_x$ ($0.5 \leq x \leq 1$) samples above room temperature due to their too high resistivity which is over the limit of the Linseis-LSR. Figure 5.10 shows the temperature dependence of electrical conductivity (σ), Seebeck coefficient (S) and power factor ($S^2\sigma$) of $\text{Bi}_2\text{O}_2\text{Te}_{1-x}\text{Se}_x$ ($x = 0; 0.25$). The electrical conductivity of these samples increases with increasing temperature, whilst the Seebeck coefficient maintains negative values. There is excellent agreement between the low- and high-temperature values of the Seebeck coefficient for each sample. The electrical conductivity value of $\text{Bi}_2\text{O}_2\text{Te}_{0.75}\text{Se}_{0.25}$ is one order lower than that of pristine $\text{Bi}_2\text{O}_2\text{Te}$ due to the decrease of charge carrier concentration and mobility during the substitution (Table 5.3). This is consistent with results found for $\text{Te}_{1-x}\text{Se}_x$ ($0 \leq x \leq 0.5$), where the electrical conductivity of a Se substituted sample decrease rapidly by more than two orders of magnitude when compared to pure Te [255]. This decrease is related to the band gap turning and the increase of scattering via mass fluctuation, which could be found in solid solution of $\text{BiOCuSe}_{1-x}\text{S}_x$ [189] and $\text{BiOCuTe}_{1-x}\text{Se}_x$ [179, 200]. The temperature dependence of the electrical conductivity of $\text{Bi}_2\text{O}_2\text{Te}$ sample follows an Arrhenius law at temperatures

beyond 305 K (Figure 5.10) while that of $\text{Bi}_2\text{O}_2\text{Te}_{0.75}\text{Se}_{0.25}$ does not follow this law at temperatures below 600 K (Figure 5.12).

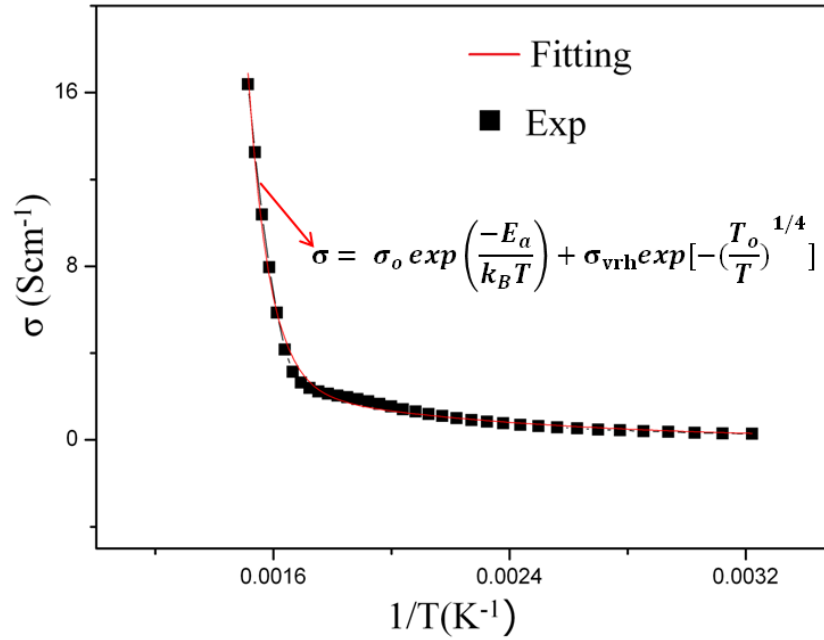


Figure 5.13. Temperature dependence of electrical conductivity (σ) of $\text{Bi}_2\text{O}_2\text{Te}_{0.75}\text{Se}_{0.25}$.

The red curve is a fit using variable range hopping model with σ_0 , σ_{vrh} and T_0 are constants.

The calculated activation energies of $\text{Bi}_2\text{O}_2\text{Te}$ and $\text{Bi}_2\text{O}_2\text{Te}_{0.75}\text{Se}_{0.25}$ are 0.12 eV at temperature range of $305 \leq T/\text{K} \leq 665$ and 0.96 eV at temperature range of $600 \leq T/\text{K} \leq 660$, respectively (Table 5.3). This indicates that the thermal excitation of charge carriers in the Se substituted sample is rather high. This consistent with results found in $\text{Te}_{1-x}\text{Se}_x$ ($0 \leq x \leq 0.5$) [255]. Moreover, J.C. Perron found that Se substitution in the $\text{Te}_{1-x}\text{Se}_x$ alloy leads to an higher hole mobility than electron mobility. In addition, short-range order with localised states in the band gap has been found in samples with increasing x [255].

At temperature range of $100 \leq T/\text{K} \leq 300$, the electrical resistivity of $\text{Bi}_2\text{O}_2\text{Te}_{0.75}\text{Se}_{0.25}$ decreases linearly as a function temperature of $1/T^{1/4}$ (Figure 5.11) while the electrical conductivity (σ) was fitted well using the combination of Arrhenius and variable range hopping (VRH) models [258] at higher temperature range of $300 < T/\text{K} < 665$ (Figure 5.13), in which σ increases with increasing temperature following below equation:

$$\sigma = \sigma_0 \exp\left(\frac{-E_a}{k_B T}\right) + \sigma_{vrh} \exp\left[-\left(\frac{T_0}{T}\right)^{1/4}\right] \quad \text{Equation (5.1)}$$

where σ_0 ($\sim 1.7 \times 10^{10} \text{ S cm}^{-1}$) is an exponential constant, k_B is the Boltzmann constant, T_0 ($\sim 4867 \text{ K}$) and σ_{vrh} ($\sim 14.98 \text{ S cm}^{-1}$) are constants.

This indicates that a localised state in the band gap with variable range hopping conduction may occur in Se-doped samples at low temperatures, below 600 K, contributing to their low electrical conductivity. Taking into account that for an intrinsic semiconductor $E_g = 2E_a$, the activation energy was used to estimate the band gap of $\text{Bi}_2\text{O}_2\text{Te}$, which is 0.23 eV (Table 5.3). This value is significantly lower than those reported for the isostructural $\text{RE}_2\text{O}_2\text{Te}$ ($E_g \sim 1.82 \text{ eV}$) [259], but comparable to that of BiOCuTe [136]. For $\text{RE}_2\text{O}_2\text{Te}$, band structure calculations indicate that the top of the valence band is dominated by contributions from the Te 5*p* and the O 2*p* states, while the bottom of the conduction band is formed by rare-earth cation states [259]. In the case of BiOCuTe , it has been found that the contribution of Bi 6*p* states to the bottom of the conduction band leads to a marked reduction in the band gap when compared with those of the rare-earth analogues [96]. A similar situation is likely to occur here.

The power factor ($S^2\sigma$) of $\text{Bi}_2\text{O}_2\text{Te}$ increases with temperature, approaching a value of $0.26 \text{ mW m}^{-1} \text{ K}^{-2}$ at 655 K, while the low electrical conductivity of $\text{Bi}_2\text{O}_2\text{Te}_{0.75}\text{Se}_{0.25}$ reduces its power factor to around zero. The values of the charge carrier concentration and mobility of $\text{Bi}_2\text{O}_2\text{Te}_{1-x}\text{Se}_x$ ($x = 0; 0.25$) at room temperature are given in Table 5.3. The charge carrier concentration of *ca.* 10^{18} cm^{-3} is relatively low for $\text{Bi}_2\text{O}_2\text{Te}$. It is even lower when Te was partly substituted by Se (*ca.* $4.5 \times 10^{17} \text{ cm}^{-3}$). For thermoelectric applications, doping would be required. The mobility of these samples compares favourably with that of undoped BiOCuTe ($\sim 9 \text{ cm}^2 \text{ V}^{-1}\text{s}^{-1}$), although it is one order of magnitude lower than that of Bi_2Te_3 [202].

Table 5.3. Charge carrier concentration (*n*), mobility (μ), electrical conductivity (σ) at room temperature, together with the activation energy (E_a) and band gap (E_g) determined over the temperature range $300 \leq T/ \text{K} \leq 665$.

x in	<i>n</i>	μ	σ	E_a	E_g
$\text{Bi}_2\text{O}_2\text{Te}_{1-x}\text{Se}_x$	(cm^{-3})	($\text{cm}^2 \text{ V}^{-1}\text{s}^{-1}$)	($\text{S}\cdot\text{cm}^{-1}$)	(eV)	(eV)
0	-1.1×10^{18}	47	7.48	0.12	0.23
0.25	-4.5×10^{17}	33	0.28	1.08	

5.3.1.4 Thermal Transport Properties and Figure of Merit ZT

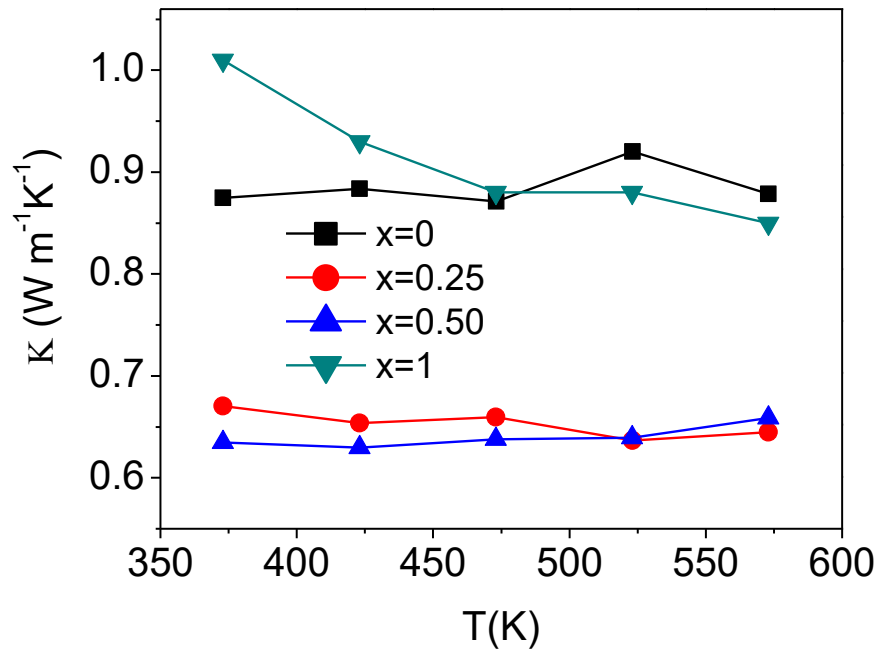


Figure 5.14. Temperature dependence of thermal conductivity of $\text{Bi}_2\text{O}_2\text{Te}_{1-x}\text{Se}_x$ ($0 \leq x \leq 0.25$) at a range of $373 \leq T/\text{K} \leq 573$.

Figure 5.14 shows the temperature dependence of the thermal conductivity (κ) of $\text{Bi}_2\text{O}_2\text{Te}_{1-x}\text{Se}_x$ ($0 \leq x \leq 1$) over the temperature range $373 \leq T/\text{K} \leq 573$. The value of thermal conductivity of $\text{Bi}_2\text{O}_2\text{Se}$ is $\sim 1 \text{ W m}^{-1} \text{ K}^{-2}$, which is consistent with that of previous report [235] while that of $\text{Bi}_2\text{O}_2\text{Te}$ is $\sim 0.91 \text{ W m}^{-1} \text{ K}^{-2}$. In the solid solution $\text{Bi}_2\text{O}_2\text{Te}_{1-x}\text{Se}_x$ ($x = 0.25$ and 0.50), the thermal conductivity is reduced to a very low value of $\sim 0.65 \text{ W m}^{-1} \text{ K}^{-2}$, which corresponds to the behaviour expected for a phonon glass material [136]. It seems likely that the reduction of the thermal conductivity of Se substituted samples might be the result of the increased phonon scattering due to mass fluctuations [260]. A similar trend could be found in the $\text{BiOCuSe}_{1-x}\text{S}_x$ solid solution [189]. When Te is completely replaced by Se, the lattice thermal conduction increases, following the normal trend of increasing thermal conductivity with decreasing atomic mass. In addition, the very high electrical resistivity of $\text{Bi}_2\text{O}_2\text{Se}$ indicates that the contribution of the electronic thermal conductivity of this sample is negligible.

Figure 5.15 shows the temperature dependence of the lattice and electronic thermal conductivity of $\text{Bi}_2\text{O}_2\text{Te}$ over the temperature range $300 \leq T/\text{K} \leq 573$. The contribution of electronic (κ_e) and lattice (κ_{lat}) thermal conductivity were estimated using the

electrical conductivity data in conjunction with Wiedemann-Franz law, using a Lorenz constant of $2.45 \times 10^{-8} \text{ W } \Omega \text{ K}^{-2}$. The lattice contribution is predominant, whilst the electronic contribution is only 0.61% of κ_{tot} at room temperature and increases to 8.5% at 573 K. In general, the thermal conductivity of the solid solution $\text{Bi}_2\text{O}_2\text{Te}_{1-x}\text{Se}_x$ ($0 \leq x \leq 1$) is significantly lower than that of Bi_2Te_3 ($\sim 2 \text{ W m}^{-1} \text{ K}^{-2}$) [202]. This might be related to the two-dimensional nature of this structure, which leads to the scattering of phonons at the interfaces between the oxide and the chalcogenide layers, as previously proposed for BiOCuQ [51]. It has also been suggested that in compounds containing cations with lone pairs, such as Sb^{3+} or Bi^{3+} , the anharmonicity of the bonds may lead to lattice thermal conductivities near the amorphous limit [261]. The very low power factor of $\text{Bi}_2\text{O}_2\text{Te}_{0.75}\text{Se}_{0.25}$ sample causes in the negligible thermoelectric figure of merit at temperatures below 600 K. Therefore, Figure 5.15 presents the thermoelectric figure of merit of $\text{Bi}_2\text{O}_2\text{Te}$ as a function of temperature only. It increases with increasing temperature and reaches a value of 0.13 at 573 K. Extrapolation of the thermal conductivity to 665 K leads to an estimated value of $ZT \sim 0.2$ which is significantly higher than that of $\text{Bi}_2\text{O}_2\text{Te}_{0.75}\text{Se}_{0.25}$ sample at the same temperature ($ZT \sim 0.1$). There is still room to improve the electrical properties of the pristine material by optimising the charge carrier concentration via electron donor doping [201].

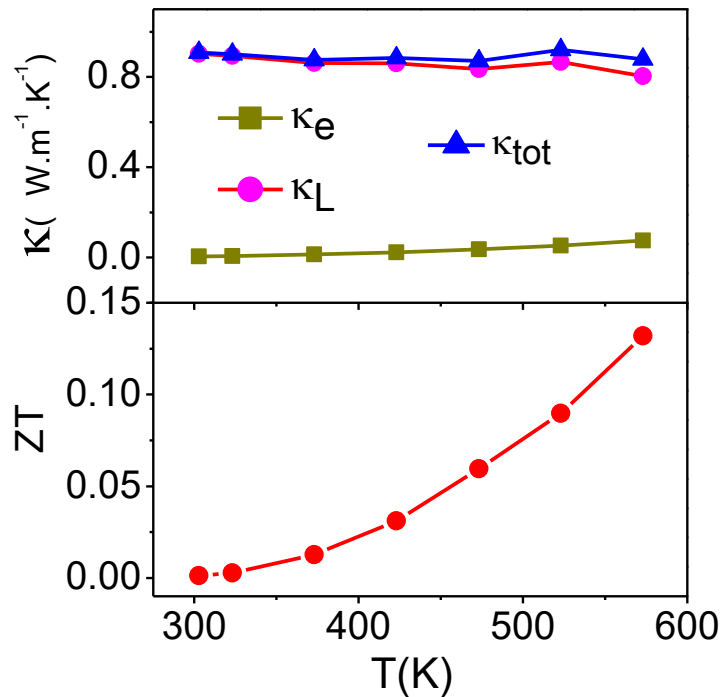


Figure 5.15. Temperature dependence of thermal conductivity and figure of merit of $\text{Bi}_2\text{O}_2\text{Te}$ over the range $300 \leq T/\text{K} \leq 573$.

5.3.2 $\text{Bi}_2\text{O}_2\text{Se}_{1\pm\delta}$ ($0.05 \leq \delta \leq 0.15$) Compounds

5.3.2.1 Structural and Morphological Characterisation

Powder X-ray diffraction data collected on as-prepared samples of $\text{Bi}_2\text{O}_2\text{Se}_{1\pm\delta}$ ($0.05 \leq \delta \leq 0.15$) is shown in Figure 5.16. A representative Rietveld refinement of $\text{Bi}_2\text{O}_2\text{Se}_{0.95}$ is presented in Figure 5.17 while those of other compounds are shown in Appendix C. A trace of very small amount of Bi_2O_3 is found in $\text{Bi}_2\text{O}_2\text{Se}_{0.95}$ sample while a small amount of Bi_2O_3 and Se is found in $\text{Bi}_2\text{O}_2\text{Se}_{1.15}$ sample.

Refined parameters are presented in Table 5.4 while selected distances and angles of X-ray diffraction data of samples is presented in Appendix C. In all cases, a good agreement between experimental and calculated patterns is obtained with reasonable values of R_{wp} . The coordination of each atom in the structure of non-stoichiometric samples is similar to that of the pristine $\text{Bi}_2\text{O}_2\text{Se}$, in which O is tetrahedrally coordinated by Bi atoms while the Se anions form a square array.

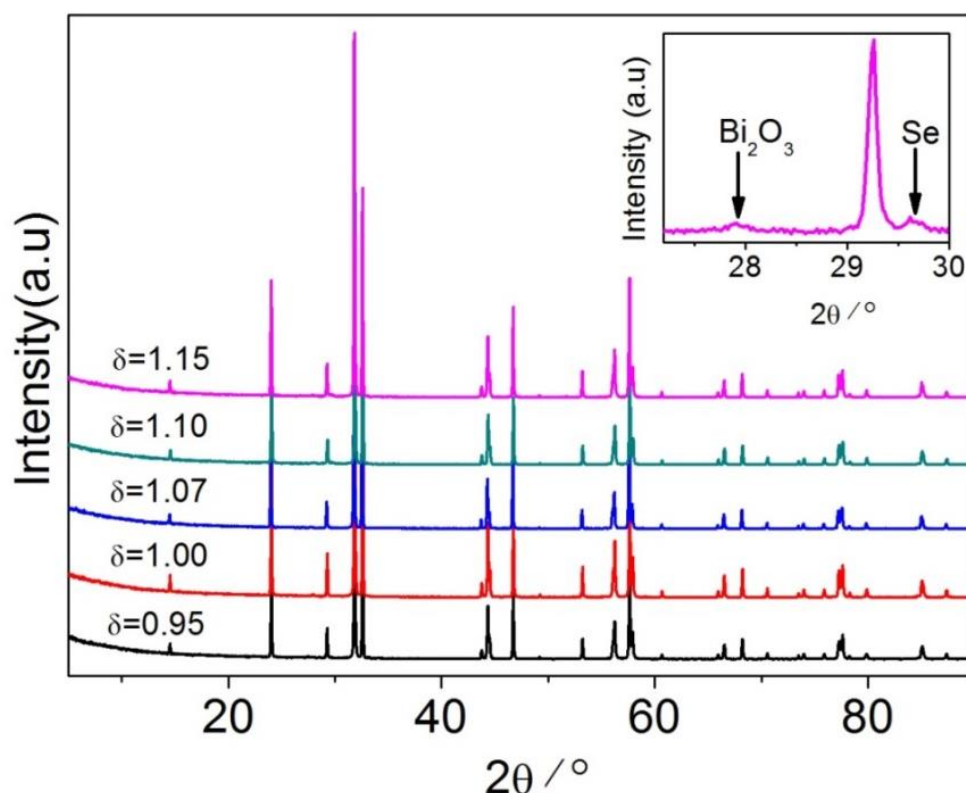


Figure 5.16. Powder X-ray diffraction patterns of $\text{Bi}_2\text{O}_2\text{Se}_{1\pm\delta}$ ($0.05 \leq \delta \leq 0.15$). The inset shows the highest intensity peak of Bi_2O_3 and Se impurity, marked by arrows.

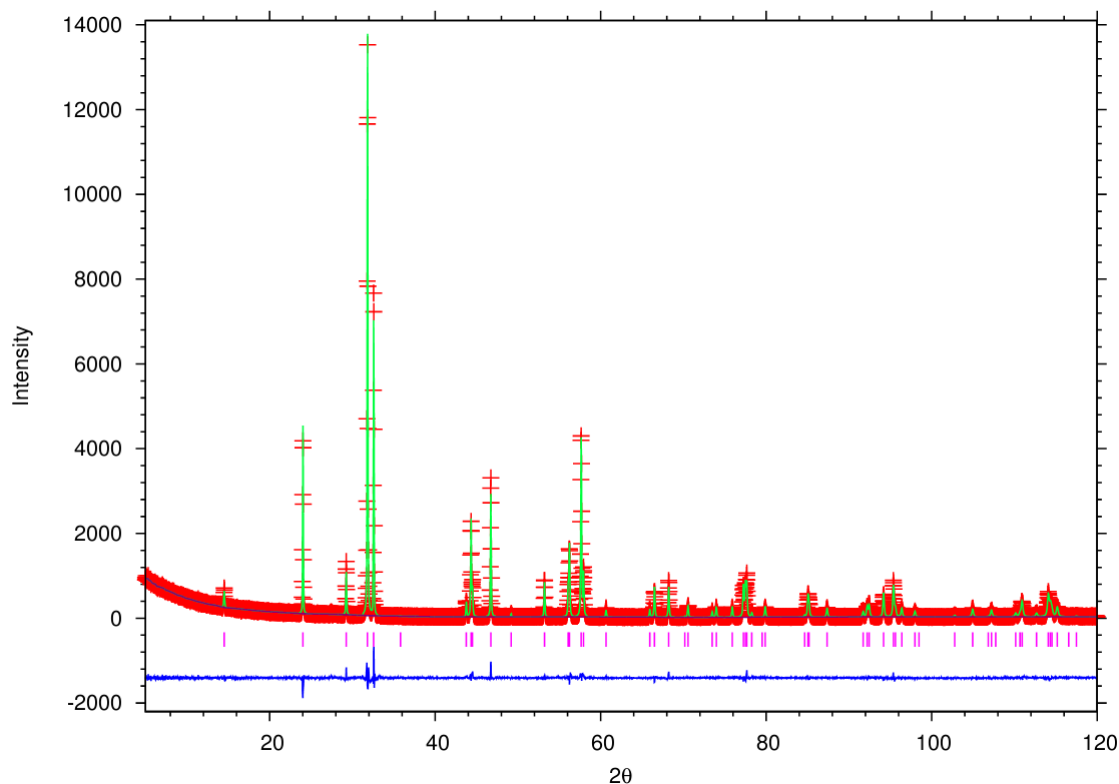


Figure 5.17. Rietveld refinement using powder X-ray diffraction data for $\text{Bi}_2\text{O}_2\text{Se}_{0.95}$. Key: observed data (red cross); difference curve (blue line); calculated pattern (green line) and reflection positions of $\text{Bi}_2\text{O}_2\text{Se}_{0.95}$ (pink markers).

The lattice parameters of non-stoichiometric compounds change little (Figure 5.18), suggesting that the deficiency or excess of selenium does not affect significantly the structure of $\text{Bi}_2\text{O}_2\text{Se}$. However, the loss of Se due to its volatility during reactions or Se remaining as an amorphous mixture should also be considered, given that a large Se excess has been added ($> 10\%$ *a.t.w*). The bond length of Bi-Bi and Bi-O increase slightly while that of Bi-Se does not change manifestly when increasing the Se content (Figure 5.19). This suggests there might be small amount of Se occupying lattice defects. The bond angle of Bi-O-Bi increases slightly when increasing the Se content, indicating that structure is slightly stretched along the a axis.

Figure 5.20 presents SEM images of selected powders and pellets of the $\text{Bi}_2\text{O}_2\text{Se}_{1\pm\delta}$ samples. The $\text{Bi}_2\text{O}_2\text{Se}_{0.95}$ powder forms agglomerates with different shapes and grain sizes of *ca.* 0.5 - 5 μm . The hot-pressed samples contain plate-like grains with a length of *ca.* 4 μm and a thickness of *ca.* 0.2 μm .

Table 5.4. Final refined parameters for $\text{Bi}_2\text{O}_2\text{Se}_{1\pm\delta}$ ($0.05 \leq \delta \leq 0.15$).

		$I \pm \delta$ in $\text{Bi}_2\text{O}_2\text{Se}_{I \pm \delta}$		
		0.95	1.00	1.07
$a/\text{Å}$		3.88484(3)	3.88528(5)	3.88463(5)
$c/\text{Å}$		12.20397(1)	12.20344(2)	12.20363(2)
Bi ^a	z	0.35341(6)	0.35361(6)	0.35362(6)
	$U_{\text{iso}}/\text{Å}^2$	0.0021(2)	0.0005(2)	0.0002(2)
O ^b	$U_{\text{iso}}/\text{Å}^2$	0.0064(4)	0.0017(3)	0.0016(3)
Se ^c	$U_{\text{iso}}/\text{Å}^2$	0.0005(7)	0.0043(7)	0.0033(7)
$R_{\text{wp}}/\%$		10.76	11.16	10.95
		$I \pm \delta$ in $\text{Bi}_2\text{O}_2\text{Se}_{I \pm \delta}$		
		1.10	1.15	
$a/\text{Å}$		3.88554(3)	3.88501(3)	
$c/\text{Å}$		12.2034(1)	12.2024(1)	
Bi ^a	z	0.35362(6)	0.35375(6)	
	$U_{\text{iso}}/\text{Å}^2$	0.0002(2)	0.0047(2)	
O ^b	$U_{\text{iso}}/\text{Å}^2$	0.0016(3)	0.0009(3)	
Se ^c	$U_{\text{iso}}/\text{Å}^2$	0.0033(7)	0.0211(8)	
$R_{\text{wp}}/\%$		11.67	11.60	

^aBi on 4(*d*) (0, 0, *z*); ^bO on 4(*e*) (1/2, 0, 1/4); ^cSe on 2(*a*) (0, 0, 0)

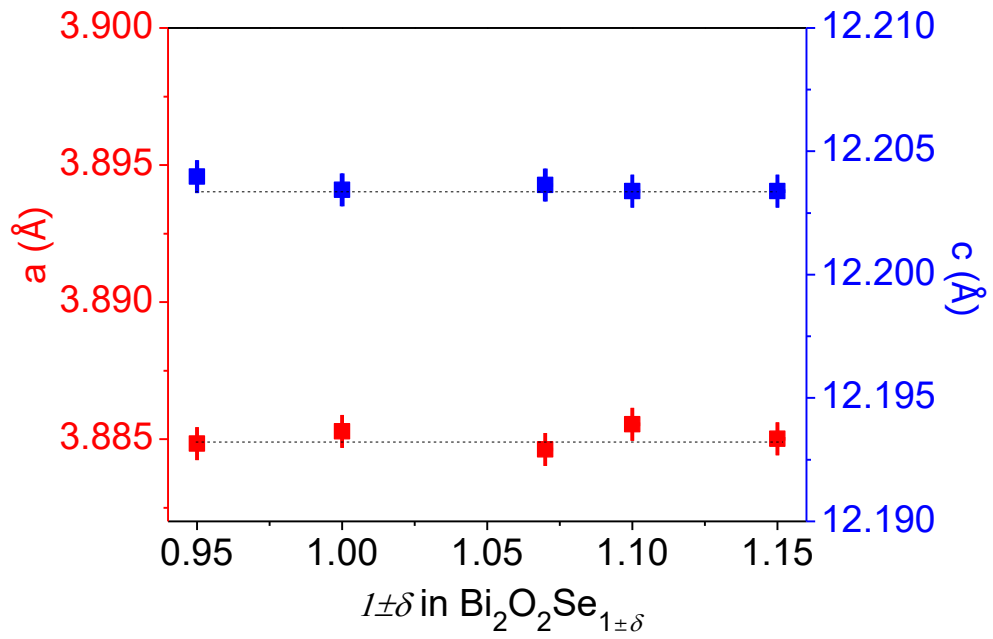


Figure 5.18. Lattice parameters of $\text{Bi}_2\text{O}_2\text{Se}_{1\pm\delta}$ samples.

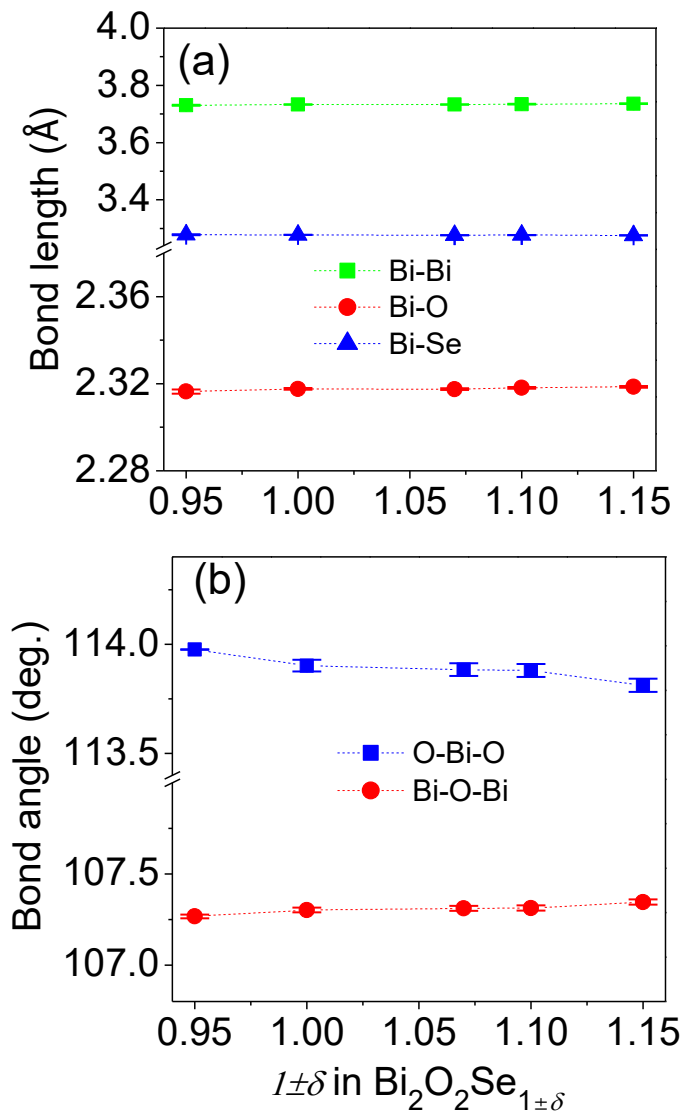


Figure 5.19. Selected bond lengths and angles of $\text{Bi}_2\text{O}_2\text{Se}_{1\pm\delta}$ ($0.05 \leq \delta \leq 0.15$).

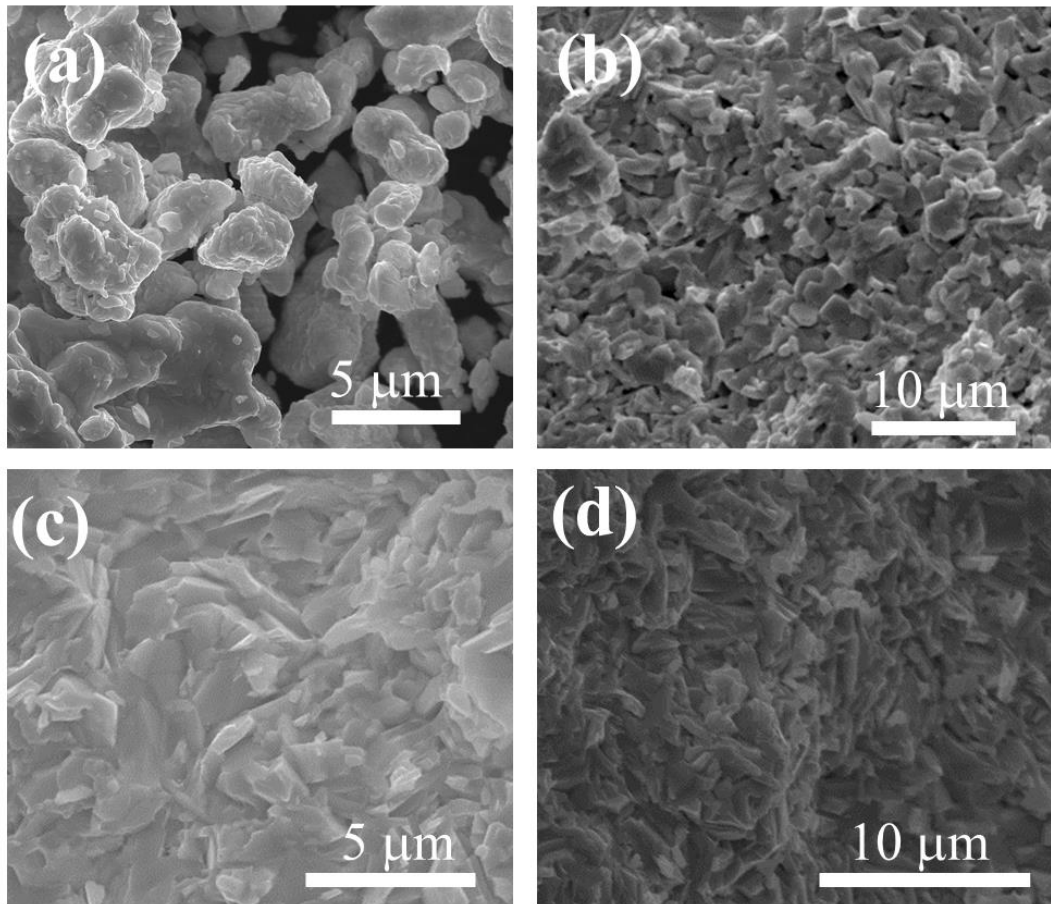


Figure 5.20. SEM images of powder (a) and pellet (b) of $\text{Bi}_2\text{O}_2\text{Se}_{0.95}$; pellet of (c): $\text{Bi}_2\text{O}_2\text{Se}_{1.07}$ and (d): $\text{Bi}_2\text{O}_2\text{Se}_{1.15}$.

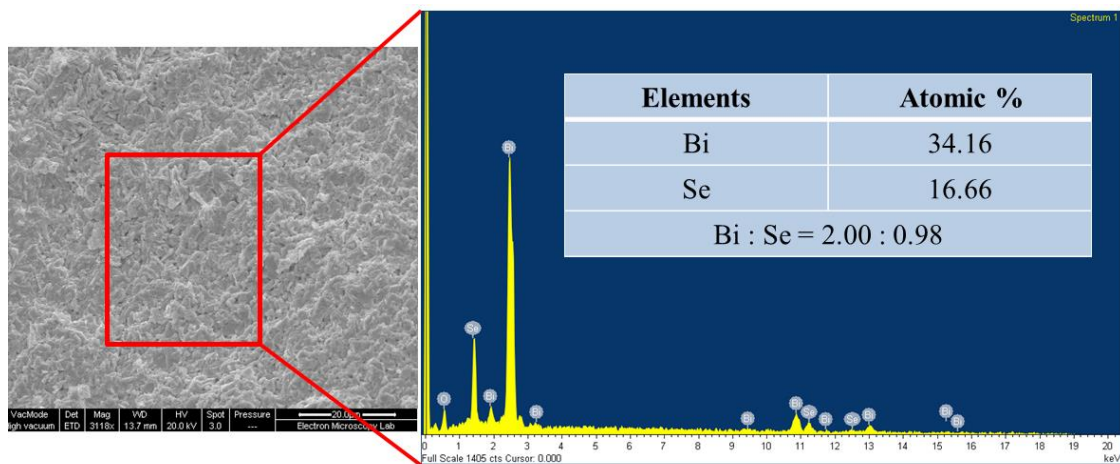


Figure 5.21. EDAX spectrum of prepared $\text{Bi}_2\text{O}_2\text{Se}$ pellet.

The EDAX spectrum and quantitative element percentages for the $\text{Bi}_2\text{O}_2\text{Se}$ pellet are shown in Figure 5.21 while those of other samples are presented in Appendix C. It is clear that $\text{Bi}_2\text{O}_2\text{Se}$ contains only Bi, O, Se elements. The ratio of atomic percent of Bi

and Se is $\sim 2 : 1$. It should be taken into account that the adsorption of oxygen on the surface of samples or instrumental errors with the light mass oxygen can cause a significant error in quantitative EDAX measurements [237]. It should be noted that EDAX is a semiquantitative technique, and therefore, the use of inductively coupled plasma (ICP) technique may be required for the quantitative analysis of this sample.

5.3.2.2 Electrical Transport Properties

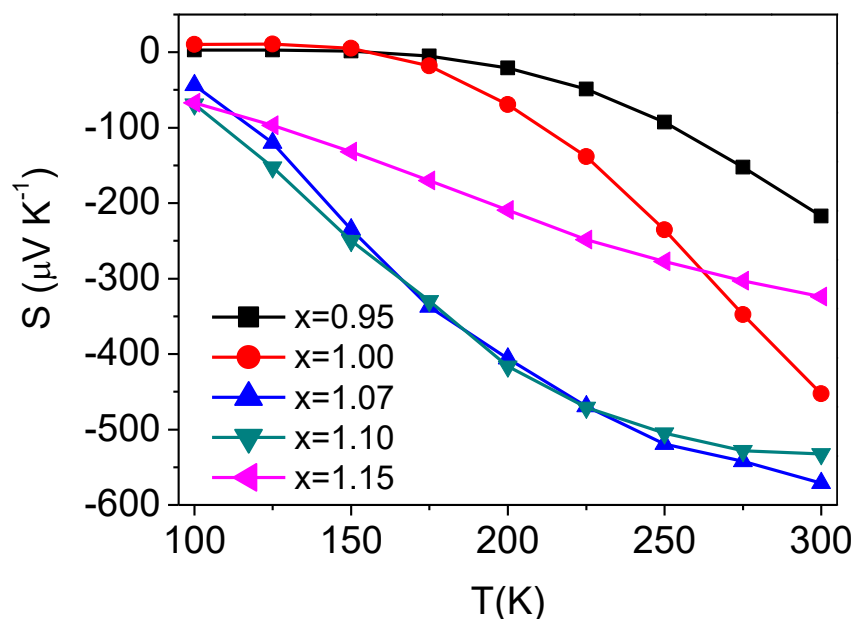


Figure 5.22. Temperature dependence of Seebeck coefficient (S) of $\text{Bi}_2\text{O}_2\text{Se}_{1\pm\delta}$ ($0.05 \leq \delta \leq 0.15$) over the temperature range $100 \leq T/\text{K} \leq 300$; x denotes Se content.

Figure 5.22 shows the temperature dependence of the Seebeck coefficient of $\text{Bi}_2\text{O}_2\text{Se}_{1\pm\delta}$ ($0.05 \leq \delta \leq 0.15$) samples over the temperature range $100 \leq T/\text{K} \leq 300$. The Seebeck coefficient of $\text{Bi}_2\text{O}_2\text{Se}_{0.95}$ and $\text{Bi}_2\text{O}_2\text{Se}$ is positive below 150 K, with a value of ~ 3 and $\sim 10 \mu\text{V}/\text{K}$ at 100 K, respectively. These values decrease and shift to negative values at higher temperatures. At 300 K, the Seebeck coefficients of these materials are ~ -217 and $\sim -453 \mu\text{V}/\text{K}$, respectively. The positive value of the Seebeck coefficient below 150 K indicates that mixed conduction exists in these samples. In contrast, negative Seebeck coefficients are observed in Se rich $\text{Bi}_2\text{O}_2\text{Se}_{1\pm\delta}$ samples with values between ~ -44 and $\sim -69 \mu\text{V}/\text{K}$ at 100 K. At higher temperature, they decrease to values between ~ -321 and $\sim -571 \mu\text{V}/\text{K}$ at 300 K. The lack of a systematic trend with changing Se content might be related to changes in the actual composition of each compound, due to

the fact that Se is volatile at temperatures above 600 K, while our hot press temperature is 823 K. It has been previously reported, in the case of sulphides (for instance, TiS_2 and NiCr_2S_4), that the properties are highly dependent on the chalcogen content, which is in turn affected by the processing method [262, 263]. In general, the Seebeck coefficient of $\text{Bi}_2\text{O}_2\text{Se}_{1\pm\delta}$ ($0.05 \leq \delta \leq 0.15$) samples is quite high (~ -217 to $-571 \mu\text{V}/\text{K}$) at room temperature which is consistent with their high electrical resistivity.

The electrical resistivity of the $\text{Bi}_2\text{O}_2\text{Se}_{1\pm\delta}$ ($0.05 \leq \delta \leq 0.15$) samples over the temperature range $100 \leq T/\text{K} \leq 300$ is shown in Figure 5.23. The electrical resistivity of $\text{Bi}_2\text{O}_2\text{Se}_{0.95}$ sample is very high, $\sim 4 \text{ K}\Omega \text{ cm}$ at room temperature, behaving as an insulator. Combined with the positive Seebeck coefficient observed at low temperature region of $100 \leq T/\text{K} \leq 150$, this indicates that the mixed charge carriers in this material may cause a very high electrical resistivity, given that charge compensation occurs when temperature increases [265]. The electrical resistivity reduces significantly in Se rich samples. This might be related to the increase in electron charge carrier concentration when negative Seebeck coefficients are observed (Figure 5.22). However, the decrease of electrical resistivity as a function of temperature in these samples does not follow an Arrhenius law (Figure 5.24).

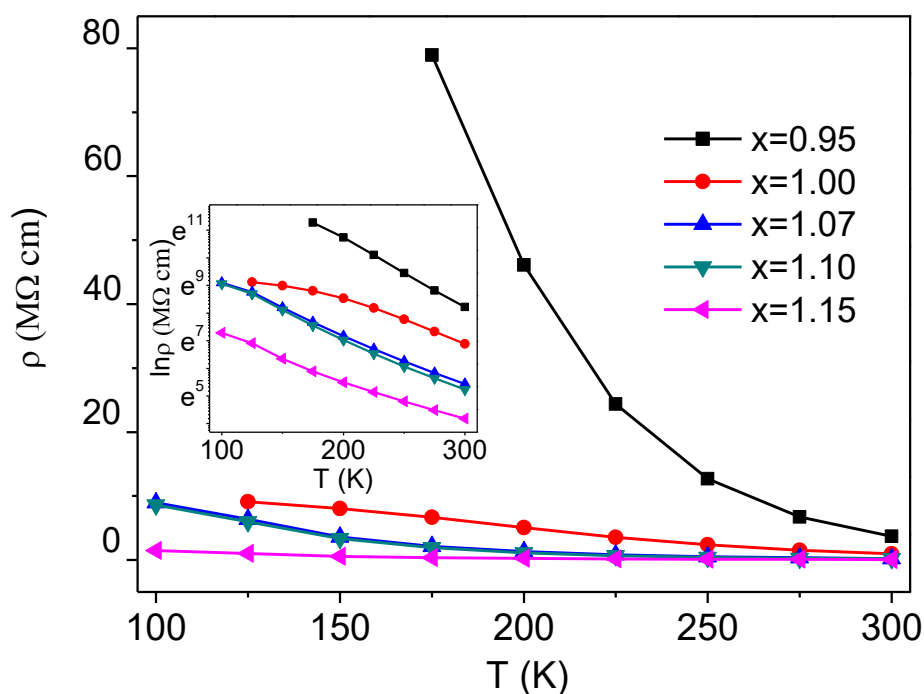


Figure 5.23. Temperature dependence of electrical resistivity (ρ) of $\text{Bi}_2\text{O}_2\text{Se}_{1\pm\delta}$ ($0.05 \leq \delta \leq 0.15$) over the temperature range $100 \leq T/\text{K} \leq 300$.

At room temperature, the lowest electrical resistivity of $\sim 65 \text{ } \Omega \text{ cm}$ is obtained for $\text{Bi}_2\text{O}_2\text{Se}_{1.15}$ sample although this is still two orders of magnitude higher than that reported in the literature [235]. This discrepancy is not well understood. However, it should be noted that the XRD pattern of sample in [235] shows a clear impurity with additional peaks. It is difficult to determine the nature of the impurity without the original X-ray pattern raw file of [235]. Therefore, this discrepancy might be related to the presence of impurities. It should be taken into account that different stoichiometries might also occur here, given that hot-pressing or SPS could cause changes in stoichiometry or reduction, because the graphite in the die is a reducing agent at high temperature [194]. In fact, mixed charge conduction is observed in Se deficient samples. In general, the room temperature electrical resistivity of $\text{Bi}_2\text{O}_2\text{Se}_{1\pm\delta}$ is high but still comparable to other oxychalcogenide layer structures such as $\text{La}_2\text{O}_2\text{FeSe}_2$ ($\sim 10^2 \text{ } \Omega\text{cm}$) [76, 264], and much lower than that of $\text{La}_2\text{O}_2\text{CdSe}_2$ ($> 10^{10} \text{ } \Omega \text{ cm}$) [100].

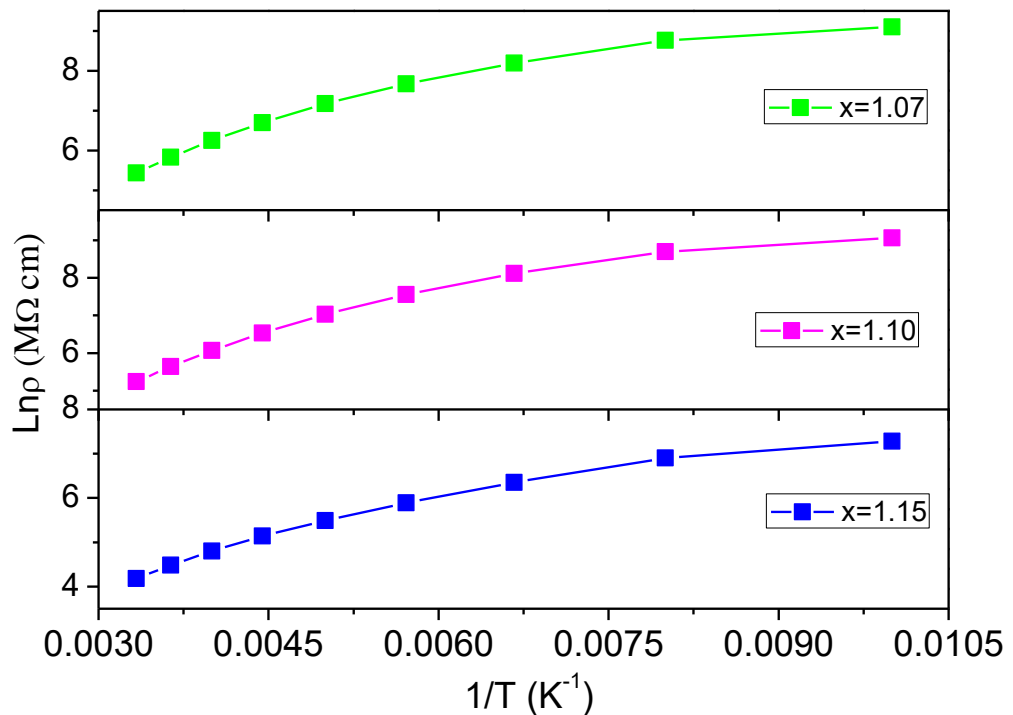


Figure 5.24. Temperature dependence of electrical resistivity (ρ): $\text{Ln } \rho$ vs $1/T$ of $\text{Bi}_2\text{O}_2\text{Se}_{1\pm\delta}$ ($0.05 \leq \delta \leq 0.15$) over the temperature range $100 \leq T/\text{K} \leq 300$.

5.3.2.3 Thermal Transport Properties

Figure 5.25 shows the temperature dependence of the thermal conductivity (κ) of $\text{Bi}_2\text{O}_2\text{Se}_{1\pm\delta}$ ($0.05 \leq \delta \leq 0.15$) over the temperature range $373 \leq T/\text{K} \leq 673$. It does not

follow a systematic trend with increasing Se content. The $\text{Bi}_2\text{O}_2\text{Se}$ sample possesses the lowest thermal conductivity with a value of $\sim 1 \text{ W m}^{-1} \text{ K}^{-2}$ at 373 K and decreases to $\sim 0.8 \text{ W m}^{-1} \text{ K}^{-2}$ at 673 K, which is much lower than that of Bi_2Te_3 [202]. $\text{Bi}_2\text{O}_2\text{Se}_{0.95}$ shows a higher thermal conductivity than that of $\text{Bi}_2\text{O}_2\text{Se}$ ($\sim 1.06 \text{ W m}^{-1} \text{ K}^{-2}$ at 373 K). This high thermal conductivity might be related to its mixed charge carriers where both of these charge carriers contribute to the thermal conduction of material [11, 265]. It might be also caused by the slight difference of density in their hot pressed pellets, given that $\text{Bi}_2\text{O}_2\text{Se}$ ($\sim 90\%$ of theoretical density) and $\text{Bi}_2\text{O}_2\text{Se}_{0.95}$ ($\sim 92\%$ of theoretical density). Increasing Se content of $\text{Bi}_2\text{O}_2\text{Se}_{1\pm\delta}$ ($0.07 \leq \delta \leq 0.15$) leads to an increase of thermal conductivity. This might be related to the reduction of point defects in the Se rich sample, leading to a decrease of point defect scattering [189]. The estimation of lattice contribution to total thermal conductivity of these materials is $\sim 99.99\%$ at room temperature. The electronic contribution to total thermal conductivity increases with increasing Se content. However, this contribution is too low ($\sim 0.001\%$ of κ) to make the clear change in these samples given that they are too electrically resistive.

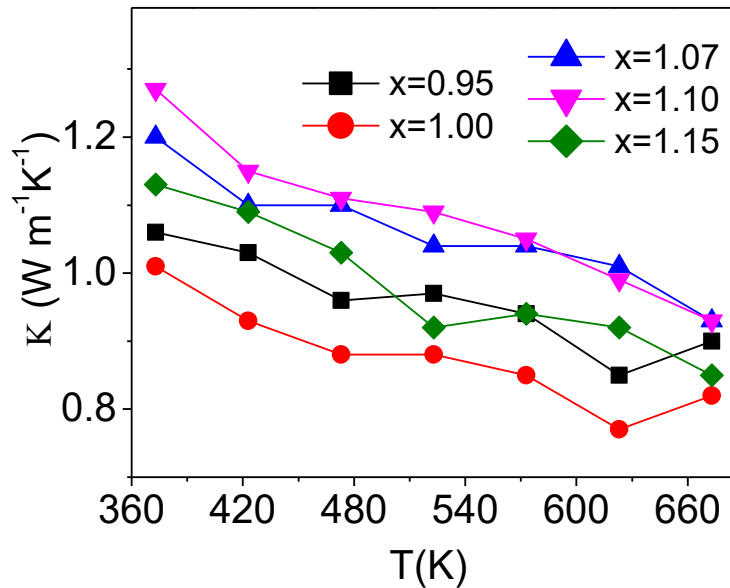


Figure 5.25. Temperature dependence of thermal conductivity (κ) of $\text{Bi}_2\text{O}_2\text{Se}_\delta$ ($0.95 \leq \delta \leq 1.15$) over the temperature range $373 \leq T/\text{K} \leq 673$.

The lower thermal conductivity of $\text{Bi}_2\text{O}_2\text{Se}_{1.15}$ than those of $\text{Bi}_2\text{O}_2\text{Se}_{1.07}$ and $\text{Bi}_2\text{O}_2\text{Se}_{1.10}$ might be related to the presence of an impurity of Se. This might be also caused by the lower density of hot pressed sample ($\sim 90\%$ theoretical density) in comparison with those of $\text{Bi}_2\text{O}_2\text{Se}_{1.07}$ ($\sim 92\%$) and $\text{Bi}_2\text{O}_2\text{Se}_{1.10}$ ($\sim 92\%$). It is impossible to obtain high

temperature values of electrical resistivity, because the magnitudes of these values are above the measurable range of the Linseis-LSR. Therefore, the quantitative calculation of lattice and electronic contribution into total thermal conductivity as a function of temperature has not been carried out. However, it should be highlighted that further investigations such as measuring their elastic properties might explain the origin of its thermal conductivity, which was described in other layered materials with very low thermal conductivities, such as SnSe and BiOCuSe [66,170]. A similar low lattice thermal conductivity ($\sim 0.5 \text{ W m}^{-1} \text{ K}^{-2}$) has been also found in the layered structure of AgCrSe₂, where a chalcogenide layer [CrSe₂]⁻ alternates with cation Ag⁺ layer [266].

Chapter 6 Conclusions

This chapter summarises all conclusions of the research carried out in this dissertation. Further works are proposed as well.

6.1 BiOCuCh ($Ch = S, Se, Te$) and Effect of Divalent Cation Doping on BiOCuSe

Neutron diffraction analysis shows that the atomic displacement parameter (ADP) for copper is significantly larger and increases more rapidly than that for other atoms in BiOCuCh ($Ch = S, Se, Te$). This shows a similar behaviour to that previously found for “rattler” atoms in skutterudite and clathrate structures [267]. The large ADP of the copper atom is related to a low frequency vibrational mode, which can reduce the thermal conductivity via scattering of heat carrying phonons. Therefore, this reveals that BiOCuCh behaves like a PGEC material in which the thermal conductivity is extremely low and electrical conductivity is very high by modifying the charge carrier concentration.

The work done so far demonstrates that the thermoelectric figure of merit of BiOCuCh ($Ch = S, Se, Te$) is improved with a change of mean atomic weight of chalcogenide element from sulphur to tellurium. Although BiOCuTe is more promising for thermoelectric applications, as discussed in Chapter 1, Te is a scarce element, very expensive. This is a big obstacle and alternative approaches have been considered. When BiOCuSe and BiOCuS are compared, BiOCuSe possesses better thermoelectric properties in terms of its electrical and thermal conductivity than those of BiOCuS. Therefore, BiOCuSe is really a promising thermoelectric material, with potential for optimising the electrical and thermal conductivities via doping or nanostructuring.

The partial substitution of lead on the bismuth site of BiOCuSe results in a marked enhancement of the thermoelectric performance when compared to other dopants. A simple ball milling process for fabricating Pb-doped BiOCuSe in air shows an improvement of thermoelectric performance in comparison of that of pristine BiOCuSe. It indicates that this is a potential technique for large scale production of p-type TE material. Although Pb doped BiOCuSe shows an outstanding thermoelectric performance, there would be still room for further study on reducing the thermal conductivity and enhancing ZT .

The substitution of divalent cations on the copper site does not switch BiOCuSe from p-type to n-type, because Cu vacancies form easily during the synthesis. However, the substitution of positive valence cations (> 3) on Cu and Bi sites or monovalent anions (for instance, fluoride, iodide) on Se and O sites should be studied in further works. If both n- and p-type of BiOCuSe based material could be fabricated, one would expect significant progress in finding promising bulk TE modules with a ZT value of above one.

6.2 Bi₂O₂Cu₄Se₃ Compound

All attempts to synthesise this compound were not successful. However, investigation on the effect of thicker chalcogenide layer in these compounds is still very interesting. For example, to the best of our knowledge, the Bi₄O₄Se₃ compound does not exist. However, the A₄O₄Se₃ (A = La-Yb, Y) compounds have been found recently [88]. Therefore, there is still possibility to investigate [Cu₄Se₃]²⁻ slabs in compounds containing La³⁺ or other rare earth elements.

6.3 Bi₂MO₄Cu₂Se₂ (M = Y) Compound

Bi₂YO₄Cu₂Se₂ exhibits metallic behaviour with p-type charge carriers, and relatively low values of the Seebeck coefficient. This behaviour is unusual in most of the reported CuCh based layered compounds, for example: Sr₂MnO₂Cu₂Se₂ [268], Sr₃Sc₂O₅Cu₂S₂ [269, 270], LaOCuS(Se) [96], BaFCuS(Se) [271], all of those show a semiconducting behaviour. Therefore, the optimisation of the hole carrier concentration via electron donor doping is required to improve ZT of Bi₂YO₄Cu₂Se₂. In addition, there are still interests in studying the thermoelectric properties of Bi₂MO₄Cu₂Se₂ family in which M are other cations such as Gd, Sm, Nd.

6.4 Bi₂O₂Ch (Ch = Te, Se) Compounds

In summary, the synthesis, crystal structure and thermoelectric properties of the solid solution Bi₂O₂Te_{1-x}Se_x ($0 \leq x \leq 1$) and Bi₂O₂Se_{1±δ} ($0.05 \leq \delta \leq 0.15$) have been reported. Bi₂O₂Te is stable only within a very restricted range of chemical composition of Te around the stoichiometric composition. In sharp contrast, the powder XRD patterns of Bi₂O₂Se shows no clear evidence of any impurity phase within a large range of Se.

$\text{Bi}_2\text{O}_2\text{Te}_{1-x}\text{Se}_x$ ($0 \leq x \leq 1$) series behave as n-type semiconductors. The thermoelectric performance of $\text{Bi}_2\text{O}_2\text{Te}$ is better than that of the solid solution $\text{Bi}_2\text{O}_2\text{Te}_{1-x}\text{Se}_x$ ($0.25 \leq x \leq 1$) or $\text{Bi}_2\text{O}_2\text{Se}_{1+\delta}$ ($0.05 \leq \delta \leq 0.15$). The increasing power factor with increasing temperature indicates that a higher ZT value for $\text{Bi}_2\text{O}_2\text{Te}$ might be approached at higher temperatures, suggesting that $\text{Bi}_2\text{O}_2\text{Te}$ is a potential n-type material for thermoelectric applications. The low lattice thermal conductivity, with a trend of decreasing to a glass-like value at higher temperature of these oxy-telluride and selenides might open new interesting research avenues. In addition, there would be still room for further reducing the thermal conductivity of these materials by nano-structuring via a ball milling technique. However, the improvement of the electrical conductivity by electron doping is indispensably needed for thermoelectric applications. Finally, the modification of Te content in Bi_2Te_3 by creating the ternary $\text{Bi}_2\text{O}_2\text{Te}$ would offer a cost reduction and contribute to the decrease of the environmental impact, if the figure of merit of $\text{Bi}_2\text{O}_2\text{Te}$ is improved to values comparable to that of Bi_2Te_3 . This is a challenge but it may be achievable in the future.

6.5 Final Remarks

The investigation of magnetic properties of oxychalcogenides have been attracted remarkably while little has been reported in thermoelectrics. As shown throughout this dissertation, there are still large opportunities in studying thermoelectric properties of existing oxychalcogenide families as well as discovering new compounds.

References

- [1] A. Mojiri, R. Taylor, E. Thomsen and G. Rosengarten, *Spectral Beam Splitting For Efficient Conversion Of Solar Energy—A Review*, *Renew. Sust. Energ. Rev.*, **2013**, 28, 654-663.
- [2] S. Mekhilef, R. Saidur and A. Safari, *A Review On Solar Energy Use In Industries*, *Renew. Sust. Energ. Rev.*, **2011**, 15, 1777-1790.
- [3] *Relative_cost_of_electricity_generated_by_different_sources* (available at http://en.wikipedia.org/wiki/Relative_cost_of_electricity_generated_by_different_sources)
- [4] S. A. Omer and D. G. Infield, *Design And Thermal Analysis Of A Two Stage Solar Concentrator For Combined Heat And Thermoelectric Power Generation*, *Energy Convers. Manage.*, **2000**, 41 (7), 737-756.
- [5] C. B. Vining, *An Inconvenient Truth About Thermoelectrics*, *Nat. Mater.*, **2009**, 8, 83-85.
- [6] *Trends in power generation from waste heat in cement plants* (available at http://www.zkg.de/en/artikel/zkg_2011-05_Trends_in_power_generation_from_waste_heat_in_cement_plants_1185560.html)
- [7] D. D. Pollock, *Thermoelectric Phenomena, Handbook of Thermoelectrics*, D. M. Rowe (ed.), CRC Press LLC, **1995**, 701 p.
- [8] H. J. Goldsmid, *Introduction to Thermoelectricity*, Springer Series in Materials Science, **2009**, 121, 242 p.
- [9] P. Vaquerio and A. V. Powell, *Recent Developments in Nanostructured Materials for High-Performance Thermoelectrics*, *J. Mater. Chem.*, **2010**, 20, 9577 – 9584.
- [10] A. J. Minnich, M. S. Dresselhaus, Z. F. Ren, G. Chen, *Bulk Nanostructured Thermoelectric Materials: Current Research And Future Prospects*, *Energ. Environ. Sci.*, **2009**, 2, 466-479.
- [11] G. J. Snyder and E. S. Toberer, *Complex Thermoelectric Materials*, *Nat. Mater.*, **2008**, 7, 105-114.
- [12] R. M. Nault, *Report on Basic Research Needs for Solar Energy Utilization*, Basic Energy Sciences Workshop on Solar Energy Utilization, **2005**, 162-163 (available at http://science.energy.gov/~media/bes/pdf/reports/files/seu_rpt.pdf)
- [13] G.D. Mahan, *Good Thermoelectrics*, *Solid State Physics* (H. Ehrenreich and F. Spaepen, eds.), Academic Press, New York, **1998**, 51, 81-157.
- [14] K. Matsubara, *Development of A High Efficient Thermoelectric Stack For A Waste Exhaust Heat Recovery of Vehicles*, 21st International Conference on Thermoelectrics, **2002**, 418-423.
- [15] F. J. DiSalvo, *Thermoelectric Cooling and Power Generation*, *Science*, **1999**, 285, 703-706.
- [16] C. B. Vining, *Semiconductors Are Cool*, *Nature*, **2001**, 413, 577-578.
- [17] H. Kawamoto, *Nanotechnology and Materials Research Unit, Science and Technology Trends*.
(<http://www.nistep.go.jp/achiev/ftx/eng/stfc/stt030e/qr30pdf/STTqr3004.pdf>)

- [18] G.S. Nolas, J. Sharp, and H.J. Goldsmid, *Thermoelectrics Basic Principles and New Materials Developments*, Springer-Verlag, Berlin Heidelberg, **2001**, 293 p.
- [19] L. D. Hicks, T. C. Harman and M. S. Dresselhaus, *Use of Quantum-Well Superlattices to Obtain A High Figure Of Merit From Nonconventional Thermoelectric Materials*, Appl. Phys. Lett., **1993**, 63, 3230-3232.
- [20] T.K. Reynolds, J. G. Bales, R. F. Kelley and F. J. DiSalvo, *The Synthetic Search for Better Thermoelectrics, Chemistry, Physics, and Materials Science of Thermoelectric Materials: Beyond Bismuth Telluride*, M.G. Kanatzidis, T.P. Hogan, S.D. Mahanti, (eds.), Springer US, **2003**, 19-34.
- [21] Y. Deng and J. Liu, *Recent Advances in Direct Solar Thermal Power Generation*, J. Renewable and Sustainable Energy, **2009**, 1 (5), 052701.
- [22] P. Sundarraj, D. Maity, S. S. Roy and R. A. Taylor, *Recent Advances In Thermoelectric Materials And Solar Thermoelectric Generators – A Critical Review*, RSC. Adv., **2014**, 4, 46860-46874.
- [23] C Wood, *Materials For Thermoelectric Energy Conversion*, Rep. Prog. Phys., **1988**, 51, 459–539.
- [24] M.Cutler, J. F. Leavy, and R. L. Fitzpatrick, *Electronic Transport In Semimetallic Cerium Sulfide*, Phys. Rev., **1964**, 133 (4A), 1143- 1152.
- [25] Y. Pei, X. Shi, A. Lalonde, H. Wang, L.D. Chen and G. J. Snyder, *Convergence Of Electronic Bands For High Performance Bulk Thermoelectrics*, Nature, **2011**, 473, 66-69.
- [26] C. Kittel, *Introduction to Solid State Physics*, 8th ed., Wiley, New York, **2005**, 704 p.
- [27] G. A. Slack, *New Materials and Performance Limits for Thermoelectric Cooling*, CRC Handbook of Thermoelectrics, D. M. Rowe (ed), CRC Press, London, **1995**, 407-437.
- [28] A. P. Gonçalves and C. Godart, *New Promising Bulk Thermoelectrics: Intermetallics, Pnictides And Chalcogenides*, Eur. Phys. J. B, **2014**, 87:42.
- [29] G. Min and D. M. Rowe, *A Serious Limitation To The Phonon Glass Electron Crystal (PGEC) Approach To Improved Thermoelectric Materials*, J. Mater. Sci. Lett., **1999**, 18 (16), 1305 – 1306.
- [30] J. W. G. Bos and R. A. Downie, *Half-Heusler Thermoelectrics: A Complex Class of Materials*, J. Phys. Condensed Matter., **2014**, 26, 433201.
- [31] J.W.G. Bos, *New Compounds And Structures In The Solid State*, RSC Ann. Rep. Prog. Chem., Sect. A: Inorg. Chem., **2012**, 108, 408-423.
- [32] M. S. Dresselhaus, G. Chen, M. Y. Tang, R. G. Yang, H. Lee, D. Z. Wang, Z. F. Ren, J. P. Fleurial and P. Gogna, *New Directions for Low-Dimensional Thermoelectric Materials*, Adv. Mater., **2007**, 19 (8), 1043-1053.
- [33] B. Poudel, Q. Hao, Y. Ma, Y. Lan, A. Minnich, B. Yu, X. Yan, D. Z. Wang, A. Muto, D. Vashaee, X. Chen, J. Liu, M. S. Dresselhaus, G. Chen and Z. Ren, *High-Thermoelectric Performance of Nanostructured Bismuth Antimony Telluride Bulk Alloys*, Science, **2008**, 320, 634-638.
- [34] G. Chen and A. Shakouri, *Heat Transfer in Nanostructures for Solid-State Energy Conversion*, J. Heat Transfer, **2002**, 124 (2), 242-252.

- [35] L.D. Hicks, M. S. Dresselhaus, *Effect Of Quantum-Well Structures On The Thermoelectric Figure Of Merit*, Phys. Rev. B, **1993**, 47, 12727-12731.
- [36] G. Chen, *Semiconductors and Semimetals*, Recent Trends in Thermoelectric Materials Research III, T. Tritt (ed), Academic Press, US, **2001**, 71, 203–259.
- [37] L. D. Hicks, T. C. Harman, X. Sun and M. S. Dresselhaus, *Experimental Study Of The Effect Of Quantum-Well Structures On The Thermoelectric Figure Of Merit*, Phys. Rev. B, **1996**, 53, 10493-10496.
- [38] N. F. Mott, H. Jones, *The Theory of the Properties of Metals and Alloys*, Dover Publications Inc., New York, **1936**, 339p.
- [39] D. Emin, *Effects of Charge Carriers' Interactions on Seebeck Coefficients*, *Thermoelectrics Handbook: Macro To Nano*, D. M. Rowe (ed.), Taylor and Francis, Boca Raton, **2006**, 5.1-5.6.
- [40] R. Venkatasubramanian, *Phonon Blocking Electron Transmitting Superlattice Structures As Advanced Thin Film Thermoelectric Materials*, Recent Trends in Thermoelectric Materials Research III, Semiconductors and Semimetals, Academic Press, **2001**, 71, 175–201.
- [41] T. C. Harman, P. J. Taylor, M. P. Walsh and B. E. LaForge, *Quantum Dot Superlattice Thermoelectric Materials And Devices*, Science, **2002**, 297 (5590), 2229-2232.
- [42] A. I. Hochbaum, R. Chen, R. D. Delgado, W. Liang, E. C. Garnett, M. Najarian, A. Majumdar and P. Yang, *Enhanced Thermoelectric Performance Of Rough Silicon Nanowires*, Nature, **2008**, 451, 163-167.
- [43] A. I. Boukai, Y. Bunimovich, J. Tahir-Kheli, J.-K. Yu, W. A. Goddard Iii and J. R. Heath, *Silicon Nanowires As Efficient Thermoelectric Materials*, Nature, **2008**, 451, 168-171.
- [44] W. Kim, J. Zide, A. Gossard, D. Klenov, S. Stemmer, A. Shakouri and A. Majumdar, *Thermal Conductivity Reduction and Thermoelectric Figure of Merit Increase by Embedding Nanoparticles in Crystalline Semiconductors*, Phys. Rev. Lett., **2006**, 96, 045901.
- [45] X. W. Wang, H. Lee, Y. C. Lan, G. H. Zhu, G. Joshi, D. Z. Wang, J. Yang, A. J. Muto, M. Y. Tang, J. Klatsky, S. Song, M. S. Dresselhaus, G. Chen and Z. Ren, *Enhanced Thermoelectric Figure Of Merit In Nanostructured N-Type Silicon Germanium Bulk Alloy*, Appl. Phys. Lett., **2008**, 93, 193121.
- [46] R. Yang, G. Chen and M. Dresselhaus, *Thermal Conductivity Of Simple And Tubular Nanowire Composites In The Longitudinal Direction*, Phys. Rev. B, **2005**, 72, 125418.
- [47] R. Yang, G. Chen and M. Dresselhaus, *Thermal Conductivity Modeling of Core–Shell and Tubular Nanowires*, Nano Lett., **2005**, 5, 1111-1115.
- [48] C. B. Vining, *A Model For The High-Temperature Transport Properties Of Heavily Doped n-Type Silicon-Germanium Alloys*, J. Appl. Phys., **1991**, 69, 331.
- [49] B. C. Sales, D. G. Mandrus and B. C. Chakoumakos, *Chapter 1, Use Of Atomic Displacement Parameters In Thermoelectric Materials Research*, Semiconduct. Semimet., **2001**, 70, 1-36.

- [50] C. Chiritescu, D.G. Cahill, N. Nguyen, D. Johnson, A. Bodapati, P. Keblinski, and P. Zschack, *Ultralow Thermal Conductivity In Disordered, Layered Wse₂ Crystals*, Science, **2007**, 315 (5810), 351-353.
- [51] C. Wan, Y. Wang, N. Wang, W. Norimatsu, M. Kusunoki, and K. Koumoto, *Development of Novel Thermoelectric Materials By Reduction of Lattice Thermal Conductivity*, Sci. Technol. Adv. Mater., **2010**, 11, 044306 (7pp).
- [52] A. P. Gonçalves and C. Godart, *Alternative Strategies For Thermoelectric Materials Development, New Materials For Thermoelectric Applications: Theory And Experiment*, V. Zlatic and A. Hewson (eds), Springer, Netherlands, **2011**, 1-24.
- [53] M. Shikano, R. Funahashi, *Electrical and Thermal Properties of Single-Crystalline (Ca₂CoO₃)_{0.7}CoO₂ With A Ca₃Co₄O₉ Structure*, Appl. Phys. Lett., **2003**, 82, 1851.
- [54] M. Tada, M. Yoshiya, and H. Yasuda, *Effect of Ionic Radius And Resultant Two-Dimensionality of Phonons on Thermal Conductivity in M_xCoO₂ (M = Li, Na, K) By Perturbed Molecular Dynamics*, J. Electro. Mater., **2010**, 39 (9), 1439-1445.
- [55] I. Terasaki, Y. Sasago and K. Uchinokura, *Large Thermoelectric Power In NaCo₂O₄ Single Crystals*, Phys. Rev. B, **1997**, 56, R12685.
- [56] G.A. Wiegers, *Misfit Layer Compounds: Structures And Physical Properties*, Prog. Solid State Chem, **1996**, 24, 1-139.
- [57] C. Wan, Y. Wang, N. Wang, W. Norimatsu, M. Kusunoki, and K. Koumoto, *Intercalation: Building A Natural Superlattice For Better Thermoelectric Performance In Layered Chalcogenides*, J. Electron. Mater., **2011**, 40 (5), 1271-1280.
- [58] L-D. Zhao, V. P. Dravid and M. G. Kanatzidis, *The Panoroscopic Approach To High Performance Thermoelectrics*, Energy Environ. Sci., **2014**, 7, 251-268.
- [59] P. Jood, R.J. Mehta, Y. Zhan, G. Peleckis, X. Wang, R. W. Siegel, T. Borca-Tasciuc, S. X. Dou, and g. Ramanath, *Al-Doped Zinc Oxide Nanocomposites With Enhanced Thermoelectric Properties*, Nano Lett., **2011**, 11 (10), 4337-4342.
- [60] J. Lan, Y.H. Lin, Y. Liu, S. Xu, and C.W. Nan, *High Thermoelectric Performance of Nanostructured In₂O₃-Based Ceramics*, J. Am. Ceram. Soc., **2012**, 95, 2465-2469.
- [61] K. Fujita, T. Mochida, K. Nakamura, *High-Temperature Thermoelectric Properties of Na_xCoO_{2-δ} Single Crystals*, Jpn. J. Appl. Phys. **2001**, 40, 4644.
- [62] T. Yin, D. Liu, Y. Ou, F. Ma, S. Xie, J.-F. Li, and J. Li, *Nanocrystalline Thermoelectric Ca₃Co₄O₉ Ceramics By Sol-Gel Based Electrospinning And Spark Plasma Sintering*, J. Phys. Chem. C., **2010**, 114, 10061-10065.
- [63] H. Kaga, R. Asahi, T. Tani, *Thermoelectric Properties of Highly Textured Ca-Doped (ZnO)_mIn₂O₃ Ceramics*, Jpn. J. Appl. Phys., **2004**, 43, 7133-7136.
- [64] D. A. Wright, *Thermoelectric Properties Of Bismuth Telluride And Its Alloys*, Nat. Mater. **1958**, 181, 834.
- [65] J. R. Sootsman, D. Y. Chung, M. G. Kanatzidis, *New and Old Concepts In Thermoelectric Materials*, Angew. Chem. Int. Ed. **2009**, 48, 8616-8639.
- [66] L-D. Zhao, S-H. Lo, Y. Zhang, H. Sun, G. Tan, C. Uher, C. Wolverton, V. P. Dravid, M. G. Kanatzidis, *Ultralow Thermal Conductivity And High Thermoelectric Figure Of Merit In SnSe Crystals*, **2014**, 508, 373-377.

- [67] S. I. Kim, K. H. Lee, H. A. Mun, H. S. Kim, S. W. Hwang, J. W. Roh, D. J. Yang, W. H. Shin, X. S. Li, Y. H. Lee, G. J. Snyder, S. W. Kim, *Dense Dislocation Arrays Embedded In Grain Boundaries For High-Performance Bulk Thermoelectrics*, Science, 2015, 348, 109-114.
- [68] http://www.alibaba.com/product-detail/bismuth-telluride-Metalloids-tellurium-metal-ingot_1762407744.html?s=p.
- [69] J. Cheng, J. Zhu, X. Wei and P. K. Shen, *Ce₂O₂S Anchored On Graphitized Carbon With Tunable Architectures As A New Promising Anode For Li-ion Batteries*, J. Mater. Chem. A, **2015**, 3, 10026-10030.
- [70] S. K. Singh, A. Kumar, B. Gahtori, G. Sharma, S. Patnaik, and V.P. S. Awana, *Bulk Superconductivity In Bismuth Oxysulfide Bi₄O₄S₃*, J. Am. Chem. Soc. **2012**, 134, 16504–16507.
- [71] Y. Mizuguchi, H. Fujihisa, Y. Gotoh, K. Suzuki, H. Usui, K. Kuroki, S. Demura, Y. Takano, H. Izawa, and O. Miura, *BiS₂-Based Layered Superconductor Bi₄O₄S₃*, Phys. Rev. B., **2012**, 86, 220510 (R).
- [72] C. I. Sathish, H. L. Feng, Y. Shi, And K. Yamaura, *Superconductivity In Bismuth Oxysulfide Bi₄O₄S₃*, J. Phys. Soc. Jpn., **2013**, 82, 074703.
- [73] R. Jha, A. Kumar, S. Kumar Singh, V.P.S. Awana, *Superconductivity At 5 K In NdO_{0.5}F_{0.5}BiS₂*, J. Appl. Phys., **2013**, 113, 056102.
- [74] Y. Mizuguchi, S. Demura, K. Deguchi, Y. Takano, H. Fujihisa, Y. Gotoh, H. Izawa, O. Miura, *Superconductivity In Novel BiS₂-Based Layered Superconductor LaO_{1-x}F_xBiS₂*, J. Phys. Soc. Jpn., **2012**, 81, 114725.
- [75] A. Meerschaut, A. Lafond, V. Meignen, and C. Deudon, *Crystal Structure And Magnetic Properties of A New Oxyselenide of Gadolinium and Titanium: Gd₄TiSe₄O₄*, J. Solid State. Chem., **2001**, 162 (2), 182-187.
- [76] E. E. McCabe, D. G. Free, B. G. Mendis, J. S. Higgins, and J. S. O. Evans, *Preparation, Characterization, and Structural Phase Transitions in A New Family Of Semiconducting Transition Metal Oxychalcogenides β-La₂O₂MSe₂ (M = Mn, Fe)*, Chem. Mater., **2010**, 22, 6171–6182.
- [77] Y-L. Sun, A. Ablimit, H-F. Zhai, J-K. Bao, Zh-T. Tang, X-B. Wang, N-L. Wang, Ch-M. Feng, and G-H. Cao, *Design And Synthesis Of A New Layered Thermoelectric Material*, Inorg. Chem. **2014**, 53, 11125–11129.
- [78] A. R. West, *Solid State Chemistry and Its Applications*, 2nd ed, Wiley, **2014**, 35-76.
- [79] H. A. Eick, *The Crystal Structure And Lattice Parameters Of Some Rare Earth Mono-Seleno Oxides*, Acta Crystallogr., **1960**, 13, 161.
- [80] M. Guittard, J. Flahaut, L. Domange, *La Série Complète Des Oxysélénures Des Terres Rares Et D'yttrium*, Acta Crystallogr., **1966**, 21, 832.
- [81] B. Morosin, D.J. Newman, *La₂O₂S Structure Refinement and Crystal Field*, Acta Crystallogr. B, **1973**, 29, 2647-2648.
- [82] H.A. Eick, *The Crystal Structure and Lattice Parameters of Some Rare Earth Mono-Seleno Oxides*, Acta Crystallogr., **1960**, 13, 161.

- [83] F.A.Weber, T. Schleid, *Ueber Oxidtelluride (M_2O_2Te) Der Leichten Lanthanide ($M = La-Nd, Sm-Ho$) Im A-Typ Mit Anti-($ThCr_2Si_2$)-Struktur*, Zeitschrift fuer Anorganische und Allgemeine Chemie (1950) (DE), **1999**, 625, 1833-1838.
- [84] W.H. Zachariasen, *Crystal Chemical Studies of The 5f-Series Of Elements. VII. The Crystal Structure of $Ce_2O_2S, La_2O_2S, Pu_2O_2S$* , Acta Crystallogr., **1949**, 2, 60-63.
- [85] F. Weber, *Präparative Studien In Den Mehrstoffsystemen Selten-Erd-Metall - Selen bzw. - Tellur und Sauerstoff*, Phd dissertation, **1999**.
- [86] P. Schmidt, O. Rademacher, H. Oppermann, S. Daebritz, *Untersuchung Der Phasenbeziehungen In Den Quaternaeren Systemen $Bi_2O_3 / Bi_2Ch'_3 / Bi_2Ch''_3$ ($Ch = S, Se, Te$) II. Zum System BiO_3* , Zeitschrift fuer Anorganische und Allgemeine Chemie, **2000**, 626, 1999-2003.
- [87] S. D. N. Luu, P. Vaqueiro, *Synthesis, Characterisation and Thermoelectric Properties Of The Oxytelluride Bi_2O_2Te* , J. Solid State Chem., **2015**, 226, 219–223.
- [88] A. J. Tuxworth, C-H Wang and J. S. O. Evans, *Synthesis, Characterisation And Properties Of Rare Earth Oxyselenides $A_4O_4Se_3$ ($A = Eu, Gd, Tb, Dy, Ho, Er, Yb$ and Y)*, Dalton Trans., **2015**, 44, 3009–3019.
- [89] E. Koyama, I. Nakai, K. Nagashima, *Crystal Chemistry of Oxide-Chalcogenides. II. Synthesis and Crystal Structure of The First Bismuth Oxide-Sulfide, Bi_2O_2S* , Acta Crystallogr, Sect. B, **1984**, 40, 105-109.
- [90] S. Strobel, A. Choudhury, P. K. Dorhout, C. Lipp and T. Schleid, *Rare-Earth Metal(III) Oxide Selenides $M_4O_4Se[Se_2]$ ($M = La, Ce, Pr, Nd, Sm$) with Discrete Diselenide Units: Crystal Structures, Magnetic Frustration, and Other Properties*, Inorg. Chem., **2008**, 47, 4936–4944.
- [91] W. Wichelhaus, *The Rare-Earth Oxide Disulfides $La_2O_2S_2, Pr_2O_2S_2, Nd_2O_2S_2$* , Naturwissenschaften, **1978**, 65, 593-594.
- [92] J. Ostorero, M.le Blanc, *Room Temperature Structure Of $La_2O_2S_2$* , Acta Crystallogr, Sect. C, **1990**, 46, 1376-1378.
- [93] E. S. Stampler, W. C. Sheets, M. I. Bertoni, W. Prellier, T. O. Mason, K. R. Poeppelmeier, *Facile Synthesis Of $BiCuOS$ By Hydrothermal Methods*, Inorg. Chem. **2008**, 47, 10009-10016.
- [94] K. Ueda, S. Inoue, S. Hirose, H. Kawazoe, H. Hosono, *Transparent P-Type Semiconductor: $LaCuOS$ Layered Oxysulfide*, Appl. Phys. Lett., **2000**, 77, 2701-2703.
- [95] K. Ueda, K. Takafuji, H. Hiramatsu, H. Ohta, T. Kamiya, M. Hirano, H. Hosono, *Electrical And Optical Properties And Electronic Structures Of $LnCuOS$ ($Ln = La \sim Nd$)*, Chem. Mater., **2003**, 15, 3692-3695.
- [96] H. Hiramatsu, H. Yanagi, T. Kamiya, K. Ueda, M. Hirano, H. Hosono, *Crystal Structures, Optoelectronic Properties, And Electronic Structures Of Layered Oxychalcogenides $MCuOCh$ ($M = Bi, La; Ch = S, Se, Te$): Effects Of Electronic Configurations of M^{3+} Ions*, Chem. Mater., **2008**, 20, 326-334.
- [97] M. Palazzi, C. Carcaly and J. Flahaut, *Un Nouveau Conducteur Ionique $(LaO)AgS$* , J. Solid State Chem., **1980**, 35, 150-155.
- [98] L. N. Kholodkovskaya, L. G. Akselrud, A. M. Kusainova, V. A. Dolgikh and B. A. Popovkin, *$BiCuSeO$: Synthesis And Crystal Structure*, Mater. Sci. Forum., **1993**, 133-136, 693-696.

- [99] V. Johnson, W. Jeitschko, *ZrCuSiAs: A "Filled" PbFCl Type*, J. Solid State Chem., **1974**, 11, 161-166.
- [100] H. Hiramatsu, K. Ueda, T. Kamiya, H. Ohta, M. Hirano and H. Hosono, *Synthesis Of Single-Phase Layered Oxychalcogenide $\text{La}_2\text{CdO}_2\text{Se}_2$ Crystal Structure, Optical And Electrical Properties*, J. Mater. Chem., **2004**, 14, 2946–2950.
- [101] C-H. Wang, Ch.M. Ainsworth, D-Y. Gui, E. E. McCabe, M. G. Tucker, I. R. Evans, and J. S. O. Evans, *Infinitely Adaptive Transition Metal Oxychalcogenides: The Modulated Structures of $\text{Ce}_2\text{O}_2\text{MnSe}_2$ and $(\text{Ce}_{0.78}\text{La}_{0.22})_2\text{O}_2\text{MnSe}_2$* , Chem. Mater., **2015**, 27, 3121–3134.
- [102] W. J. Zhu, and P. H. Hor, *Unusual Layered Transition-Metal Oxysulfides: $\text{Sr}_2\text{Cu}_2\text{MO}_2\text{S}_2$ ($M = \text{Mn}, \text{Zn}$)*, J. Solid State Chem., **1997**, 130, 319-321.
- [103] E. Brechtel, G. Cordier, H. Schafer, *Über Oxidpnictide: Zur Kenntnis Von $\text{A}_2\text{Mn}_3\text{B}_2\text{O}_2$ Mit $A = \text{Sr}, \text{Ba}$ Und $B = \text{As}, \text{Sb}, \text{Bi}$* , Z. Naturforsch., **1979**, 34b, 777-780.
- [104] Y. B. Park, D. C. Degroot, J. L. Schindler, C. R. Kannewurf and M. G. Kanatzidis, *Intergrowth Of Two Different Layered Networks In The Metallic Copper Oxyselenide $\text{Na}_{1.9}\text{Cu}_2\text{Se}_2\text{Cu}_2\text{O}$* , Chem. Mater., **1993**, 5, 8-10.
- [105] J. M. Mayer, L. F. Schneemeyer, T. Siegrist, J. V. Waszczak, B. Van Dover, *New Layered Iron-Lanthanum-Oxide-Sulfide And Selenide Phases: $\text{Fe}_2\text{La}_2\text{O}_3\text{E}_2$ ($E = \text{S}, \text{Se}$)*, Angew. Chem. Int. Ed. Engl., **1992**, 31 (12), 1645-1647.
- [106] W. J. Zhu, P. H. Hor, *Crystal Structure of New Layered Oxysulfides: $\text{Sr}_3\text{Cu}_2\text{Fe}_2\text{O}_5\text{S}_2$ and $\text{Sr}_2\text{CuMO}_3\text{S}$ ($M = \text{Cr}, \text{Fe}, \text{In}$)*, J. Solid State Chem., **1997**, 134, 128-131.
- [107] J. S. O. Evans, E. B. Brogden, A. L. Thompson, R. L. Cordiner, *Synthesis And Characterisation of The New Oxyselenide $\text{Bi}_2\text{YO}_4\text{Cu}_2\text{Se}_2$* , Chem. Commun., **2002**, 912-913.
- [108] Z. A. Ga'1, O. J. Rutt, C. F. Smura, T. P. Overton, N. Barrier, S. J. Clarke, J. Hadermann, *Structural Chemistry And Metamagnetism Of An Homologous Series Of Layered Manganese Oxysulfides*, J. Am. Chem. Soc., **2006**, 128, 8530-8540.
- [109] N. Barrier, S. J. Clarke, *A Novel Layered Oxysulfide Intergrowth Compound $\text{Sr}_4\text{Mn}_2\text{Cu}_5\text{O}_4\text{S}_5$ Containing A Fragment of The $A\text{-Cu}_2\text{S}$ Antifluorite Structure*, Chem. Commun., **2003**, 164-165.
- [110] O. J. Rutt, G. R. Williams, S. J. Clarke, *Reversible Lithium Insertion And Copper Extrusion In Layered Oxysulfides*, Chem. Commun., **2006**, 2869.-2871.
- [111] S. Indris, J. Cabana, O. J. Rutt, S. J. Clarke, C. P. Grey, *Layered Oxysulfides $\text{Sr}_2\text{MnO}_2\text{Cu}_{2m-0.5}\text{S}_{m+1}$ ($m = 1, 2, \text{ and } 3$) As Insertion Hosts For Li Ion Batteries*, J. Am. Chem. Soc., **2006**, 128, 13354-13355.
- [112] S. J. Clarke, P. Adamson, S. J. C. Herkelrath, O. J. Rutt, D. R. Parker, M. J. Pitcher, and C. F. Smura, *Structures, Physical Properties, And Chemistry of Layered Oxychalcogenides And Oxypnictides*, Inorg. Chem, **2008**, 47 (9), 8473–8486.
- [113] L-D. Zhao, J. He, D. Berardan , Y. Lin , J-F Li , C-W. Nan and N. Dragoe, *BiCuSeO Oxyselenides: New Promising Thermoelectric Materials*, Energy Environ. Sci., **2014**, 7, 2900-2924.

- [114] C. Barreteau, L. Pan, Y-L. Pei, L-D. Zhao, D. Berardan and N. Dragoe, *Oxychalcogenides As New Efficient P-Type Thermoelectric Materials*, *Func. Mater. Lett.*, **2013**, 6 (5), 1340007.
- [115] J.G. Bednorz and K.A. Müller, *Possible High Tc Superconductivity In The Ba-La-Cu-O System*, *Z. Phys.B. Con. Mat.*, **1986**, 64, 189-193.
- [116] H. Hiramatsu, K. Ueda, H. Ohta, M. Hirano, T. Kamiya and H. Hosono, *Degenerate P-Type Conductivity In Wide-Gap LaCuOS_{1-x}Se_x (x = 0–1) Epitaxial Films*, *Appl. Phys. Lett.*, **2003**, 82, 1048.
- [117] H. Hiramatsu, K. Ueda, H. Ohta, M. Hirano, M. Kikuchi, H. Yanagi, T. Kamiya and h. Hosono, *Heavy Hole Doping Of Epitaxial Thin Films Of A Wide Gap P-Type Semiconductor, LaCuOSe, and Analysis Of The Effective Mass*, *Appl. Phys. Lett.*, **2007**, 91, 012104.
- [118] Y. Kamihara, T. Wanatabe, M. Hirano, ans H. Hosono, *Iron-Based Layered Superconductor La[O_{1-x}F_x]FeAs (x = 0.05–0.12) with T_c = 26 K*, *J. Am. Chem. Soc.*, **2008**, 130 (11), 3296-3297.
- [119] L. P.-Gaudart, D. Berardan, J. Bobroffet, N. Dragoe, *Large Seebeck Coefficients In Iron - Oxypnictides: A New Route Towards N - Type Thermoelectric Materials*, *Phys. Stat. Sol. (RRL)*, **2008**, 2 (4), 185-187.
- [120] L.D. Zhao, D. Berardan, Y. L. Pei, C. Byl, L. Pinsard-Gaudart, N. Dragoe, *Bi_{1-x}Sr_xCuSeO Oxyselenides As Promising Thermoelectric Materials*, *App. Phys. Lett.*, **2010**, 97, 092118.
- [121] Masuda. Y, Nagahama. D, Itahara. H, Tani. T, Seoc. W. S, Koumotoa. K., *Thermoelectric Performance Of Bi- and Na-Substituted Ca₃Co₄O₉ Improved Through Ceramic Texturing*, *J. Mater. Chem.*, **2003**, 13, 1094-1099.
- [122] R. Venkatasubramanian, E. Siivola, T. Colpitts, and B. O'Quinn, *Thin-Film Thermoelectric Devices With High Room-Temperature Figures Of Merit*, *Nature*, **2001**, 413, 597-602.
- [123] I. Chowdhury , R. Prasher, K. Lofgreen, G. Chrysler, S. Narasimhan, R. Mahajan, D. Koester, R. Alley and R. Venkatasubramanian, *On-Chip Cooling By Superlattice-Based Thin-Film Thermoelectrics*, *Nat. Nanotechnol.*, **2009**, 4 , 235-238.
- [124] J. S. Benjamin, *Dispersion Strengthened Superalloys By Mechanical Alloying*, *Metall.Trans.*, **1970**, 1 (10), 2943-2951.
- [125] B. S. Murty and S. Ranganathan, *Novel Materials Synthesis By Mechanical Alloying/Milling*, *Inter. Mater. Rev.*, **1998**, 43, 3.
- [126] P. Baláž, *Mechanochemistry in Nanoscience and Minerals Engineering*, Chapter 2, High - Energy Milling, Springer-Verlag Berlin Heidelberg, **2008**.
- [127] www.retsche.com.
- [128] R. Novelline, *Squire`s Fundamentals of Radiology*, Havard University Press, 5th Ed, **1997**.
- [129] J. Hasek, *X-ray and Neutron Structure Analysis in Materials Science*, Springer US, **1989**.
- [130] www.bruker-axs.com/d8_advance.html.
- [131] <http://www.bruker-axs.com/eva.html>.
- [132] J. Chadwick, *Possible Existence of a Neutron*, *Nature*, **1932**, 129, 312.

- [133] M. Potter, H. Fritzsche, D. H. Ryan and L. M. D. Cranswick, *Low-Background Single-Crystal Silicon Sample Holders For Neutron Powder Diffraction*, J. Appl. Cryst., **2007**, 40, 489–495.
- [134] <http://www.isis.stfc.ac.uk>.
- [135] R. I. Smith and S. Hull, *User Guide for the Polaris Powder Diffractometer at ISIS*, available from: <http://www.isis.stfc.ac.uk/instruments/polaris/>.
- [136] P. Vaqueiro, G. Guelóu, M. Stec, E. Guilmeaub and A. V. Powell, *A Copper-Containing Oxytelluride As A Promising Thermoelectric Material For Waste Heat Recovery*, J. Mater. Chem. A, **2013**, 1, 520–523.
- [137] Bruker AXS GmbH, *Topas3*, Karlsruhe, Germany, **2005**.
- [138] H.M. Rietveld, *A Profile Refinement Method For Nuclear And Magnetic Structures*, J. Appl. Cryst. **1969**, 2, 65-71.
- [139] L.B. McCusker, R. B. Von Dreele, D.E. Cox, D. Louer, P. Scardi, *Rietveld Refinement Guidelines*, J. Appl. Cryst, **1999**, 32, 36-50.
- [140] J.J. Olivero., R.L. Longbothum, *Empirical Fits To The Voigt Line Width: A Brief Review*, J. Quant. Spectrosc. Radiat. Transfer, **1977**, 17 (2), 233–236.
- [141] A. C. Larson and R. B. von Dreele, *General Structure Analysis System (GSAS)*, Los Alamos National Laboratory Report LAUR, **2004**, 86-748.
- [142] G.D. Mahan, *Solid State Physics*, Academic Press, New York, **1998**, 51, 81-157.
- [143] R.A. Young, *The Rietveld Method*, International Union of Crystallography, Oxford University Press, **1993**.
- [144] R. Smith, “*Refinement of time-of-flight Profile Parameters in GSAS*”, <http://www.isis.stfc.ac.uk/instruments/polaris/data-analysis/refinement-of-profile-parameters-with-polaris-data11478.pdf>.
- [145] http://www.afrinc.com/products/tgplus/FULL_TGPLUS.pdf.
- [146] <http://www.tainstruments.com/pdf/brochure/sdt.pdf>.
- [147] Radiation Safety Requirements for Use of Electron Microscopes, University of Virginia ([www.http://ehs.virginia.edu/ehs/ehs.rs/rs.rpeelectronmicroscope.html](http://ehs.virginia.edu/ehs/ehs.rs/rs.rpeelectronmicroscope.html)).
- [148] J. Goldstein, D. Newbury, D. Joy, C. Lyman, P. Echlin, E. Lifshin, L. Sawyer and J. Michael, *Scanning Electron Microscopy And X-Ray Microanalysis*, Kluwer Academic, Plenum Publishers, New York, **2003**, 689.
- [149] R. F. Egerton, *Physical Principles Of Electron Microscopy: An Introduction To TEM, SEM, and AFM*, Springer, **2005**, 202.
- [150] A. R. Clarke, C. N. Eberhardt, *Microscopy Techniques For Materials Science*, CRC Press, Cambridge, England, Woodhead Publishing, **2002**.
- [151] L. Reimer, *Scanning Electron Microscopy: Physics Of Image Formation And Microanalysis*, Springer Berlin Heidelberg, **1998**, 45.
- [152] <http://www.fei.com/products/sem/quanta-sem/>
- [153] www.mtixtl.com.
- [154] K. A. Borup, J. D. Boor, H. Wang, F. Drymiotis, F. Gascoin, X. Shi, L-D. Chen, M. I. Fedorov, E. Müller, B. B. Iversen, and G. J. Snyder, *Measuring Thermoelectric Transport Properties Of Materials*, Energy Environ. Sci., **2015**, 8, 423–435
- [155] CF1200 cryostat operator`s Handbook.

- [156] <http://www.linseis.com/en/our-products/seebeck-coefficient-electric-resistivity/lsr-3/>
- [157] E. H. Hall, *On a New Action of the Magnet on Electric Currents*, Am. J. Math., **1879**, 2 (3), 287–292.
- [158] K. A. Borup, E. S. Toberer, L. D. Zoltan, G. Nakatsukasa, M. Errico, J-P. Fleurial, B. B. Iversen and G. J. Snyder, *Measurement Of The Electrical Resistivity And Hall Coefficient At High Temperatures*, Rev. Sci. Instrum., **2012**, 83, 123902.
- [159] L. J. Van der Pauw, *A Method Of Measuring The Resistivity And Hall Coefficient On Lamellae Of Arbitrary Shape*, Philips Tech. Rev., **1958**, 20, 220–224.
- [160] P. S. Gaal, M. A. Thermitus, D. E. Stroe, *Thermal Conductivity Measurements Using The Flash Method*, J. Therm. Anal. Cal., **2004**, 78, 185-189.
- [161] W. J. Parker, R. J. Jenkins, C. P. Butler, G. L. Abbott, *Flash Method of Determining Thermal Diffusivity, Heat Capacity, and Thermal Conductivity*, J. Appl. Phys., **1961**, 32 (9), 1679-1684.
- [162] <http://www.netzsch-thermal-analysis.com/en/home.html>
- [163] LFA 447 NanoFlash Manual (http://www.netzsch-thermal-analysis.com/uploads/tx_nxnetzschmedia/files/LFA_447_E_0912_07.pdf)
- [164] <http://www.anter.com/FL3000.htm>.
- [165] H. Hiramatsu, H. Kamioka, K. Ueda, M. Hirano, H. Hosono, *Electrical and Photonic Functions Originating from Low-Dimensional Structures in Wide-Gap Semiconductors LnCuOCh (Ln = lanthanide, Ch = chalcogen): A Review*, J. Ceram. Soc. Jpn., **2005**, 113 (1), 10-16.
- [166] A.P. Richard, J.A. Russell, A. Zakutayev, L.N. Zakharov, D.A. Keszler, J. Tate, *Synthesis, Structure, and Optical Properties of BiCuOCh (Ch = S, Se, and Te)*, J. Solid State Chem., **2012**, 187, 15-19.
- [167] H. Kamioka, H. Hiramatsu., M. Hirano, K. Ueda, T. Kamiya and H. Hosono, *Excitonic Properties Related To Valence Band Levels Split By Spin–Orbit Interaction In Layered Oxychalcogenide LaCuOCh (Ch = S, Se)*, J. Lumin., **2005**, 112, 66–70.
- [168] L-X. Pan, Q-L. Xia, S-L. Ye, N. Ding, Z-R. Liu, *First Principles Study of Electronic Structure, Chemical Bonding and Elastic Properties of BiOCuS*, T. Nonferr Metal Soc., **2012**, 22 (5), 1197-1202.
- [169] C. Barreteau, D. Berardan, E. Amzallag, L-D. Zhao, N. Dragoë, *Structural and Electronic Transport Properties in Sr-Doped BiCuSeO*, Chem. Mater, **2012**, 24 (16), 3168-3178.
- [170] Y-L. Pei, J. He, J-F. Li, F. Li, Q. Liu, W. Pan, C. Barreteau, D. Berardan, N. Dragoë and L- D. Zhao, *High Thermoelectric Performance From An Oxyselenide: Intrinsically Low Thermal Conductivity Of Ca-Doped BiCuSeO*, NPG Asia Mater., **2013**, 5, e47.
- [171] J. Li, J. Sui, Y. Pei, C. Barreteau, D. Berardan, N. Dragoë, W. Cai, J. He and L-D. Zhao, *A High Thermoelectric Figure Of Merit $ZT > 1$ in Ba Heavily Doped BiCuSeO Oxyselenides*, Energy Environ. Sci, **2012**, 5, 8543-8547.

- [172] J. Li, J. Sui, C. Barreteau, D. Berardan, N. Dragoe, W. Cai, Y. Pei and L. D. Zhao, *Thermoelectric Properties Of Mg Doped p-type BiCuSeO Oxyselenides*, J. Alloys Compd., **2013**, 551, 649-653.
- [173] I.R. Shein, A.L. Ivanovskii., *Electronic Band Structure And Inter-Atomic Bonding In Tetragonal BiOCuS As A Parent Phase For Novel Layered Superconductors*, Solid State Commun., **2010**, 150 (13), 640-643.
- [174] J-L.Lan, B. Zhan, Y-C. Liu, B. Zheng, Y. Liu, Y.-H.Linand C-W. Nan, *Doping For Higher Thermoelectric Properties In P-Type BiCuSeO Oxyselenide*, Appl. Phys. Lett., **2013**, 102, 123905.
- [175] F. Li, T.-R. Wei, F. Kang, J-F. Li, *Enhanced Thermoelectric Performance Of Ca-Doped BiCuSeO In A Wide Temperature Range*, J. Mater. Chem. A, **2013**, 1, 11942–11949.
- [176] D. S. Lee, T.-H. An, M. Jeong, H.-S.Choi, Y. S Lim, W.-S.Seo C.-H. Park, C. Park and H.-H. Park, *Density Of State Effective Mass And Related Charge Transport Properties In K-doped BiCuOSe*, Appl. Phys. Lett., **2013**, 103, 232110.
- [177] J. Li, J. Sui, Y. Pei, X. Meng, D. Berardan, N. Dragoe, W.Cai and L-D Zhao, *The Roles Of Na Doping In BiCuSeO Oxyselenides As A Thermoelectric Material*, J. Mater. Chem. A., **2014**, 2, 4903–4906.
- [178] Y. Liu, L.-D. Zhao, Y. Liu, J. Lan, W. Xu, F. Li, B-P. Zhang, D. Berardan, N. Dragoe, Y-H.Lin, C-W.Nan, J-F. Li and H. Zhu, *Remarkable Enhancement in Thermoelectric Performance of BiCuSeO by Cu Deficiencies*, J. Am. Chem. Soc., **2011**, 133, 20112–20115.
- [179] Y. Liu, J. Lan, W. Xu, Y-C. Liu, Y-L.Pei, B. Cheng, D-B.Liu, Y-H.Lin and L-D. Zhao, *Enhanced Thermoelectric Performance of A BiCuSeO System Via Band Gap Tuning*, Chem. Commun., **2013**, 49, 8075–8077.
- [180] F. Li, J.-F.Li, L.-D.Zhao, K. Xiang, Y. Liu, B.-P.Zhang, Y-H.Lin, C-W. Nan and H-M Zhu, *Polycrystalline BiCuSeO Oxide As A Potential Thermoelectric Material*, Energy Environ. Sci., **2012**, 5, 7188–7195.
- [181] S. K Karna, C-H. Hung, C-M Wu, C-W Wang, W-H Li, R. Sankar, F.C. Chou and M. Avdeev, *Large Magnetoresistance And Charge Transfer Between The Conduction And Magnetic Electrons In Layered Oxyselenide BiOCu_{0.96}Se*, Dalton Trans., **2013**, 42, 15581-15590.
- [182] S. K Karna, C-W Wang, C-M Wu, C-K. Hsu, D. Hsu, C-J.Wang, W-H Li, R. Sankar, F-C. Chou, *Spin, Charge and Lattice Couplings In Cu-Deficient Oxysulphide BiOCu_{0.94}S*, J. Phys.: Condens. Matter, **2012**, 24, 266004.
- [183] D. Zou, S. Xie, Y. Liu, J. Lin and J. Li, *Electronic Structures And Thermoelectric Properties of Layered BiCuOCh Oxychalcogenides (Ch = S, Se and Te): First-Principles Calculations*, J. Mater. Chem. A, **2013**, 1, 8888-8896.
- [184] T. M. Tritt, *Recent Trend In Thermoelectric Materials Research II, Chap 1, Use of Atomic Displacement Parameters In Thermoelectric Materials Research*, Semiconduct. Semimet., Academic Press, **2001**, 70, 1-34.
- [185] B. Sales, B. Chakoumakos, and D. Mandrus, *Thermoelectric Properties of Thallium-Filled Skutterudites*, Phys. Rev. B, **2000**, 61, 2475.

- [186] G. S. Nolas, *The Physics and Chemistry of Inorganic Clathrates, Springer Series in Materials Science*, Springer Netherlands, **2014**, 199.
- [187] P. Vaqueiro, S. D. N. Luu, G. Guélou, A. V. Powell, R. I. Smith, R. A. R. A. Orabi, J-P. Song, D. Wee, and M. Fornari, *The Role Of Copper Rattling In The Thermal Conductivity Of Thermoelectric Oxychalcogenides Do Lone Pairs Matter?* (submitted).
- [188] L. Pan, D. Bérardan, L-D. Zhao, C. Barreateau, and N. Dragoë, *Influence of Pb Doping On The Electrical Transport Properties Of BiCuSeO*, *J. App. Phys. Lett.*, **2013**, 102, 023902.
- [189] D. Bérardan, J. Li, E. Amzallag, S. Mitra, J. Sui, W. Cai and N. Dragoë, *Structure and Transport Properties of the BiCuSeO-BiCuSO Solid Solution*, *MPDI. Mater*, **2015**, 8, 1043-1058.
- [190] C. Barreateau, D. Bérardan, and N. Dragoë, *Studies On The Thermal Stability Of BiCuSeO*, *J. Solid State Chem.*, **2015**, 222, 53–59.
- [191] R. D. Abelson, Ch. 56, *Space Missions and Applications, Thermoelectrics Handbook: Macro to Nano*, ed. D.M. Rowe, CRC Press, Boca Raton, FL, **2006**.
- [192] E. S. Stampler, W. C. Sheets, M. I. Bertoni, W. Prellier, T. O. Mason, and K. R. Poeppelmeier, *Temperature Driven Reactant Solubilization Synthesis of BiCuOSe*, *Inorg.Chem.*, **2008**, 47, 10009-10016.
- [193] M. Palazzi, C. Carcaly, P. Laruelle, J. Flahaut, *Crystal Structure and Properties of (LaO)CuS and (LaO)AgS, The Rare Earths in Modern Science and Technology*, G. J. McCarthy *et al.* (eds.), Springer US, **1982**, 3, 347-350.
- [194] R. W. Rice, *Ceramic Fabrication Technology*, Marcel Dekker, New York Basel, **2003**.
- [195] A. M. Kusainova, P. S. Berdonosov, L. G. Akselrud, L. N. Kholodkovskaya, V. A. Dolgikh and B. A. Popovkin, *New Layered Compounds with the General Composition (MO) (CuSe), Where M = Bi, Nd, Gd, Dy, and BiOCuS: Syntheses and Crystal Structure*, *J. Solid State Chem.*, **1994**, 112, 189-191.
- [196] G. H. Chan, B. Den, M. Bertoni, J. R. Ireland, M. C. Hersam, T. O. Mason, R. P. Van Duyne and J. A. Ibers, *Syntheses, Structures, Physical Properties, and Theoretical Studies of CeM_xOS (M = Cu, Ag; x ≈ 0.8) and CeAgOS*, *Inorg. Chem.*, **2006**, 45 (20), 8264-8272.
- [197] M. L. Liu, L. B. Wu, F. Q. Huang, L. D. Chen and J. A. Ibers, *Syntheses, Crystal And Electronic Structure, And Some Optical And Transport Properties Of LnCuOTe (Ln = La, Ce, Nd)*, *J. Solid State Chem.*, **2007**, 180, 62-69.
- [198] K. Ueda, H. Hiramatsu, M. Hirano, T. Kamiya and H. Hosono, *Wide-Gap Layered Oxychalcogenide Semiconductors: Materials, Electronic Structures And Optoelectronic Properties*, *Thin Solid Films*, **2006**, 496 (1), 8-15.
- [199] G. S. Nolas, J. Sharp and H. J. Goldsmid, *Thermoelectrics: Basic Principles and New Materials Developments*, Springer, Berlin Heidelberg, **2001**.
- [200] C. Barreateau, D. Bérardan, L-D. Zhao, and N. Dragoë, *Influence of Te Substitution On The Structural And Electronic Properties Of Thermoelectric BiCuSeO*, *J. Mater. Chem. A*, **2013**, 1, 2921–2926.
- [201] T.-H. An, Y.S. Lim, H.-S. Choi, W.-S. Seo, C.-H. Park, G.-R. Kim, C. Park, C.H. Lee, J.H. Shim, *Point Defect-Assisted Doping Mechanism And Related*

- Thermoelectric Transport Properties In Pb-Doped BiCuOTe*, J. Mater. Chem. A, **2014**, 2, 19759–19764.
- [202] H. Scherrer and S. Scherrer, Ch. 19, *CRC Handbook of Thermoelectrics*, ed. D. M. Rowe, CRC Press, Boca Raton, FL, **1995**.
- [203] <http://minerals.usgs.gov/minerals/pubs/commodity/selenium/>
- [204] L-Börnstein, *Numerical Data and Functional Relationships in Science and Technology*, W. Martienssen (Ed), *Group III: Condensed Matter, Crystal Structures of Inorganic Compounds*, Springer-Verlag Berlin Heidelberg, **2007**, 43.
- [205] S. G. Tan, D. F. Shao, W. J. Lu, B. Yuan, Y. Liu, J. Yang, W. H. Song, H. Lei, and Y. P. Sun, *CuSe-Based Layered Compound Bi₂YO₄Cu₂Se₂ As A Quasi-Two-Dimensional Metal*, Phys. Rev. B, **2014**, 90, 085144.
- [206] Sui J Li J He J Pei Y-L Berardan D Wu H Dragoë N Cai W and Zhao L-D, *Texturation Boosts The Thermoelectric Performance Of BiCuSeO Oxyselenides*, Energy Environ. Sci., **2013**, 6 2916-2920.
- [207] V. Pele, C. Barreateau, D. Berardan, L-D. Zhao, N. Dragoë, *Direct Synthesis Of BiCuChO-Type Oxychalcogenides By Mechanical Alloying*, J. Solid State Chem., **2013**, 203, 187-191.
- [208] Y-C Liu, Y-H Zheng, B. Zhan, K. Chen, S. Butt, B. Zhang, Y-H Lin, *Influence Of Ag Doping On Thermoelectric Properties Of BiCuSeO*, J. Eur. Ceram. Soc., **2015**, 35, 845–849.
- [209] W. S. Liu, B. P. Zhang, J. F. Li, and L. D. Zhao, *Effects Of Sb Compensation On Microstructure, Thermoelectric Properties And Point Defect Of CoSb₃ Compound*, J. Phys. D, Appl. Phys., **2007**, 40, 6784–6790.
- [210] J. Corps, P. Vaquero and A. V. Powell, *Co₃M₂S₂ (M = Sn, In) Shandites As Tellurium-Free Thermoelectrics*, J. Mater. Chem. A, **2013**, 1, 6553-6557.
- [211] J.-L. Lan, Y.-C. Liu, B. Zhan, Y.-H. Lin, B. Zhang, X. Yuan, W. Zhang, W. Xu and C. W. Nan, *Enhanced Thermoelectric Properties Of Pb-Doped BiCuSeO Ceramics* Adv. Mater., **2013**, 25, 5086–5090.
- [212] Y.-C. Liu, J.-L. Lan, B. Zhan, J. Ding, Y. Liu, Y.-H. Lin, B. Zhang and C.-W. Nan, *Thermoelectric Properties Of Pb-Doped BiCuSeO Ceramics*, J. Am. Ceram. Soc., **2013**, 96, 2710–2713.
- [213] R. D. Shannon, *Revised Effective Ionic Radii And Systematic Studies Of Interatomic Distances In Halides And Chalcogenides*, Acta Crystallogr., Sect. A., **1976**, A32, 751-767.
- [214] D. Kenfaui, G. Bonnefont, D. Chateigner, G. Fantozzi, M. Gomina, and J. G. Noudem, *Ca₃Co₄O₉ Ceramics Consolidated By SPS Process: Optimisation Of Mechanical And Thermoelectric Properties*, Mater. Res. Bull., **2010**, 45 (9), 1240–1249.
- [215] T. Caillat, J.-P. Fleurial and A. Borshchevsky, *Preparation and Thermoelectric Properties of Semiconducting Zn₄Sb₃*, J. Phys. Chem. Solids, **1997**, 58, 1119-1125.
- [216] D. J. Singh and I. I. Mazin, *Calculated Thermoelectric Properties Of La-Filled Skutterudites*, Phys. Rev. B, **1997**, 56, R1650(R).

- [217] W. Liu, Z. Ren, and G. Chen, *Nanostructured Thermoelectric Materials, Thermoelectric Nanomaterials*, K. Koumoto, T. Mori (eds), Springer-Verlag Berlin Heidelberg, **2013**, 182, 255-285.
- [218] J. O. Carneiro, S. Azevedo, F. Fernandes, E. Freitas, M. Pereira, C. J. Tavares, S. Lanceros-Méndez, V. Teixeira, *Synthesis Of Iron-Doped TiO₂ Nanoparticles By Ball-Milling Process: The Influence Of Process Parameters On The Structural, Optical, Magnetic And Photocatalytic Properties*, J Mater Sci., **2014**, 49,7476–7488.
- [219] P. Scherrer, *Bestimmung Der Grösse Und Der Inneren Struktur Von Kolloidteilchen Mittels Röntgenstrahlen*, Nachr. Ges. Wiss. Göttingen., **1918**, 26, 98-100.
- [220] H. Wu, J. Carrete, Z. Zhang, Y. Qu, X. Shen, Z. Wang, L-D. Zhao and J. He, *Strong Enhancement Of Phonon Scattering Through Nanoscale Grains In Lead Sulfide Thermoelectrics*, NPG Asia Mater., **2014**, 6, e108.
- [221] Y. Song, Q. Sun, L.D. Zhao and F. Wang, *Rapid Synthesis Of Bi Substituted Ca₃Co₄O₉ By A Polyacrylamide Gel Method And Its High-Temperature Thermoelectric Power Factor* , Key Eng. Mat., **2010**, 434-435, 393 -396.
- [222] M. Ohtaki, *Nanostructured Oxide Thermoelectric Materials with Enhanced Phonon Scattering*, Oxide Thin Films, Multilayers, and Nanocomposites, P. Mele, T. Endo, S. Arisawa, C. Li, T. Tsuchiya (eds), Springer International Publishing, **2015**, 108-122.
- [223] P.H. M. Böttger, K. Valset, S. Deledda, and T. G. Finstad, *Influence of Ball-Milling, Nanostructuring, and Ag Inclusions on Thermoelectric Properties of ZnSb*, J. Electron. Mater., **2010**, 39 (9), 1583-1588.
- [224] M. Ohtaki, K. Araki and K. Yamamoto, *High Thermoelectric Performance of Dually Doped ZnO Ceramics*, J. Electron. Mater., **2009**, 38, 1234–1238.
- [225] J. P. Heremans, V. Jovovic, E. S. Toberer, A. Saramat, K. Kurosaki, A. Charoenphakdee, S. Yamanaka and G. J. Snyder, *Enhancement of Thermoelectric Efficiency In PbTe By Distortion of The Electronic Density of States*, Science, **2008**, 321, 554–557.
- [226] J. Liu, C.L. Wang, H. Peng, W.B. Su, H.C Wang, J.C. Li, J. L. Zhang, and L. M. Mei, *Thermoelectric Properties of Dy-Doped SrTiO₃ Ceramics*, J. Electron. Mater., **2012**, 41, 11, 3073-3076.
- [227] D. R. Clarke, *Materials Selection Guidelines For Low Thermal Conductivity Thermal Barrier Coatings*, Surf. Coat. Tech., **2003**, 163-164, 67-74.
- [228] G. Ren, S. Butt, Ch. Zeng, Y. Liu, B. Zhan, J. Lan, Y. Lin, C. Nan, *Electrical and Thermal Transport Behavior in Zn-Doped BiCuSeO Oxyselenides*, J. Electron. Mater., **2015**, 44 (6), 1627-1631.
- [229] G. Ren, S. Butt, Y. Liu, J. Lan, Y. Lin, C. Nan, F.Fu, and X. Tang, *Enhanced Thermoelectric Performance Of Zn-Doped Oxyselenides: BiCu_{1-x}Zn_xSeO*, Phys. Status Solidi. A, **2014**, 211 (11), 2616–2620.
- [230] C. Barreateau, L Pan, E. Amzalla, L D Zhao, D. Berardan and N. Dragoe, *Layered Oxychalcogenide in The Bi–Cu–O–Se System As Good Thermoelectric Materials*, Semicond. Sci. Tech., **2014**, 29, 064001.

- [231] M. J. Pitcher, C. F. Smura, S. J. Clarke, *Stoichiometric CeCuOS – A Well-Behaved Ce(III) Layered Oxysulfide*, Inorg. Chem., **2009**, 48 (19), 9054-9056.
- [232] K. Ueda, S. Hirose, H. Kawazoe, H. Hosono, *Electrical and Optical Properties of Layered Oxysulfides with CuS Layers: Sr–Cu–M–O–S System (M = Zn, Ga, In)*, Chem. Mater., **2001**, 13 (5), 1880-1883.
- [233] C. Persson, Y.-J. Zhao, S. Lany and A. Zunger, n-Type Doping of CuInSe₂ and CuGaSe₂, Phys. Rev. B, **2005**, 72, 035211.
- [234] L.-D. Zhao, J. He, Ch.-I. Wu, T. P. Hogan, X. Zhou, C. Uher, V. P. Dravid, and M. G. Kanatzidis, *Thermoelectrics With Earth Abundant Elements: High Performance p-Type PbS Nanostructured With SrS And CaS*, J. Am. Chem. Soc. **2012**, 134, 7902 – 7912.
- [235] P. Ruleova, C. Drasar, P. Losak, C.-P. Li, S. Ballikaya, C. Uher, *Thermoelectric Properties of Bi₂O₂Se*, Mater. Chem. Phys. **2010**, 119, 299–302.
- [236] C. Drasar, P. Ruleova, L. Benes, P. Lostak, *Preparation and Transport Properties of Bi₂ O₂ Se Single Crystals*, J. Electron. Mater., **2012**, 41, 2317–2321.
- [237] K. Zhang, C. Hu, Z. Kang, S. Wang, Y. Xi, H. Liu, *Synthesis And Thermoelectric Properties Of Bi₂O₂Se Nanosheets*, Mater. Res. Bull., **2013**, 48, 3968–3972.
- [238] T. V. Quang, H. Lim, M. Kim, *Temperature and Carrier-Concentration Dependences of The Thermoelectric Properties of Bismuth Selenide Dioxide Compounds*, J. Korean. Phys. Soc., **2012**, 61, 1728–1731.
- [239] D. Guo, C. Hu, Y. Xi, and K. Zhang, *Strain Effects To Optimize Thermoelectric Properties of Doped Bi₂O₂Se via Tran–Blaha Modified Becke–Johnson Density Functional Theory*, J. Phys. Chem. C., **2013**, 117, 21597–21602.
- [240] H. Boller, *Die Kristallstruktur von Bi₂O₂Se*, Monatsh. Chem., **1973**, 104, 916–919.
- [241] H. Oppermann, H. Göbel, H. Shadow, V. Vassilev, I. Markova-Deneva, *Thermochemische Untersuchungen zum System Bi/Se/O. I Das Phasendreieck Bi₂Se₃/Bi₂O₂Se/Se*, Z. Anorg. Allg. Chem., **1996**, 622, 2115–2218.
- [242] H. Oppermann, H. Göbel, U. Petasch, *Zustandsbarogramme Zustandsdiagramme Durch Gesamtdruckmessungen*, J. Therm. Anal., **1996**, 47, 595–604.
- [243] H. Oppermann, H. Göbel, *Phase Barograms – Phase Diagrams By Total Pressure Measurements*, Solid State Ionics, **1997**, 101–103, 1267–1272.
- [244] P. Schmidt, O. Rademacher, H. Opperman, *Untersuchung Der Phasenbeziehungen In Quaternären Systemem Bi₂O₃/Bi₂Ch₃/Bi₂Ch₃ (Ch = S, Se, Te)*, Z. Anorg. Allg. Chem., **1999**, 625, 255–261.
- [245] H. Oppermann, H. Göbel, P. Schmidt, H. Shadow, V. Vassilev, I. Markova-Deneva, *Thermochemische Untersuchungen Am System Bi/Se/O III. Zum quasibinären System Bi₂O₃- Bi₂Se₃ Und Zum Bereich Bi₂O₃-Bi₂O₂Se-Se-SeO₂*, Z. Naturforsch., **1999**, 54b, 261–269.
- [246] P. Schmidt, H. Oppermann, *Zum System Bi₂O₃/Bi₂Se₃/BiCl₃ I. Das Zustandsdiagramm Bi₂O₃/Bi₂Se₃/BiCl₃*, Z. Naturforsch., **2000**, 55b 603–613.
- [247] P. Schmidt, H. Oppermann, *Zur Chemie Von Mischphasen In Komplexen Zustandsdiagrammen. Das System Bi₂O₃/Bi₂Se₃/Bi₂Te₃*, Z. Naturforsch., **2000**, 55b, 627–637.

- [248] S. D. N. Luu and P. Vaqueiro, *Synthesis, Structural Characterisation and Thermoelectric Properties of $\text{Bi}_{1-x}\text{Pb}_x\text{OCuSe}$* , J. Mater. Chem. A., **2013**, 1, 12270 – 12275.
- [249] http://www.fiz-karlsruhe.de/icsd_web.html.
- [250] R. Benz, W. H. Zachariasen, *Crystal Structure of The Compounds $\text{U}_2\text{N}_2\text{X}$ And $\text{Th}_2\text{N}_2\text{X}$ With $\text{X} = \text{Sb}, \text{Te}$ And Bi* , Acta Cryst., **1970**, B26, 823–827.
- [251] R. Benz, *$\text{Ce}_2\text{O}_2\text{Sb}$ And $\text{Ce}_2\text{O}_2\text{Bi}$ Crystal Structure*, Acta Cryst. B., **1971**, 27 853–854.
- [252] H. Mizoguchi, H. Hosono, *A Metal–Insulator Transition In $\text{R}_2\text{O}_2\text{Bi}$ With An Unusual Bi^{2-} Square Net ($\text{R} = \text{Rare Earth or Y}$)*, J. Am. Chem. Soc., **2011**, 133, 2394–2397.
- [253] R. Patschke, M. G. Kanatzidis, *Polytelluride Compounds Containing Distorted Nets of Tellurium*, Phys. Chem. Chem. Phys., **2002**, 4, 3266–3281.
- [254] O. V. Magdysyuk, J. Nuss, M. Jansen, *Modulated Crystal Structure Of Pr_2SbO_2* , Acta Cryst., **2013**, B69, 547–555.
- [255] J.C. Perron, *Electrical and Thermoelectrical Properties of Selenium-Tellurium Liquid Alloys*, Adv. Phys., **1967**, 16 (64), 657-666.
- [256] J. W. Sharp, E. C. Jones, R. K. Williams, P M Martin, and B. C. Sales, *Thermoelectric Properties of CoSb_3 and Related Alloys*, J. Appl. Phys. **1995**, 78 (2),1013-1018.
- [257] B. Zhan, S. Butt, Y. Liu, J-L. Lan, C-W. Nan, Y-H. Lin, *High Temperature Thermoelectric Behaviours of Sn-Doped n-Type $\text{Bi}_2\text{O}_2\text{Se}$ Ceramics*, J Electroceram, **2014**, 5p.
- [258] N. F. Mott, *Conduction In Glasses Containing Transition Metal Ions*, J. Non-Cryst. Solids, **1968**, 1, 1-17; N. F. Mott, *Conduction in Non-Crystalline Materials*, 2nd ed, Clarendon Press, Oxford, **1993**.
- [259] A. Mahmood, S.M. Ramay, Y. Saeed, *First Principles Study of Band Structure And Density of States Of Rare Earth Oxytellurides $\text{R}_2\text{O}_2\text{Te}$ ($r = \text{La}, \text{Ce}, \text{Pr}$ and Nd)*, Optoelectron. Adv. Mat., **2014**, 8, 724–726.
- [260] B. Abeles, *Lattice Thermal Conductivity of Disordered Semiconductor Alloys At High Temperatures*, Phys. Rev. **1963**, 131, 1906.
- [261] M. D. Nielsen, V. Ozolins, J. P. Heremans, *Lone Pair Electrons Minimize Lattice Thermal Conductivity*, Energy Environ. Sci., **2013**, 6, 570–578.
- [262] M. Beaumale, T. Barbier, Y. Bréard, G. Guelou, A.V. Powell, P. Vaqueiro, E. Guilmeau, *Electron Doping And Phonon Scattering In $\text{Ti}_{1+x}\text{S}_2$ Thermoelectric Compounds*, Acta Mater., **2014**, 78, 86-92.
- [263] A. Kaltzoglou, P. Vaqueiro, T. Barbier, E. Guilmeau, and A. V. Powell, *Ordered-Defect Sulfides As Thermoelectric Materials*, J. Electron. Mater., **2014**, 43, 2029-2034.
- [264] J.-X. Zhu, R. Yu, H. Wang; L. L. Zhao, M. D. Jones, J. Dai, E. Abrahams, E.; Fang, M. Morosan, Q. Si, *Band Narrowing And Mott Localization In Iron Oxychalcogenides $\text{La}_2\text{O}_2\text{Fe}_2\text{O}(\text{Se},\text{S})_2$* , Phys. Rev. Lett., **2010**, 104, 216405.
- [265] H. J. Goldsmid, *Bismuth Telluride and Its Alloys as Materials for Thermoelectric Generation*, Materials, **2014**, 7, 2577-2592.

- [266] F. Gascoin and A. Maignan, *Order–Disorder Transition In AgCrSe₂: A New Route To Efficient Thermoelectrics*, Chem. Mater., **2011**, 23, 2510–2513.
- [267] C. Godart, A. P. Gonçalves, E. B. Lopes and B. Villeroy, *Role of Structures on Thermal Conductivity in Thermoelectric Materials, Properties and Applications of Thermoelectric Materials*, Zlatić V, Hewson A (eds),. NATO ASI Series B – Phys. Biophys., Springer, Netherlands, **2009**, 19–49.
- [268] S. Jin, X. Chen, J. Guo, M. Lei, J. Lin, J. Xi, W. Wang, and W. Wang, *Sr₂Mn₃Sb₂O₂ Type Oxyselenides: Structures, Magnetism, and Electronic Properties of Sr₂AO₂M₂Se₂ (A = Co, Mn; M = Cu, Ag)*, Inorg. Chem., **2012**, 51, 10185-10192.
- [269] M.-L. Liu, L.-B. Wu, F.-Q. Huang, L.-D. Chen, I.-W. Chen, *A Promising p-Type Transparent Conducting Material: Layered Oxysulfide [Cu₂S₂][Sr₃Sc₂O₅]*, J. Appl. Phys., **2007**, 102, 116108.
- [270] D. O. Scanlon, and G. W. Watson, *(Cu₂S₂)(Sr₃Sc₂O₅)—A Layered, Direct Band Gap, p-Type Transparent Conducting Oxychalcogenide: A Theoretical Analysis*, Chem. Mater., **2009**, 21, 5435-5442.
- [271] H. Yanagi, J. Tate, S. Park, C.-H. Park, D. A. Keszler, M. Hirano, and H. Hosono, *Valence Band Structure Of BaCuSF and BaCuSeF*, J. Appl. Phys., **2006**, 100, 083705.

Appendix A

This appendix consists of additional data and results relating to Chapter 3: Layered Oxychalcogenides BiOCuCh ($Ch = S, Se, Te$) and Bi₂YO₄Cu₂Se₂.

Table 1. Lattice parameters (a & c), volume (V), weighted residual error (R_{wp}), and Chi-square value (χ^2) using powder neutron diffraction data for BiOCuS samples as a function of temperature. The errors were shown as standard deviations.

Temperature	a (Å)	c (Å)	V (Å ³)	R_{wp} (%)	χ^2
T=293K	3.86921(1)	8.56111(4)	128.166(1)	1.46	2.137
T=373K	3.87744(1)	8.57672(5)	128.947(1)	1.59	2.786
T=473K	3.88678(1)	8.59522(5)	129.848(1)	1.48	2.071
T=573K	3.89646(1)	8.61525(5)	130.800(1)	1.50	2.287
T=623K	3.90137(1)	8.62567(6)	131.289(1)	1.53	2.567
T=673K	3.90633(2)	8.63652(6)	131.788(1)	1.71	2.510

Table 2. Bond lengths and angles using powder neutron diffraction data for BiOCuS samples. The errors are shown as standard deviations.

Bond lengths				
Temperature	Bi-O (Å)	Bi-S (Å)	Cu-S (Å)	
T=293K	2.3138(3)	3.1517(5)	2.4158(7)	
T=373K	2.3169(3)	3.1557(6)	2.4255(8)	
T=473K	2.3211(3)	3.1664(6)	2.4284(9)	
T=573K	2.3249(3)	3.1742(6)	2.4362(9)	
T=623K	2.3270(4)	3.1784(7)	2.4398(1)	
T=673K	2.3277(4)	3.1820(8)	2.4460(1)	
Bond angles				
	O-Bi-O (deg.)	S-Cu-S (deg.)	S-Cu-S (deg.)	Cu-S-Cu (deg.)
T=293K	113.48(2)	106.41(4)	111.02(2)	68.98(2)
T=373K	113.60(2)	106.13(5)	111.17(3)	68.83(3)
T=473K	113.71(3)	106.31(5)	111.07(3)	68.93(3)
T=573K	113.85(3)	106.20(6)	111.13(3)	68.87(3)
T=623K	113.92(3)	106.17(6)	111.15(3)	68.85(3)
T=673K	114.09(3)	105.98(7)	111.24(4)	68.76(4)

Table 3. Site occupancy factors (SOF), coordinates, and thermal factors (U_{iso}) using powder neutron diffraction data for BiOCuS samples as a function of temperature. The errors were shown as standard deviations.

	Atom	SOF	x	y	z	$U_{iso}(\text{\AA}^2)$
293K	Bi	1.0	1/4	1/4	0.14825(6)	0.0066(9)
	O	1.0	3/4	1/4	0	0.0058(1)
	Cu	1.0	3/4	1/4	1/2	0.0160(1)
	S	1.0	1/4	1/4		0.0074(3)
373K	Bi	1.0	1/4	1/4	0.14791(7)	0.0093(1)
	O	1.0	3/4	1/4	0	0.0076(2)
	Cu	1.0	3/4	1/4	1/2	0.0220(2)
	S	1.0	1/4	1/4	0.6697(1)	0.0109(4)
473K	Bi	1.0	1/4	1/4	0.14765(7)	0.0129(1)
	O	1.0	3/4	1/4	0	0.0101(2)
	Cu	1.0	3/4	1/4	1/2	0.0313(2)
	S	1.0	1/4	1/4	0.6694(2)	0.0149(4)
573K	Bi	1.0	1/4	1/4	0.14727(7)	0.0167(1)
	O	1.0	3/4	1/4	0	0.0124(2)
	Cu	1.0	3/4	1/4	1/2	0.0401(2)
	S	1.0	1/4	1/4	0.6698(2)	0.0166(4)
623K	Bi	1.0	1/4	1/4	0.14709(7)	0.0180(1)
	O	1.0	3/4	1/4	0	0.0144(2)
	Cu	1.0	3/4	1/4	1/2	0.0451(3)
	S	1.0	1/4	1/4	0.6699(2)	0.0194(4)
673K	Bi	1.0	1/4	1/4	0.14661(9)	0.0204(2)
	O	1.0	3/4	1/4	0	0.0151(2)
	Cu	1.0	3/4	1/4	1/2	0.0498(3)
	S	1.0	1/4	1/4	0.6705(2)	0.0205(5)

Table 4. Lattice parameters (a & c), volume (V), weighted residual error (R_{wp}), and Chi-square value (χ^2) using powder neutron diffraction data for BiOCuSe samples as a function of temperature. The errors were shown as standard deviations.

Temperature	a (Å)	c (Å)	V (Å ³)	R_{wp} (%)	χ^2
T=293K	3.93011(1)	8.93188(5)	137.960(1)	1.60	2.917
T=373K	3.93870(1)	8.94748(5)	138.805(1)	1.35	2.786
T=473K	3.94829(1)	8.96511(6)	139.757(1)	1.37	2.545
T=573K	3.95835(2)	8.98410(7)	140.768(1)	1.86	3.394
T=623K	3.96350(2)	8.99385(7)	141.288(1)	1.49	3.046
T=673K	3.96870(1)	9.00408(7)	141.819(1)	1.49	3.057

Table 5. Bond lengths and angles using powder neutron diffraction data for BiOCuSe samples. The errors are shown as standard deviations.

Bond lengths				
Temperature	Bi-O (Å)	Bi-Se (Å)	Cu-Se (Å)	
T=293K	2.3283(2)	3.2312(3)	2.5143(3)	
T=373K	2.3323(2)	3.2385(3)	2.5195(3)	
T=473K	2.3363(3)	3.2479(4)	2.5245(4)	
T=573K	2.3389(4)	3.2593(5)	2.5298(5)	
T=623K	2.3414(3)	3.2643(5)	2.5322(4)	
T=673K	2.3442(4)	3.2689(5)	2.5350(5)	
Bond angles				
	O-Bi-O (deg.)	Se-Cu-Se (deg.)	Se-Cu-Se (deg.)	Cu-Se-Cu (deg.)
T=293K	115.12(2)	102.81(2)	112.90(1)	67.09(1)
T=373K	115.21(2)	102.82(2)	112.90(1)	67.11(1)
T=473K	115.34(2)	102.89(2)	112.86(1)	67.14(1)
T=573K	115.60(3)	102.95(3)	112.83(2)	67.17(2)
T=623K	115.64(3)	103.00(3)	112.80(1)	67.20(1)
T=673K	115.67(3)	103.03(3)	112.79(1)	67.22(1)

Table 6. Site occupancy factors (SOF), coordinates, and thermal factors (U_{iso}) using powder neutron diffraction data for BiOCuSe samples as a function of temperature. The errors were shown as standard deviations.

	Atom	SOF	x	y	z	$U_{iso}(\text{\AA}^2)$
293K	Bi	1.0	1/4	1/4	0.13982(5)	0.0071(1)
	O	1.0	3/4	1/4	0	0.0065(2)
	Cu	1.0	3/4	1/4	1/2	0.0147(2)
	Se	1.0	1/4	1/4	0.67542(6)	0.0069(2)
373K	Bi	1.0	1/4	1/4	0.13966(5)	0.0101(1)
	O	1.0	3/4	1/4	0	0.0086(2)
	Cu	1.0	3/4	1/4	1/2	0.0209(2)
	Se	1.0	1/4	1/4	0.67564(6)	0.0097(1)
473K	Bi	1.0	1/4	1/4	0.13936 (6)	0.0138(2)
	O	1.0	3/4	1/4	0	0.0115(2)
	Cu	1.0	3/4	1/4	1/2	0.0288(2)
	Se	1.0	1/4	1/4	0.67552(6)	0.0129(2)
573K	Bi	1.0	1/4	1/4	0.13873 (8)	0.0166(3)
	O	1.0	3/4	1/4	0	0.0132(3)
	Cu	1.0	3/4	1/4	1/2	0.0362(4)
	Se	1.0	1/4	1/4	0.6752(1)	0.0148(3)
623K	Bi	1.0	1/4	1/4	0.13864(7)	0.0192(2)
	O	1.0	3/4	1/4	0	0.0158(3)
	Cu	1.0	3/4	1/4	1/2	0.0425(3)
	Se	1.0	1/4	1/4	0.67527(8)	0.0179(2)
673K	Bi	1.0	1/4	1/4	0.13860(8)	0.0239(2)
	O	1.0	3/4	1/4	0	0.0171(3)
	Cu	1.0	3/4	1/4	1/2	0.0498(3)
	Se	1.0	1/4	1/4	0.67521(9)	0.0206(2)

Table 7. Lattice parameters (a & c), volume (V), weighted residual error (R_{wp}), and Chi-square value (χ^2) using powder neutron diffraction data for BiOCuTe samples as a function of temperature. The errors were shown as standard deviations.

Temperature	a (Å)	c (Å)	V (Å ³)	R_{wp} (%)	χ^2
T=293K	4.03920(1)	9.52660(6)	155.428(1)	1.52	2.452
T=373K	4.04922(1)	9.54293(7)	156.467(1)	1.58	2.274
T=473K	4.06023(2)	9.56161(7)	157.628(1)	1.43	2.232
T=573K	4.07134(2)	9.58244(9)	158.837(2)	1.53	3.075
T=623K	4.07691(2)	9.59381(8)	159.460(1)	1.35	1.967
T=673K	4.08230(2)	9.60610(1)	160.088(2)	1.62	3.058

Table 8. Bond lengths and angles using powder neutron diffraction data for BiOCuTe samples. The errors are shown as standard deviations.

Bond lengths				
Temperature	Bi-O (Å)	Bi-Te (Å)	Cu-Te (Å)	
T=293K	2.3553(3)	3.3953(5)	2.6498(5)	
T=373K	2.3599(3)	3.4052(6)	2.6539(6)	
T=473K	2.3650(3)	3.4150(6)	2.6598(6)	
T=573K	2.3677(4)	3.4302(8)	2.6631(7)	
T=623K	2.3723(4)	3.4327(7)	2.6670(7)	
T=673K	2.3756(5)	3.4353(9)	2.6725(8)	
Bond angles				
	O-Bi-O (deg.)	Te-Cu-Te (deg.)	Te-Cu-Te (deg.)	Cu-Te-Cu (deg.)
T=293K	118.07(2)	99.31(3)	114.78(1)	65.22(1)
T=373K	118.17(3)	99.44(3)	114.71(2)	65.29(2)
T=473K	118.28(3)	99.51(3)	114.67(2)	65.33(2)
T=573K	118.58(4)	99.71(4)	114.56(2)	65.44(2)
T=623K	118.47(3)	99.69(3)	114.57(2)	65.43(2)
T=673K	118.46(4)	99.59(4)	114.62(2)	65.38(2)

Table 9. Site occupancy factors (SOF), coordinates, and thermal factors (U_{iso}) using powder neutron diffraction data for BiOCuTe samples as a function of temperature. The errors were shown as standard deviations.

	Atom	SOF	x	y	z	$U_{iso}(\text{\AA}^2)$
293K	Bi	1.0	1/4	1/4	0.12721(5)	0.0106(1)
	O	1.0	3/4	1/4	0	0.0076(2)
	Cu	1.0	3/4	1/4	1/2	0.0157(2)
	Te	1.0	1/4	1/4	0.68007(8)	0.0091(2)
373K	Bi	1.0	1/4	1/4	0.12705(7)	0.0147(2)
	O	1.0	3/4	1/4	0	0.0103(2)
	Cu	1.0	3/4	1/4	1/2	0.0223(2)
	Te	1.0	1/4	1/4	0.67980(9)	0.0122(2)
473K	Bi	1.0	1/4	1/4	0.12687(7)	0.0193(2)
	O	1.0	3/4	1/4	0	0.0142(2)
	Cu	1.0	3/4	1/4	1/2	0.0313(2)
	Te	1.0	1/4	1/4	0.67972(9)	0.0164(2)
573K	Bi	1.0	1/4	1/4	0.12619(9)	0.0252(2)
	O	1.0	3/4	1/4	0	0.0181(3)
	Cu	1.0	3/4	1/4	1/2	0.0419(3)
	Te	1.0	1/4	1/4	0.6792(1)	0.0197(3)
623K	Bi	1.0	1/4	1/4	0.12648(8)	0.0275(2)
	O	1.0	3/4	1/4	0	0.0199(3)
	Cu	1.0	3/4	1/4	1/2	0.0472(3)
	Te	1.0	1/4	1/4	0.6793(1)	0.0227(3)
673K	Bi	1.0	1/4	1/4	0.1265(1)	0.0297(3)
	O	1.0	3/4	1/4	0	0.0225(3)
	Cu	1.0	3/4	1/4	1/2	0.0534(4)
	Te	1.0	1/4	1/4	0.6796(1)	0.0245(3)

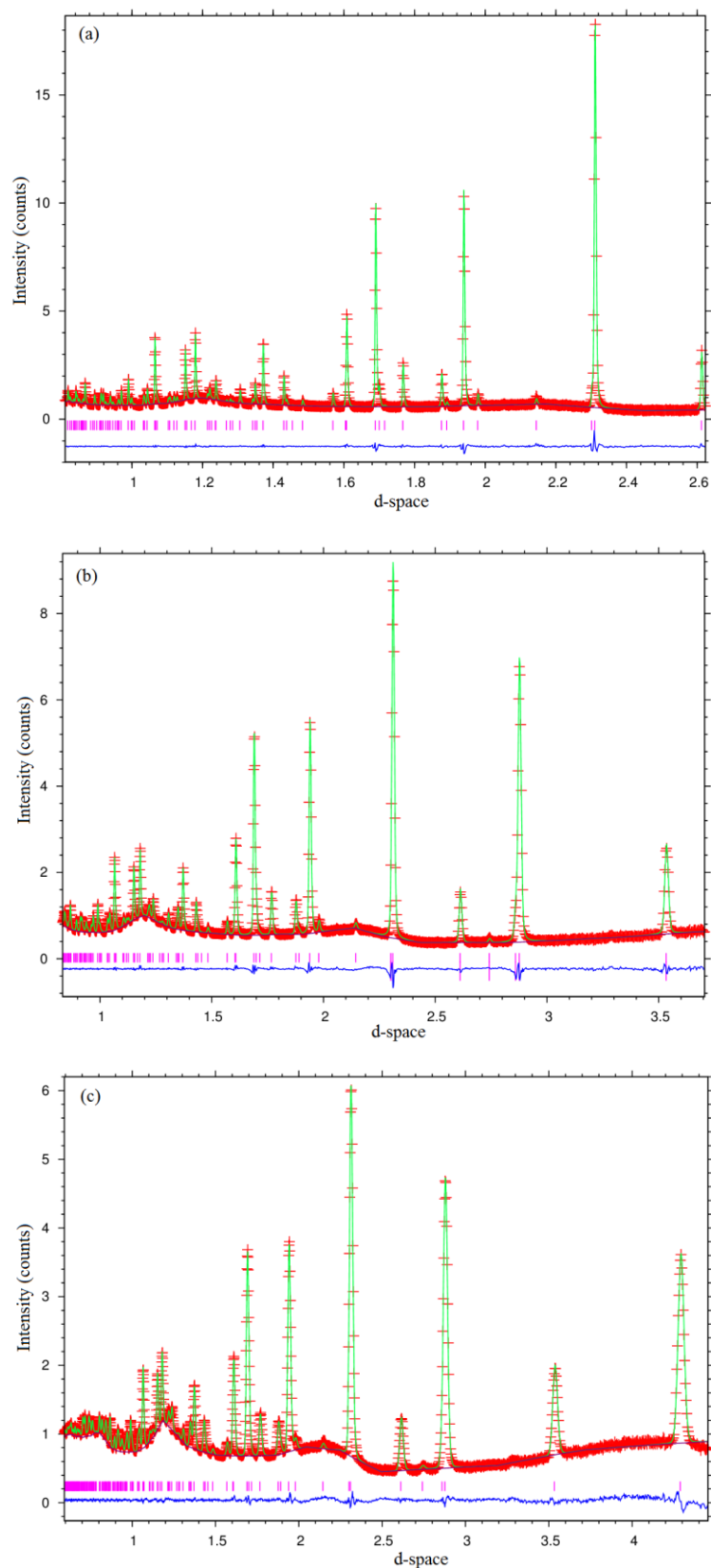


Figure 1. Rietveld refinement using powder neutron diffraction data collected on POLARIS for BiOCuS at 373 K from (a) backscattering bank ($2\theta = 146.72^\circ$), (b) 92.59° bank and (c) low angle bank ($2\theta = 52.21^\circ$). Key: observed data (red cross); difference curve (blue line); calculated pattern (green line) and reflection positions (pink markers).

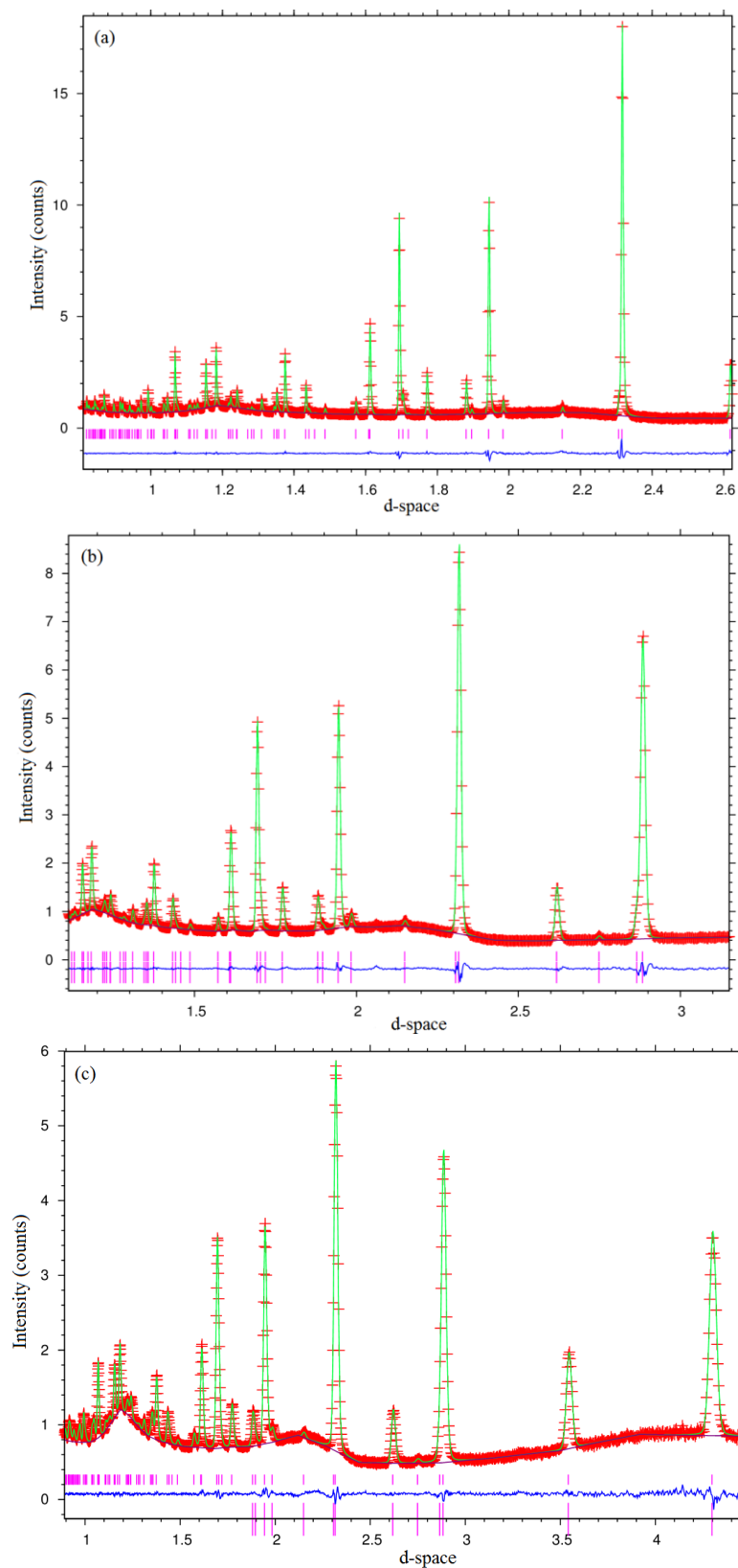


Figure 2. Rietveld refinement using powder neutron diffraction data collected on POLARIS for BiOCuS at 473 K from (a) backscattering bank ($2\theta = 146.72^\circ$), (b) 92.59° bank and (c) low angle bank ($2\theta = 52.21^\circ$). Key: observed data (red cross); difference curve (blue line); calculated pattern (green line) and reflection positions (pink markers).

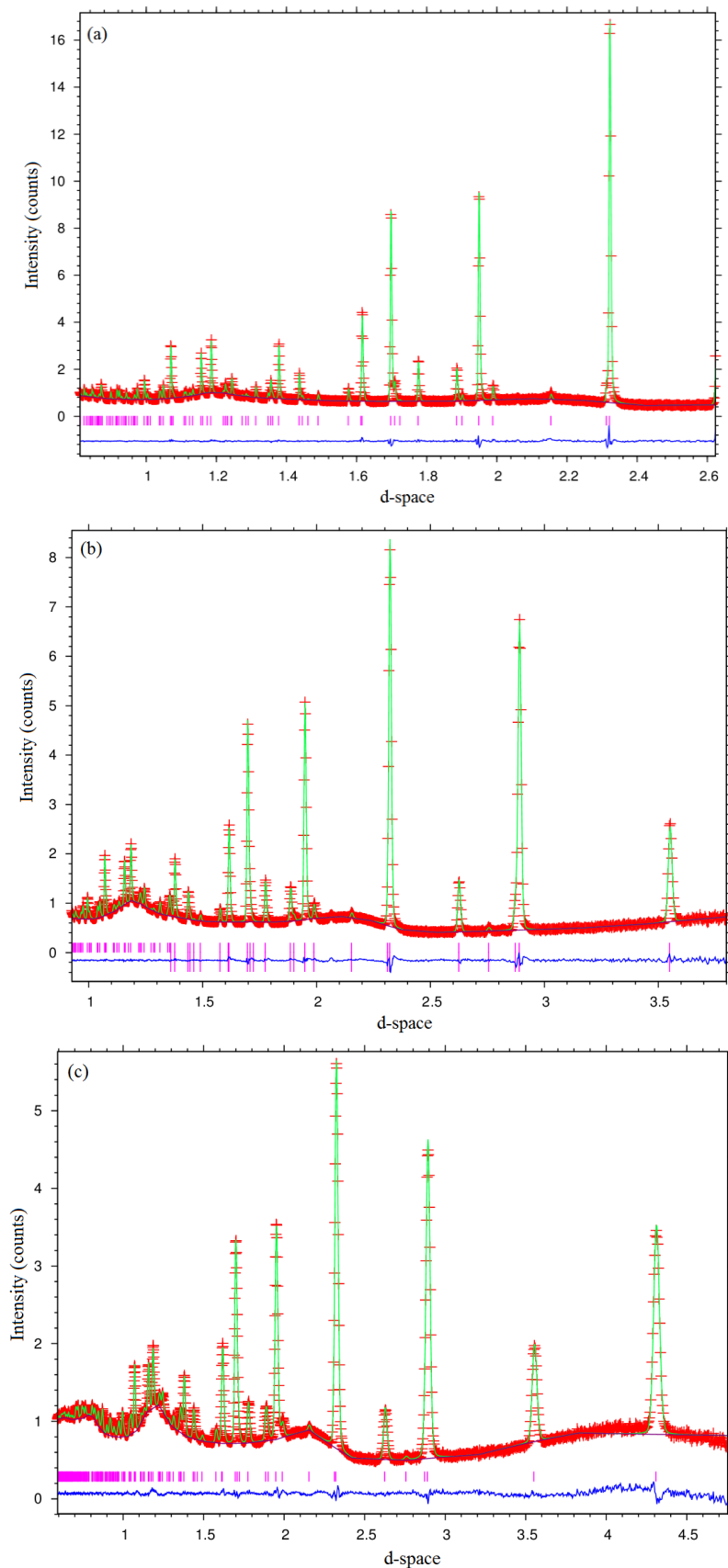


Figure 3. Rietveld refinement using powder neutron diffraction data collected on POLARIS for BiOCuS at 573 K from (a) backscattering bank ($2\theta = 146.72^\circ$), (b) 92.59° bank and (c) low angle bank ($2\theta = 52.21^\circ$). Key: observed data (red cross); difference curve (blue line); calculated pattern (green line) and reflection positions (pink markers).

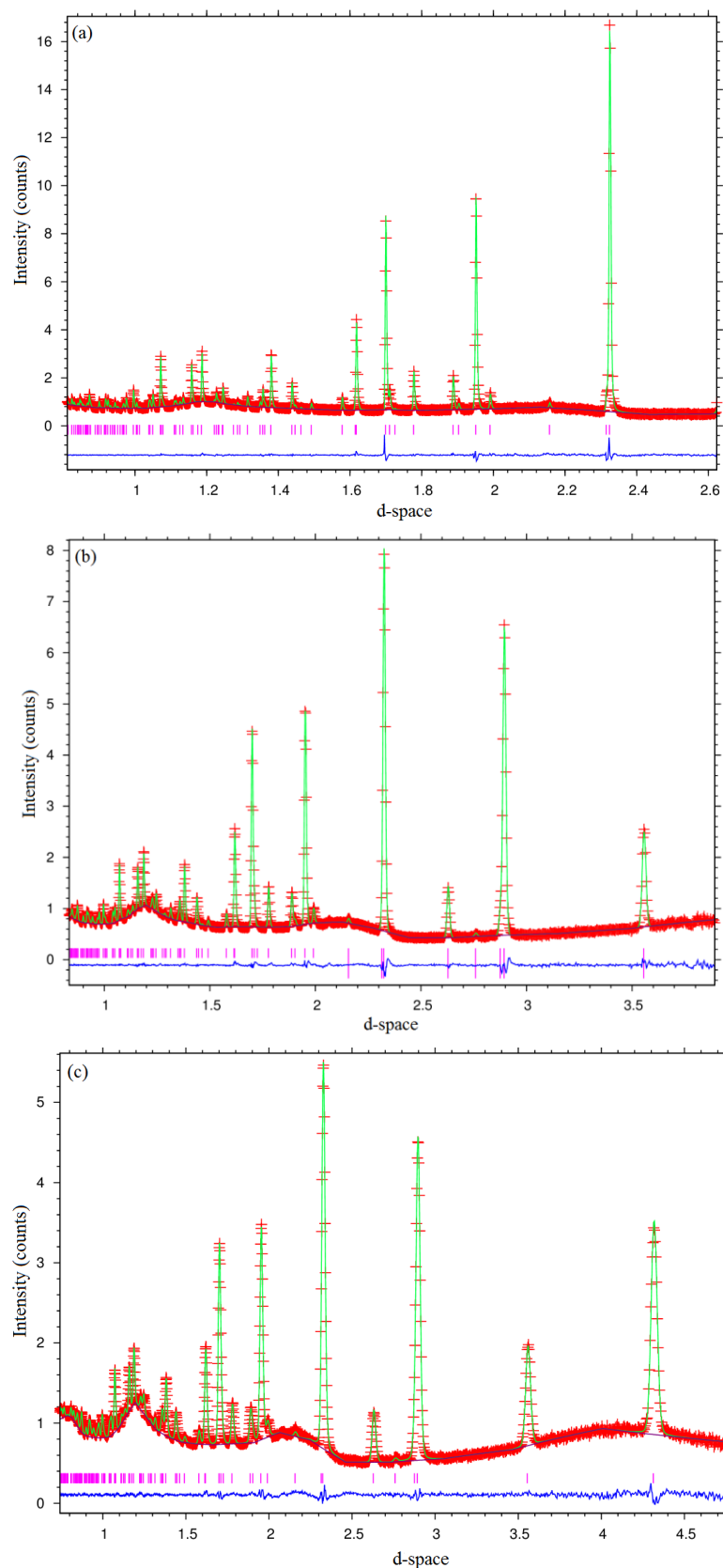


Figure 4. Rietveld refinement using powder neutron diffraction data collected on POLARIS for BiOCuS at 623 K from (a) backscattering bank ($2\theta = 146.72^\circ$), (b) 92.59° bank and (c) low angle bank ($2\theta = 52.21^\circ$). Key: observed data (red cross); difference curve (blue line); calculated pattern (green line) and reflection positions (pink markers).

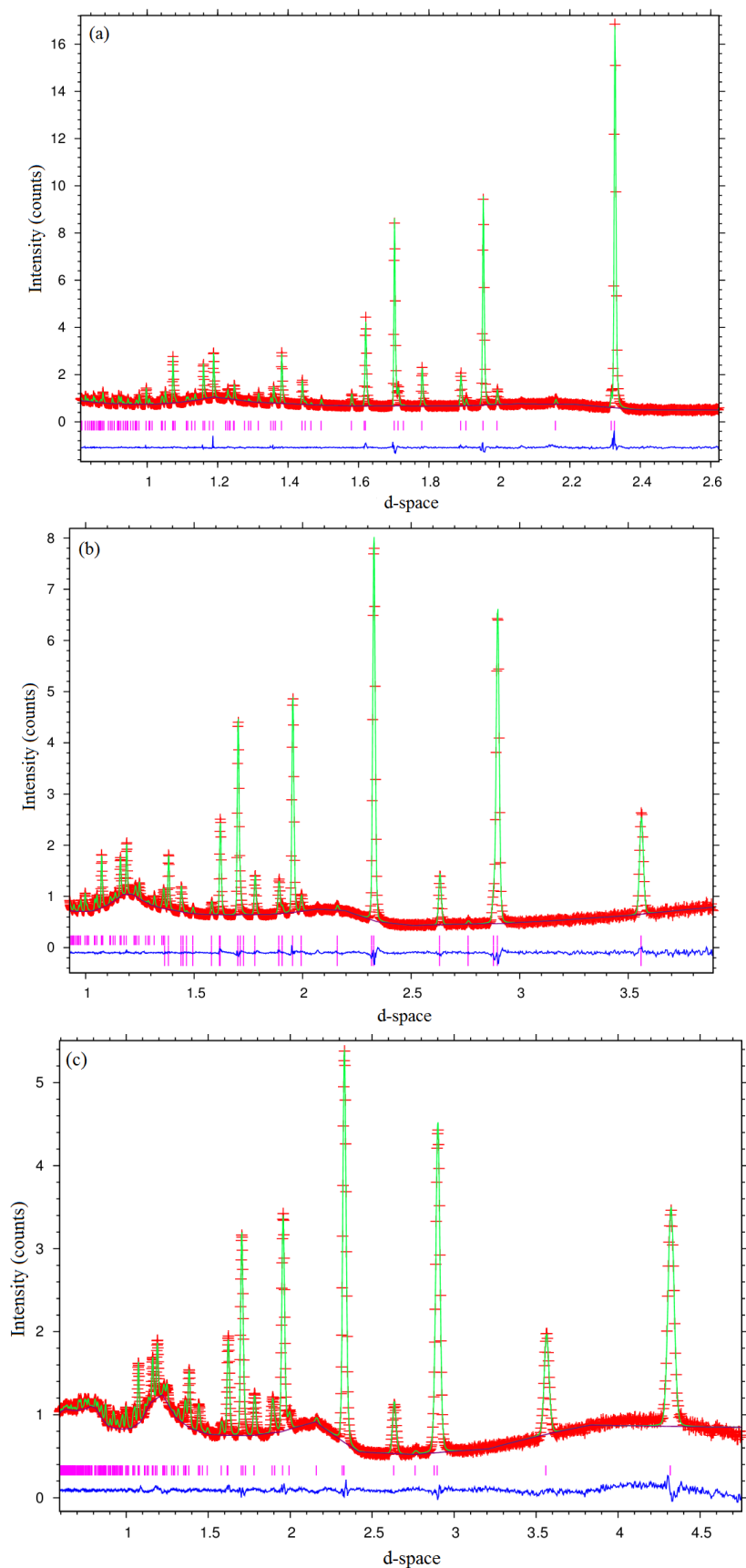


Figure 5. Rietveld refinement using powder neutron diffraction data collected on POLARIS for BiOCuS at 673 K from (a) backscattering bank ($2\theta = 146.72^\circ$), (b) 92.59° bank and (c) low angle bank ($2\theta = 52.21^\circ$). Key: observed data (red cross); difference curve (blue line); calculated pattern (green line) and reflection positions (pink markers).

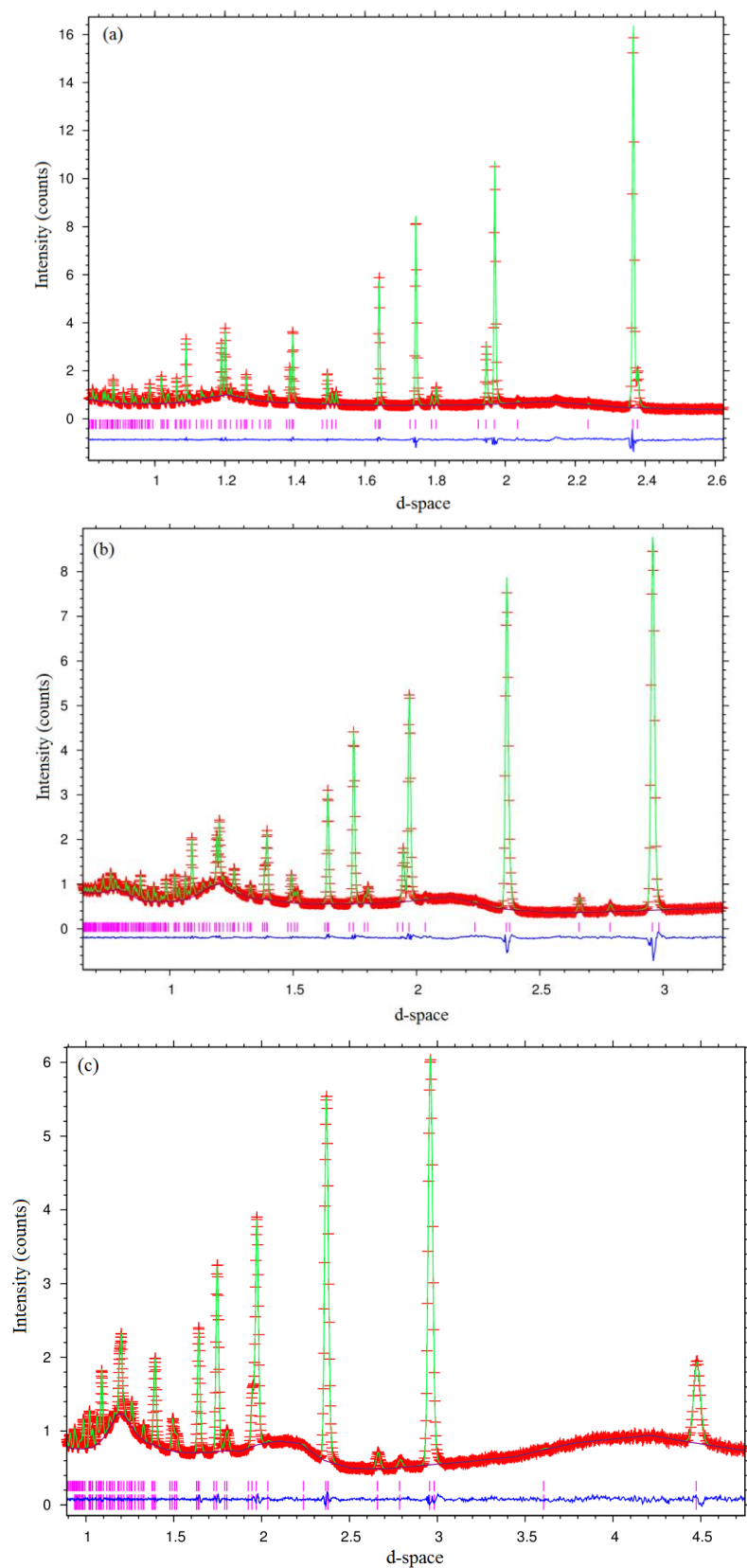


Figure 6. Rietveld refinement using powder neutron diffraction data collected on POLARIS for BiOCuSe at 373 K from (a) backscattering bank ($2\theta = 146.72^\circ$), (b) 92.59° bank and (c) low angle bank ($2\theta = 52.21^\circ$). Key: observed data (red cross); difference curve (blue line); calculated pattern (green line) and reflection positions (pink markers).

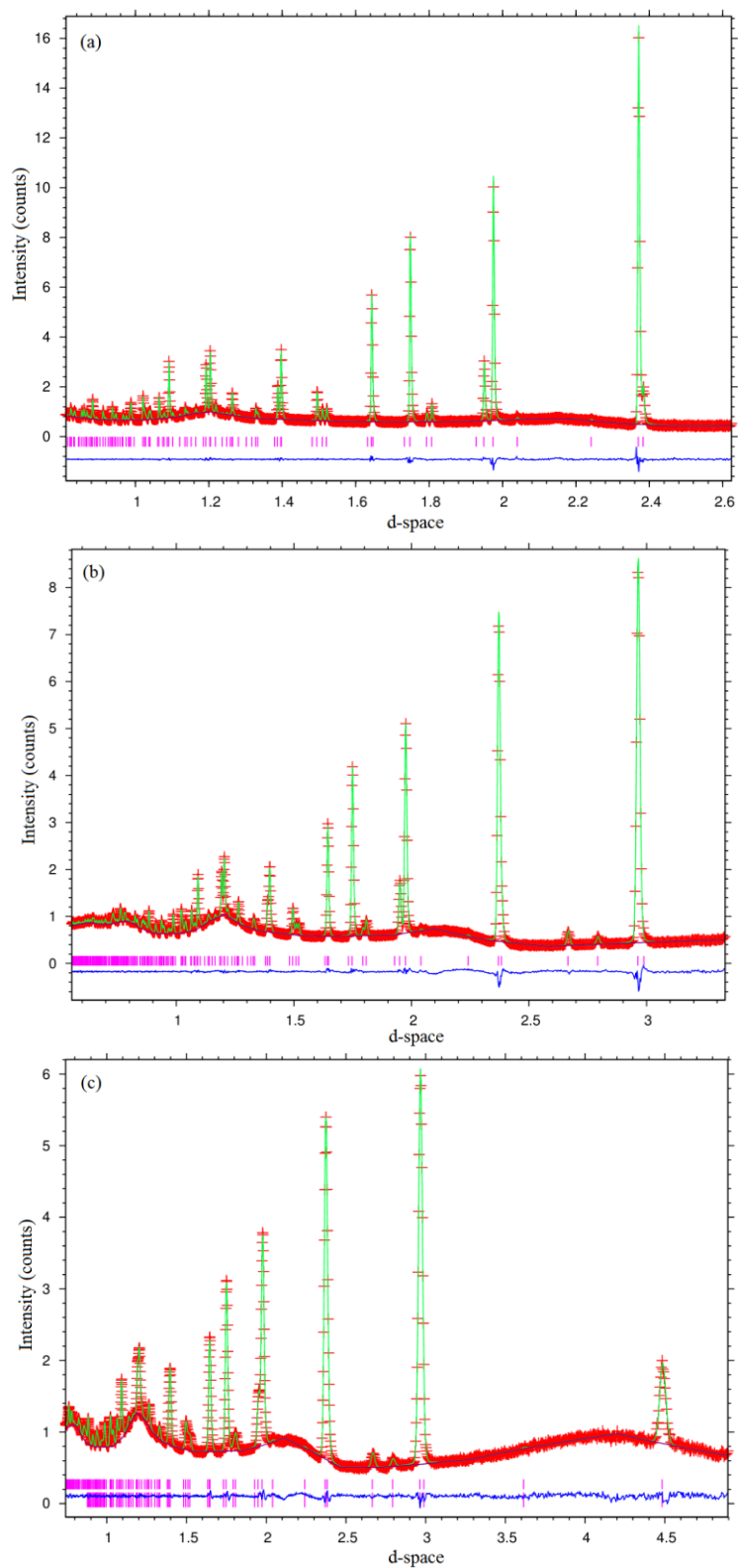


Figure 7. Rietveld refinement using powder neutron diffraction data collected on POLARIS for BiOCuSe at 473 K from (a) backscattering bank ($2\theta = 146.72^\circ$), (b) 92.59° bank and (c) low angle bank ($2\theta = 52.21^\circ$). Key: observed data (red cross); difference curve (blue line); calculated pattern (green line) and reflection positions (pink markers).

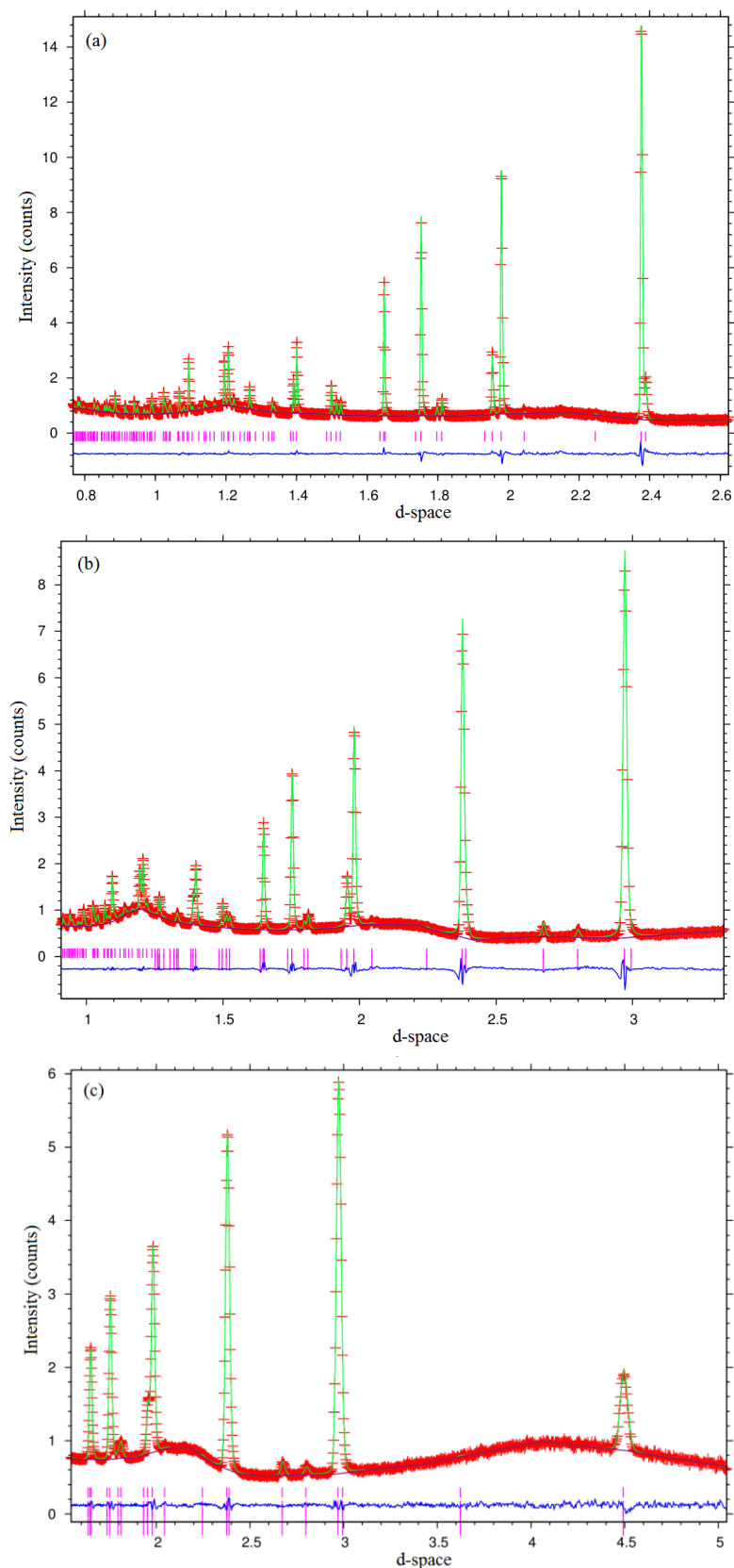


Figure 8. Rietveld refinement using powder neutron diffraction data collected on POLARIS for BiOCuSe at 573 K from (a) backscattering bank ($2\theta = 146.72^\circ$), (b) 92.59° bank and (c) low angle bank ($2\theta = 52.21^\circ$). Key: observed data (red cross); difference curve (blue line); calculated pattern (green line) and reflection positions (pink markers).

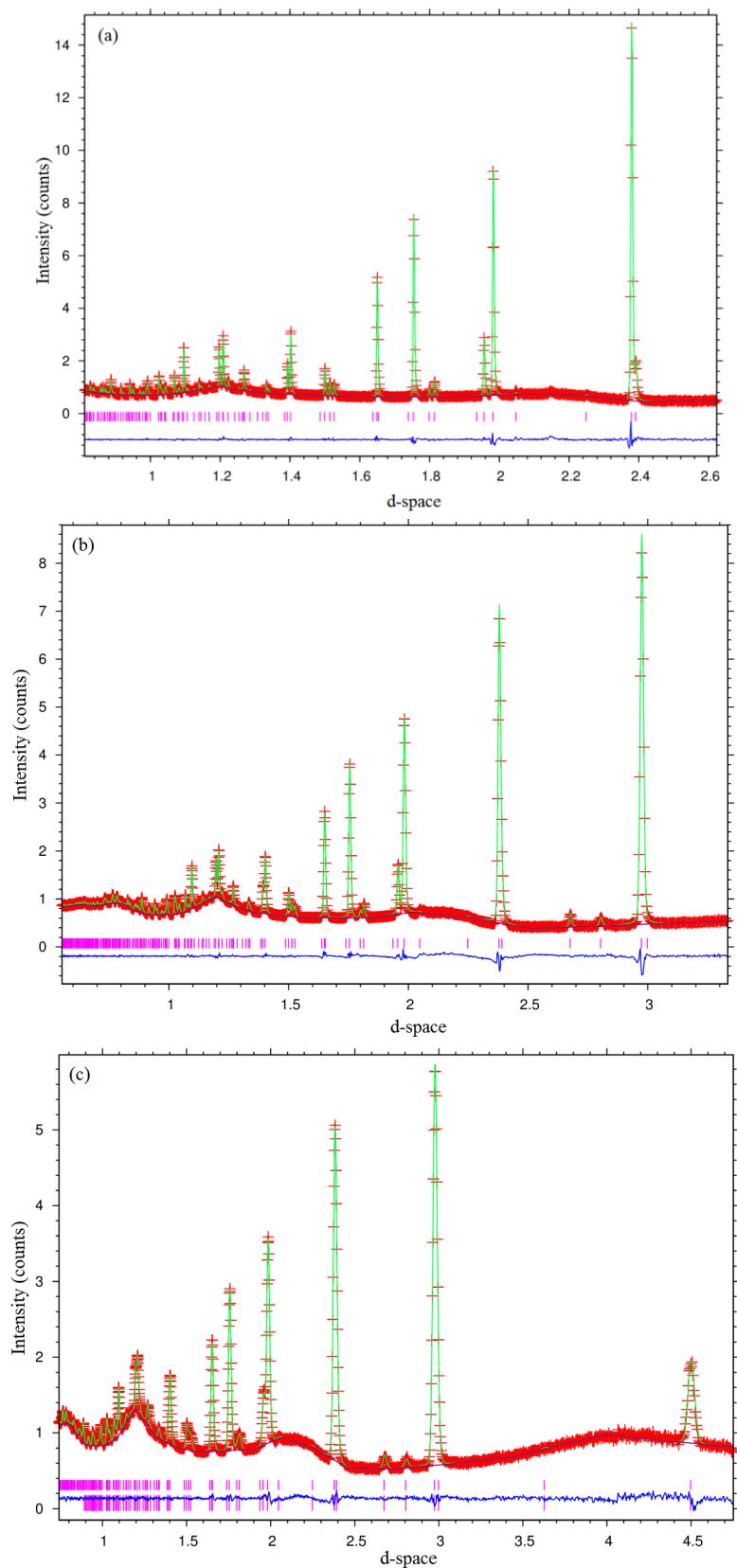


Figure 9. Rietveld refinement using powder neutron diffraction data collected on POLARIS for BiOCuSe at 623 K from (a) backscattering bank ($2\theta = 146.72^\circ$), (b) 92.59° bank and (c) low angle bank ($2\theta = 52.21^\circ$). Key: observed data (red cross); difference curve (blue line); calculated pattern (green line) and reflection positions (pink markers).

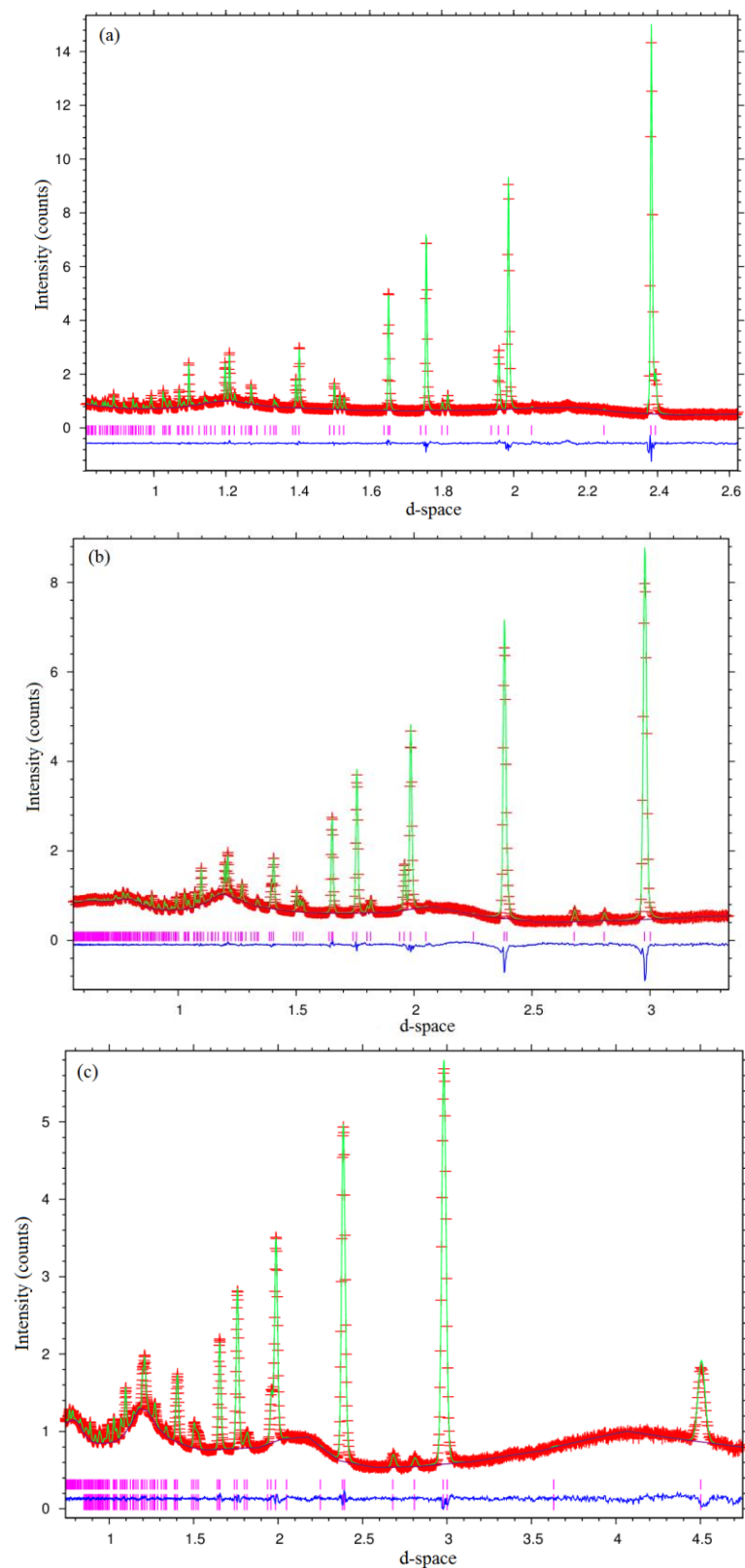


Figure 10. Rietveld refinement using powder neutron diffraction data collected on POLARIS for BiOCuSe at 673 K from (a) backscattering bank ($2\theta = 146.72^\circ$), (b) 92.59° bank and (c) low angle bank ($2\theta = 52.21^\circ$). Key: observed data (red cross); difference curve (blue line); calculated pattern (green line) and reflection positions (pink markers).

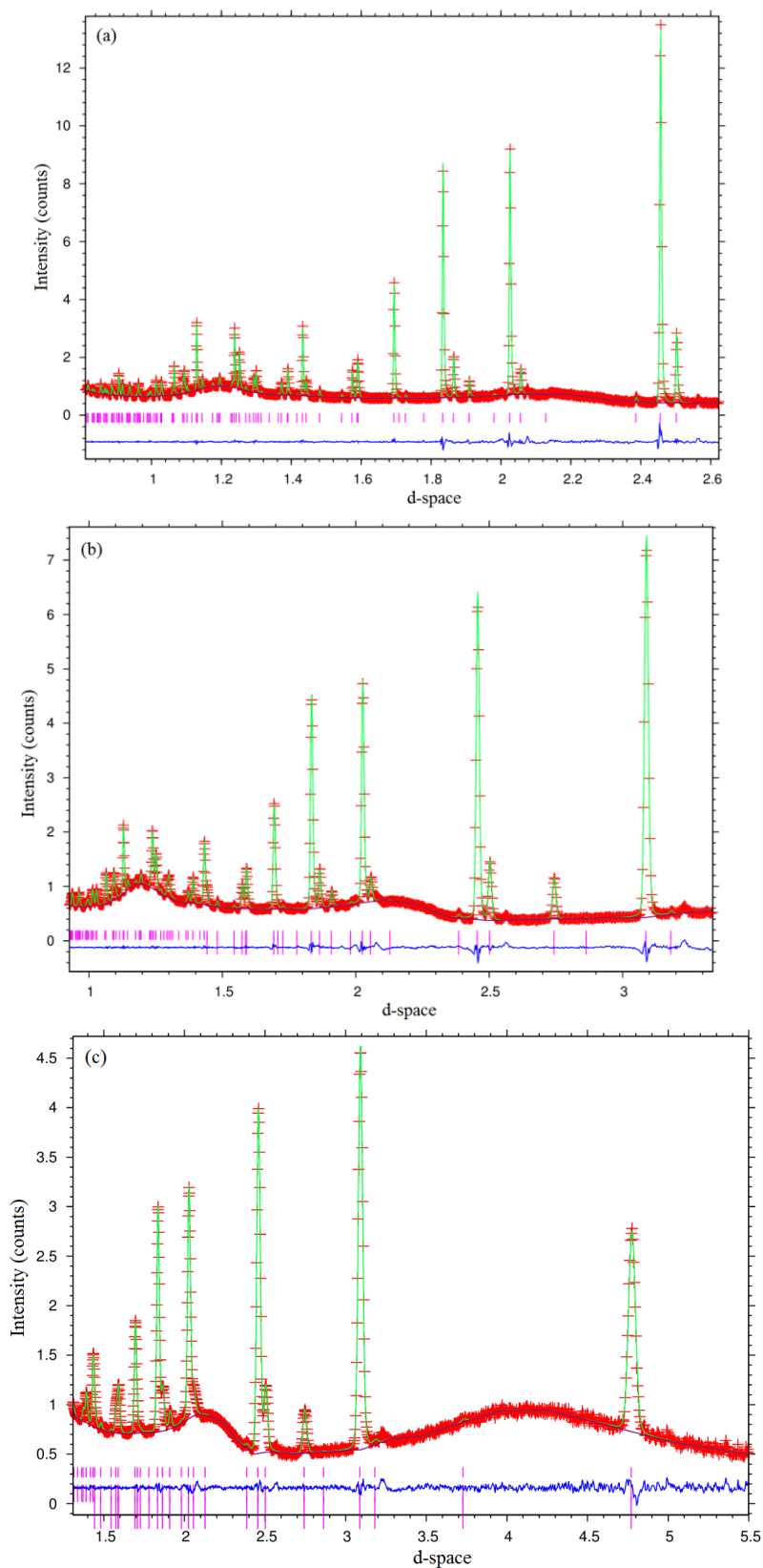


Figure 11. Rietveld refinement using powder neutron diffraction data collected on POLARIS for BiOCuTe at 373 K from (a) backscattering bank ($2\theta = 146.72^\circ$), (b) 92.59° bank and (c) low angle bank ($2\theta = 52.21^\circ$). Key: observed data (red cross); difference curve (blue line); calculated pattern (green line) and reflection positions (pink markers).

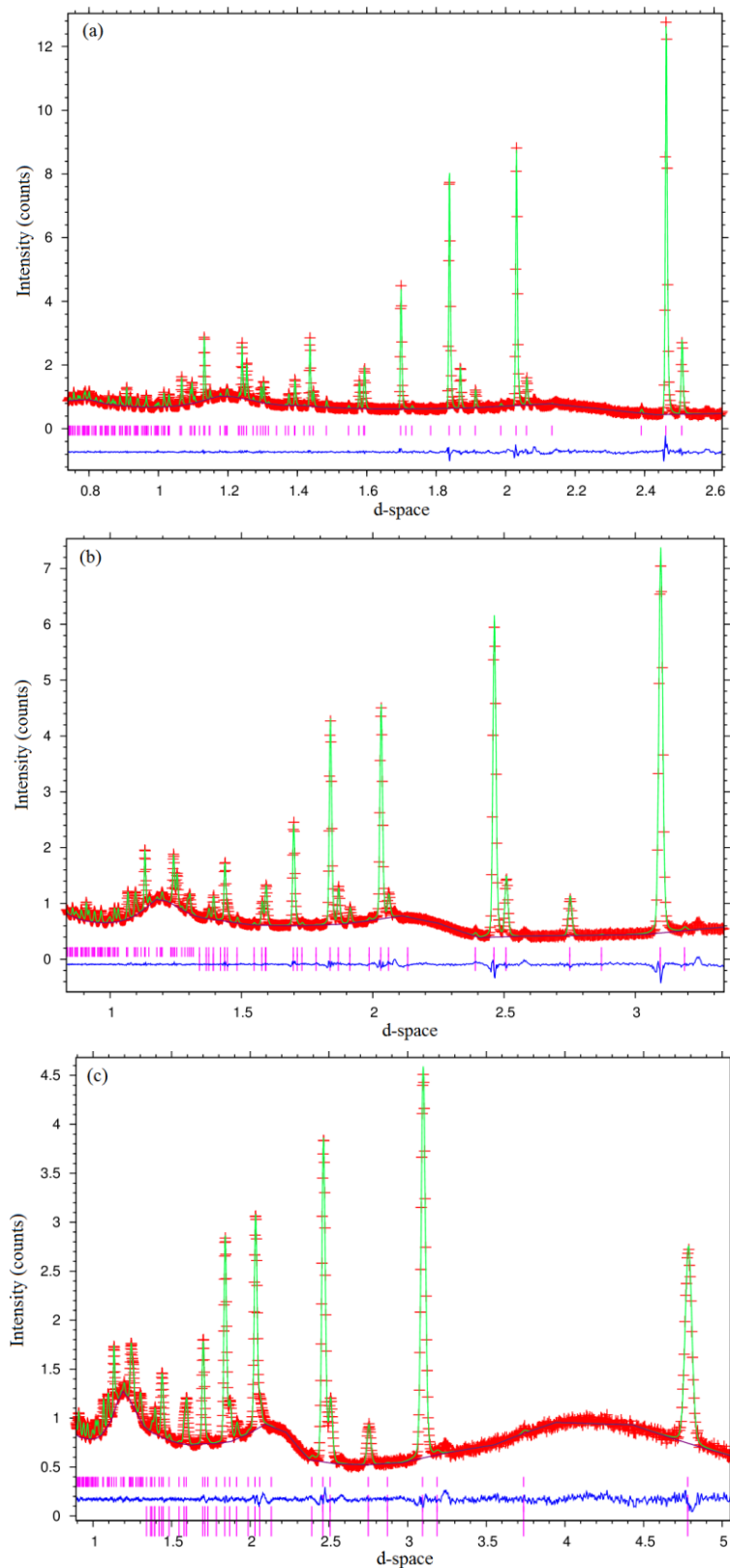


Figure 12. Rietveld refinement using powder neutron diffraction data collected on POLARIS for BiOCuTe at 473 K from (a) backscattering bank ($2\theta = 146.72^\circ$), (b) 92.59° bank and (c) low angle bank ($2\theta = 52.21^\circ$). Key: observed data (red cross); difference curve (blue line); calculated pattern (green line) and reflection positions (pink markers).

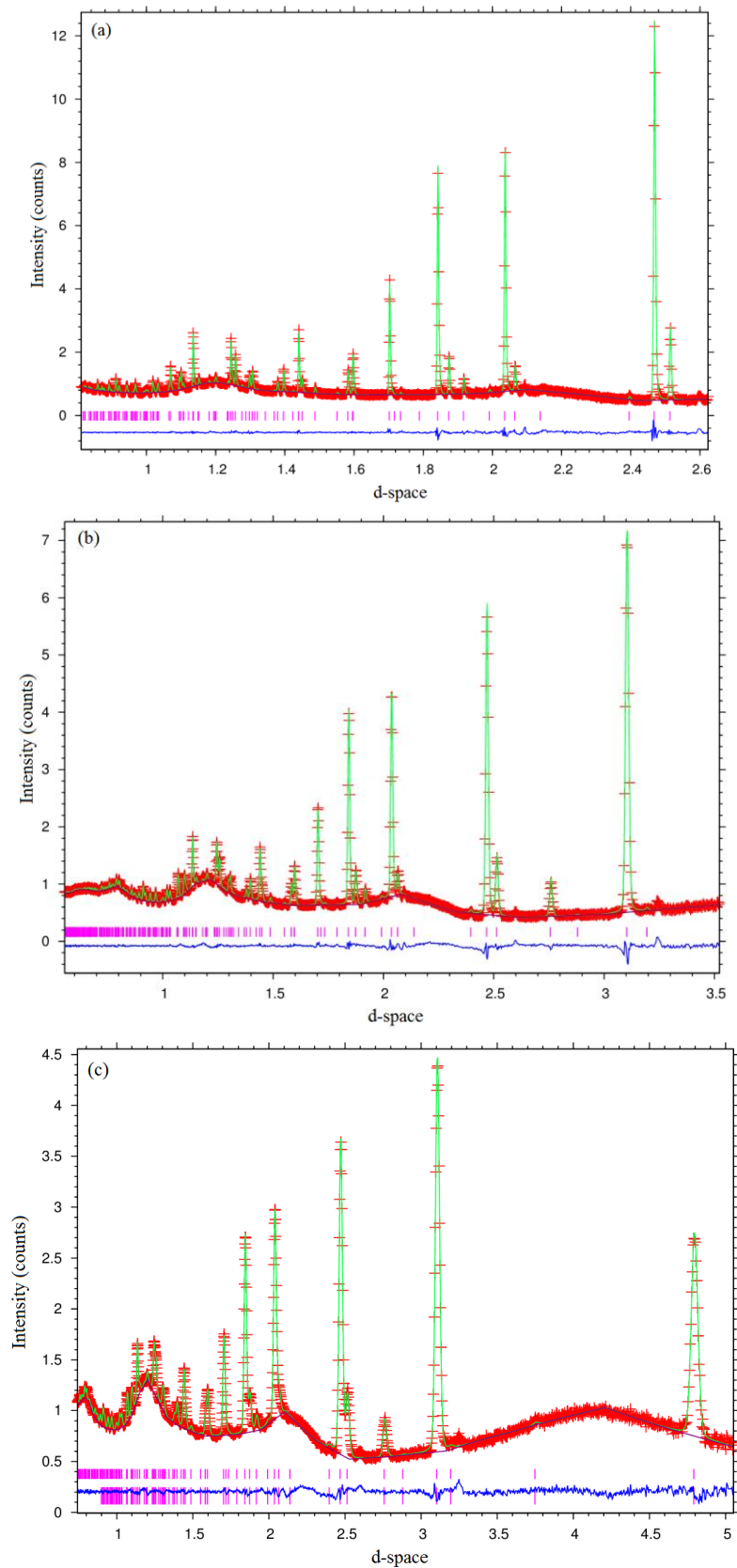


Figure 13. Rietveld refinement using powder neutron diffraction data collected on POLARIS for BiOCuTe at 573 K from (a) backscattering bank ($2\theta = 146.72^\circ$), (b) 92.59° bank and (c) low angle bank ($2\theta = 52.21^\circ$). Key: observed data (red cross); difference curve (blue line); calculated pattern (green line) and reflection positions (pink markers).

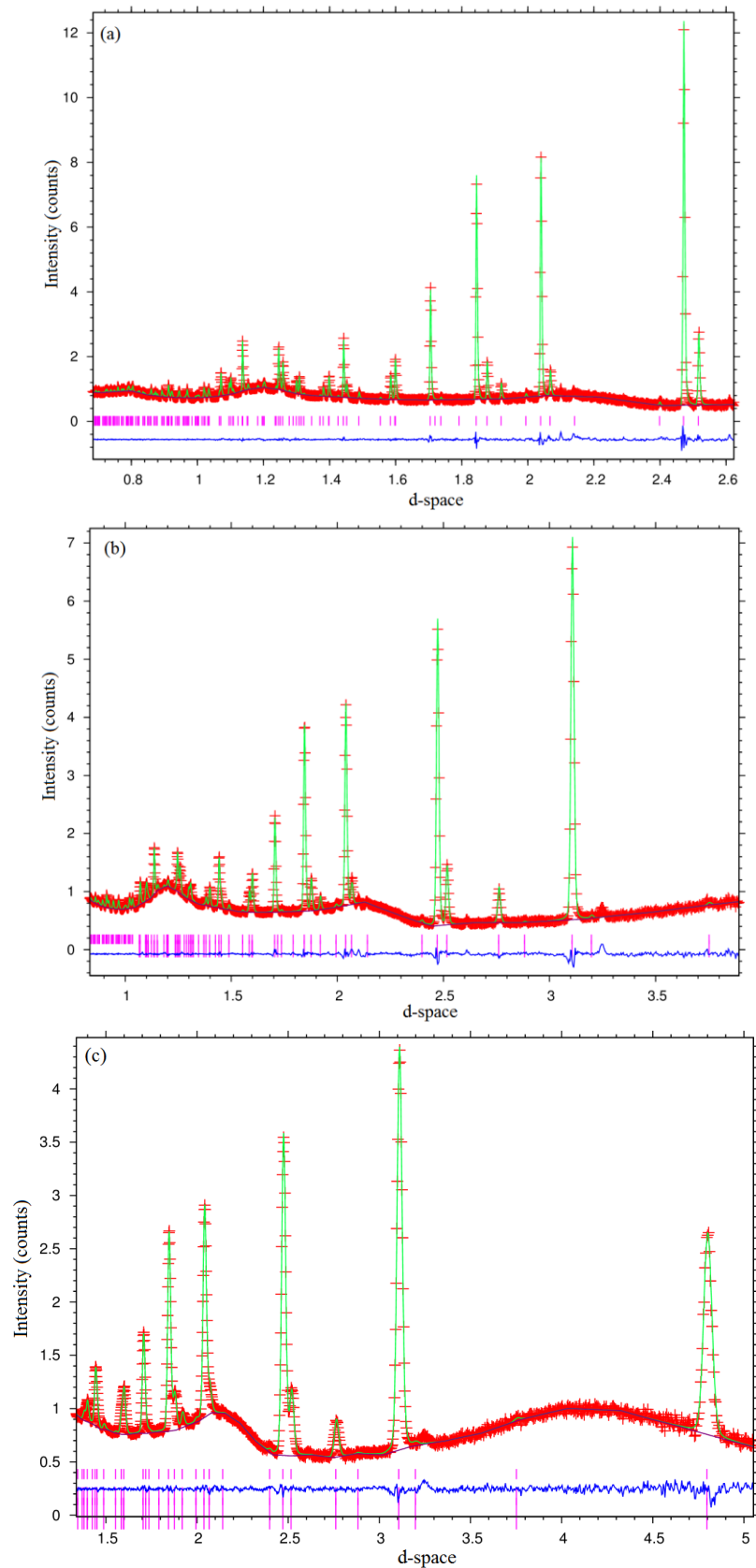


Figure 14. Rietveld refinement using powder neutron diffraction data collected on POLARIS for BiOCuTe at 623 K from (a) backscattering bank ($2\theta = 146.72^\circ$), (b) 92.59° bank and (c) low angle bank ($2\theta = 52.21^\circ$). Key: observed data (red cross); difference curve (blue line); calculated pattern (green line) and reflection positions (pink markers).

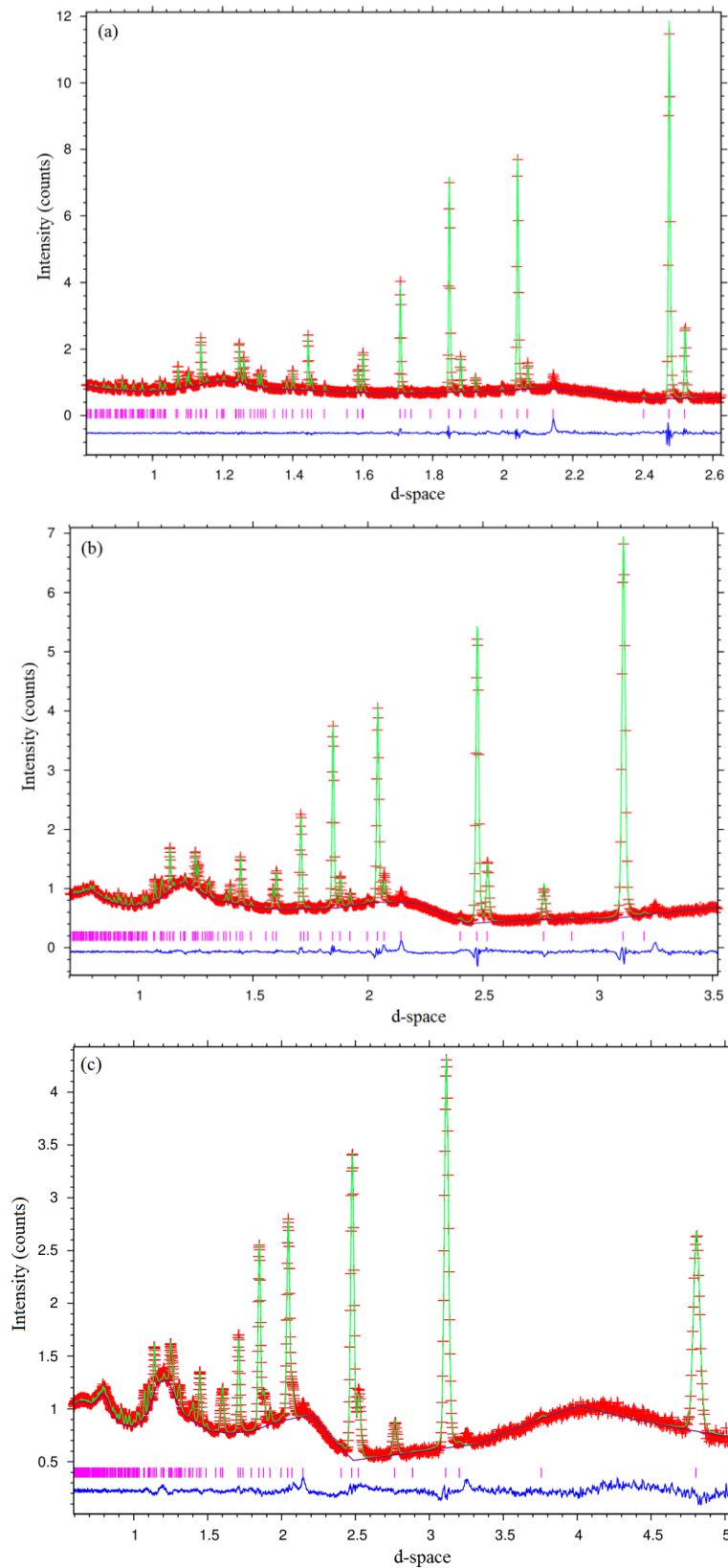


Figure 15. Rietveld refinement using powder neutron diffraction data collected on POLARIS for BiOCuTe at 673 K from (a) backscattering bank ($2\theta = 146.72^\circ$), (b) 92.59° bank and (c) low angle bank ($2\theta = 52.21^\circ$). Key: observed data (red cross); difference curve (blue line); calculated pattern (green line) and reflection positions (pink markers).

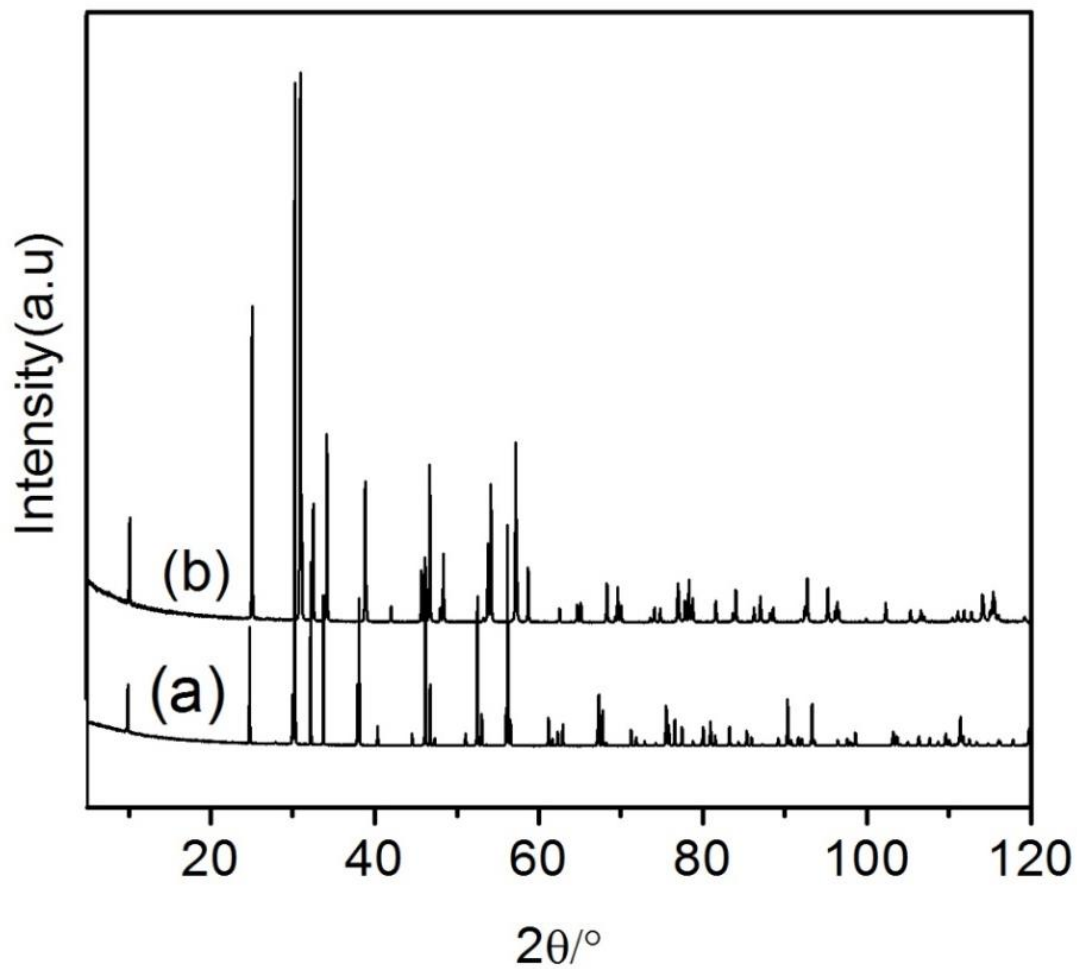


Figure 16. Powder X-ray patterns of (a) BiOCuS and (b) BiOCuSe.

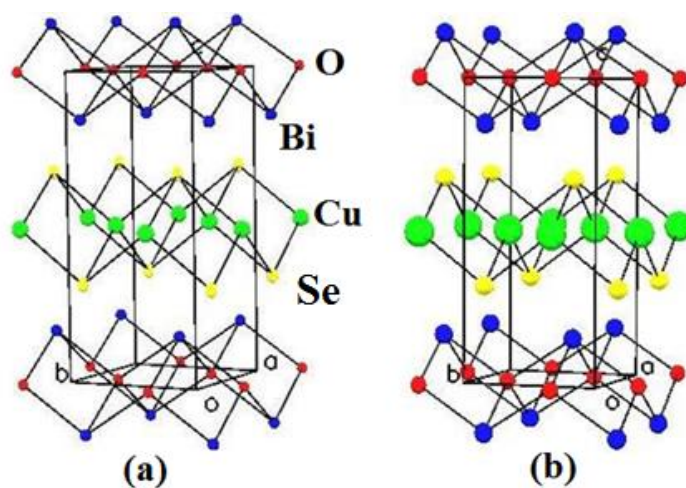


Figure 17. Thermal ellipsoids of atoms in BiOCuSe at (a) 293K and (b) 673K.

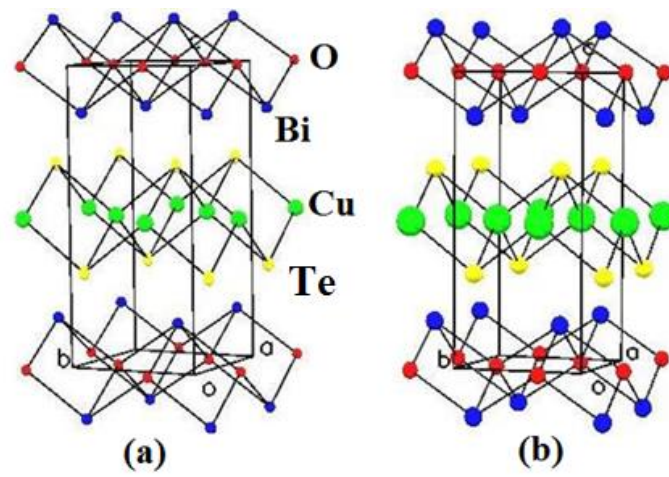


Figure 18. Thermal ellipsoids of atoms in BiOCuSe at (a) 293K and (b) 673K.

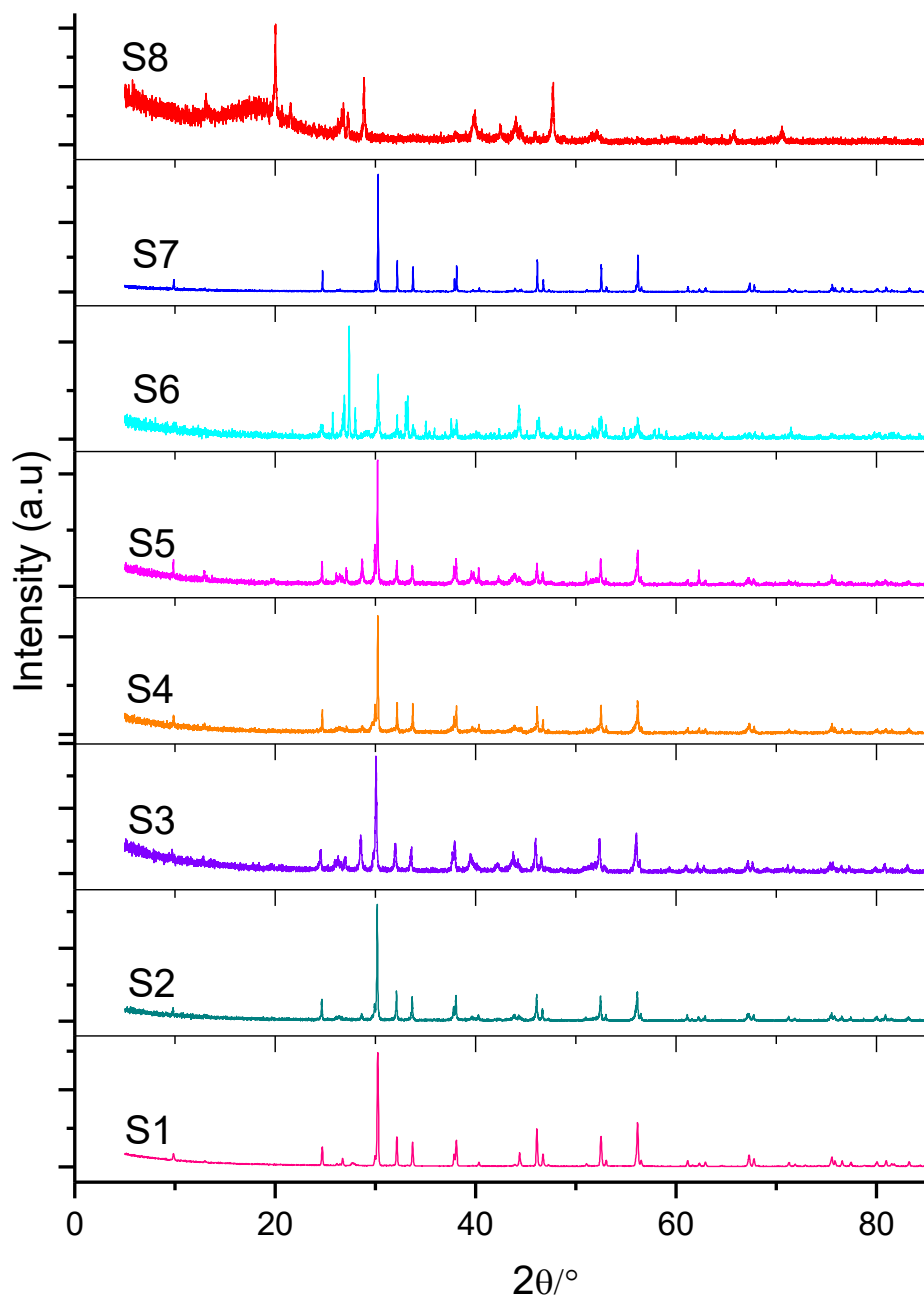


Figure 19. X-ray patterns of all batches of Bi₂O₂Cu₄Se₃.

Table 10. Reaction time and temperatures of all batches of $\text{Bi}_2\text{YO}_4\text{Cu}_2\text{Se}_2$.

Sample	Reaction temperature (K) and time (hrs)	Notes
S1	773 K - 10hrs	
S2	773 K - 10hrs and then 1123 K - 22hrs	
S3	1173 K - 24hrs-direct -in-out	
S4	1173 K - 114hrs - direct in and out	
S5	623 K-20hrs – 773 K-8.5hrs and then 1123 K-30hrs	
S6	623 K - 20hrs and then 773 K - 9hrs	
S7	623 K - 20hrs and then 773 K - 17hrs	
S8	623 K - 20hrs; 773 K- 17hrs and then 823 K - 48hrs	
S9	623 K - 20hrs; 773 K- 17hrs; 823 K - 48hrs and then 1123 K - 40hrs	
S10	623 K - 20hrs; 773 K- 17hrs and then 1073 K-48hrs	
S11	623 K - 20hrs; 773 K- 17hrs - 1073 K-48hrs and then 1123 K-40hrs	
S12	673 K-19hrs-1073 K-5hrs	
S13	cool-pressed – 673 K-19hrs	$\text{Bi}_2\text{Y}_{1.05}\text{O}_4\text{Cu}_2\text{Se}_2$
S14	cool-pressed 673 K-19hrs-3 K/min-cool-pressed and then 1073 K-4hrs	$\text{Bi}_2\text{Y}_{1.05}\text{O}_4\text{Cu}_2\text{Se}_2$
S15	673 K-19hrs-1073 K- 4hrs-10 K/min and then 0.5hrs-1°C min	
S16	pellet-673 K-19hrs-3 K/min-pellet 1073 K-4hrs-10 K/min-pellet-1073 K - 4.5hrs, 1 K/min	
S17	pellet-673 K-19hrs-3 K/min-pellet-1073 K-4.5hrs-1 K/min	$\text{Bi}_2\text{YO}_{3.5}\text{Cu}_2\text{Se}_2$

Appendix B

This appendix includes additional data and results relating to Chapter 4: Substitution of Divalent Cations on BiOCuSe and Synthesis by Mechanical Ball Milling.

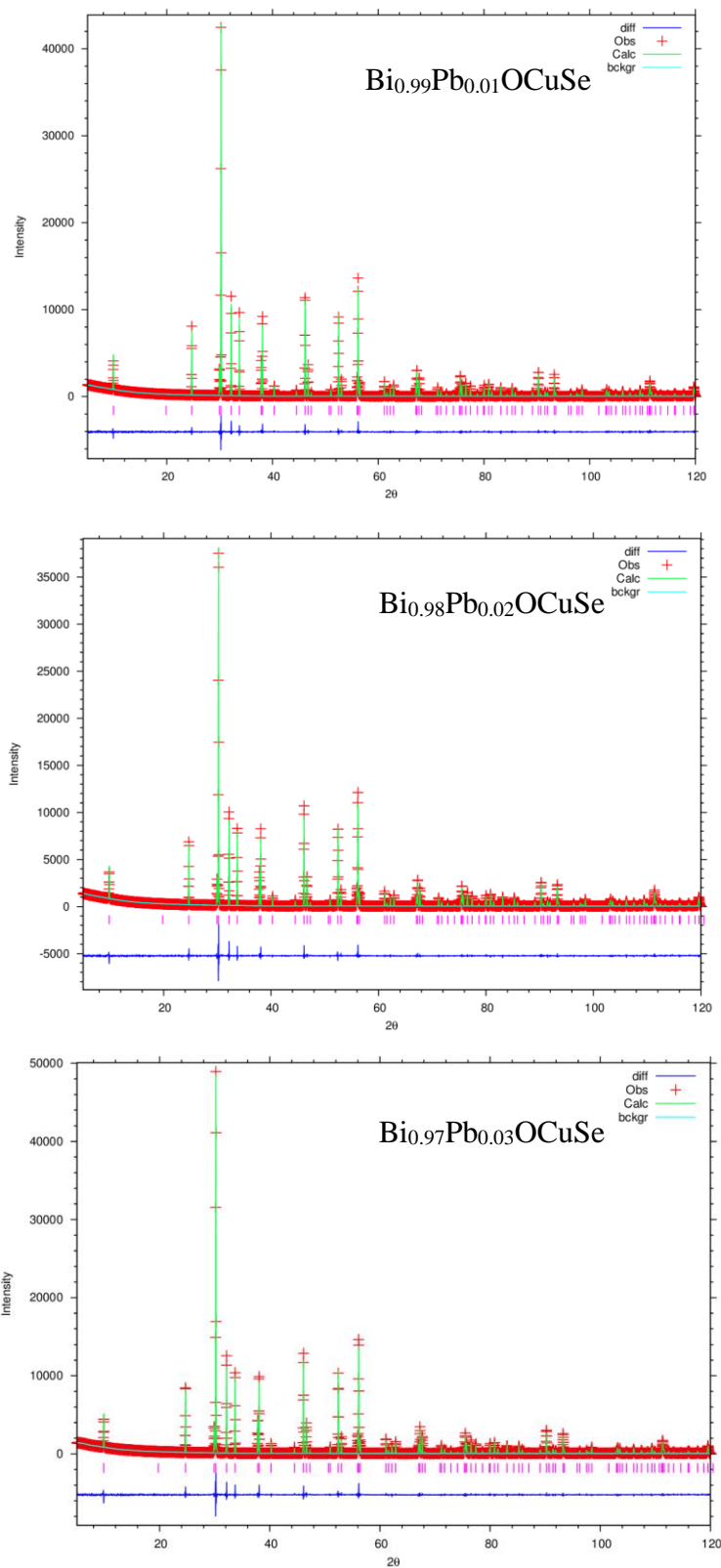


Figure 20. Rietveld refinements using powder X-ray diffraction data for $\text{Bi}_{1-x}\text{Pb}_x\text{OCuSe}$ ($0.01 \leq x \leq 0.03$)

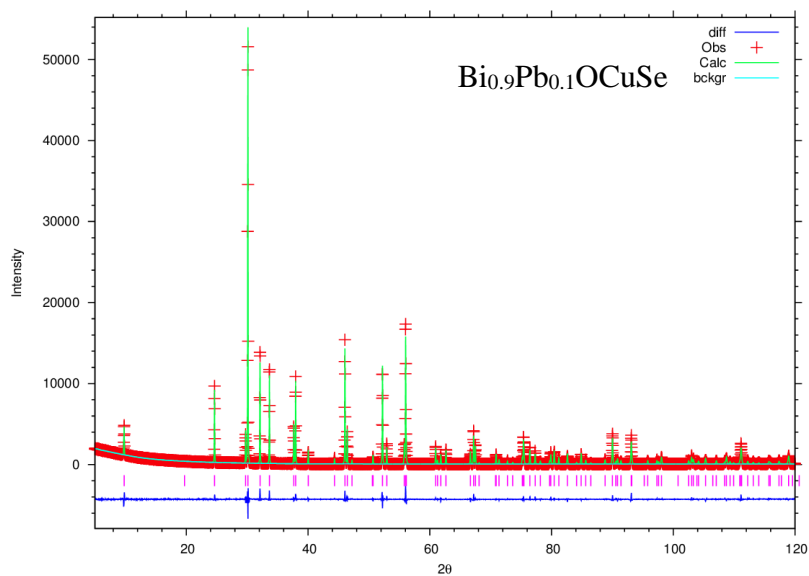
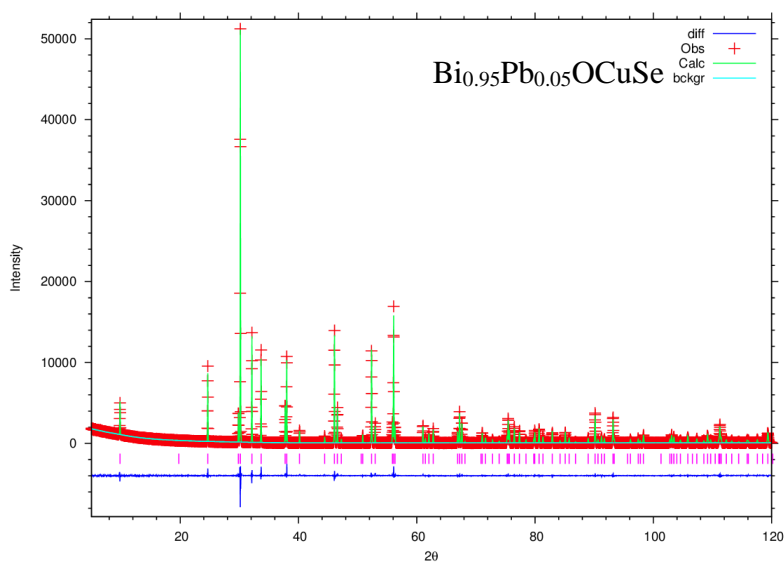
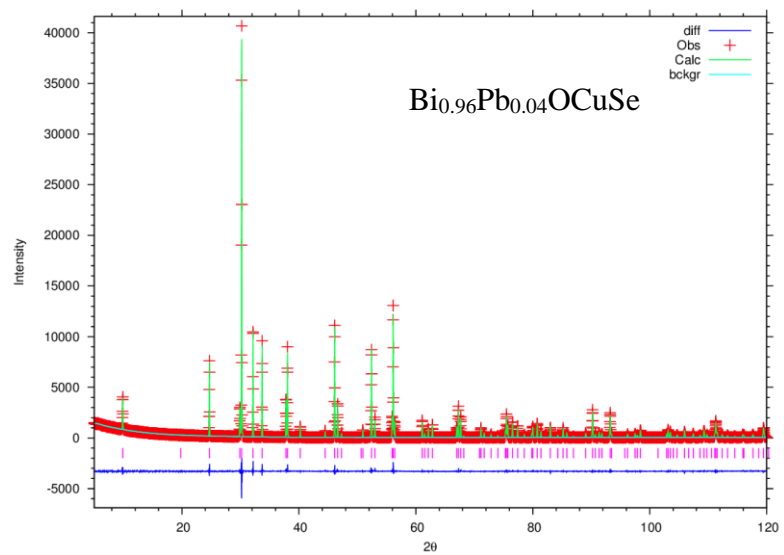


Figure 21. Rietveld refinements using powder X-ray diffraction data for Bi_{1-x}Pb_xOCuSe (0.04 ≤ x ≤ 0.10)

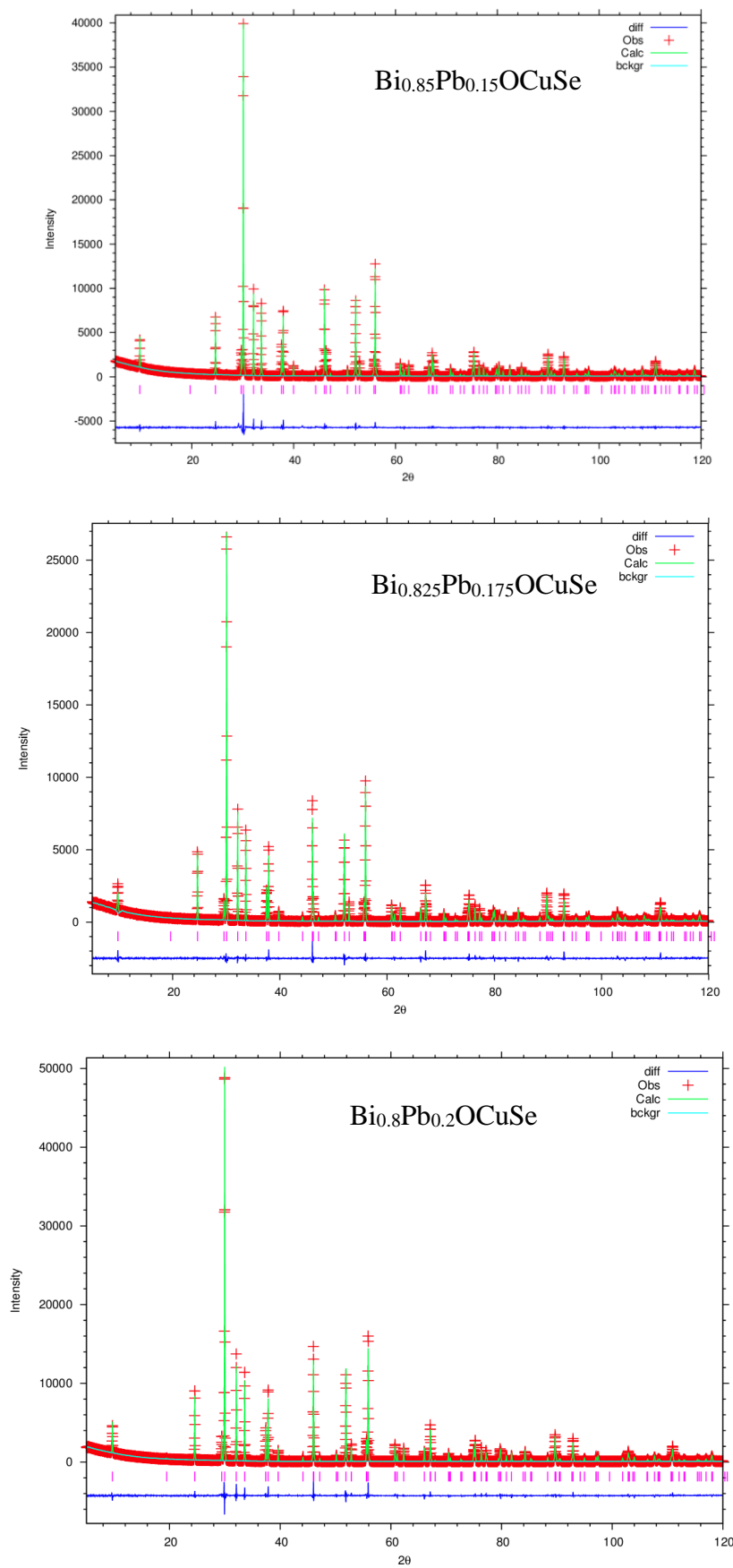


Figure 22. Rietveld refinements using powder X-ray diffraction data for $\text{Bi}_{1-x}\text{Pb}_x\text{OCuSe}$ ($0.15 \leq x \leq 0.20$)

Table 11. Final refined parameters using powder X-ray diffraction data for $\text{Bi}_{1-x}\text{Pb}_x\text{OCuSe}$ ($0 \leq x \leq 0.2$). Site occupancy factors for Bi and Pb were fixed at the stoichiometric composition.

		x in $\text{Bi}_{1-x}\text{Pb}_x\text{OCuSe}$				
		0.0	0.01	0.02	0.03	0.04
	$a/\text{\AA}$	3.93026(2)	3.93077(1)	3.93117(2)	3.93202(2)	3.93271(1)
	$c/\text{\AA}$	8.93193(5)	8.93786(4)	8.94302(6)	8.94846(5)	8.95591(4)
Bi/Pb ^a	z	0.14021(6)	0.14005(6)	0.13992(7)	0.13979(7)	0.13957(6)
	$U_{iso}/\text{\AA}^2$	0.0012(2)	0.0023(3)	0.0013(2)	0.0040(2)	0.0019(2)
O ^b	$U_{iso}/\text{\AA}^2$	0.003(2)	0.0048(2)	0.0034(3)	0.008(3)	0.007(3)
Cu ^c	$U_{iso}/\text{\AA}^2$	0.0104(5)	0.0113(6)	0.0099(6)	0.0129(6)	0.0107(6)
Se ^a	z	0.6756(2)	0.6753(2)	0.6748(2)	0.6744(2)	0.6747(2)
	$U_{iso}/\text{\AA}^2$	0.0011(4)	0.0022(4)	0.0014(4)	0.0039(4)	0.003(4)
$R_{wp}/\%$		8.980	9.979	10.380	10.340	10.040
		x in $\text{Bi}_{1-x}\text{Pb}_x\text{OCuSe}$				
		0.05	0.10	0.15	0.175	0.20
	$a/\text{\AA}$	3.93324(1)	3.93629(2)	3.93719(3)	3.93881(3)	3.93867(2)
	$c/\text{\AA}$	8.96231(4)	8.99652(7)	9.01514(9)	9.05608(9)	9.07746(8)
Bi/Pb ^a	z	0.13946(6)	0.13855(8)	0.13810(8)	0.13725(8)	0.13707(8)
	$U_{iso}/\text{\AA}^2$	0.0010(2)	0.0027(2)	0.0015(2)	0.0061(5)	0.0054(2)
O ^b	$U_{iso}/\text{\AA}^2$	0.006(3)	0.007(2)	0.003(3)	0.004(3)	0.004(3)
Cu ^c	$U_{iso}/\text{\AA}^2$	0.0095(6)	0.010(7)	0.0083(7)	0.012(1)	0.0116(7)
Se ^a	z	0.6741(2)	0.6719(2)	0.6712(2)	0.6690(2)	0.6679(2)
	$U_{iso}/\text{\AA}^2$	0.0011(3)	0.0019(5)	0.0013(5)	0.0032(5)	0.0055(5)
$R_{wp}/\%$		9.450	11.710	10.410	11.460	10.750

^aBi/Pb and Se on 2(c) (1/4, 1/4, z); ^bO on 2(a) (3/4, 1/4, 0); ^cCu on 2(b) (3/4, 1/4, 1/2).

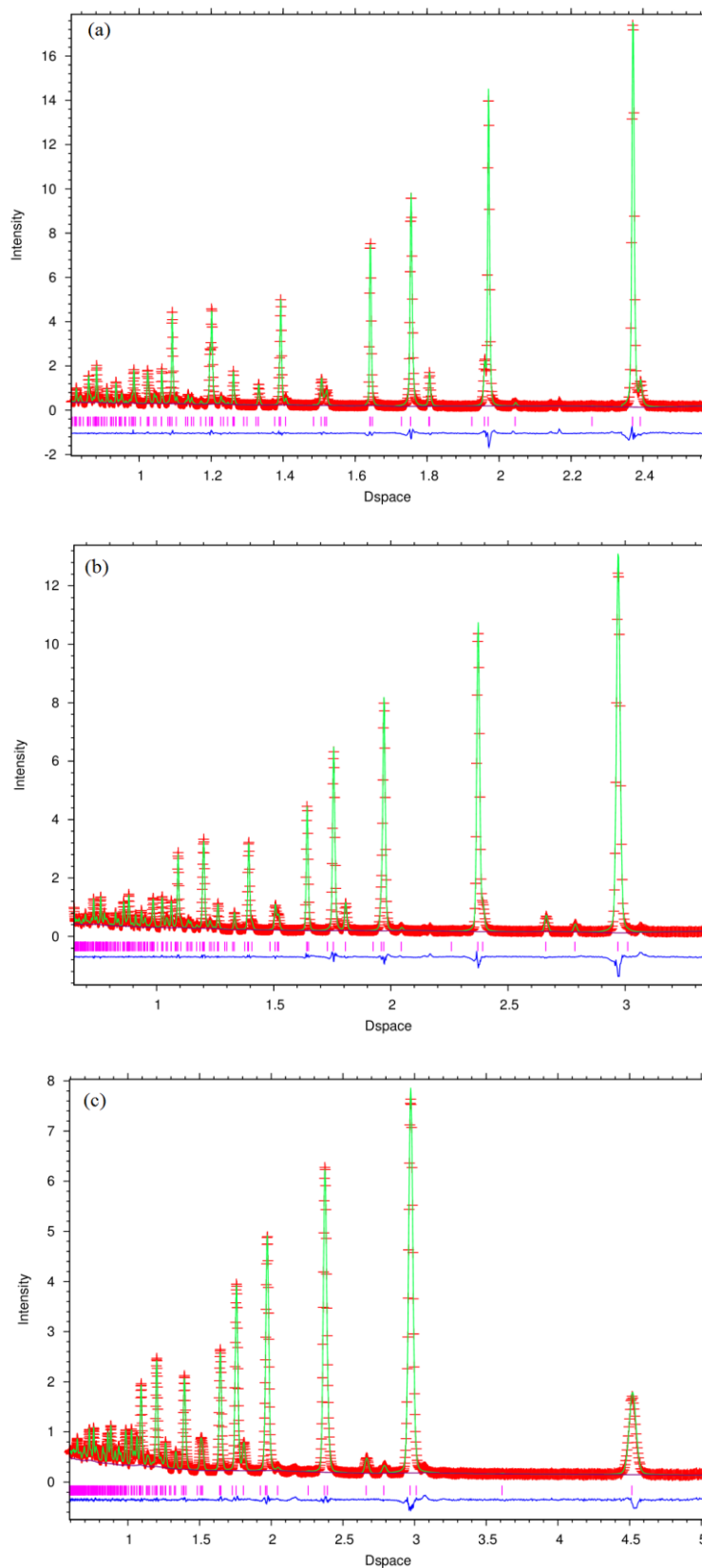


Figure 23. Rietveld refinement using powder neutron diffraction data collected on POLARIS for $\text{Bi}_{1.85}\text{Pb}_{0.15}\text{OCuSe}$ at room temperature from (a) backscattering bank ($2\theta = 146.72^\circ$), (b) 92.59° bank and (c) low angle bank ($2\theta = 52.21^\circ$). Key: observed data (red cross); difference curve (blue line); calculated pattern (green line) and reflection positions (pink markers)

Table 12. Selected bond lengths and angles from powder X-ray diffraction data for $\text{Bi}_{1-x}\text{Pb}_x\text{OCuSe}$ ($0 \leq x \leq 0.20$).

Sample	Bond lengths		
	Bi-O (Å)	Bi-Se (Å)	Cu-Se (Å)
x=0	2.3302(2)	3.2298(7)	2.5140(8)
x=0.01	2.3301(0)	3.2327(1)	2.5132(1)
x=0.02	2.3301(3)	3.2361(9)	2.5115(9)
x=0.03	2.3302(3)	3.2397(8)	2.5100(9)
x=0.04	2.3300(3)	3.2403(8)	2.5129(9)
x=0.05	2.3302(3)	3.2448(8)	2.5102(9)
x=0.10	2.3296(4)	3.2640(1)	2.5031(1)
x=0.15	2.3302(4)	3.2710(1)	2.5015(1)
X=0.175	2.3288(4)	3.2922(1)	2.4937(1)
x=0.20	2.3294(4)	3.3000(1)	2.4904(1)
Sample	Bond angles		
	O-Bi-O (deg.)	Se-Cu-Se (deg.)	Se-Cu-Se (deg.)
x=0	114.98(2)	102.83(5)	112.89(3)
x=0.01	115.01(0)	102.89(0)	112.86(0)
x=0.02	115.04(3)	103.00(5)	112.79(3)
x=0.03	115.07(2)	103.12(5)	112.74(3)
x=0.04	115.11(2)	103.01(5)	112.79(3)
x=0.05	115.13(2)	103.15(5)	112.72(3)
x=0.10	115.31(3)	103.68(6)	112.44(3)
x=0.15	115.30(3)	103.76(7)	112.40(4)
X=0.175	115.49(3)	104.33(7)	112.10(4)
x=0.20	115.43(3)	104.52(6)	112.00(3)

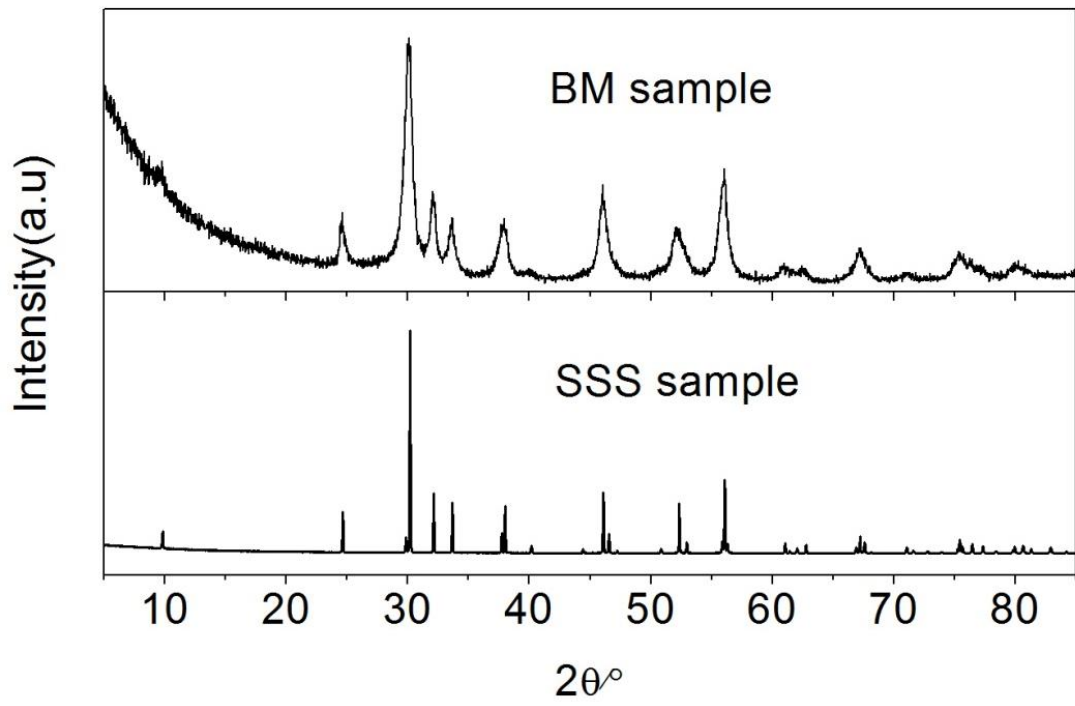


Figure 24. Powder X-ray diffraction patterns of BM and SSS $\text{Bi}_{1.95}\text{Pb}_{0.05}\text{OCuSe}$.

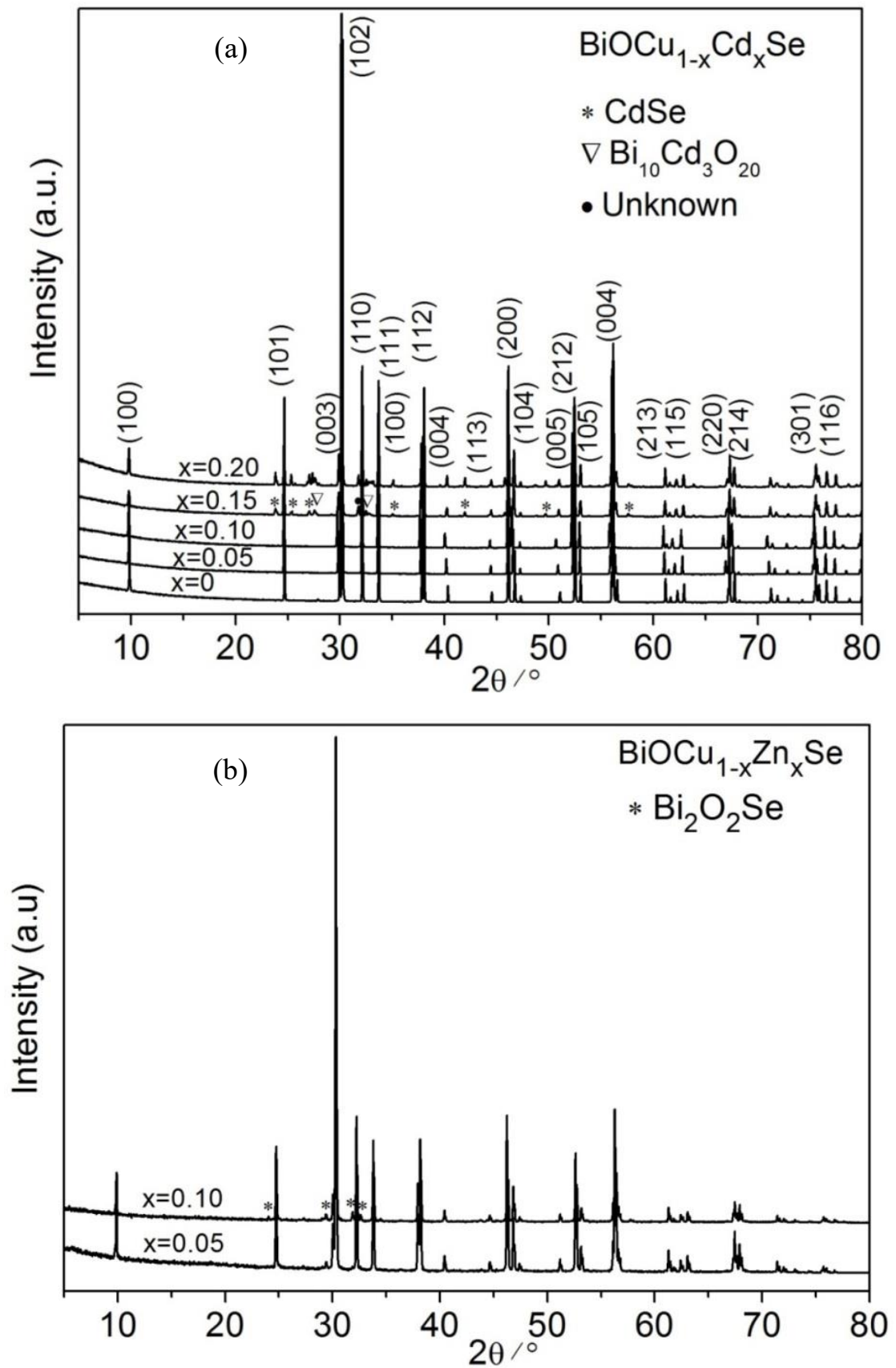


Figure 25. Powder X-ray diffraction patterns of (a) $\text{BiOCu}_{1-x}\text{Cd}_x\text{Se}$ ($x = 0.05; 0.10; 0.15$ and 0.20) and (b) $\text{BiOCu}_{1-x}\text{Zn}_x\text{Se}$ ($x = 0.05; 0.10$)

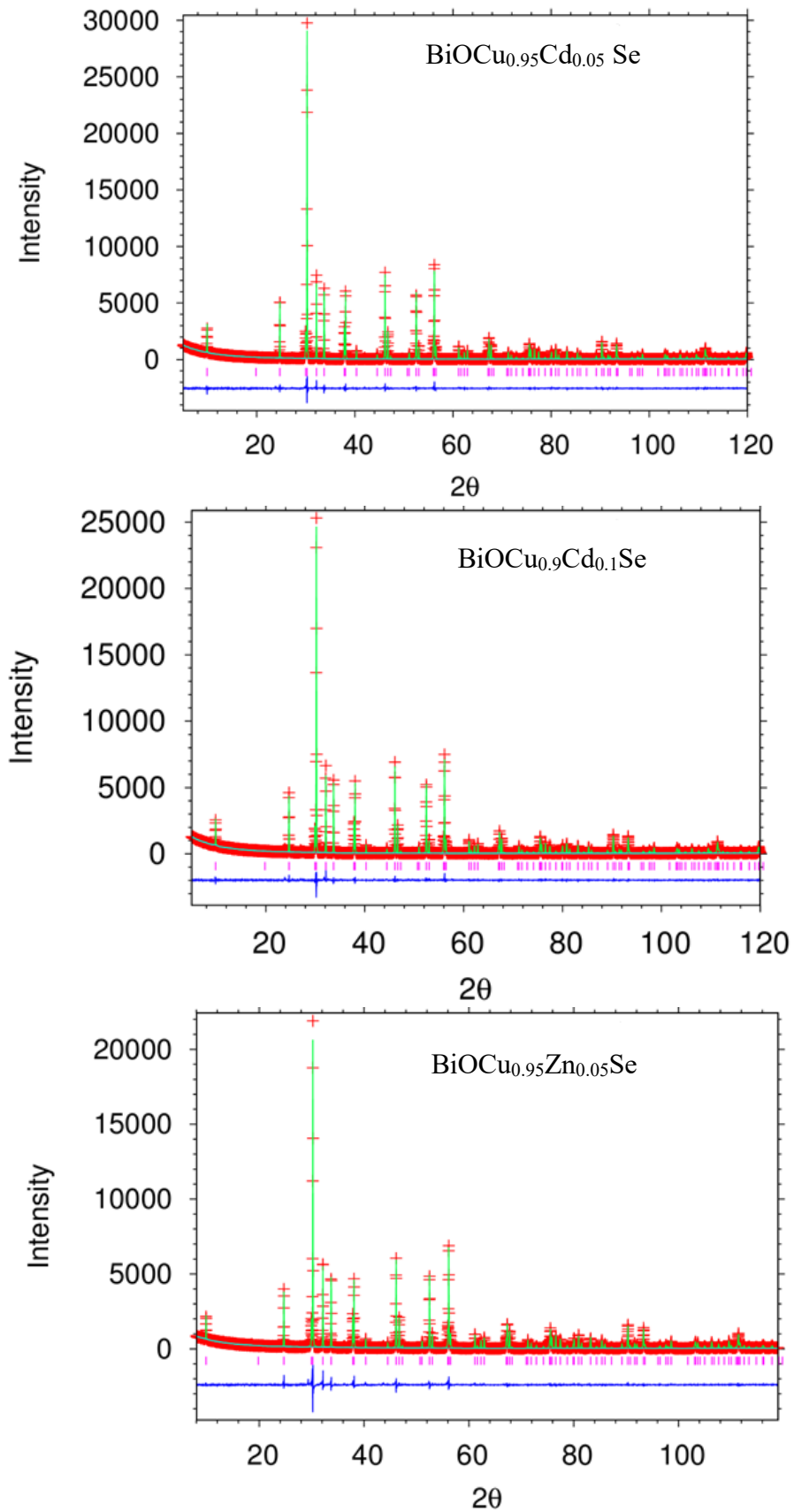


Figure 26. Rietveld refinements using power diffraction data for $\text{BiOCu}_{1-x}\text{M}_x\text{Se}$ ($M = \text{Cd}$, and Zn & $x = 0.05$ and 0.10): the observed XRD pattern (red cross); difference between observed and simulated patterns (blue line); simulated pattern (light green line); background (light blue line) and Bragg diffraction positions (pink line).

Table 13. Final refined parameters for BiOCu_{1-x}M_xSe (M = Cd, and Zn & x = 0; 0.05; and 0.10).

Site occupancy factors for Cu and Cd/Zn were fixed at the stoichiometric composition.

		x in BiOCu _{1-x} Cd _x Se			BiOCu _{0.95} Zn _{0.05} Se
		0.0	0.05	0.10	
	<i>a</i> /Å	3.93026(2)	3.92978(1)	3.93065(1)	3.928871(42)
	<i>c</i> /Å	8.93193(5)	8.93321(5)	8.94043(1)	8.9299(1)
Cu/Cd/Zn ^a	<i>U</i> _{iso} /Å ²	0.0104(5)	0.0179(7)	0.0221(7)	0.010(1)
Bi ^b	<i>z</i>	0.14021(6)	0.14004(7)	0.13974(7)	0.1399(1)
	<i>U</i> _{iso} /Å ²	0.0012(2)	0.0048(2)	0.0038(2)	0.0021(6)
O ^c	<i>U</i> _{iso} /Å ²	0.003(2)	0.001(2)	0.001(3)	0.022(5)
Se ^b	<i>z</i>	0.6756(2)	0.6757(2)	0.6759(2)	0.6756(3)
	<i>U</i> _{iso} /Å ²	0.0011(4)	0.0056(5)	0.0029(5)	0.0022(9)
R _{wp} /%		8.980	10.71	10.68	14.25

^aCu/Cd/Zn on 2(*b*) (3/4, 1/4, 1/2), ^bBi and Se on 2(*c*) (1/4, 1/4, *z*); ^cO on 2(*a*) (3/4, 1/4, 0)

Appendix C

This appendix contains additional data and results relating to Chapter 5: Structures and Thermoelectric Properties of n-type Oxychalcogenide $\text{Bi}_2\text{O}_2\text{Ch}$ ($\text{Ch} = \text{Te}, \text{Se}$) Materials.

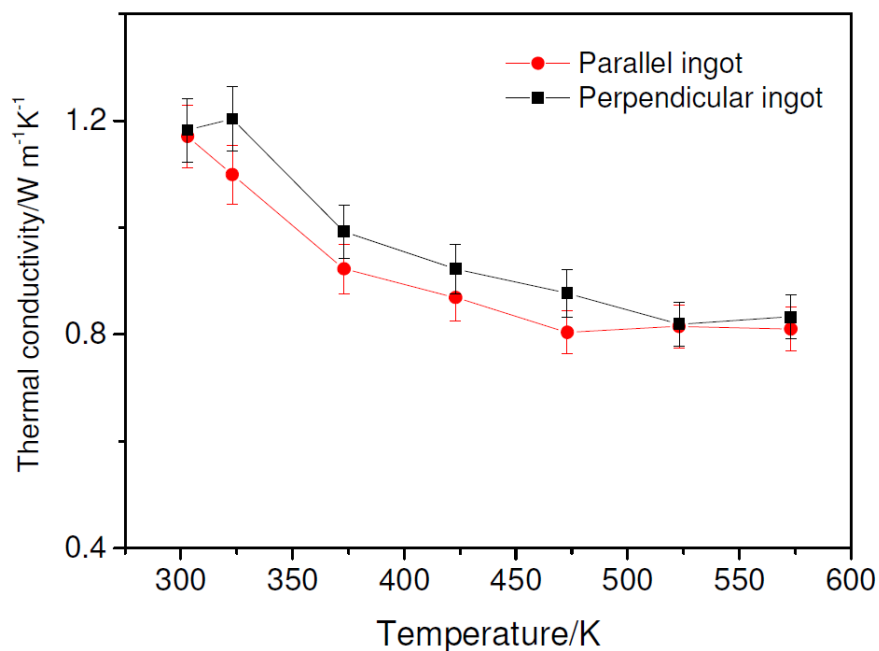


Figure 27. Thermal conductivity of $\text{Bi}_2\text{O}_2\text{Te}$ measured using square ingots cut parallel and perpendicular to the direction of pressing.

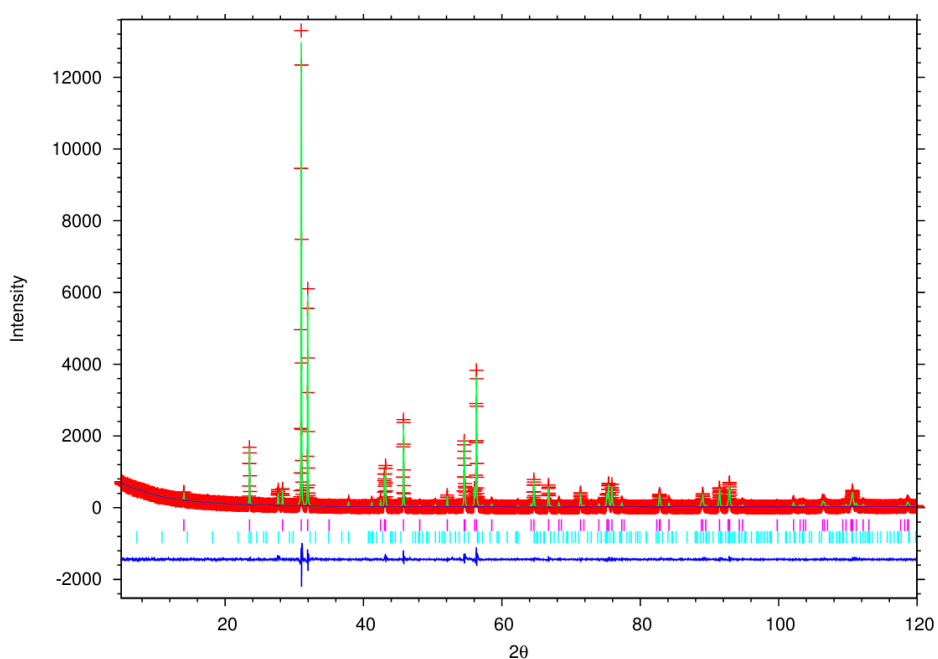


Figure 28. Rietveld refinement using powder X-ray diffraction data for $\text{Bi}_2\text{O}_2\text{Te}_{0.75}\text{Se}_{0.25}$. Key: observed data (red cross); difference curve (blue line); calculated pattern (green line) and reflection positions of $\text{Bi}_2\text{O}_2\text{Te}_{0.75}\text{Se}_{0.25}$ (pink markers).

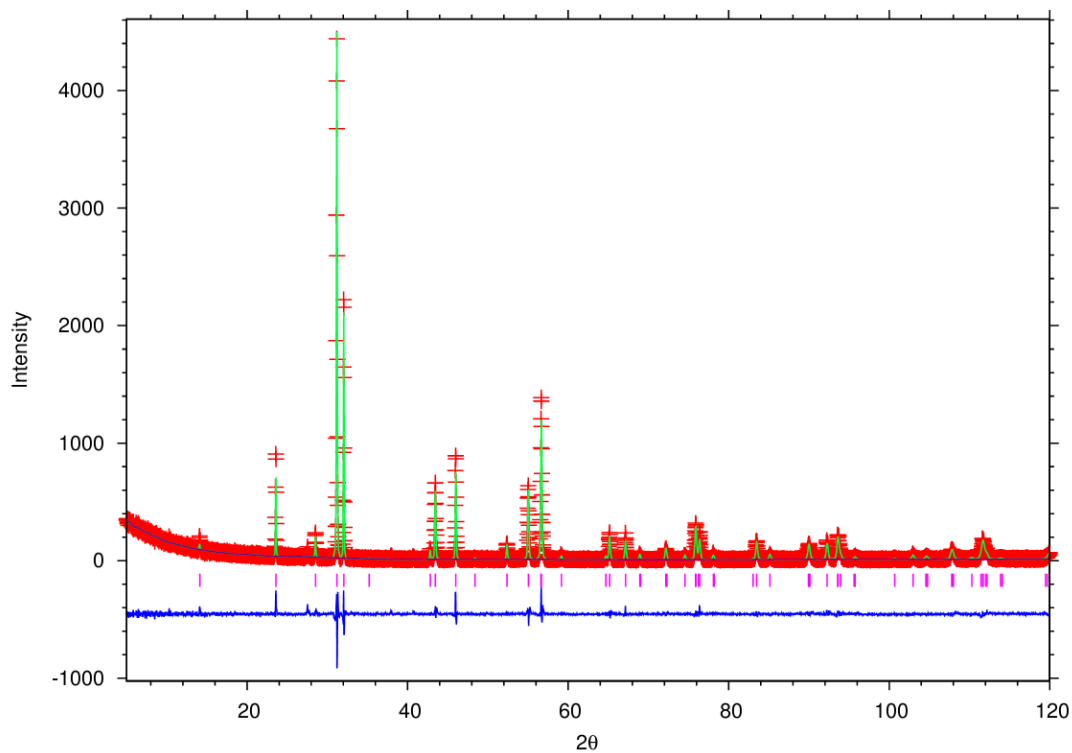


Figure 29. Rietveld refinement using powder X-ray diffraction data for $\text{Bi}_2\text{O}_2\text{Te}_{0.5}\text{Se}_{0.5}$. Key: observed data (red cross); difference curve (blue line); calculated pattern (green line) and reflection positions of $\text{Bi}_2\text{O}_2\text{Te}_{0.5}\text{Se}_{0.5}$ (pink markers).

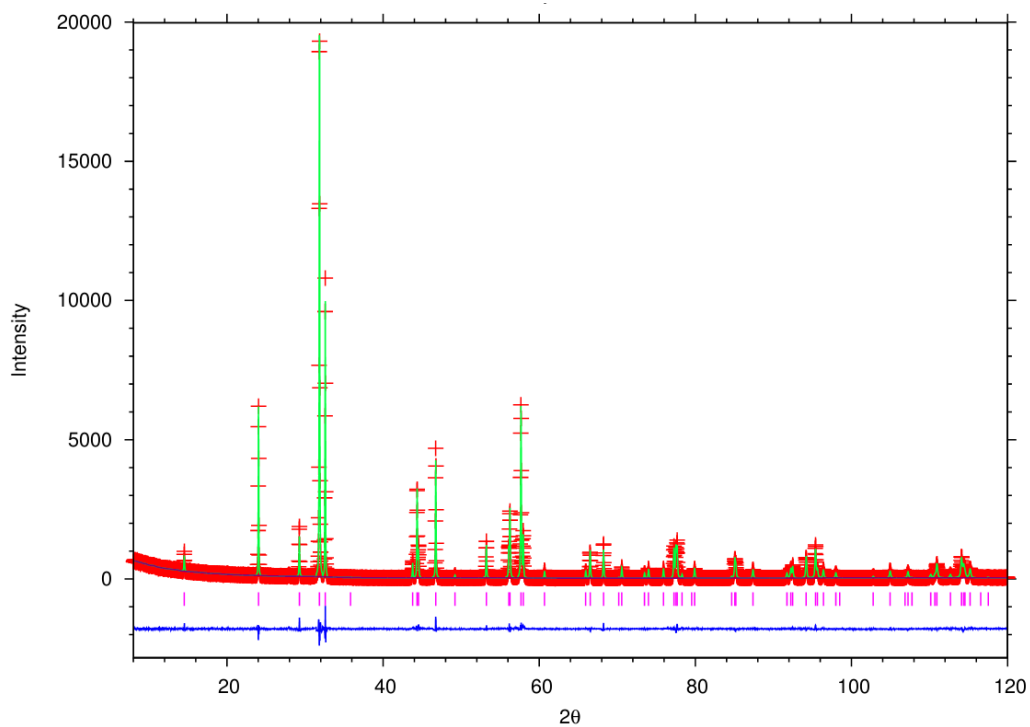


Figure 30. Rietveld refinement using powder X-ray diffraction data for $\text{Bi}_2\text{O}_2\text{Se}$. Key: observed data (red cross); difference curve (blue line); calculated pattern (green line) and reflection positions of $\text{Bi}_2\text{O}_2\text{Se}$ (pink markers).

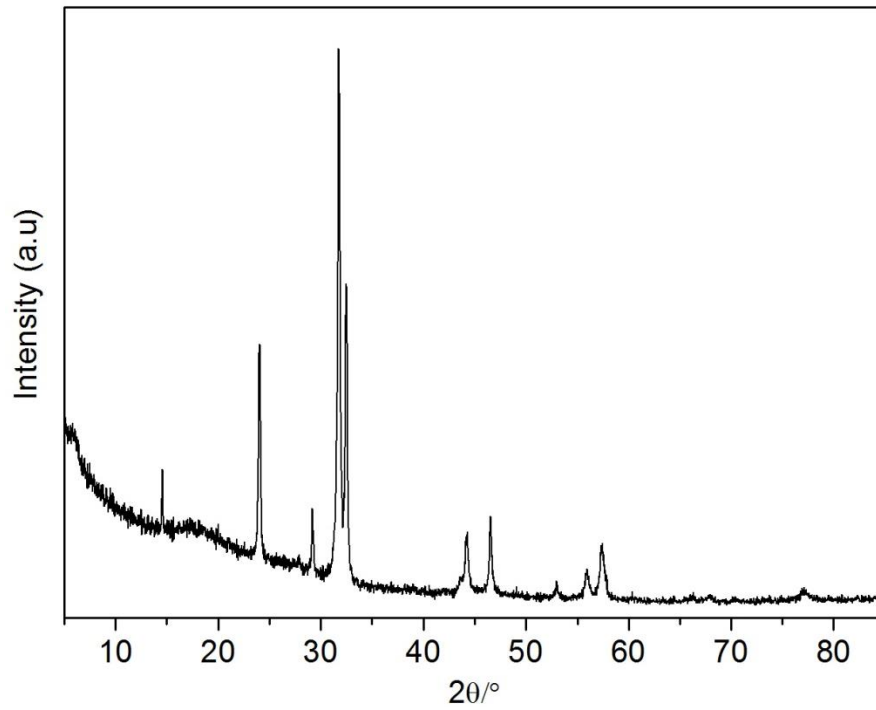


Figure 31. XRD pattern of hot pressed $\text{Bi}_2\text{O}_2\text{Se}$ pellet.

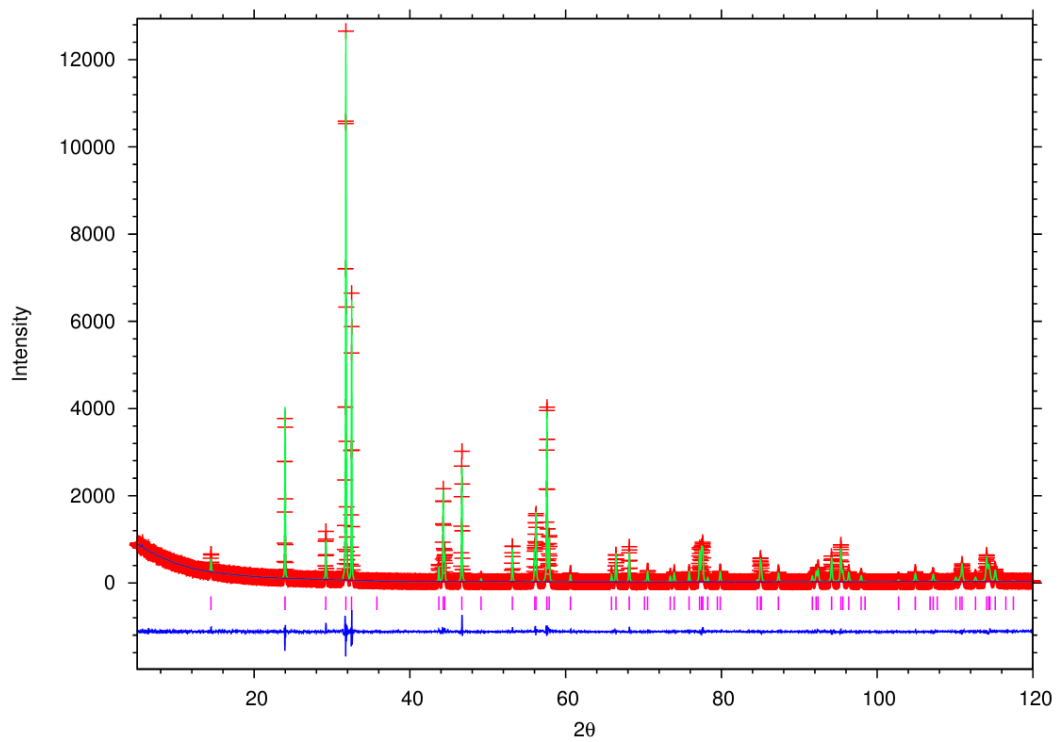


Figure 32. Rietveld refinement using powder X-ray diffraction data for $\text{Bi}_2\text{O}_2\text{Se}_{1.07}$. Key: observed data (red cross); difference curve (blue line); calculated pattern (green line) and reflection positions of $\text{Bi}_2\text{O}_2\text{Se}_{1.07}$ (pink markers).

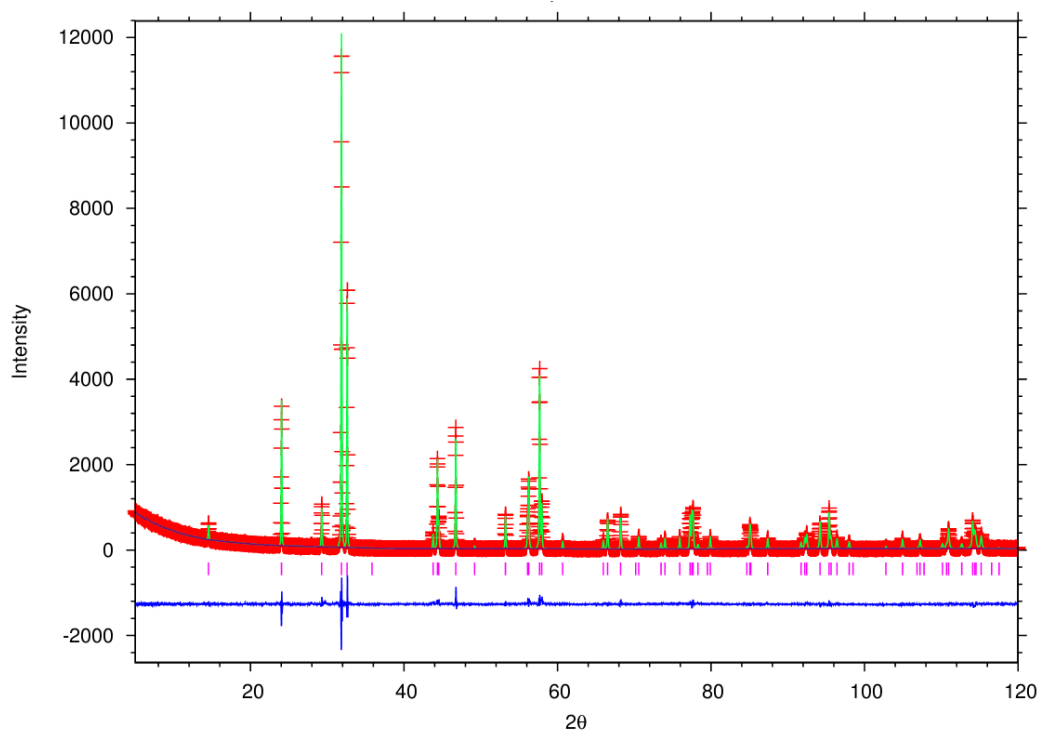


Figure 33. Rietveld refinement using powder X-ray diffraction data for $\text{Bi}_2\text{O}_2\text{Se}_{1.10}$. Key: observed data (red cross); difference curve (blue line); calculated pattern (green line) and reflection positions of $\text{Bi}_2\text{O}_2\text{Se}_{1.10}$ (pink markers).

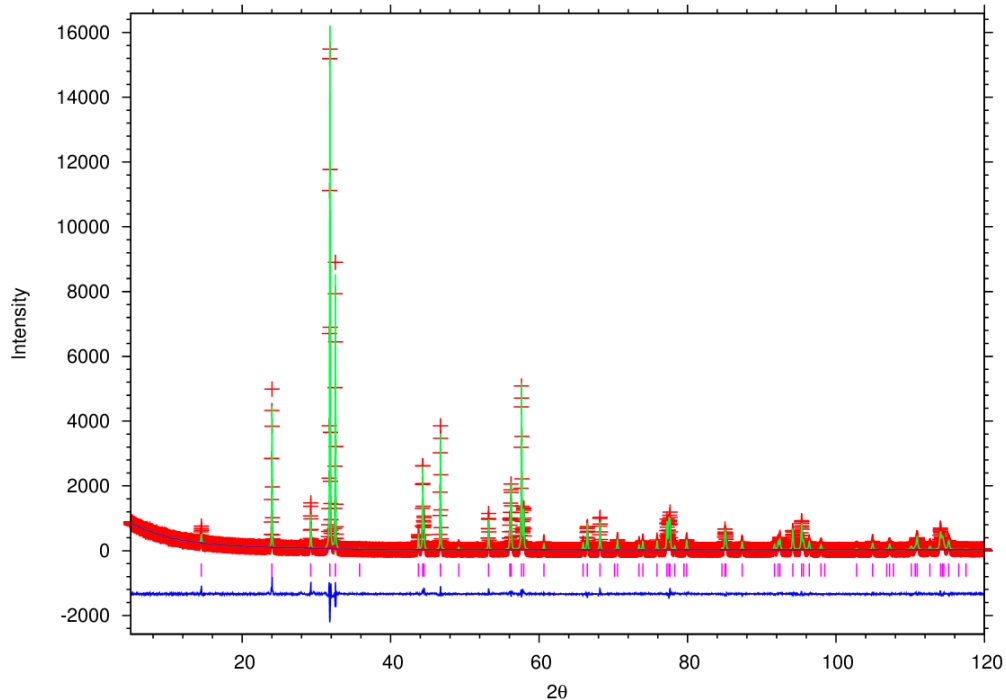


Figure 34. Rietveld refinement using powder X-ray diffraction data for $\text{Bi}_2\text{O}_2\text{Se}_{1.15}$. Key: observed data (red cross); difference curve (blue line); calculated pattern (green line) and reflection positions of $\text{Bi}_2\text{O}_2\text{Se}_{1.15}$ (pink markers).

Table 14. Selected bond lengths and angles from powder X-ray diffraction data for $\text{Bi}_2\text{O}_2\text{Se}_{1\pm\delta}$ ($0.05 \leq \delta \leq 0.15$).

Se content in $\text{Bi}_2\text{O}_2\text{Se}_{1\pm\delta}$	Bond length			Bond angle	
	Bi-Bi (Å)	Bi-O (Å)	Bi-Se (Å)	O-Bi-O (deg.)	Bi-O-Bi (deg.)
0.95	3.7305(2)	2.3164(1)	3.2782(2)	113.98(1)	107.27(1)
1.00	3.7333(9)	2.3176(4)	3.2773(4)	113.90(3)	107.30(1)
1.07	3.7333(1)	2.3175(4)	3.2764(4)	113.88(3)	107.31(1)
1.10	3.7343(1)	2.3181(4)	3.2771(4)	113.88(3)	107.31(1)
1.15	3.7360(1)	2.3186(4)	3.2759(4)	113.81(3)	107.35(1)

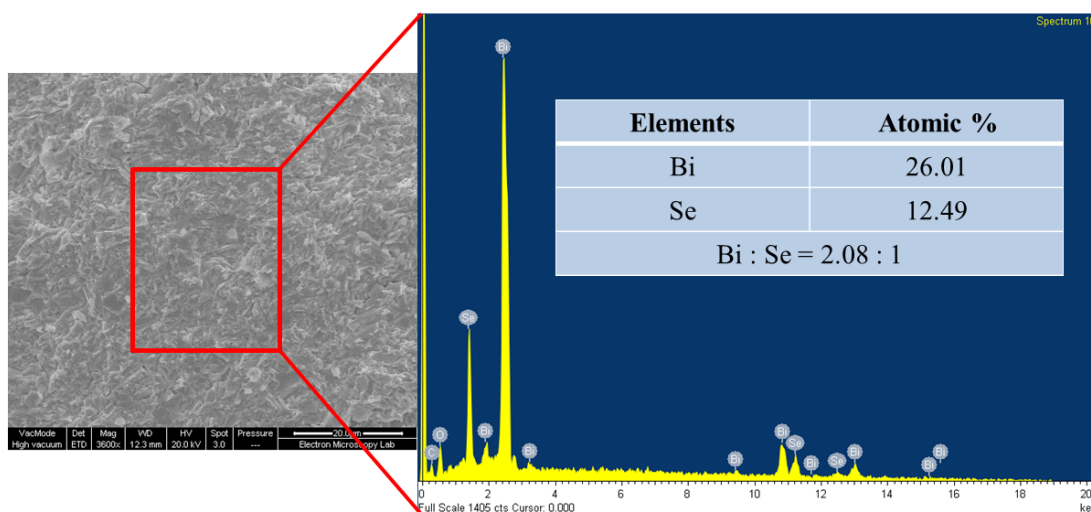


Figure 35. EDAX spectrum of prepared $\text{Bi}_2\text{O}_2\text{Se}_{1.07}$ pellet.

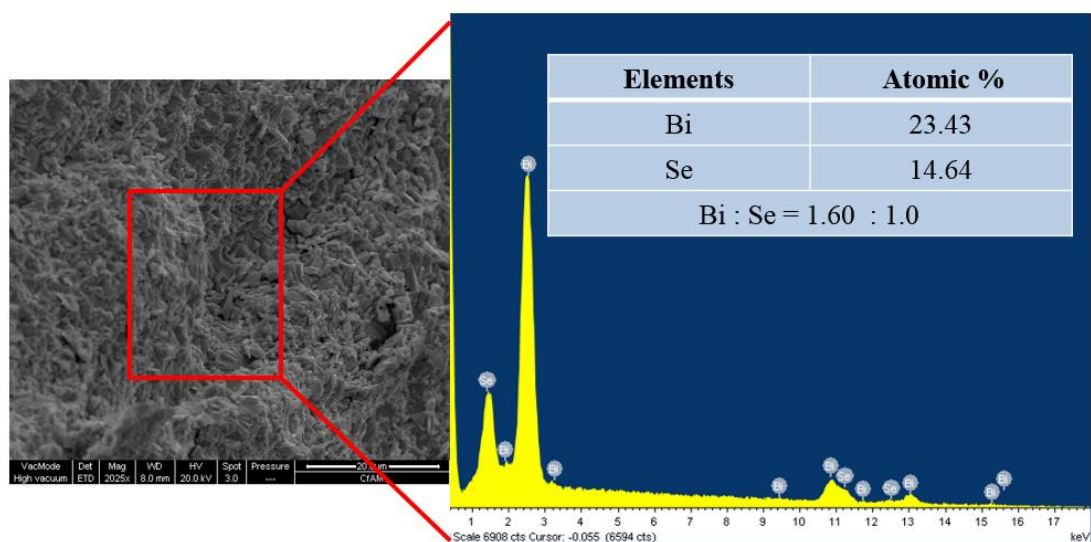


Figure 36. EDAX spectrum of prepared $\text{Bi}_2\text{O}_2\text{Se}_{1.10}$ pellet.

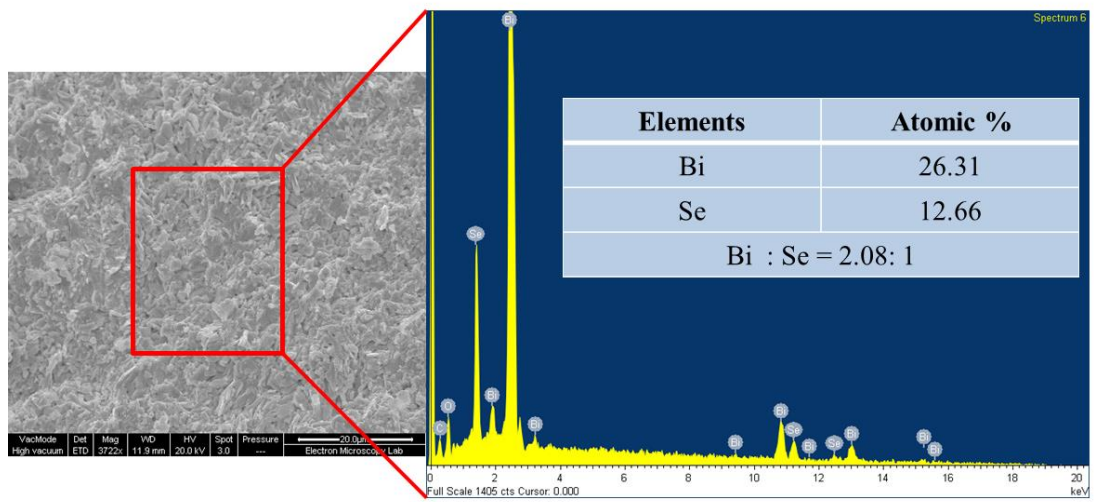


Figure 37. EDAX spectrum of prepared $\text{Bi}_2\text{O}_2\text{Se}_{1.15}$ pellet.